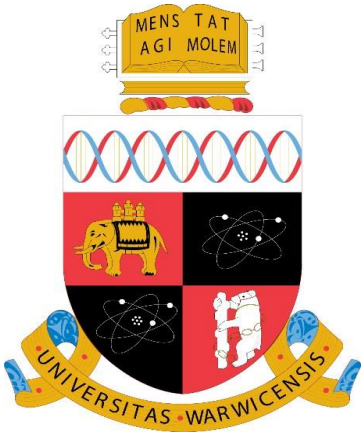

Characterisation of organic solids using solid-state NMR spectroscopy

by

Anjali Krishna Menakath

Thesis

Submitted to the University of Warwick

for the degree of

Doctor of Philosophy

Department of Physics

September 2019

THE UNIVERSITY OF
WARWICK

Contents

List of Figures

Lst of Tables

Acknowledgments

Completion of this Ph.D. has only been made possible through the extremely valuable contributions of several notable people. First and foremost, I would like to thank my supervisor, Professor Steven P. Brown, for giving this incredible opportunity to pursue a Ph.D. with him and for allowing me to present my research on various occasions. His patience with my many mistakes and silly questions over the last four years is admirable. His constant reassurance, encouragement, and supervision have helped me tremendously; for that, I thank him very much. I also thank him for patiently reading my thesis.

I am very grateful to Dr T.G Ajith Kumar, NCL, India, for introducing me to the wonders of solid-state NMR. I am also very thankful to my feedback supervisor Dr Józef Lewandoski, for all the advice given to me on my reports and poster.

I am indebted to all my collaborators for their assistance. My thanks go to Dr Helen Blade and Dr Leslie Huges from AstraZeneca, Dr Charles Blundell, and Dr Hugh. R. W. Dannatt from C4X Discovery for TFA samples and their advice and support with the scoring function project. I am grateful to Dr James T. A. Jones (Bruker) and Rebecca Williams (DSTL) for the SBA:iPMPA samples and particularly, James for his insightful discussions about the functionalised mesoporous materials. I must thank Luning Wang and his supervisor Dr Bryan Eichhorn (University of Maryland) for the SEI samples and their assistance in the research performed with them. My sincere gratitude to Dr Dinu Iuga, for his help with 850 MHz measurements. Furthermore, I would like to thank Dr Albert Bartok-Partay (CCPNC) for his constant willingness to assist with the computational work.

I want to acknowledge the University of Warwick for Chancellor's international scholarship, which gave me the chance to participate in exciting scientific research.

To the members of Warwick solid-state NMR group, I would like to thank Dr Trent Franks for teaching me about pulse programming and for fixing spectrometer problems. Sarah, Zainab, and Kiran for helping with my grammar. Thanks to Sam, Emily, Ben, Ann, Gemma, Nick, Adam, Jacquelline, Angello, Becky, and to all the previous members of our group with whom I have made epic memories across my time in Warwick.

I would like to thank the special people in my life for supporting and encouraging me in no specific order, Priya, Anu, Vani, Sreekutty, Piya and their husbands and adorable kids. I am very grateful to my family, my siblings, Ajay and Anil, sisters-in-law Suvarna and Arathy and nephew, Akshay and Niece, Nainika, and my parents in law, Rajasree and Soman for their love and support

throughout the years. Special thanks to my mother, Omana Menakath, for providing me much needed emotional support. Finally, I thank Sandeep, my husband, for his encouragement, help, and for giving me every day a reason to be happy. I'm, not sure how I would have managed to see this journey to the end without all your backing.

Declarations

The work presented in this thesis is the outcome of my original research under the supervision of Professor Steven P. Brown at the University of Warwick, conducted between October 2015-March, 2019. Where other contributions are included, they are specified in the text. This work has not been submitted for any degree.

Results presented in Chapter 7 have recently been accepted for publication.

Wang. L, Menakath. A, Han. F, Wang. Y, Zavalij. P.Y, Gaskell. K. J, Borodin. O, Iuga. D, Brown. S. P, Wang. C, Xu. K, Eichhorn. B W. Identifying the components of the solid–electrolyte interphase in Li-ion batteries, Nature Chemistry, **2019**, 11, 789-796.

Abstract

This thesis utilizes high-resolution solid-state magic angle spinning (MAS) NMR technique for the characterisation of various organic compounds, specifically pharmaceutical APIs, mesoporous silica loaded with iPMPA, and solid electrolyte interphase layer (SEI) components of lithium-ion batteries. Solid-state NMR is highly sensitive to the local environment, and hence MAS experiments in particular two-dimensional experiments can be used to probe $^{1}H-^{1}H$ and $^{1}H-X$ ($X=^{7}Li$, ^{13}C, ^{14}N, ^{29}Si, ^{31}P) proximities. Some of the presented results have used an NMR crystallography approach, whereby chemical shifts are calculated using the gauge-including projector augmented wave (GIPAW) method for structures usually obtained from diffraction. Moreover, intermolecular hydrogen bonding motifs can be probed by a comparison of chemical shifts calculated for the full crystal to those calculated chemical shift for an isolated molecule.

The first application concerns conformational polymorphism, which is the existence in distinct solid-state forms of the same molecule in different conformations due to variation in torsion angle and has importance for the development of pharmaceutical products. $^{1}H-^{1}H$ homonuclear and $^{13}C-^{1}H$ and $^{14}N-^{1}H$ heteronuclear correlation solid-state NMR approaches are used to elucidate crystal packing and internuclear proximities between nuclei. This Chapter considers the development of a scoring function for evaluating crystal structures of tolfenamic acid (TFA) using solution- and solid-state NMR data. To build this scoring function, we experimentally measured (Form I and Form II) and calculated (Form I, II, III, and IV) ^{1}H and ^{13}C chemical shifts in both the solid state and in solution. The implementation of solid-state NMR chemical shift data in conjunction with both experimental and calculated changes in solution NMR chemical shifts allowed the scoring function to discriminate amongst four similar TFA polymorphs. This approach has the potential to improve the efficiency and accuracy of crystal structure prediction (CSP) by incorporating solution-state NMR conformational and chemical shift data into solid-state NMR based NMR crystallography approaches. Importantly, this novel approach provides a way to predict the conformation of a new polymorphic form for which experimental NMR data is accessible but there is no crystal structure.

In a second application, a range of isopropyl methyl (iPMPA, a degradation product of the chemical warfare agent Sarin) loaded mesoporous silica samples are investigated through multinuclear solid-state NMR. ^{13}C cross polarisation (CP) MAS NMR spectra confirmed the presence of iPMPA molecules in the silica matrix. ^{1}H, ^{31}P, and two-dimensional heteronuclear experiments are applied to probe the number of phosphorous sites and hydrogen bonding motifs.

Variable-temperature ^{1}H and ^{31}P MAS NMR experiments provided information about the mobility of acidic protons involved in hydrogen bonding. A structural model for the iPMPA loading in the pores of the mesoporous silica is presented.

In a third application, a series of standard components of an solid-electrolyte interphase (SEI) layer along with the SEI generated on graphite electrode was investigated using fast MAS NMR. Specifically, high-resolution ^{1}H, ^{7}Li, ^{1}H-^{1}H DQ/MAS, ^{7}Li-^{1}H HMQC, and ^{13}C CP MAS techniques are used, in conjunction with GIPAW calculated NMR chemical shifts to provide an understanding about likely components in the SEI layer. Specifically, a solid-state NMR characterisation of lithium ethylene dicarbonate (LEDC) and lithium mono carbonate (LMC) is presented.

Abbreviations

ADP: Ammonium Dihydrogen Phosphonate

AIDS: Acquired Immune Deficiency Syndrome

AIRSS: Ab-initio Random Structure Searching

AHT: Average Hamiltonian Theory

AMPM: Amplitude Modulated TPPM

BABA: BAck to BAck

BFSG: Broyden-Fletcher-Goldfarb-Shanno scheme

COSY: COrrelated SpectroscopY

CPMAS: Cross Polarisation under Magic Angle Spinning

CRAMPS: Combined Rotation And Multiple Pulse Spectroscopy

CSA: Chemical Shift Anisotropy

CSP: Crystal Structure Prediction

CWAs: Chemical Warfare Agents

DCM: DiChloroMethane

DEC: DiEthyl Carbonates

DFT: Density Functional Theory

DMC: DiMethyl Carbonates

DQ: Double Quantum

DRAMA: Dipolar Recovery At the Magic Angle

DRENAR: Double Quantum- based Dipolar Recoupling Effects Nuclear Alignment Reduction

DUMBO: Decoupling Using Mind Bogging Optimisation

EC: Ethylene Carbonate

EMC: Ethyl Methyl Carbonate

FID: Free Induction Decay

FMPM: Frequency Modulated and Phase-Modulated

FSLG: Frequency Switched Lee-Goldberg

FWHM: Full Width at Half Maximum Height

GGA: Generalized Gradient Approximation

GIPAW: Gauge-Including Projector Augmented Wave

HETCOR: HETeronuclear COrrelation

HMQC: Heteronuclear Multiple–Quantum Correlation

iPMPA: IsoPropylMethyl Phosphonic acid

INEPT: Insensitive Nuclei Enhancement by Polarisation Transfer

LAB: Laboratory Frame

LDA: Local Density Approximation

LEC: Lithium Ethyl Carbonate

LEDC: Lithium Ethylene Di Carbonate

LEMC: Lithium Ethylene Mono Carbonate

LG: Lee-Goldburg

LIBs: Lithium-Ion Batteries

LMC: Lithium Methyl Carbonate

MAS: Magic Angle Spinning

NMR: Nuclear Magnetic Resonance

NOESY: Nuclear Overhauser SpectroscopY

PAS: Principal Axis System

PAW: Projector Augmented Wave

POST-C7: Permutationally Offset Stabilised C7

PMLG: Phase Modulated Lee-Goldberg

PXRD: Powder XRD

RF: Radio Frequency

RFDR: Radio-Frequency Driven Recoupling

R^3: Rotary Resonance Recoupling

SEI: Solid-Electrolyte Interphase

SPINAL: Small Phase Incremental Alteration

SQ: Single Quantum

SXRD: Single-crystal XRD

TFA: Tolfenamic Acid

TMS: TetraMethylSilane

TPPI: Time Proportional Phase Incrementation

TPPM: Two-Pulse Phase Modulation

VT: Variable-Temperature

XRD: X-Ray Diffraction

2D: Two Dimensional

Chapter 1: Introduction

1.1 Introduction to Solid-State NMR

The history of Nuclear magnetic resonance (NMR) presented in this section is based on four reviews[1-4]. NMR is a unique technique which was first applied in physics and then over the past 70 years has found many applications in chemistry, biochemistry, material science as well as pharmaceuticals and geophysics. Numerous studies were reported about the concepts of electron spin and magnetic moment during the early 1920s. Among those, the most significant one was by Stern and Gerlach[5], where they showed the splitting of a beam when passed through an inhomogeneous magnetic field due to the magnetic effect from the quantised orbital angular momentum of the electron. In 1939, Rabi and his colleagues placed a homogenous magnetic field in the middle of the inhomogeneous field, and the molecule was subjected to radiofrequency (*rf*) radiation. The molecules absorbed energy at a defined frequency, and this absorption caused a small deflection in the beam[6-7]. This observation led Rabi to win a Nobel Prize in physics in 1944. Prior to this, in 1936, Gorter made an unsuccessful attempt to measure magnetic resonance absorption in solid LiF and $KAl(SO_4)_2.12H_2O$. The attempt was made again in 1942, which was also a failure[8]. In 1945, three physicists, Edward M Purcell, Henry C Torrey, and Robert V Pound, decided to use radiofrequency techniques developed during the Second World War and observed the first NMR signal from a large sample of paraffin wax[9]. While in 1946, Felix Bloch, W.W.Hansen, and Martin Pickard observed a signal from a sample of water by a method called nuclear induction[10]. Both groups were observing two different aspects of the same phenomenon called nuclear magnetic resonance. In 1952, Bloch and Purcell shared the Nobel Prize in physics for the independent and concurrent discoveries. In 1946, Dr Bernard Rollin, a British pioneer in NMR reported the proton and fluorine NMR for a range of liquids and solids[11]. A year later, Rollin and Hatton reported the measurement of T_1 and T_2 relaxation at low temperature for the first time[12].

The spatial dependence of the magnetic dipolar interaction, propotional to $(3\cos^2\theta - 1)\, r^{-3}$, where r is the internuclear distance between the adjacent nuclei and θ is the angle between them, increases the usefulness of NMR for the structure determination of solid systems. The significance of the dipolar interaction and hence the motivation for high-resolution solid-state NMR was first reported by George Pake in 1948, using a single crystal of gypsum $CaSO_4.2H_2O$[13]. The observed doublet in the ^1H NMR spectrum is fitted to the dipolar angular dependence, and the orientations of the proton pair in the non-equivalent water molecules were extracted. The fact that the NMR spectra can give structural information makes NMR a complementary technique to X-ray crystallography. Following this, Andrew and Bershon analysed solid-state NMR spectra for

organic molecules containing isolated methyl groups, where the nuclei are arranged in a triangular pattern[14]. The complexity of NMR spectra due to a larger number of interacting nuclei was taken into account by Van Vleck using a summation that describes the underlying dipolar interactions[15].

The use of NMR as an analytical method for chemists was unclear until 1951 when Packard, Arnold, and Dharmatti resolved NMR signals for three types of hydrogen atoms in ethanol[16]. Since then, ^{1}H NMR has become one of the most common and powerful analytical tools of the scientific community. A year later, Gutowsky and McCall reported that neighbouring spins cause splitting of lines in the spectra[17], which led to the development of a new concept called indirect spin-spin coupling or scalar coupling[18]. Shortly afterward, the term chemical exchange was developed, when the spin system failed to produce the expected multiplets[19-20]. This revolutionised NMR and Varian launched the first commercial nuclear magnetic resonance spectrometer at a ^{1}H Larmor frequency 30 MHz in 1952. The continuous wave (CW) method, which varies the frequency through the resonance condition, was used as the standard procedure to record the spectrum.

The CW method has over time given way to the pulse method, which was immensely stimulated by Erwin Hahn's fortunate discovery of the spin-echo experiment in 1950[21] and Henry Torrey's study on the concept of the nutation frequency[22]. The spin-echo experiments applies two closely spaced pulses to generate an echo, thus allowing the measurement of the transverse relaxation time. At the same time, Lowe and Norberg introduced the concept of free induction, which became significant to the whole solid-state NMR community. They reported that the free induction decay (FID) is the Fourier transform of the NMR CW spectrum[23]. The NMR pulse method saves time compared to the CW method because the length of the NMR pulse is sufficient to excite all the nuclei to produce the FID.

One of the key characteristics of solid-state NMR spectra compared to those for liquids is their broad linewidth, due to their static anisotropic interaction as noted by Van Vleck[15]. To overcome this, during the late 1950s, Edward Andrew *et al.*[24-25] and I.J Lowe[26] independently demonstrated, both experimentally and theoretically, that by rapidly spinning the solid sample at a certain angle, $\theta = 54^{\circ}.74'$, it was possible to remove the anisotropic broadening. The sources of broadening were described as second rank tensor interactions, and on rapid rotation, it was reduced by a factor of $\frac{1}{2}(3\cos^2\theta - 1)$, where θ is the angle between the applied magnetic field and the axis of rotation. This particular angle is known as the 'magic angle'[27] and has now become one of the standard techniques both in academia and industry, for the analysis by NMR of a broad range of solid systems. The magic angle spinning (MAS) technique is detailed in Chapter 2.

Over time, these developments have been combined to yield advanced multiple pulse NMR experiments that are routinely used today by solid-state NMR researchers. However, the field of pulsed NMR did not gain much attention until the mid-1960s. Mansfield and Ware[28] and Ostroff and Waugh,[29] in 1966, separately applied a train of pulses to narrow the NMR spectrum of the solids by obtaining a set of solid echoes with a prolonged envelope. The array of pulses imposes a time dependence on the spin term of the dipolar interaction, thus causing successive reorientations of the nuclear spins in the rotating frame. Special care and effort have been taken in the arrangement of multiple pulses because it reduces the time-averaged interactions to zero, and eliminates the effects of finite pulse length, *rf* field inhomogeneity and second order effects. Cycles of three, four and six pulses and more pulses have been combined and led to the development of many complex pulse sequences[30]. Two shorter pulse sequences are WAHUHA[31] and MREV[32], which are based on the average Hamiltonian theory (AHT)[33]. Averaging of interactions was successfully explained by AHT in static samples, and Floquet theory[34] has been utilized to explain the complexity of homonuclear decoupling under MAS and *rf*.

A further advance at this time was the development of homonuclear dipolar decoupling reported by Lee and Goldburg in 1965, using a pulse strategy to average out the dipolar interaction between like nuclei[35-36]. The Lee-Goldburg (LG) method applies continuous off-resonance irradiation, so that the spins in the rotating frame align at the magic angle with respect to the direction of the off-resonance radiation, thus removing the second-order tensor of the dipolar interaction. While averaging the dipolar interactions, the multiple pulse method does not remove other anisotropic interactions such as the chemical shift anisotropy (CSA). The LG method has been refined with the introduction of improved versions in Frequency Switched Lee-Goldburg (FSLG)[37-38] and Phase Modulated Lee-Goldburg (PMLG)[39]. Spectral quality can be improved when homonuclear decoupling sequences are combined with MAS; this combination is known as combined rotation and multiple pulse spectroscopy (CRAMPS)[40-42]. Another commonly used decoupling scheme is the Decoupling Using Mind Bogging Optimisation (DUMBO)[43] approach and an experimentally optimised version e-DUMBO[44], which make use of constant-amplitude, phase-modulated *rf* irradiation to achieve homonuclear dipolar decoupling.

Another milestone in the field of NMR is the development of recoupling sequences. The dipolar coupling and other anisotropic interactions removed via MAS can be reintroduced for selected periods of the experiment by designing the pulse sequence carefully. Early recoupling sequences are rotary resonance recoupling (R^3)[45], which is discussed in Chapter 3, and the DRAMA (Dipolar Recovery at the Magic Angle) sequence developed by Tycko and Dabbagh[46]. Other commonly used recoupling schemes include RFDR (radio-Frequency Driven Recoupling)[47], POST-C7

(Permutationally Offset Stabilised C7)[48] and BABA (Back to Back)[49]. The work presented in this thesis involves the use of R^3 and BABA to obtain structural information.

Another significant achievement was the introduction of the double resonance method which led to the famous cross polarisation (CP) experiment proposed by Hartman and Hahn in 1962[50-51]. The double resonance method decouples the strong proton heteronuclear dipolar interactions and *J* couplings and enhances the weak NMR signal of dilute spins like ^{13}C, ^{15}N, ^{29}Si, ^{31}P by transferring proton polarization by using the Hartman- Hahn condition which is explained in detail in Chapter 3. Hence, the efficiency of this experiment also depends on the application of heteronuclear decoupling during the acquisition of the free-induction decay. In 1970s Pines *et al.* reported more experimental results using polarisation transfer[52-53]. Following this, in 1976 Stejskal *et al.* combined CP with MAS to yield ^{13}C spectra of three solid systems[50]. ^{1}H–^{13}C, ^{1}H–^{31}P, and ^{1}H–^{29}Si CPMAS spectra are presented in this thesis.

It was Jeener at the AMPERE summer school in 1971, who introduced the idea of two-dimensional Fourier NMR. Jeener's experiment consisted of two *rf* pulses separated by an increasing evolution time t_1. This experiment is now known as COSY (Correlated Spectroscopy)[54]. Richard Ernst implemented his idea experimentally[55-56], and soon after it was shown that two-dimensional Fourier NMR is also capable of offering information on multiple quantum transitions[57-58]. Currently, multi-dimensional experiments, particularly two-dimensional experiments, have proven most effective for characterising molecular structure and for probing various inter and intramolecular interactions and dynamics in solid systems. ^{1}H-^{1}H double quantum experiments utilizing a recoupling sequence, and two-dimensional heteronuclear experiments incorporating homonuclear decoupling are commonly used in modern solid-state NMR, as in this thesis, to extract dipolar coupling information between the nuclei[59].

It is well known that dipolar couplings are several times stronger than scalar couplings and are appropriate for polarisation transfer in solids. Nonetheless, due to the isotropic nature of scalar couplings, they can transfer polarisation 100% and hence can be more attractive than dipolar couplings. Averaging out all the anisotropic interaction is crucial for scalar coupling mediated experiment in solids; hence, these experiments are only feasible in the presence of MAS and homonuclear dipolar decoupling[60]. Heteronuclear *J* couplings are scaled by a factor of $1/\sqrt{3}$ (depends on the sequence) on applying the homonuclear decoupling during the evolution time. Emsley and co-workers developed one bond C-H and N-H experiments in the solid-state based on the solution-state HMQC, HSQC and INEPT[61] experiments with the solid-state implementation being referred to as MAS J-HMQC[62], MAS-J-HSQC[63], and Refocused INEPT[64]. A detailed

explanation of the HMQC and refocused INEPT sequences are presented in Chapter 3. These experiments have been widely used to achieve complete chemical shift assignments for small molecules. With MAS frequencies reaching up to 140 kHz[65], solid-state NMR, particularly ^{1}H NMR, is becoming a powerful tool.

1.2 X-ray Diffraction (XRD)

Determining a solid-state structure is a crucial requirement for designing new products. In the solid state, atoms have a fixed position, and the structure can be described by a periodic arrangement of atoms or ions in three-dimensional space, and the whole crystal is the repetition of the unit cell. XRD has been the primary standard for studying solids, since its discovery by William Lawrence Bragg and William Henry Bragg in 1913[66]. This technique depends on the constructive interference of the x-rays and the sample being studied. Diffraction patterns of the samples are formed on satisfying Bragg's law $n\lambda = 2d \sin\theta$, where λ is the wavelength of the x-ray radiation and d is the spacing between the parallel planes, and angle θ is the angle between the incident radiation and set of planes. Hence the diffraction pattern of a sample is the plot of diffraction intensity as a function of 2θ, which is equivalent to the d spacing. The d spacing gives information about the unit cell parameters, and the diffraction pattern reflects the arrangement of the atoms. Hence, these rely on the long-range order and periodicity, which are the characteristics of a crystalline solid.

XRD will always remain as the 'gold standard' technique for the characterisation of solids. However, there are some limitations to this technique. For instance, it is not always plausible to obtain suitable single crystals for analysis. It is hard to access the mobility at the molecular level and to locate hydrogen atoms accurately. It is also challenging to tackle the structure of spatially disordered systems.

Fortunately, NMR can act both as a supplementary and complementary technique. NMR can provide information about coordination number, covalent bonding, the interaction between atom and molecules, and dynamics and can also supply information missed by XRD[67]. The advances in the field solid-state NMR and diffraction resulted in the development of a new field termed as NMR crystallography[68-70], where solid-state NMR is used in conjunction with other techniques, such as single crystal XRD (SXRD), powder XRD (PXRD), or neutron diffraction to resolve or refine solid structures. The development of NMR crystallography and theoretical aspects behind the computational method shall be described in detail later.

1.3 Thesis Overview

This thesis demonstrates the applicability of solid-state NMR for the structural characterisation of different organic materials. Specifically, intermolecular interactions and crystallographic properties are probed using high-resolution solid-state NMR and first-principle density functional theory (DFT) calculations.

Chapter two details the theoretical concepts behind NMR spectroscopy; a particular focus is given to solid-state NMR. This Chapter starts off with a background to the quantum mechanical concepts behind NMR including density operator theory, product operator formalism and ends with the Hamiltonian description of key external and internal spin interactions and their effect under magic angle spinning. Chapter three discusses the practical aspects of performing an NMR experiment, including two-dimensional line shapes and phase cycling; furthermore, techniques like dipolar decoupling and recoupling are introduced. Finally, different pulse sequences such as cross polarisation, ^{1}H-^{13}C refocused INEPT, heteronuclear correlation experiment, ^{1}H-^{1}H double quantum, and ^{14}N-^{1}H HMQC experiments are described; these experiments are used in this thesis. Chapter four introduces the theoretical background of computational techniques used within this thesis, focussing on the first principle DFT, NMR shielding calculations, and how to reference to experimental solid-state NMR data.

Chapter five is the first experimental result Chapter and is divided into two subchapters. The first describes an NMR crystallography approach for the characterisation of two polymorphs of tolfenamic acid (TFA). Solid-state NMR experiments in conjunction with first principle DFT calculation allowed full assignment of ^{1}H and ^{13}C chemical shifts of two TFA polymorphs (Form I and Form II). In addition, O-H···O intermolecular interactions are probed by comparing the GIPAW calculated chemical shifts for the full crystal structures and extracted isolated molecules. The second subchapter introduces a novel scoring function to discriminate conformational polymorphs of TFA by comparing experimentally measured and DFT calculated changes in chemical shift between the solution- and solid-state. The calculation of solution chemical shifts starts from an ensemble of TFA conformations that were modelled by C4X discovery; this represents the solution dynamic 3D structures. The chemical shift of each conformer was calculated by placing them in a large unit cell and under the constraint of fixing specific torsion angle to maintain the conformation. The calculated values for each conformation were weighted according to the dynamic solution 3D structure to produce calculated values for the solution chemical shifts. Solid-state chemical shifts for the polymorphs are calculated using the published crystal structures. Experimental and calculated changes in chemical shifts on going from solution

to solid-state were determined. Finally, a scoring function is defined by plotting experimentally observed against the calculated changes in chemical shifts. This method provides a way within crystal structure prediction (CSP) for reducing search space by refining possible alternative structures. The scoring function is also suitable to confirm how well a crystal structure matches with the experimental solid-state chemical shifts. Furthermore, this approach is shown to be able to predict the most likely conformation of a solid form without prior knowledge of the crystal structure.

Chapter 6 deals with the characterisation of mesoporous silica loaded with variable concentrations of isopropyl methyl phosphonic acid (iPMPA); this is the main hydrolysis product of the chemical warfare agent sarin. The local structures of the phosphonic acid group and their interactions with the silica surface are studied by extensive multinuclear solid-state NMR experiments. The ^{13}C and ^{31}P NMR results confirmed that loading had occurred. ^{31}P CPMAS revealed the presence of two distinct phosphorus environments and two-dimensional heteronuclear experiments confirmed the close proximity and hydrogen bonding interaction of the phosphonic acid with the surface silanol group. Moreover, the temperature dependence of ^{1}H and ^{31}P NMR chemical shifts were investigated to understand the relative motion of the phosphonic acid group within the silica pores allowing us to present a structural model.

Finally, Chapter 7 describes the high-resolution fast MAS NMR characterisation of three main primary organic components of the solid electrolyte interphase layer (SEI) of Li-ion batteries, lithium ethylene mono carbonate (LEMC), lithium ethylene dicarbonate (LEDC), and lithium methyl carbonate (LMC). The existing literature suggests that LEDC is the primary organic compound of the SEI layer. ^{1}H, ^{13}C, ^{7}Li and two- dimensional NMR ^{1}H-^{1}H DQ and ^{7}Li-^{1}H HMQC spectra for LEMC, LEDC and LMC are shown. GIPAW calculated chemical shifts for LMC and LEMC are compared with the corresponding solid-state NMR spectra. The spectra for the SEI layer generated on the graphite electrode was broad, which precluded the identification of the model compound on the SEI layer. However, the solid-state NMR results taken together with analysis by solution NMR, FTIR, and diffraction suggest that it is LEMC, instead of LEDC that is the principal component of the SEI layer.

Chapter 2: Solid-State NMR Theory

Solid-state NMR is a versatile tool that provides atomic-level structural information on molecular systems, due to its ability to selectively manipulate different anisotropic spins. NMR observes the transition between the magnetic energy levels which takes place when a nuclear spin is subjected to a static external magnetic field and electromagnetic radiation with a specific frequency. In this Chapter, the basic principles of NMR are described, followed by a quantum mechanical theory of nuclear magnetism. The theory and Equations contained within this Chapter are based on references[71-75].

2.1. Spin Angular Momentum and an NMR Experiment

Nuclei have an intrinsic property called spin along with mass, energy, and charge. Specifically, each isotope has an associated spin angular momentum quantum number, I, which can take values I = 0, 1/2, 1, 3/2... Nuclei with I greater than zero possess spin angular momentum whose quantized magnitude is

$$|\underline{S}| = \hbar\sqrt{I(I+1)}\,. \tag{2.1}$$

The z component of $\underline{S}$, is :

$$S_z = m\hbar\,, \tag{2.2}$$

where $\hbar$ is Planck's constant divided by 2π and m is the azimuthal (or Projection) quantum number, which takes values $+I, (+I-1)\ldots\ldots -I$.

As a consequence of possessing spin angular momentum, nuclei with non-zero spin have an intrinsic magnetic moment $\underline{\mu}$, given by:

$$\underline{\mu} = \gamma\underline{S}\,, \tag{2.3}$$

where γ is the gyromagnetic or magnetogyric ratio, which is a constant for each isotope.

In the presence of a magnetic field (assumed to be along the z-axis), the spin states split into $(2I + 1)$ levels (this is referred to as the Zeeman interaction). The potential energy of a magnetic moment in a magnetic field along the z-axis of magnitude B_z (as discussed below, this is approximately equal to the strength, B_0, of the superconducting magnet in an NMR experiment) is:

$$E = -\mu_z B_z \,. \tag{2.4}$$

Substituting Equations 2.2 and 2.3 into the above Equation gives:

$$E = -\gamma m \hbar B_z \,. \tag{2.5}$$

For a single nucleus with I = 1/2, there are two states, m = +1/2 or m = –1/2 (see Figure 2.1), whereby the energy for the m = +1/2 state is:

$$E = \frac{-\gamma \hbar B_z}{2} \tag{2.6}$$

and the energy for the m = –1/2 state is:

$$E = \frac{\gamma \hbar B_z}{2} \,. \tag{2.7}$$

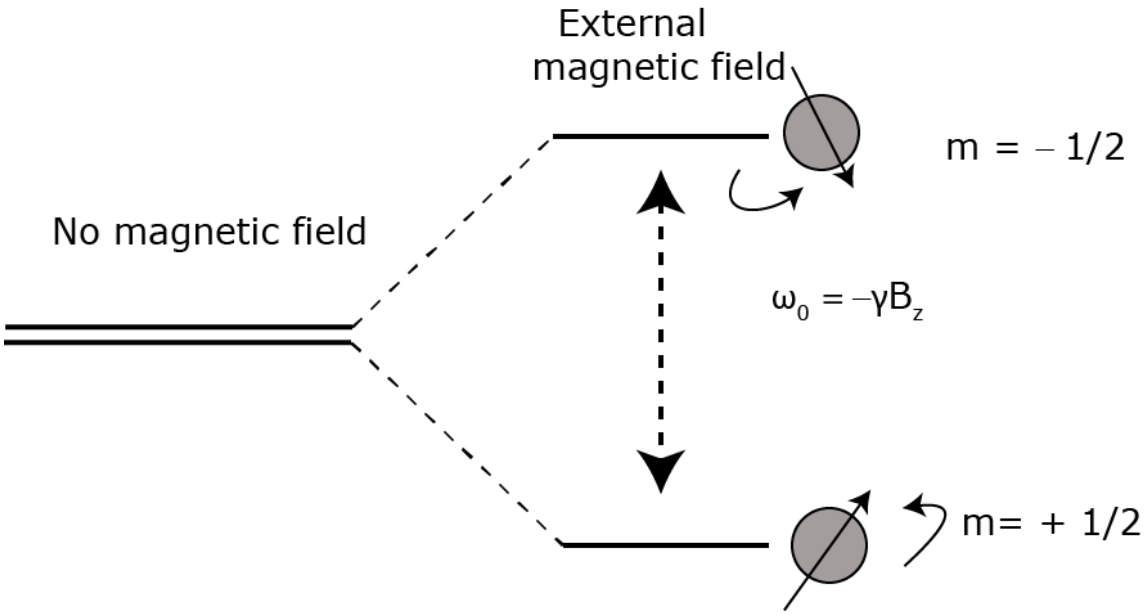

Figure 2.1: The energy level diagram of spin ½ nucleus in the presence and absence of the external magnetic field.

Thus, the energy difference between the two states corresponding to an allowed transition with $\Delta m = \pm 1$ is

$$\Delta E = \frac{-\gamma \hbar B_z}{2} - \frac{\gamma \hbar B_z}{2} = -\gamma \hbar B_z \,. \tag{2.8}$$

The energy difference and angular frequency are related by:

$$\Delta E = \hbar \omega_0 \,. \tag{2.9}$$

This leads to the derivation of the Larmor frequency, corresponding to the splitting between energy states:

$$\omega_0 = -\gamma B_z \,. \tag{2.10}$$

In the presence of an external magnetic field, a nucleus precesses about the direction of the field (see Figure 2.2); this is known as Larmor precession, and the frequency of precession is known as the Larmor frequency as defined in Equation 2.10.

Figure 2.2: Spin precession, taken from Figure 2.8 of Ref[74].

At thermal equilibrium, nuclei in a sample are distributed across the available spin states. By the Boltzmann distribution, the population difference between the spin states is described by:

$$\frac{N_{upper}}{N_{lower}} = e^{-\gamma Bz / k_B T} \,, \tag{2.11}$$

where N is the number of nuclei in the respective spin states, k_B is the Boltzmann constant and T is the temperature. For a proton spin in a 14.1 T magnet as T = 298 K,

$$\frac{N_{upper}}{N_{lower}} = 1.0001 . \quad (2.12)$$

This means that, at room temperature, for every 10,000 nuclei in the upper energy state, there are 10,001 nuclei in the lower energy state. This small population difference makes NMR an insensitive technique. At thermal equilibrium, the population difference leads to a bulk magnetisation in the direction of the *z*-axis due to the applied magnetic field. It may take milliseconds to seconds to reach this equilibrium, and this phenomenon is known as relaxation, as discussed further below.

In NMR, this bulk magnetization is disturbed by applying a second magnetic field $\underline{B_1}$ that is perpendicular to $\underline{B_0}$. This $\underline{B_1}$ field is obtained by applying an oscillating radio wave with frequency ω_{rf}, i.e.,

$$\underline{B_1} = B_1 \cos(\omega_{rf} t + \phi) , \quad (2.13)$$

B_1 is the amplitude of the oscillating magnetic field and ϕ is the phase. The phase is important because it provides information about the direction of the applied oscillating magnetic field and the direction of the magnetization that results from the application of an *rf* pulse and is discussed in detail later.

Typically, a NMR spectrum comprises multiple peaks, hence it not plausible to set the transmitter frequency equal to the Larmor frequency for every resonance. Therefore, resonance offset or offset frequency (the difference between the Larmor frequency and ω_{rf}) has to be considered,

$$\Omega = \omega_0 - \omega_{rf} . \quad (2.14)$$

The resonance offset is usually non-zero, thus leading to a residual field. The magnetization precesses around this residual field when the pulse is switched on. The sense and frequency of precession are determined by the sign and magnitude of the offset frequency. The rotating field assumes that the $\underline{B_1}$ field is stationary with two counter rotating fields, rotating at the transmitter frequencies $+\omega_{rf}$ and $-\omega_{rf}$. Since only $+\omega_{rf}$ is near enough to ω_0 to influence the magnetisation, that component is retained and the off-resonance component can be ignored safely. Hence in the rotating field a pulse is viewed as the application of an *rf* field, which is orthogonal to the static

field $\underline{B_0}$.

When the on-resonance condition is achieved (i.e., when ω_{rf} is set equal to the Larmor frequency), the bulk magnetization nutates around the direction of the applied $\underline{B_1}$ field at a nutation frequency ω_1

$$\omega_1 = -\gamma \underline{B}_1 . \tag{2.15}$$

The angle β through which the bulk magnetization nutates is known as the flip angle. For a 90° on-resonance *rf* pulse along the +*x* axis applied at thermal equilibrium, the magnetization is rotated to lie along the –*y*-axis as shown in Figure 2.3.

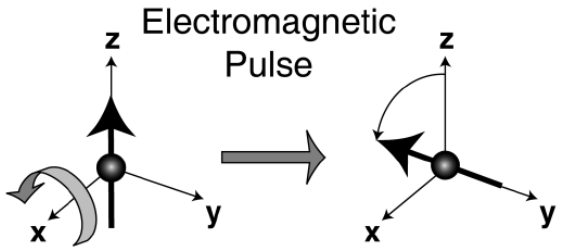

Figure 2.3: For an on-resonance electromagnetic pulse, the bulk magnetisation nutates in the rotating frame about the *x*-axis. Taken from Figure 2.10 of Ref[74].

For the case of bulk magnetization that has been flipped to the –*y*-axis, when the $\underline{B_1}$ field is turned off, there is Larmor precession in the transverse plane as shown in Figure 2.4.

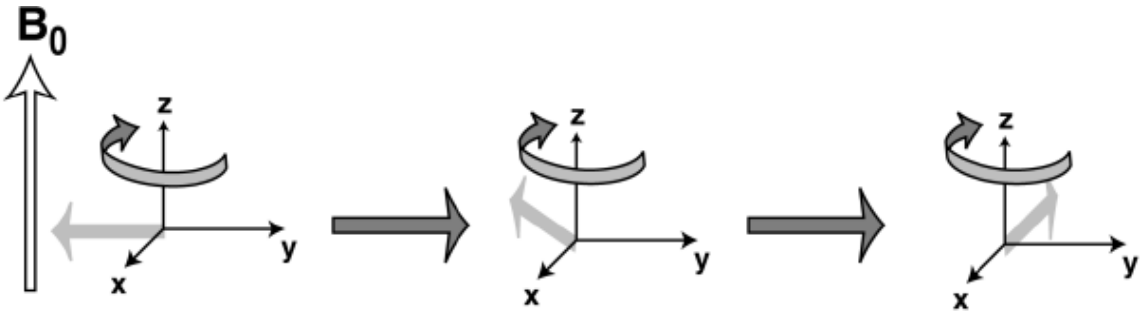

Figure 2.4: Precession of transverse magnetization upon the removal of the *rf* pulse. This precession does not last forever: this non-equilibrium state undergoes relaxation back to the equilibrium state. Taken from Figure 2.20 of Ref[74].

This precession and decay of the magnetisation can be detected since the precessing magnetisation induces an oscillating electric current in a *rf* coil, with the same coil used to generate the *rf* pulse. This oscillating electric current is known as the NMR signal or free induction decay.

The magnetic field B_0 induces a flow of currents in the electron orbits. This circulating magnetic field produces an additional magnetic field. This additional magnetic field opposes B_0 and the magnetic field experienced by the nucleus B_z is reduced. This mechanism is known as chemical shielding (σ):

$$B_z = (1-\sigma)B_0 , \tag{2.16}$$

where B_0 is the magnitude of $\underline{B_0}$ in the z direction. Hence, the Larmor frequency (see Equation 2.10) depends upon the nature of the local electronic environment. A B_0 independent parameter, the chemical shift (δ), is defined as

$$\delta_{ppm} = \frac{\omega_0 - \omega_{ref}}{\omega_{ref}} \times 10^6 , \tag{2.17}$$

where ω_{ref} is the frequency of a reference compound, e.g., tetramethylsilane (TMS) for ^{1}H, ^{13}C or ^{29}Si.

2.2. A Quantum Mechanical Approach to NMR

In this section, a quantum mechanical approach for describing NMR experiments for spin ½ nuclei is presented. According to quantum mechanics, the value of the observable quantity energy is

represented via a Hamiltonian operator. The nuclear spin angular momentum operator is represented as $\hat{I}$ where

$$\hat{I}^2 = \hat{I}_x^2 + \hat{I}_y^2 + \hat{I}_z^2 , \tag{2.18}$$

where $\hat{I}_x$, $\hat{I}_y$, and $\hat{I}_z$ are the *x*, *y*, and *z* components of the nuclear spin angular momentum operator.

If we are measuring an observable, then the result will be one of the eigenvalues of the particular operator which represents the observable. $\Psi_{1/2}$ and $\Psi_{-1/2}$ are the eigenfunctions of the nuclear spin angular momentum operator, $\hat{I}_z$, corresponding to the $m = +1/2$ and $m = -1/2$ states of a spin-half nucleus:

$$\hat{I}_z \Psi_{+1/2} = +\frac{1}{2}\hbar\Psi_{+1/2} , \tag{2.19}$$

$$\hat{I}_z \Psi_{-1/2} = -\frac{1}{2}\hbar\Psi_{-1/2} . \tag{2.20}$$

Hence, $+\frac{1}{2}\hbar$ and $-\frac{1}{2}\hbar$ are the eigenvalues of the z component of the spin angular momentum operator. In general, we can write:

$$\hat{I}_z \Psi_m = m\hbar\Psi_m . \tag{2.21}$$

In the same way, we can represent the energy of interaction of the spin with the magnetic field for $m = +1/2$ and $m = -1/2$ states as:

$$\hat{H} \Psi_{+1/2} = -\frac{1}{2}\hbar\gamma B_z \Psi_{+1/2} , \tag{2.22}$$

$$\hat{H} \Psi_{-1/2} = \frac{1}{2}\hbar\gamma B_z \Psi_{-1/2} . \tag{2.23}$$

where $\hat{H}$ represents the Hamiltonian (the operator of total energy of the system) for a single spin and $-\frac{1}{2}\hbar\gamma B_z$ and $\frac{1}{2}\hbar\gamma B_z$ are the eigenvalues of the Hamiltonian; this corresponds to Equation 2.8 above:

$$E_m = -m\hbar\gamma B_z . \tag{2.24}$$

To understand the working of NMR, a wave function Ψ is introduced which is the linear combination of the spin states,

$$\Psi = c_{1/2}\Psi_{1/2} + c_{-1/2}\Psi_{-1/2} ,$$

where $c_{1/2}$ and $c_{-1/2}$ are coefficients which can change over time. We can refer to the 1/2 and −1/2 states as α (spin-up) or β (spin down), so we can write the Equation as:

$$\Psi = c_\alpha \Psi_\alpha + c_\beta \Psi_\beta . \tag{2.25}$$

In 1939, Paul Dirac introduced the ket-Bra notation to represent the quantum states, so the wave function is represented as:

$$|\Psi\rangle = c_\alpha |\alpha\rangle + c_\beta |\beta\rangle , \tag{2.26}$$

and the complex conjugate of the above function is

$$\langle\Psi| = c_\alpha^* \langle\alpha| + c_\beta^* \langle\beta| . \tag{2.27}$$

$|\alpha\rangle$ and $|\beta\rangle$ are the eigenfunction of the operator $\hat{I}_z$, hence

$$\hat{I}_z|\alpha\rangle = \frac{1}{2}|\alpha\rangle . \tag{2.28}$$

$$\hat{I}_z|\beta\rangle = -\frac{1}{2}|\beta\rangle . \tag{2.29}$$

In quantum mechanics, the average value of any observable is known as the expectation value and is defined as:

$$\left\langle \hat{Q} \right\rangle = \frac{\left\langle \Psi \middle| \hat{Q} \middle| \Psi \right\rangle}{\left\langle \Psi \middle| \Psi \right\rangle}. \tag{2.30}$$

A wave function is said to be normalised if

$$\left\langle \Psi \middle| \Psi \right\rangle = \int \Psi^* \Psi d\tau = 1. \tag{2.31}$$

Two wave functions Ψ_α and Ψ_β, are said to be orthogonal if

$$\left\langle \Psi_\alpha \middle| \Psi_\beta \right\rangle = \int \Psi_\alpha{}^* \Psi_\beta d\tau = 0. \tag{2.32}$$

The value of $\left\langle \Psi \middle| \Psi \right\rangle$ can be calculated as shown below

$$\left\langle \Psi \middle| \Psi \right\rangle = [c_\alpha^* \left\langle \alpha \right| + c_\beta^* \left\langle \beta \right|][c_\alpha \left| \alpha \right\rangle + c_\beta \left| \beta \right\rangle] \tag{2.33}$$

$$= c_\alpha^* c_\alpha \underbrace{\left\langle \alpha \middle| \alpha \right\rangle}_{1} + c_\alpha^* c_\beta \underbrace{\left\langle \alpha \middle| \beta \right\rangle}_{0} + c_\beta^* c_\alpha \underbrace{\left\langle \beta \middle| \alpha \right\rangle}_{0} + c_\beta^* c_\beta \underbrace{\left\langle \beta \middle| \beta \right\rangle}_{1}$$

$$= c_\alpha^* c_\alpha + c_\beta^* c_\beta. \tag{2.34}$$

We can calculate the expectation value for the *x y* and *z* components of the nuclear spin angular momentum operator, as shown below:

$$\left\langle \hat{I}_z \right\rangle = \left\langle \Psi \middle| \hat{I}_z \middle| \Psi \right\rangle. \tag{2.35}$$

$$= [c_\alpha^* \left\langle \alpha \right| + c_\beta^* \left\langle \beta \right|] \hat{I}_z [c_\alpha \left| \alpha \right\rangle + c_\beta \left| \beta \right\rangle]$$

$$= c_\alpha^* c_\alpha \left\langle \alpha \middle| \hat{I}_z \middle| \alpha \right\rangle + c_\alpha^* c_\beta \left\langle \alpha \middle| \hat{I}_z \middle| \beta \right\rangle + c_\beta^* c_\alpha \left\langle \beta \middle| \hat{I}_z \middle| \alpha \right\rangle + c_\beta^* c_\beta \left\langle \beta \middle| \hat{I}_z \middle| \beta \right\rangle \tag{2.36}$$

Substituting Equations 2.28 and 2.29 into Equation 2.36 leads to

$$\left\langle \hat{I}_z \right\rangle = \frac{1}{2} c_\alpha^* c_\alpha \underbrace{\left\langle \alpha \middle| \alpha \right\rangle}_{1} - \frac{1}{2} c_\alpha^* c_\beta \underbrace{\left\langle \alpha \middle| \beta \right\rangle}_{0} + \frac{1}{2} c_\beta^* c_\alpha \underbrace{\left\langle \beta \middle| \alpha \right\rangle}_{0} - \frac{1}{2} c_\beta^* c_\beta \underbrace{\left\langle \beta \middle| \beta \right\rangle}_{1}$$

$$= \frac{1}{2} c_\alpha^* c_\alpha - \frac{1}{2} c_\beta^* c_\beta . \tag{2.37}$$

Similarly, we can calculate the values of the *x* and *y* components of the spin angular momentum as:

$$\left\langle \hat{I}_x \right\rangle = \frac{1}{2} c_\alpha^* c_\beta + \frac{1}{2} c_\beta^* c_\alpha \tag{2.38}$$

$$\left\langle \hat{I}_y \right\rangle = \frac{1}{2} i c_\beta^* c_\alpha - \frac{1}{2} i c_\alpha^* c_\beta . \tag{2.39}$$

The bulk magnetization of the sample along the *z*-direction is the sum of the z-component of the magnetic moment of each spin, hence:

$$M_z = \gamma \left\langle \hat{I}_z \right\rangle^{(1)} + \gamma \left\langle \hat{I}_z \right\rangle^{(2)} + \gamma \left\langle \hat{I}_z \right\rangle^{(3)} + \ldots$$

$$= \gamma \left[\frac{1}{2} c_\alpha^{(1)*} c_\alpha{}^{(1)} - \frac{1}{2} c_\beta^{(1)*} c_\beta{}^{(1)} \right] + \gamma \left[\frac{1}{2} c_\alpha^{(2)*} c_\alpha{}^{(2)} - \frac{1}{2} c_\beta^{(2)*} c_\beta{}^{(2)} \right] + \ldots$$

$$= \frac{1}{2} \gamma N \left(\overline{c_\alpha^* c_\alpha - c_\beta^* c_\beta} \right)$$

$$= \frac{1}{2} \gamma N \overline{\langle I_z \rangle}, \tag{2.40}$$

where *N* is the number of spins, and the overbar represents the ensemble average.

Similarly, we can calculate the value for transverse magnetization:

$$M_x = \frac{1}{2} \gamma N \left(\overline{c_\alpha^* c_\beta + c_\beta^* c_\alpha} \right), \tag{2.41}$$

$$M_y = \frac{1}{2} i \gamma N \left(\overline{c_\beta^* c_\alpha - c_\alpha^* c_\beta} \right). \tag{2.42}$$

The change in a wave function with time is given by the time-dependent Schrödinger Equation (note written here in frequency):

$$\frac{d\psi(t)}{dt} = -i\hat{H}\,\Psi(t)\,. \tag{2.43}$$

The Dirac notation for this Equation is

$$\frac{d\left|\psi(t)\right\rangle}{dt} = -i\hat{H}\left|\Psi(t)\right\rangle. \tag{2.44}$$

The Hamiltonian for a single spin in the absence of an *RF* field in the rotating frame is given by:

$$\hat{H} = \Omega\hat{I}_z\,. \tag{2.45}$$

Introducing a time dependence into Equation 2.26, the wavefunction of this single spin is

$$\left|\psi(t)\right\rangle = c_\alpha(t)\left|\alpha\right\rangle + c_\beta(\mathrm{t})\left|\beta\right\rangle. \tag{2.46}$$

Substituting Equation 2.46 into the Schrödinger Equation 2.43 leads to an expression for the time evolution of this superposition state under free precession due to a resonance offset:

$$\frac{d\left[c_\alpha(t)\left|\alpha\right\rangle + c_\beta(\mathrm{t})\left|\beta\right\rangle\right]}{dt} = -i\Omega\hat{I}_z\left[c_\alpha(t)\left|\alpha\right\rangle + c_\beta(\mathrm{t})\left|\beta\right\rangle\right]$$

$$\therefore \frac{dc_\alpha(t)}{dt}\left|\alpha\right\rangle + \frac{dc_\beta(\mathrm{t})}{dt}\left|\beta\right\rangle = -\frac{1}{2}i\Omega c_\alpha(t)\left|\alpha\right\rangle + \frac{1}{2}i\Omega c_\beta(\mathrm{t})\left|\beta\right\rangle.$$

Multiplying both sides with $\left\langle\alpha\right|$ gives:

$$\left\langle\alpha\right|\frac{dc_\alpha(t)}{dt}\left|\alpha\right\rangle + \left\langle\alpha\right|\frac{dc_\beta(\mathrm{t})}{dt}\left|\beta\right\rangle = \left\langle\alpha\right|\left[-\frac{1}{2}i\Omega c_\alpha(t)\left|\alpha\right\rangle\right] + \left\langle\alpha\right|\left[\frac{1}{2}i\Omega c_\beta(\mathrm{t})\left|\beta\right\rangle\right]$$

$$\therefore \frac{dc_\alpha(t)}{dt}\underset{1}{\left\langle\alpha\right|\left.\alpha\right\rangle} + \frac{dc_\beta(\mathrm{t})}{dt}\underset{0}{\left\langle\alpha\right|\left.\beta\right\rangle} = -\frac{1}{2}i\Omega c_\alpha(t)\underset{1}{\left\langle\alpha\right|\left.\alpha\right\rangle} + \frac{1}{2}i\Omega c_\beta(\mathrm{t})\underset{0}{\left\langle\alpha\right|\left.\beta\right\rangle}.$$

Therefore,

$$\frac{dc_\alpha(t)}{dt} = -\frac{1}{2}i\Omega c_\alpha(t)\,. \tag{2.47}$$

The solution for the above Equation and the corresponding one of the $c_\beta(t)$ coefficient is:

$$c_\alpha(t) = c_\alpha(0)\exp(-\frac{1}{2}i\Omega t), \tag{2.48}$$

$$c_\beta(\mathrm{t}) = c_\beta(0)\exp(\frac{1}{2}i\Omega t), \tag{2.49}$$

where $c_\alpha(0)$ and $c_\beta(0)$ are the value of coefficients at time zero.

In this way, the effect of free evolution under a resonance offset on the *x*, y and *z* components of the spin angular momentum can be evaluated. Specifically, substituting Equations 2.48 and Equation 2.49 into Equation 2.37 leads to:

$$\left\langle \hat{I}_z \right\rangle(t) = \frac{1}{2}\left[c_\alpha(0)\exp(-\frac{1}{2}i\Omega t)\right]^*\left[c_\alpha(0)\exp(-\frac{1}{2}i\Omega t)\right] - \frac{1}{2}\left[c_\beta(0)\exp(\frac{1}{2}i\Omega t)\right]^* \times\left[c_\beta(0)\exp(\frac{1}{2}i\Omega t)\right]$$

$$= \frac{1}{2}\left[c_\alpha{}^*(0)\exp(\frac{1}{2}i\Omega t)\right]\left[c_\alpha(0)\exp(-\frac{1}{2}i\Omega t)\right] - \frac{1}{2}\left[c_\beta{}^*(0)\exp(-\frac{1}{2}i\Omega t)\right]\left[c_\beta(0)\exp(\frac{1}{2}i\Omega t)\right]$$

$$= \frac{1}{2}c_\alpha{}^*(0)c_\alpha(0) - \frac{1}{2}c_\beta{}^*(0)c_\beta(0). \tag{2.50}$$

i.e., the *z* component of the spin angular momentum is not affected by the free evolution under a resonance offset.

Similarly, we can compute the time evolution of the *x* component of the spin angular momentum as:

$$\left\langle \hat{I}_x \right\rangle(t) = \frac{1}{2}c_\alpha{}^*(0)c_\beta(0)\exp(i\Omega t) + \frac{1}{2}c_\beta{}^*(0)c_\alpha(0)\exp(-i\Omega t), \tag{2.51}$$

which shows that the *x*-component of the spin angular momentum precesses at a frequency Ω, i.e., the resonance offset given in Equation 2.14.

As explained in section 2.1, when an *rf* pulse is applied, the effect of the B_1 magnetic field can be explained by switching to a rotating frame. Specifically, if the *rf* pulse is applied on resonance, the magnetization nutates about the direction of the B_1 magnetic field at the nutation frequency (Equation 2.15).

The Hamiltonian for an on-resonance pulse along the *x*-axis is defined as:

$$\hat{H} = \omega_1 \hat{I}_x \,. \tag{2.52}$$

It then follows the differential Equations for the coefficients are:

$$\frac{dc_\alpha(t)}{dt} = -\frac{1}{2} i\omega_1 c_\beta(t) \tag{2.53}$$

$$\frac{dc_\beta(\mathrm{t})}{dt} = -\frac{1}{2} i\omega_1 c_\alpha(t)\,. \tag{2.54}$$

The solution for the above Equations is

$$\begin{aligned} c_\alpha(\mathrm{t}) &= \cos(\frac{1}{2}\omega_1 t)c_\alpha(0) - i\sin(\frac{1}{2}\omega_1 t)c_\beta(0) \\ c_\beta(\mathrm{t}) &= \cos(\frac{1}{2}\omega_1 t)c_\beta(0) - i\sin(\frac{1}{2}\omega_1 t)c_\alpha(0). \end{aligned} \tag{2.55}$$

Using these Equations, we can calculate the expectation value of the *x*, *y*, and *z* components of the spin angular momentum resulting from the application of an *rf* pulse:

$$\left\langle \hat{I}_x \right\rangle(t) = \frac{1}{2} c_\alpha^{\,*}(0)c_\beta(0) + \frac{1}{2} c_\beta^{\,*}(0)c_\alpha(0).$$

$$\left\langle \hat{I}_z \right\rangle(t) = \frac{1}{2}\left[c_\alpha^{\,*}(0)c_\alpha(0) - c_\beta^{\,*}(0)c_\beta(0) \right]\cos(\omega_1 t) + \frac{1}{2} i\left[c_\alpha(0)c_\beta^{\,*}(0) - c_\beta(0)c_\alpha^{\,*}(0) \right]\sin(\omega_1 t)$$

$$\left\langle \hat{I}_y \right\rangle(t) = -\frac{1}{2} i\left[c_\alpha^{\,*}(0)c_\beta(0) - c_\alpha(0)c_\beta^{\,*}(0) \right]\cos(\omega_1 t) - \frac{1}{2}\left[c_\alpha^{\,*}(0)c_\alpha(0) - c_\beta(0)c_\alpha^{\,*}(0) \right]\sin(\omega_1 t)$$

which, on simplification gives

$$\begin{aligned}
\left\langle \hat{I}_x \right\rangle(t) &= \hat{I}_x(0) \\
\left\langle \hat{I}_y \right\rangle(t) &= \hat{I}_y(0)\cos(\omega_1 t) - \hat{I}_z(0)\sin(\omega_1 t) \\
\left\langle \hat{I}_z \right\rangle(t) &= \hat{I}_z(0)\cos(\omega_1 t) + \hat{I}_y(0)\sin(\omega_1 t).
\end{aligned} \tag{2.56}$$

From this, we can calculate the bulk magnetization as before to be:

$$\begin{aligned}
M_x(t) &= M_x(0) \\
M_y(t) &= M_y(0)\cos(\omega_1 t) - M_z(0)\sin(\omega_1 t) \\
M_z(t) &= M_z(0)\cos(\omega_1 t) + M_y(0)\sin(\omega_1 t).
\end{aligned} \tag{2.57}$$

These relationships predict precisely the same as the classical approach of NMR, which was explained in Section 2.1 (see e. g. Figure 2.3).

2.3. Density Operator Formalism

In order to simplify the above approach, an alternative method called the density operator formalism is introduced, which is particularly useful for coupled nuclear spins and is defined as:

$$\langle \hat{\rho} \rangle = \overline{|\Psi\rangle\langle\Psi|}, \tag{2.58}$$

where $\hat{\rho}$ represents the density operator and the overbar again represents an ensemble average.

In this approach, the components of the angular momentum are always expressed in terms of products of two coefficients c_α and c_β, and it is these products that can undergo an averaging process while taking the ensemble average. Note that the matrix representation in this thesis is distinguished from the operator by the normal font.

The matrix representation of the density operator is (note italic only font with no hats is used for matrices)

$$\rho = \begin{bmatrix} \langle \alpha | \hat{\rho} | \alpha \rangle & \langle \alpha | \hat{\rho} | \beta \rangle \\ \langle \beta | \hat{\rho} | \alpha \rangle & \langle \beta | \hat{\rho} | \beta \rangle \end{bmatrix}$$

$$= \begin{pmatrix} \rho_{11} & \rho_{12} \\ \rho_{21} & \rho_{22} \end{pmatrix}$$

$$= \begin{pmatrix} c_\alpha c_\alpha^* & c_\alpha c_\beta^* \\ c_\beta c_\alpha^* & c_\beta c_\beta^* \end{pmatrix}. \tag{2.59}$$

The diagonal elements of the density matrix represent population states, while the off-diagonal elements correspond to so-called coherence.

Consider the multiplication of the density matrix, ρ, with a matrix corresponding to a given operator $\hat{A}$ acting upon a system:

$$\begin{aligned} \rho A &= \begin{pmatrix} c_\alpha^* c_\alpha & c_\beta^* c_\alpha \\ c_\alpha^* c_\beta & c_\beta^* c_\beta \end{pmatrix} \begin{pmatrix} A_{\alpha\alpha} & A_{\alpha\beta} \\ A_{\beta\alpha} & A_{\beta\beta} \end{pmatrix} \\ &= \begin{pmatrix} c_\alpha^* c_\alpha A_{\alpha\alpha} + c_\beta^* c_\alpha A_{\beta\alpha} & c_\alpha^* c_\alpha A_{\alpha\beta} + c_\beta^* c_\alpha A_{\beta\beta} \\ c_\alpha^* c_\beta A_{\alpha\alpha} + c_\beta^* c_\beta A_{\beta\alpha} & c_\alpha^* c_\beta A_{\alpha\beta} + c_\beta^* c_\beta A_{\beta\beta} \end{pmatrix}. \end{aligned} \tag{2.60}$$

Importantly, the expectation value of $\hat{A}$ corresponds to the sum of all the diagonal terms of the resulting matrix; this is known as the trace of the matrix:

$$\left\langle \hat{A} \right\rangle = Tr\left[\rho A\right]. \tag{2.61}$$

2.3.1. The Equilibrium Density Operator

$c_\alpha c_\alpha^*$ and $c_\beta c_\beta^*$ are related to the populations, n_α, and n_β, of the two states:

$$\begin{aligned} c_\alpha c_\alpha^* &= n_\alpha / N \\ c_\beta c_\beta^* &= n_\beta / N \end{aligned}, \tag{2.62}$$

where N corresponds to the sum of n_α and n_β.

Hence, the diagonal elements of the density matrix ρ can be expressed in terms of the population

states. The $c_\alpha^* c_\beta$ and $c_\beta^* c_\alpha$ terms are zero at equilibrium. Thus, the density matrix can be represented as follows:

$$\hat{\rho}_{eq} = \begin{pmatrix} n_{\alpha,eq} / N & 0 \\ 0 & n_{\beta,eq} / N \end{pmatrix}. \tag{2.63}$$

This is considered as the starting point for an NMR experiment, i.e., for a sample at thermal equilibrium.

2.3.2. The Evolution of the Density Operator as a Time-Dependent Function

The time evolution of the density operator can be explained using the Equation presented in Equation 2.44 together with the complex conjugate form of Equation 2.44:

$$\frac{d\langle\psi(t)|}{dt} = i\langle\psi(t)|\hat{H}. \tag{2.64}$$

Differentiation of the density operator gives:

$$\frac{d\,\hat{\rho}(t)}{dt} = \frac{d}{dt}\left(|\Psi(t)\rangle\langle\psi(t)|\right) = \left(\frac{d}{dt}|\Psi(t)\rangle\right).\langle\psi(t)| + |\Psi(t)\rangle.\left(\frac{d}{dt}\langle\psi(t)|\right)$$

$$= \left[-i\hat{H}|\Psi(t)\rangle.\langle\psi(t)|\right] + \left[|\Psi(t)\rangle.i\langle\psi(t)|\hat{H}\right].$$

$$= -i(\hat{H}\,\hat{\rho}(t) - \hat{\rho}(t)\,\hat{H}). \tag{2.65}$$

This is known as the Liouville-von Neumann Equation, and the solution to this Equation when the Hamiltonian is constant for some time, *t*, is:

$$\hat{\rho}(t) = e^{-i\hat{H}t}\,\hat{\rho}(0)e^{+i\hat{H}t}. \tag{2.66}$$

On applying a RF pulse, Equation 2.66 can be rewritten as,

$$\hat{\rho}(t) = e^{-i\omega_1 t I_x}\,\hat{\rho}(0)e^{+i\omega_1 t I_x}, \tag{2.67}$$

where $\hat{\rho}(t)$ and $\hat{\rho}(0)$ are the density operator acting at time *t*, and zero respectively.

The Hamiltonian operator is always Hermitian, and thus the corresponding operator is Unitary. For a time-independent Hamiltonian, the unitary propagator can be expressed as,

$$\hat{U}(t) = \exp(-i\hat{H}t) \tag{2.68}$$

and Equation 2.67 can be simplified as,

$$\hat{\rho} = \hat{U}(t)\,\hat{\rho}(0)\hat{U}(t)^{-1}. \tag{2.69}$$

$\hat{U}(t)$ is the propagator for the Hamiltonian acting between times $t = 0$ and $t = t$.

Solving the Liouville-von Neumann Equation is more difficult when the Hamiltonian varies with time. If the Hamiltonian acting during the time period $t = 0$ and $t = t$ is not constant but can be represented as different Hamiltonian each acting successively during the period of time *t*, then the propagator will be the product of these Hamiltonians:

$$\hat{U}(t) = e^{-i\hat{H}_n t_n} \ldots e^{-i\hat{H}_3 t_3} e^{-i\hat{H}_2 t_2} e^{-i\hat{H}_1 t_1}. \tag{2.70}$$

2.4. Product Operators

Product operators are another way of describing NMR experiments. This approach is particularly useful for coupled spin systems because the matrix representation of such systems using the density operator formalism becomes very complicated. Product operators are limited to weak couplings and hence are convenient for describing experiments based upon *J* coupling interactions, though they can also be used to explain dipolar based solid-state NMR experiments.

For an isolated spin ½ nucleus, four operators are required to explain NMR experiments: $1/2E$, I_x, I_y, I_z, where *E* is simply the identity operator and the other three operators correspond to the *x*, *y* and *z* magnetisation of a single spin in the rotating frame. The effect of an *rf* pulse along the *x*-axis on the magnetisation can be represented as follows:

$$I_x \xrightarrow{\beta I_x} I_x$$

$$I_y \xrightarrow{\beta I_x} I_y \cos\beta + I_z \sin\beta$$

$$I_z \xrightarrow{\beta I_x} I_z \cos\beta - I_y \sin\beta\,, \tag{2.71}$$

where β is the flip angle, see Section 2.5.1.1, Equation 2.96. Similarly, the evolution of magnetisation under a resonance offset can be described as:

$$I_x \xrightarrow{\Omega t I z} I_x \cos\Omega t + I_y \sin\Omega t$$

$$I_y \xrightarrow{\Omega t I z} I_y \cos\Omega t - I_x \sin\Omega t$$

$$I_z \xrightarrow{\Omega t I z} I_z\,. \tag{2.72}$$

In a system of two weakly *J*-coupled spins *I* and *S*, the set of product operators can be generated using the four operators stated at the beginning of this Section. The 16 operators can be constructed using the products of the four operators for the individual spin *I* and *S* as shown in Table 2.1.

Table 2.1: Product operators for two *J*-coupled spin ½ nuclei, labelled *I* and *S*.

	½ *E*	S_x	S_y	S_z
½ *E*	½ *E*	S_x	S_y	S_z
$2I_x$	I_x	$2I_xS_x$	$2I_xS_y$	$2I_xS_z$
$2I_y$	I_y	$2I_yS_x$	$2I_yS_y$	$2I_yS_z$
$2I_z$	I_z	$2I_zS_x$	$2I_zS_y$	$2I_zS_z$

The factor of 2 on the left of I_x, I_y, and I_z for the 2-spin terms is the result of normalisation. The operators $2I_xS_x$, $2I_xS_y$, $2I_yS_x$, $2I_yS_y$, represent multiple quantum coherence in NMR. I_x, I_y, I_z, S_x, S_y,

and S_z are referred as in-phase single quantum operators operators whereas $2I_xS_z$, $2I_yS_z$, $2I_zS_x$, and $2I_zS_y$ are known as antiphase operators. The evolution of I_x and I_y operator under the influence of a J coupling between two spins (J_{IS}) is described as:

$$I_x \xrightarrow{\pi J_{IS} t 2I_z S_z} I_x \cos(\pi J_{IS} t) + 2I_y S_z \sin(\pi J_{IS} t)$$

$$I_y \xrightarrow{\pi J_{IS} t 2I_z S_z} I_y \cos(\pi J_{IS} t) - 2I_y S_z \sin(\pi J_{IS} t) . \quad (2.73)$$

From the above Equations, it is clear that the magnetisation, which exists only on the I spin at the initial state is transferred to S spin during the time t under a J-coupling. Such magnetization transfer is seen in experiments like INEPT, which will be discussed in detail in Chapter 3.

2.5. Hamiltonians and Interactions

NMR interactions can be classified as either internal or external interactions. As described in Section 2.1, there are two sources of external interactions: the first source is the interaction of the spin system with a strong longitudinal static magnetic field, B_0, i.e., the Zeeman interaction and the second is the interaction with a transverse magnetic field, B_1, which is oscillating at the radio frequency and is generated by a coil. Hence the total average Hamiltonian is:

$$\hat{H}_{total} = \hat{H}^{ext} + \hat{H}^{\text{int}} , \quad (2.74)$$

where

$$\hat{H}^{ext} = \hat{H}_z + \hat{H}_{RF} . \quad (2.75)$$

$$\hat{H}^{\text{int}} = \hat{H}_{CS} + \hat{H}_D + \hat{H}_J + \hat{H}_Q . \quad (2.76)$$

The H^{ext} term comprises the Zeeman interaction ($\hat{H}_z$) (dominant) and the perturbing interaction due to the oscillating radio frequency magnetic field ($\hat{H}_{RF}$), which is used to create the spin coherences. The internal Hamiltonian consists of the chemical shielding ($\hat{H}_{CS}$), dipolar coupling ($\hat{H}_D$), J coupling ($\hat{H}_J$), and quadrupolar interaction ($\hat{H}_Q$); these interactions are used to reveal chemical information and are described in more detail later in this Section.

In a general frame, the Hamiltonian for interactions can be represented in Cartesian form as:

$$\hat{H} = \hat{I}.\tilde{A}.\hat{S}, \tag{2.77}$$

where $\tilde{A}$ is a second rank tensor which represents the particular interaction, $\hat{I}$ represents the spin operator and $\hat{S}$ can be an external magnetic field or another spin operator. The matrix representation of the above Equation is:

$$\hat{H} = \begin{bmatrix} I_x I_y I_z \end{bmatrix} \begin{pmatrix} A_{xx} & A_{xy} & A_{xz} \\ A_{yx} & A_{yy} & A_{yz} \\ A_{zx} & A_{zy} & A_{zz} \end{pmatrix} \begin{bmatrix} S_x \\ S_y \\ S_z \end{bmatrix}. \tag{2.78}$$

2.5.1. The External Hamiltonian

In a static, uniform magnetic field, B_0, the Hamiltonian of the Zeeman interaction between the nuclear spin, I, and the static external magnetic field, B_0 (as presented in Equation 2.45 for the rotating frame) is expressed in the laboratory frame as:

$$H_Z = -\gamma B_0 \hat{I}_z = \omega_0 \hat{I}_Z . \tag{2.79}$$

The magnetic field used for solid-state NMR is generally of the order of 5-25 tesla.

2.5.1.1 Application of an Oscillating *rf* Field

As demonstrated in Section 2.1, at thermal equilibrium, the magnetisation is in a population state aligned with I_z, while only a coherence state (I_x and I_y) can be observed in the NMR experiment. An oscillating magnetic field, $B_1(t)$ (see Equation 2.13), which is much weaker than the static field is introduced to manipulate the spin systems. The oscillating magnetic field can be expressed as:

$$\underline{B_1}(t) = 2B_1 \cos\left\{\omega_{rf} t + \phi\right\} \underline{i}$$

$$= B_1 (e^{+i\omega_{rf} t} + e^{-i\omega_{rf} t}) \underline{i} \text{ if } \phi = 0, \tag{2.80}$$

where ϕ is the phase of the *rf* field, and i is the unit vector along the x-axis. According to the above

Equation, the weak magnetic field $B_1(t)$ have two counter-rotating fields with distinct frequencies $+\omega_{rf}$ and $-\omega_{rf}$ (as noted above, the one with the opposite sign to the Larmor frequency can then be neglected). The Hamiltonian of such an *rf* pulse can be represented as follows:

$$\hat{H}_{RF} = \omega_1\{\hat{I}_x \cos(\omega_{rf}t + \phi) + \hat{I}_y \sin(\omega_{rf}t + \phi)\}. \tag{2.81}$$

This Hamiltonian can be expressed in the rotating frame, the concept of which was introduced in Section 2.1 so that it becomes time-independent:

$$\hat{H}_{RF}^{rot} = \omega_1[\hat{I}_x \cos(\phi) + \hat{I}_y \sin(\phi)]. \tag{2.82}$$

Hence it is the initial phase of the pulse which determines the initial position of the *rf* pulse in the *x*-*y* plane of the rotating frame. If the initial phase of the pulse is 0, then it reduces Equation 2.82 to that in Equation 2.52:

$$\hat{H}_{RF}^{rot} = \omega_1 \hat{I}_x. \tag{2.83}$$

The evolution of the time-dependent density matrix for such an applied B_1 magnetic field can be expressed using the solution to the Liouville von-Neumann Equation 2.66.

The matrix representation of the density operator at equilibrium is shown in Equation 2.63. The $n_{\alpha,\,eq}$ and $n_{\beta,\,eq}$ in the Equation 2.63 can be expressed using the Boltzmann distribution:

$$n_{\alpha,eq} = \frac{1}{2}N(1 + E_\alpha / k_B T) \tag{2.84}$$

$$n_{\beta,eq} = \frac{1}{2}N(1 - E_\beta / k_B T). \tag{2.85}$$

Equation 2.85 can be simplified used Equations 2.6 and 2.7, therefore:

$$\begin{aligned} n_{\alpha,eq} &= \frac{1}{2}N(1 + \hbar\gamma B_0 / 2k_B T) \\ n_{\beta,eq} &= \frac{1}{2}N(1 - \hbar\gamma B_0 / 2k_B T). \end{aligned} \tag{2.86}$$

From these Equations, the average populations can be computed as:

$$n_{av} = \frac{1}{2}\left(n_{\alpha,eq} + n_{\beta,eq}\right) = \frac{1}{N}, \tag{2.87}$$

and the difference in population is:

$$\Delta n = n_{\alpha,eq} - n_{\beta,eq}. \tag{2.88}$$

The population of the two energy levels can be represented as:

$$\begin{aligned} n_{\alpha,eq} &= n_{av} + \frac{1}{2}\Delta n \\ n_{\beta,eq} &= n_{av} - \frac{1}{2}\Delta n, \end{aligned} \tag{2.89}$$

Therefore Equation 2.63 now becomes:

$$\rho_{eq} = \begin{bmatrix} n_{av} + \frac{1}{2}\Delta n & 0 \\ 0 & n_{av} - \frac{1}{2}\Delta n \end{bmatrix}. \tag{2.90}$$

Equation 2.90 can be represented in terms of the matrix representations of $\hat{E}$ and $\hat{I}_z$:

$$\begin{aligned} \hat{\rho}_{eq} &= \frac{n_{av}}{N}\begin{bmatrix} 1 & 0 \\ 0 & 1 \end{bmatrix} + \frac{\Delta n}{N}\begin{bmatrix} \frac{1}{2} & 0 \\ 0 & -\frac{1}{2} \end{bmatrix}. \\ &= \frac{n_{av}}{N}\hat{E} + \frac{\Delta n}{N}\hat{I}_z \end{aligned} \tag{2.91}$$

The matrix $\hat{E}$ can be ignored because it does not yield any observable magnetization, hence Equation 2.88 can be simpled as:

$$\hat{\rho}_{eq} = k_1 \hat{I}_z, \tag{2.92}$$

where $k_1 = \frac{\Delta n}{N}$. The factor k_1 can be ignored for simplicity and hence at the initial state of the system for spin ½ nuclei, the equilibrium density matrix is represented as follows:

$$\rho(0) = I_z = \begin{pmatrix} \frac{1}{2} & 0 \\ 0 & -\frac{1}{2} \end{pmatrix}. \tag{2.93}$$

In matrix form, ρ(t) which was presented in Equation 2.67 can be shown to be:

$$\rho(t) = \frac{1}{2}\begin{pmatrix} \cos(\omega_1 t) & i\sin(\omega_1 t) \\ -i\sin(\omega_1 t) & \cos(\omega_1 t) \end{pmatrix}. \tag{2.94}$$

From the above Equation, it is clear that the *rf* pulse generated off-diagonal terms, i.e, corresponding to coherence between the spin eigenstates, in addition to population states (diagonal).

The expectation value of each spin operator is:

$$\left\langle \hat{I}_x(t) \right\rangle = Tr\left\{\rho(t) I_x\right\} = \begin{pmatrix} \frac{1}{4} i\sin(\omega_1 t) & \frac{1}{4}\cos(\omega_1 t) \\ -\frac{1}{4}\cos(\omega_1 t) & \frac{1}{4} i\sin(\omega_1 t) \end{pmatrix} = 0$$

$$\left\langle \hat{I}_y(t) \right\rangle = Tr\left\{\rho(t) I_y\right\} = \begin{pmatrix} -\frac{1}{4}\sin(\omega_1 t) & -\frac{1}{4} i\cos(\omega_1 t) \\ -\frac{1}{4} i\cos(\omega_1 t) & -\frac{1}{4}\sin(\omega_1 t) \end{pmatrix} = -\frac{1}{2}\sin(\omega_1 t)$$

$$\left\langle \hat{I}_z(t) \right\rangle = Tr\left\{\rho(t) I_z\right\} = \begin{pmatrix} \frac{1}{4}\cos(\omega_1 t) & -\frac{1}{4} i\sin(\omega_1 t) \\ -\frac{1}{4} i\sin(\omega_1 t) & \frac{1}{4}\cos(\omega_1 t) \end{pmatrix} = \frac{1}{2}\cos(\omega_1 t). \tag{2.95}$$

Applying an *rf* pulse, aligned along the *x*-direction rotates the magnetisation around the *x*-axis by a flip angle (β), which depends on the strength of ω_1 and time of the applied pulse (t_p);

$$\beta = \omega_1 t_p . \tag{2.96}$$

Similarly, one can also compute the evolution of the density matrix under a resonance offset.

In this case, consider an initial state corresponding to *x* magnetisation, i.e., after a 90º *rf* pulse:

$$\rho(0) = I_x = \begin{pmatrix} 0 & \frac{1}{2} \\ \frac{1}{2} & 0 \end{pmatrix}. \tag{2.97}$$

$$\hat{\rho}(t) = e^{-i\Omega t \hat{I}_z} \hat{\rho}(0) e^{i\Omega t \hat{I}_z} \tag{2.98}$$

where from Equation 2.45:

$$\hat{H} = \Omega \hat{I}_z .$$

Solving Equation 2.98 gives,

$$\hat{\rho}(t) = \begin{pmatrix} \exp(-\frac{1}{2} i\Omega t) & 0 \\ 0 & \exp(\frac{1}{2} i\Omega t) \end{pmatrix} \begin{pmatrix} 0 & \frac{1}{2} \\ \frac{1}{2} & 0 \end{pmatrix} \begin{pmatrix} \exp(\frac{1}{2} i\Omega t) & 0 \\ 0 & \exp(-\frac{1}{2} i\Omega t) \end{pmatrix}$$

$$= \begin{pmatrix} 0 & -\frac{1}{2} e^{-i\Omega t} \\ \frac{1}{2} e^{i\Omega t} & 0 \end{pmatrix}. \tag{2.99}$$

It is clear from the off-diagonal terms that the transverse magnetization is evolving and measurement of this transverse magnetization for the time domain signal can be obtained by taking the trace of ρ(t) and by multiplying with the matrix representation of the complex conjugate $\hat{I}_- = \hat{I}_+^+$:

$$\hat{I}_+ = I_x + i I_y = \begin{pmatrix} 0 & 1 \\ 0 & 0 \end{pmatrix}. \tag{2.100}$$

Therefore,

$$s(t) = Tr\left[\rho(t)\, I_{+}\right], \tag{2.101}$$

$$= Tr\left\{\begin{pmatrix} 0 & \frac{1}{2}e^{-i\Omega t} \\ \frac{1}{2}e^{i\Omega t} & 0 \end{pmatrix}\begin{pmatrix} 0 & 1 \\ 0 & 0 \end{pmatrix}\right\}.$$

$$= Tr\begin{pmatrix} 0 & 0 \\ 0 & \frac{1}{2}e^{i\Omega t} \end{pmatrix}$$

$$= \frac{1}{2}e^{i\Omega t}$$

$$= \frac{1}{2}\cos(\Omega t) + i\sin(\Omega t). \tag{2.102}$$

Equation 2.101 indicates that the real and imaginary part components of the transverse magnetization rotate in the transverse plane, inducing a current in a coil corresponding to the NMR signal.

2.5.2 Internal Interactions

It is more convenient to represent the Hamiltonian of each internal interaction in their own principal axis system (PAS), where the interaction tensor is diagonal. The interaction Hamiltonian in the PAS can be defined as:

$$\hat{H}^{P} = \hat{I}.\tilde{A}^{P}.\hat{S},$$

$$= \begin{pmatrix} I_x & I_y & I_z \end{pmatrix} \begin{pmatrix} A_{xx} & 0 & 0 \\ 0 & A_{yy} & 0 \\ 0 & 0 & A_{zz} \end{pmatrix} \begin{pmatrix} S_x \\ S_y \\ S_z \end{pmatrix}, \tag{2.103}$$

where the P superscript in $\hat{H}_{\wedge}^{P}$ refers to the PAS of the $\wedge$ interaction. Each interaction tensor has a separate PAS, and the orientation of the principal axis system is determined by the local environment to which the interaction pertains. In order to explain the Hamiltonian of the internal interaction, it is necessary to transform the interaction tensor from the PAS to the laboratory frame (LAB) defined by B_0. The transformations between the frames are described in terms of Euler angles (α, β, γ).

2.5.3 Rotations: Euler Angles and Spherical Tensors

A rotation between coordinate frames can be described well using the spherical tensor formalism where the Hamiltonian is represented as:

$$\hat{H} = \sum_{j=0}^{2} \sum_{m=-j}^{+j} (-1)^m A_{jm} \hat{T}_{j-m}, \tag{2.104}$$

where $\hat{T}_{j-m}$ and A_{jm} represent the spin-field tensors and spatial components respectively. Rotation of the set of axes by the Euler angles is depicted in Figure 2.5:

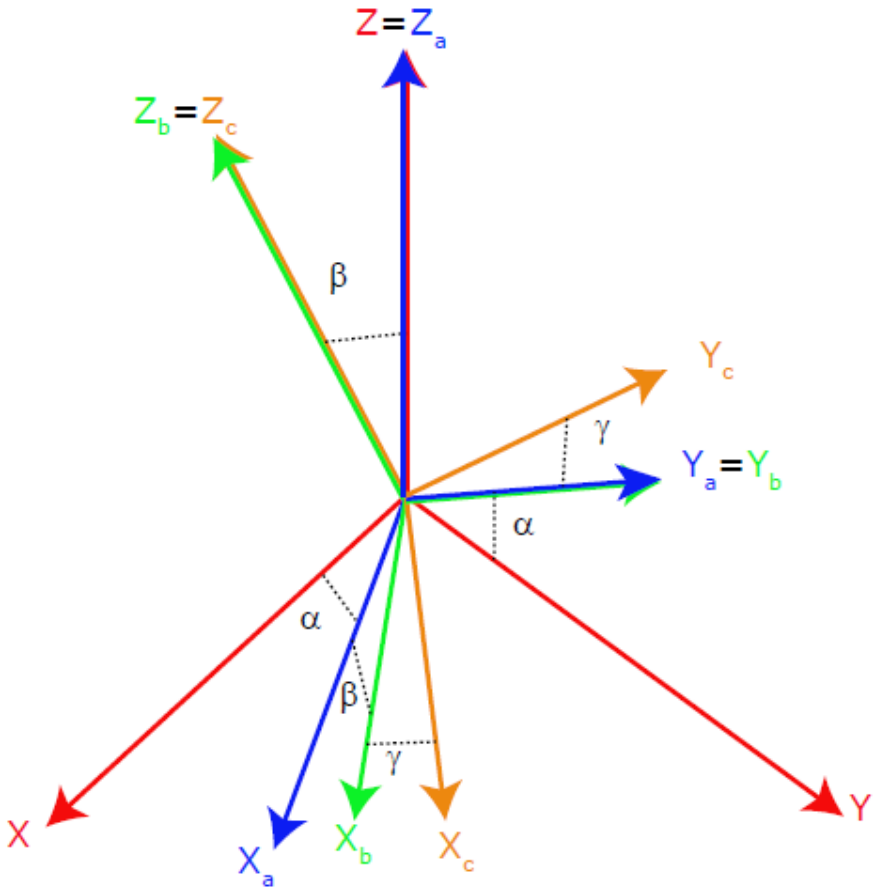

Figure 2.5: Rotation of a set of orthogonal axes (X, Y, Z) through the Euler angles α, β, and γ.

The full transformation from the PAS to LAB frame is given by:

$$R(A_{jm}^{start}) = \sum_{m'=-j}^{m'=+j} D_{m'm}^{j}(\alpha\beta\gamma) A_{jm'}^{end} \,, \tag{2.105}$$

where A_{jm}^{start} is the initial frame (PAS) and $A_{jm'}^{end}$ is the final (LAB) frame.

The rotation of the spatial components is described by:

$$D_{mm'}^{j}(\alpha\beta\gamma) = \exp(-im'\alpha) d_{kl}^{j}(\beta) \exp(-im\gamma) \,, \tag{2.106}$$

where $d^{j}_{mm'}$ are the reduced Wigner matrices and α, β and γ are the Euler angles which describe the rotation.

Therefore, the spherical component on rotating from PAS to LAB can be represented as:

$$A^{l}_{jm'} = \sum_{m=-j}^{+j} A^{P}_{jm} D^{j}_{mm'}(\alpha_{PL}\ \beta_{PL}\ \gamma_{PL}), \tag{2.107}$$

where $(\alpha_{PL}\ \beta_{PL}\ \gamma_{PL})$ describe the Euler angles between the PAS and LAB. Thus, the Hamiltonian is represented as

$$\hat{H}^{L} = \sum_{j=0}^{2} \sum_{m=-j}^{+j} (-1)^{m} A^{PAS}_{jm} D^{j}_{mm'}(\alpha_{pl}\beta_{pl}\gamma_{pl}) \hat{T}_{j-m}\,. \tag{2.108}$$

2.5.4. The Secular Approximation

The Equation for the Hamiltonian for an interaction expressed in spherical form can be simplified using the secular or high field approximation. This approximation considers the Zeeman interaction as the dominant interaction ($\hat{H}_0$) and the specific nuclear spin interaction as a perturbation ($\hat{H}_1$). According to this approximation, interactions must be eigenfunctions of the dominant interaction (Zeeman interaction). These eigenfunctions are just the Zeeman basis set *I* and *m*, where *I* represent the total spin for the system and *m* its component along the static field. The parts of the $\hat{H}_1$ which affect the spin system must have the same eigenfunctions as of the Zeeman eigenfunctions, i.e., the Hamiltonian for $\hat{H}_0$ and $\hat{H}_1$ must commute. According to the following commutation relation,

$$\left[\hat{I}_z, \hat{T}_{jm}\right] = m\hat{T}_{jm}\,. \tag{2.109}$$

This relation shows that the commutator is zero only when $m = 0$.

2.5.5. Chemical Shielding ($\hat{H}_{cs}$)

As discussed in Section 2.1, this arises from the applied magnetic field inducing a current in the electrons surrounding the nucleus, resulting in the formation of an additional magnetic field. This additional magnetic field results in a change in the magnetic field experienced by the nucleus. This interaction is called the shielding interaction and the frequency shift this interaction causes in an NMR spectrum is known as the chemical shift, when a reference frequency, $\omega_{\text{ref,}}$ is used as in Equation 2.17

The chemical shielding Hamiltonian on a spin I is,

$$\hat{H}_{cs} = \gamma \hat{I} \cdot \tilde{\sigma} \cdot \hat{B}_0 . \tag{2.110}$$

The Hamiltonian in the LAB frame is:

$$\hat{H}_{CS} = \left\{ \sigma^{iso} \omega_0 + \frac{1}{2} \omega_0 \sigma_{aniso} (3\cos^2 \beta_{RL} - 1 + \eta \sin^2 \beta_{RL} \cos 2\alpha_{PL}) \right\}, \tag{2.111}$$

where σ is the second rank tensor which in the PAS has an isotropic contribution, which is given by:

$$\sigma^{iso} = \frac{1}{3} (\sigma_{XX} + \sigma_{YY} + \sigma_{zz}) . \tag{2.112}$$

Furthermore,

$$\sigma_{aniso} = \sigma_{zz} - \sigma^{iso} \tag{2.113}$$

$$\eta = \frac{\sigma_{XX} - \sigma_{YY}}{\sigma_{aniso}} , \tag{2.114}$$

where σ_{aniso} is the anisotropy and η is the asymmetry parameter. The chemical shielding interaction causes an isotropic chemical shift, which is dependent on the external magnetic field $B_{0,}$ as shown in Equation 2.110. The chemical shielding has both anisotropic and isotropic characteristics and is dependent on the orientation of the nucleus with respect to the laboratory frame. In the liquid state, molecules undergo rapid tumbling motion on the NMR timescale; this will average out all the anisotropic components of the chemical shielding over all orientations. The angular dependent

anisotropic term i.e., the dependence on β_{RL} and α_{PL} in Equation 2.111, in solids can be averaged out using magic angle spinning technique which will be discussed below.

2.5.6. Dipolar Coupling

There exist interactions between the magnetic moments of the nuclei that are close in space (see Figure 2.6). This through-space interaction is known as the dipolar interaction. The strength of the interaction depends on the internuclear distance and on the molecular orientation. According to a quantum mechanical description, for a simple case of coupling between two spin ½ nuclei, four possible Zeeman transition states are possible as shown in Figure 2.7, the transition between the degenerate energy levels $|\alpha\beta\rangle$ and $|\beta\alpha\rangle$ corresponds to zero quantum coherence and the transition between $|\alpha\alpha\rangle$ and $|\beta\beta\rangle$ represents double quantum coherence, which is described by two-spin product operators in Section 2.4. Double quantum coherence is created only when a spin is coupled with a second spin and cannot be seen for isolated spin ½ nuclei.

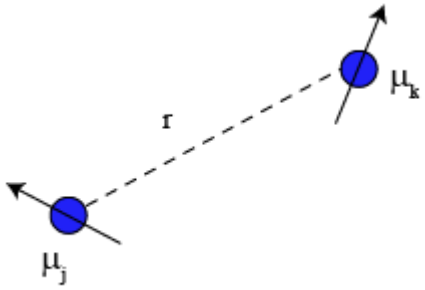

Figure 2.6: Interaction between two dipoles.

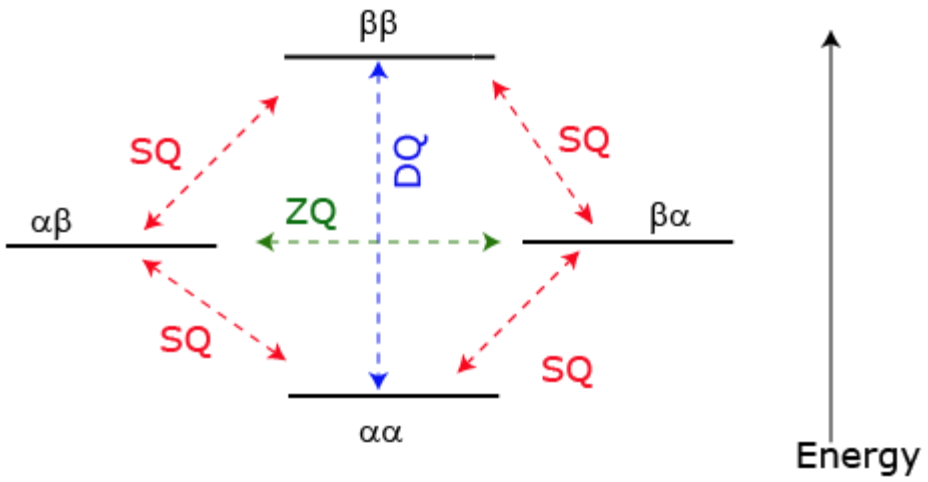

Figure 2.7: The Energy level diagram for two coupled spin ½ nuclei.

The Hamiltonian for the dipolar interaction in PAS is given by:

$$\hat{H}_D = \hat{I} \cdot \tilde{D} \cdot \hat{S}\,, \tag{2.115}$$

In Equation 2.115, $\tilde{D}$ is the second-rank Cartesian dipole–coupling tensor which represents the interaction between two spins I and S and has principal values of $-d/2$, $-d/2$, $+d$, where d is the dipolar constant and is given by,

$$d = -\hbar\left(\frac{\mu_0}{4\pi}\right)\frac{1}{r^3}\gamma_I\gamma_S\,. \tag{2.116}$$

The magnitude of the dipolar constant depends upon the gyromagnetic ratios of the two nuclei, γ_I and γ_S, and the inverse cubed separation, r, between the nuclei. μ_0 is the permeability of free space.

The $\tilde{D}$ tensor is traceless and axially symmetric; hence, the dipolar Hamiltonian can be simplified as:

$$\hat{H}_D = A_{20}^{p}\hat{T}_{20}\,, \tag{2.117}$$

where

$$A_{20}^{p} = \sqrt{6}d\,. \tag{2.118}$$

When rotated into the laboratory frame using the Equation 2.106, the spatial components of the dipolar Hamiltonian can be expressed in terms of a single reduced Wigner rotation matrix. Specifically, A_{20}^{L} is given by,

$$A_{20}^{L} = A_{20}^{p} D_{00}^{2} = \sqrt{6} d \frac{1}{2}(3\cos^2\theta - 1). \tag{2.119}$$

The spin term is,

$$\hat{T}_{20} = \frac{1}{\sqrt{6}}\left(\hat{I}_z \hat{S}_z - \frac{1}{2}\left(\hat{I}_x \hat{S}_x + \hat{I}_y \hat{S}_y \right) \right). \tag{2.120}$$

For two spin 1/2 nuclei, the matrix form of Equation 2.116 is expressed as:

$$T_{20} = \frac{1}{2\sqrt{6}} \begin{bmatrix} 1 & 0 & 0 & 0 \\ 0 & -1 & -1 & 0 \\ 0 & -1 & -1 & 0 \\ 0 & 0 & 0 & 1 \end{bmatrix}. \tag{2.121}$$

The Hamiltonian of the dipole interaction is then given by combining the spin and spatial term:

$$\hat{H}_D = d \frac{1}{2}(3\cos^2\theta - 1)\left(2\hat{I}_z \hat{S}_z - (\hat{I}_x \hat{S}_x + \hat{I}_y \hat{S}_y) \right). \tag{2.122}$$

The Hamiltonian for the heteronuclear case can be written as:

$$\hat{H}_D = d \frac{1}{2}(3\cos^2\theta - 1)\left(2\hat{I}_z \hat{S}_z \right). \tag{2.123}$$

For a heteronuclear dipolar coupling, the off-diagonal elements of the corresponding matrix are zero, since only the $\hat{I}_z \hat{S}_z$ term remains. For a powdered sample, θ, the angle between the internuclear vector and B_0 can take values from 0 to π, with a sinθ weighting. A typical lineshape, acquired under static condition for a heteronuclear dipolar coupling is shown in Figure 2.8 and is known as a Pake doublet[13]. The two horns reflect two different crystallite orientations, both perpendicular to the external magnetic field, B_0, and the separation between the two horns is equal

to *d*. This implies that the broadening effect due to heteronuclear dipolar coupling has an inherent orientation dependence and therefore MAS can completely remove the effect from this interaction.

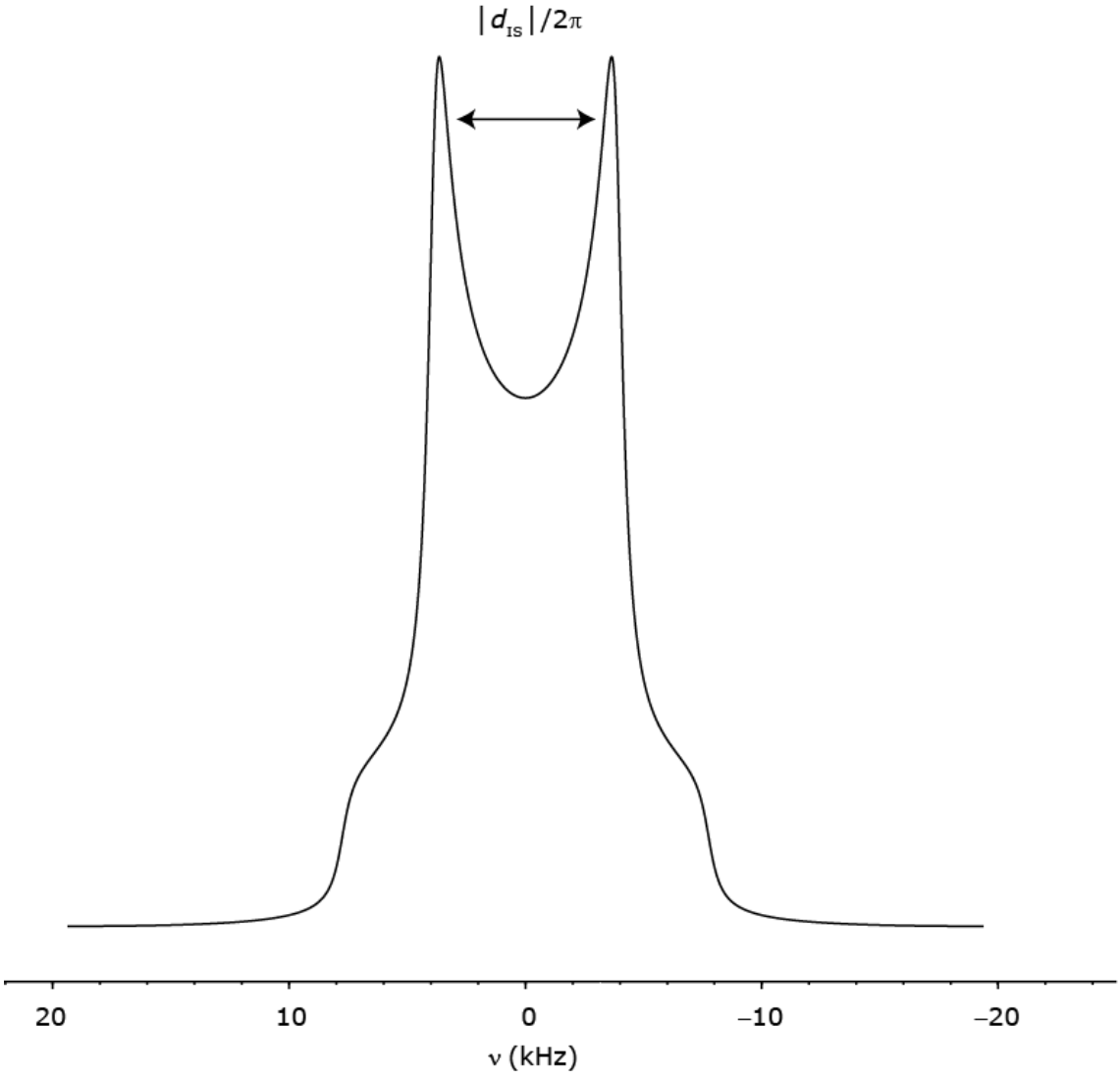

Figure 2.8: A simulated heteronuclear Pake doublet for a dipolar coupled pair of spin ½ nuclei.

For the homonuclear dipolar coupling, a complication arises due to the presence of the additional term, $\hat{I}_x \hat{S}_x + \hat{I}_y \hat{S}_y$. These terms can be expressed in terms of lowering and raising operators and is referred as flip-flop term:

$$\hat{I}_x \hat{S}_x + \hat{I}_y \hat{S}_y = \left(\hat{I}_- \hat{S}_+ + \hat{I}_+ \hat{S}_- \right). \tag{2.124}$$

The broadening effects of the dipolar coupling on the solid-state NMR spectrum can be explained by the spin angular momentum terms in the Equation 2.122. These terms can be represented as matrices:

$$2I_z S_z = \begin{pmatrix} \frac{1}{2} & 0 & 0 & 0 \\ 0 & -\frac{1}{2} & 0 & 0 \\ 0 & 0 & -\frac{1}{2} & 0 \\ 0 & 0 & 0 & \frac{1}{2} \end{pmatrix}, I_x S_x + I_y S_y = \begin{pmatrix} 0 & 0 & 0 & 0 \\ 0 & 0 & \frac{1}{2} & 0 \\ 0 & \frac{1}{2} & 0 & 0 \\ 0 & 0 & 0 & 0 \end{pmatrix}. \quad (2.125)$$

From the matrix form of the $I_x S_x + I_y S_y$ term, it is clear that for a two spin ½ system, the spin eigenstates are no longer straightforward Zeeman product states, but include linear combinations of degenerate Zeeman levels. Therefore, in a system with a large number of dipolar coupled protons, there exist several degenerate eigenstates, which contribute different transition frequencies; this is the reason for significant broadening in a ^{1}H solid-state NMR spectrum. This implies that the dipolar Hamiltonian no longer commutes with itself at different points. Importantly, this anisotropic line broadening due to homonuclear dipolar coupling cannot be removed entirely under MAS.

2.5.7. Interactions under Magic Angle Spinning

Magic-angle spinning (MAS) is widely applied in the vast majority of solid-state NMR experiments because it can remove the effect of anisotropy present for internal interactions. Experimentally, MAS is the physical rotation of the sample at a particular angle with respect to B_0, the so-called magic angle. To describe this mathematically, another frame called the rotor frame is required in addition to the PAS and LAB frame. Rotation is by the specific Euler angles, R(α_{PR}, β_{PR},γ_{PR}), followed by R(α_{RL}, β_{RL}, γ_{RL}), where PR represents the rotation from the PAS to the rotor frame, and RL specifies the rotation from the rotor frame to the LAB frame. A schematic representation of MAS is depicted in Figure 2.9. α_{RL} is subtended by rotation of the rotor, at $\omega_{R,}$ and γ_{PR} represents the phase of the rotor. Note that: θ in Equation 2.119 above corresponds to β_{RL}.

The non-zero term, for the chemical shielding (for $\eta = 0$) and dipolar Hamiltonian after double transformation (PAS to the rotor, followed by LAB frame), A_{20}^{p}, can be expressed using the secular approximation as follows:

$$A_{20}^{L} = A_{20}^{P} \sum_{m'=-2}^{2} D_{0m'}^{2}\left(\alpha_{PR,}\beta_{PR},\gamma_{PR}\right) d_{m'0}^{2}(\beta_{RL}) e^{-im'\omega_r t} \tag{2.126}$$

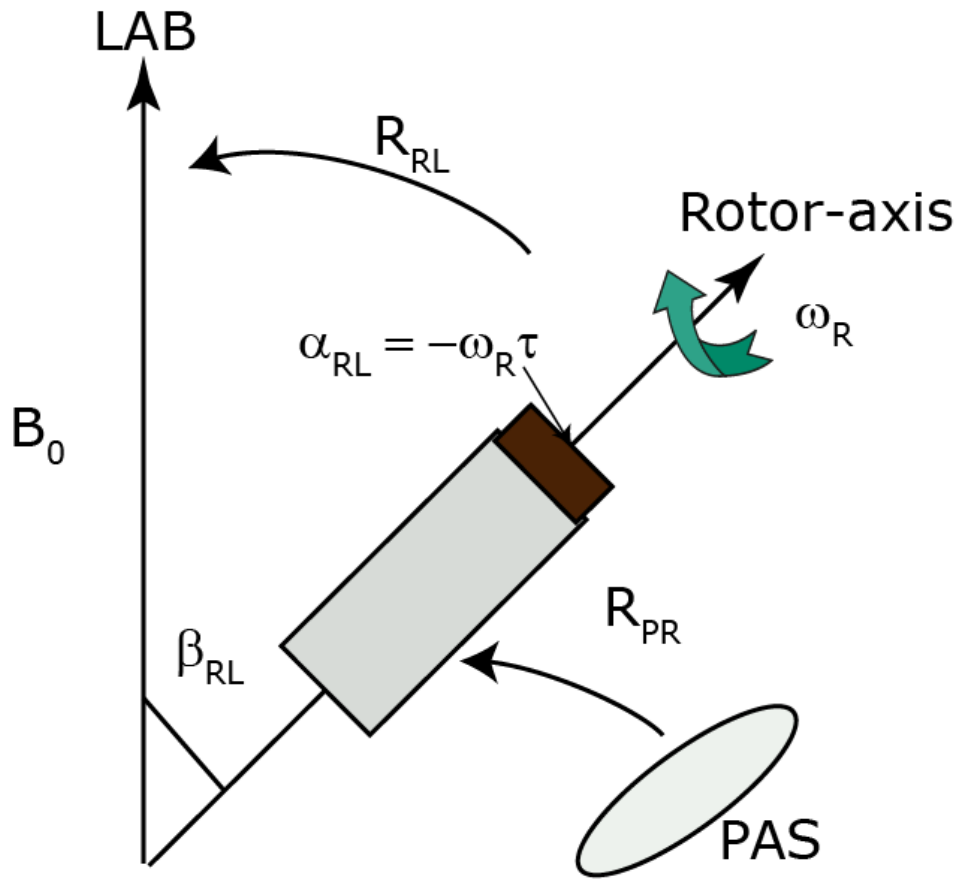

Figure 2.9: Representation of the rotor rotated around a fixed axis at β_{RL} with respect to the static field B_0.

The transformation to the rotor frame introduces a time dependence to the spatial tensor, given by the angle, $\alpha_{RL} = -\omega_R t$, hence depending upon the spinning frequency, ω_R. As a result of this, the interaction Hamiltonian becomes periodic with the rotor period $\tau_r = 2\pi / \omega_R$. According to the average Hamiltonian theory[33], the effect of spinning can be determined by considering the Hamiltonian at a specific time separated by this periodic time interval. Experimentally, this can be achieved by detecting the NMR signal at a point separated by τ_r, which is known as rotor

synchronised detection. The integral of the time-dependent term in the Hamiltonian averages to zero when m' is zero, over a complete rotation (one rotor period), i.e., $\int_0^{\tau_R} e^{im'\omega_r t} dt = 0$. Equation 2.126 then becomes:

$$\left\langle A_{20}^{L} \right\rangle \tau_r = A_{20}^{P} \left[\frac{1}{4} \left(3\cos^2 \beta_{PR} - 1 \right) \left(3\cos^2 \beta_{RL} - 1 \right) \right]. \qquad (2.127)$$

According to the above Equation, the orientation is now solely dependent upon the Euler angle, β_{RL}. The anisotropies can be averaged to zero by aligning the sample rotor at an axis with respect to the applied field B_0, i.e.

$$\beta_{RL} = \cos^{-1}(1/\sqrt{3}) = 54.74° \qquad (2.128)$$

and this angle is known as the magic angle.

Consider the case where the NMR signals are not acquired in a rotor synchronised manner, then all the spatial components must be included, and Equation 2.127 becomes;

$$A_{20}^{L} = A_{20}^{P} \left[\frac{1}{2} \left(\sin^2 \beta_{PR} \cos(2\gamma_{PR} + 2\omega_r t \right) - \sqrt{2} \sin 2\beta_{PR} \cos(\gamma_{PR} + \omega_r t) \right], \qquad (2.129)$$

and a periodicity of the anisotropic interaction remains. This is exhibited in the NMR spectrum by the appearance of spinning sidebands. Spinning sidebands are sharp lines, found at multiples of the spinning frequency away from the isotropic resonance. If the spinning frequency is significantly higher than the size of anisotropy, the spinning sidebands are reduced in intensity, appearing in the fast spinning limit as a single narrow centre band resonance.

2.5.8. *J* Coupling or Scalar Coupling

J coupling is the indirect interaction between the nuclear spins through electrons. A *J* coupling can only be measured if the spins are connected via a small number of bonds. It, therefore, gives information on molecular level connectivity and questions of molecular conformation. The coupling constant is represented as *J* and has great significance in liquid state NMR compared to solid-state NMR. This is because the magnitude of the anisotropic component of the *J* coupling is negligible for light elements being typically less than 1 kHz, and the size of the isotropic

component is small when compared to the other interactions. The Hamiltonian for the interaction is given by:

$$\hat{H} = 2\pi \hat{I} \cdot \tilde{J}_{IS} \cdot \hat{S} \tag{2.130}$$

From the Equation, it is clear that interaction is, like the dipolar coupling in Section 2.5.6, independent of the B_0 magnetic field.

2.5.9. Quadrupolar Coupling ($\hat{H}_Q$)

NMR active nuclei with spin higher than ½ are known as quadrupolar. Such nuclei possess an electric quadrupole moment in addition to a magnetic moment. This electric quadrupole moment interacts with an electric field gradient at the nucleus along with other magnetic field interactions. The strength of the interaction depends upon the magnitude of the nuclear quadrupole moment and the strength of the electric field gradient. The Hamiltonian for this interaction is:

$$\hat{H}_Q = \frac{eQ}{2I(2I-1)} \hat{I} . \tilde{V} . \hat{I} , \tag{2.131}$$

where $\tilde{V}$ is a tensor describing the electric field gradient at the nucleus, Q is the nuclear quadrupole moment, and e is the electric charge. The $\tilde{V}$ can be expressed in matrix form using the Cartesian components of electric field gradients as follows:

$$V = \begin{bmatrix} V_{xx} & V_{xy} & V_{xz} \\ V_{yx} & V_{yy} & V_{yz} \\ V_{zx} & V_{zy} & V_{zz} \end{bmatrix}.$$

As explained above, in the PAS, only the diagonal elements of the tensor $\tilde{V}$ are non-zero. The asymmetry quadrupole parameter is then given by:

$$\eta_Q = \frac{V_{xx} - V_{yy}}{V_{zz}} . \tag{2.132}$$

The asymmetry parameter, $\eta_{Q,}$ defines the relative strength of the electric field gradient (EFG) in three orthogonal directions. The EFG is axially symmetric if the η_Q value is zero, and a value of one represents high asymmetry. Another relevant term is the quadrupolar coupling constant which describes the strength of the quadrupolar moment, and is typically on the order of MHz and is given by:

$$C_Q = \frac{eQV_{zz}}{h}. \tag{2.133}$$

A small C_Q value suggests that a site is spherically symmetric, and higher C_Q values indicate that the large electric field gradient transverses the nucleus. For relatively low coupling constants, a first-order perturbation to the Zeeman energy is applicable. For moderately large coupling constants, second-order perturbations must be considered.

In the PAS, the quadrupolar Hamiltonian is:

$$\hat{H}_Q^{PAS} = \frac{2\pi}{2I(2I-1)}(A_{20}^{PAS}\hat{T}_{20} - A_{22}^{PAS}\hat{T}_{2-2} - A_{2-2}^{PAS}\hat{T}_{22}), \tag{2.134}$$

The spatial term is defined by:

$$A_{20}^{PAS} = \sqrt{\frac{3}{2}}C_Q,$$

$$A_{22}^{PAS} = A_{2-2}^{PAS} = \frac{1}{2}\eta_Q C_Q. \tag{2.135}$$

The Hamiltonian in the laboratory frame, in spherical tensor form, is expressed as:

$$\hat{H}_Q^{LAB} = \frac{2\pi}{2I(2I-1)}(A_{20}^{LAB}\hat{T}_{20} - A_{21}^{LAB}\hat{T}_{2-1} - A_{2-1}^{LAB}\hat{T}_{21} + A_{22}^{LAB}\hat{T}_{2-2} + A_{2-2}^{LAB}\hat{T}_{22}) \tag{2.136}$$

If a perturbation of the first order is considered, then the secular approximation can be assumed, hence only the spatial term A_{20}^{LAB} needs to be considered.

$$A_{20}^{LAB} = A_{20}^{PAS} D_{00}^{2} + A_{22}^{PAS} D_{20}^{2} + A_{2-2}^{PAS} D_{-20}^{2}. \tag{2.137}$$

On applying relevant rotation matrices, then the spatial component can be expressed as:

$$A_{20}^{LAB} = \sqrt{\frac{3}{2}} \frac{C_Q}{2I(2I-1)} \frac{1}{2} \left[(3\cos^2 \beta_{PL} - 1) + \eta_Q \sin^2 \beta_{PL} \cos 2\alpha_{PL} \right]. \tag{2.138}$$

Therefore, the first-order quadrupolar Hamiltonian can be expressed as:

$$\hat{H}_Q^{LAB} = \sqrt{\frac{3}{2}} \frac{C_Q}{2I(2I-1)} \frac{1}{2} \left[(3\cos^2 \beta_{PL} - 1) + \eta_Q \sin^2 \beta_{PL} \cos 2\alpha_{PL} \right] \hat{T}_{20}. \tag{2.139}$$

For $\eta_Q = 0$, the same angular dependence as for the dipolar coupling in Equation 2.122 and 2.123 is observed.

The first-order perturbation of the Zeeman interaction is given as:

$$E_m^{(1)} = \left\langle m \left| \hat{H}^1 \right| m \right\rangle. \tag{2.140}$$

Substituting Equation 2.139 into Equation 2.140 yields the first-order perturbation to the Zeeman transition energy.

For nuclei with the spin- 1 such as ^{14}N, three energy levels are feasible ($m = 0,+1,-1$, and therefore, two energy transitions are possible as presented in Figure 2.10. The total transition energy between m= +1 and −1 is unchanged relative to the energy of Zeeman splitting. However, the SQ (single quantum) transition i.e., between $m = +1 \rightarrow 0$ and $m = 0 \rightarrow -1$ have different energies.

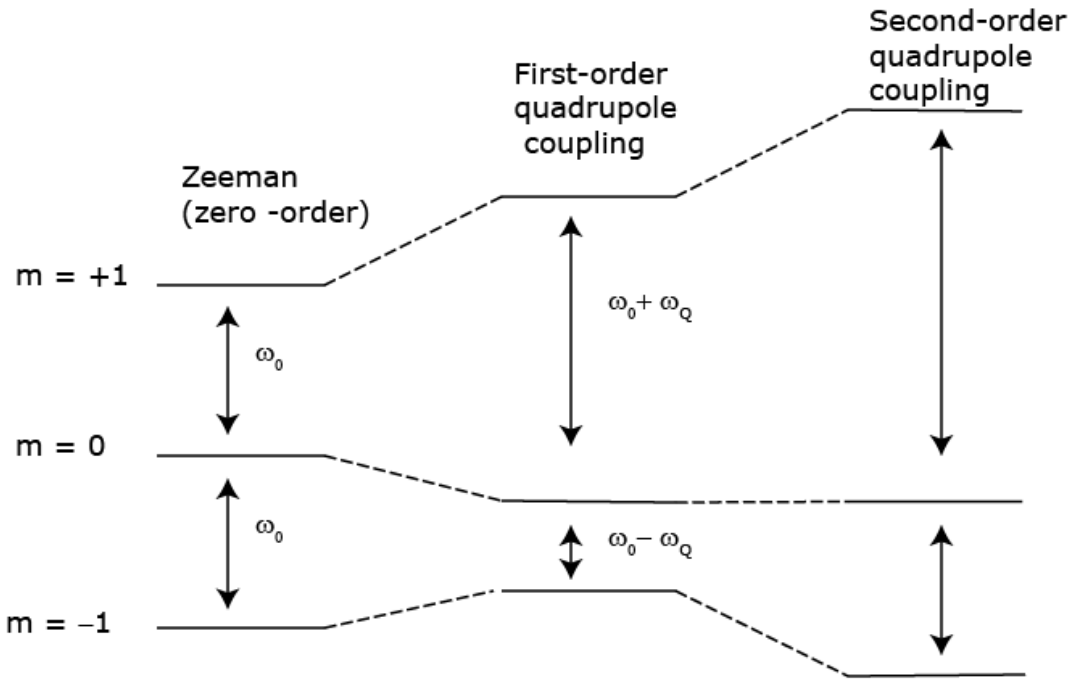

Figure 2.10: Perturbation to the Zeeman energy levels of spin-1 nucleus on considering first and the second-order perturbation.

As mentioned above, for nuclei with large C_Q, a second-order perturbation must be considered, and the Zeeman energy is written as:

$$E_m^{(2)} = \sum_{m \neq n} \frac{\left\langle n \left| \hat{H}^1 \right| m \right\rangle \left\langle m \left| \hat{H}^1 \right| n \right\rangle}{E_n^{(0)} - E_m^{(0)}} . \qquad (2.141)$$

To calculate the second-order Hamiltonian, all $A_{2-m,\ldots,m}^{LAB}$ have to be considered, since the secular approximation is no longer applicable. These terms are calculated in the same way as shown for the A_{20}^{LAB}. A second-order perturbation is performed by multiplying the A_{2m}^2 spatial terms. The product of A_{2m}^2. A_{2m}^2 generates Wigner rotation matrices of zero, second and fourth rank, which have significant consequences for the effect of MAS on quadrupolar lineshapes. The second-order perturbation can be written as:

$$E_m^{(2)} = -\left(\frac{C_Q}{4I(2I-1)}\right)^2 \frac{2}{\omega_0}\begin{bmatrix}\left[I(I+1)-3m^2\right]D_{00}^{0(Q)} \\ +\left[8I(I+1)-12m^2-3\right]D_{20}^{2(Q)} \\ +\left[18I\left(I+1\right)-34m^2-5\right)\right]D_{40}^{4(Q)}\end{bmatrix}, \tag{2.142}$$

where:

$$\begin{aligned} D_{00}^{0(Q)} &= -\frac{1}{5}\left(3+\eta_Q^2\right), \\ D_{20}^{2(Q)} &= \frac{1}{28}\left[\left(\eta_Q^2-3\right)\left(3\cos^2\beta_{PL}-1\right)+6\eta_Q\sin^2\beta_{PL}\cos 2\alpha_{PL}\right], \\ D_{40}^{4(Q)} &= \frac{1}{81}\begin{bmatrix}\frac{1}{140}\left(18+\eta_Q^2\right)\left(35\cos^4\beta_{PL}-30\cos^2\beta_{PL}+3\right) \\ +\frac{3}{7}\eta_Q\sin^2\beta_{PL}\left(7\cos^2\beta_{PL}-1\right)\cos 2\alpha_{PL} \\ +\frac{1}{4}\eta_Q^2\sin^4\beta_{PL}\cos 4\alpha_{PL}\end{bmatrix}. \end{aligned} \tag{2.143}$$

Under a second-order perturbation, the transition is perturbed relative to the first-order quadrupolar interaction, and it is clear from Equation 2.138 that the magnitude of the second-order perturbation is inversely proportional to ω_0, hence the effect from the quadrupolar interaction is reduced at higher field B_0 strengths.

The zero-rank term is isotropic; hence, the NMR spectrum of quadrupolar nuclei includes a further isotropic shift that depends on the quadrupolar coupling parameters as well as the isotropic chemical shift. This is known as the isotropic second-order quadrupolar shift[76], δ_{iso}^{Q}, and is expressed in the ppm scale for the transition $m \rightarrow m-1$ and is given as:

$$\delta_{iso}^{Q} = -\left(\frac{3}{40}\right)\left(\frac{P_Q}{\upsilon_0}\right)^2 \frac{\left[I\left(I+1\right)-9m\left(m-1\right)-3\right]}{\left[I^2\left(2I-1\right)^2\right]}\times 10^6. \tag{2.144}$$

When I =1 and m = 0 or m = +1, Equation 2.144 becomes,

$$\delta_{iso}^{Q} = -\left(\frac{3}{40}\right)\left(\frac{P_Q}{\upsilon_0}\right)^2 \times 10^6, \tag{2.145}$$

where P_Q is known as quadrupolar product and is defined as:

$$P_Q = C_Q \sqrt{1 + \frac{\eta_Q^2}{3}} \,. \tag{2.146}$$

Both second and fourth rank terms are anisotropic; however these cannot be removed simultaneously under MAS. Hence, a residual quadrupolar broadening exists even under MAS.

Chapter 3: Experimental Techniques

3.1 Line Shapes

To convert the NMR signal to a digital form, an analog to digital converter is used. In this, the signal is mixed down with a waveform oscillating at ω_{rf}, which gives the offset frequency. This offset frequency can be positive or negative; in order to determine the sign, the signal is mixed with cosine and sine waves oscillating at ω_{rf}. This is known as quadrature detection. The two signals so acquired have a sine or cosine modulation at the offset frequency. They can be regarded as the real and imaginary part of time domain signal of the form (see Equation 2.102):

$$s(\mathrm{t}) = [\cos \Omega \mathrm{t} + i \sin \Omega \mathrm{t}] \exp(-\lambda \mathrm{t}) . \tag{3.1}$$

Equation 3.1 can be rewritten as

$$s(\mathrm{t}) = \exp(i\Omega - \lambda)t , \tag{3.2}$$

where $l = \frac{1}{T_2}$, λ is the coherence rate decay constant and T_2 is the transverse relaxation time, which describes the loss of transverse magnetization. There is another important relaxation process known as longitudinal relaxation (T_1) which describes the restoring of the magnetization to its equilibrium value in the direction of the static applied magnetic field.

The time-domain signal is then Fourier transformed into a frequency domain signal

$$s(\mathrm{t}) \xrightarrow{FT} S(\omega), \tag{3.3}$$

i.e.,

$$\mathrm{S}(\omega) = \int_{-\infty}^{\infty} s(t) \exp(-i\omega t) dt . \tag{3.4}$$

Solving Equation 3.4 gives a real part function which is known as an absorption Lorentzian and an imaginary part function which is known as a dispersion Lorentzian (see Figure 3.1)

$$S(\omega) = A(\Delta\omega) - iD(\Delta\omega)$$

Real part $$A(\omega) = \frac{1/T_2^2}{\left(1/T_2^2\right) + (\omega - \Omega)^2}.$$

Imaginary part $$D(\omega) = \frac{(\omega - \Omega)}{1/T_2^2 + (\omega - \Omega)^2}. \quad (3.5)$$

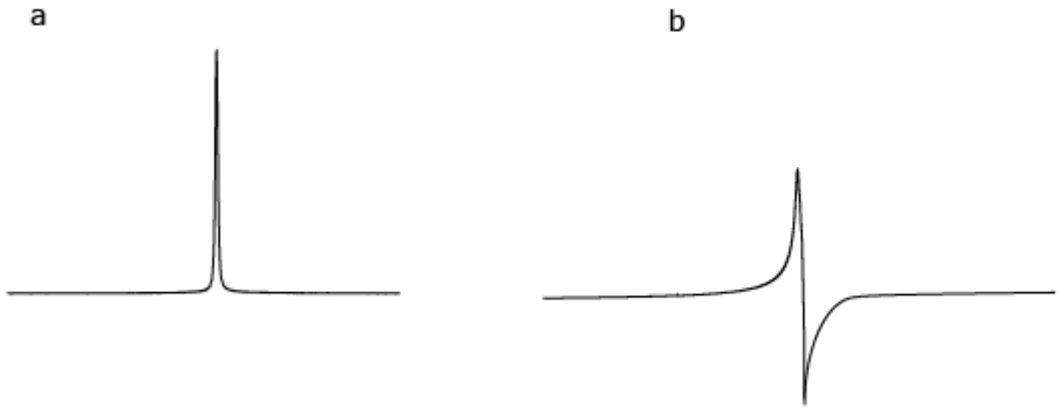

Figure 3.1: Absorption (real, a) and dispersion (imaginary, b) Lorentzian lineshapes.

In an NMR spectrum, only the real part is retained i.e., corresponding to absorption Lorentzian line shapes, which are positive and centred at the resonance offset ($\omega = \Omega$) with a full width at half maximum height (FWHM) of $1/\pi T_2$ (measured in Hz).

3.2 Two-Dimensional (2D) Spectroscopy

Multidimensional NMR experiments are useful for characterizing a sample beyond the information content of a simple one-dimensional NMR. The pulse sequence of a multi-dimensional experiment includes four steps, specifically:

Preparation – Evolution – Mixing – Detection.

Figure 3.2 illustrates the general form of a two-dimensional NMR experiment. The free induction decay is acquired in the detection period, the time axis of which is labelled as t_2. An uninterrupted free precession is observed during the evolution period for a time t_1. During the preparation period, a single $\pi/2$ pulse can be used to excite transverse magnetization. Mixing steps also include a $\pi/2$ pulse as depicted in Figure 3.2. During t_1, the magnetization precesses at the offset frequency until the second $\pi/2$ pulse flips the vector into the transverse plane. The amplitude of the observed free induction decay depends on the duration of the evolution time t_1. Hence a series of experiments

performed at increasing values of the delay t_1 give rise to a modulated series of one-dimensional spectra after Fourier transform with respect to t_2.

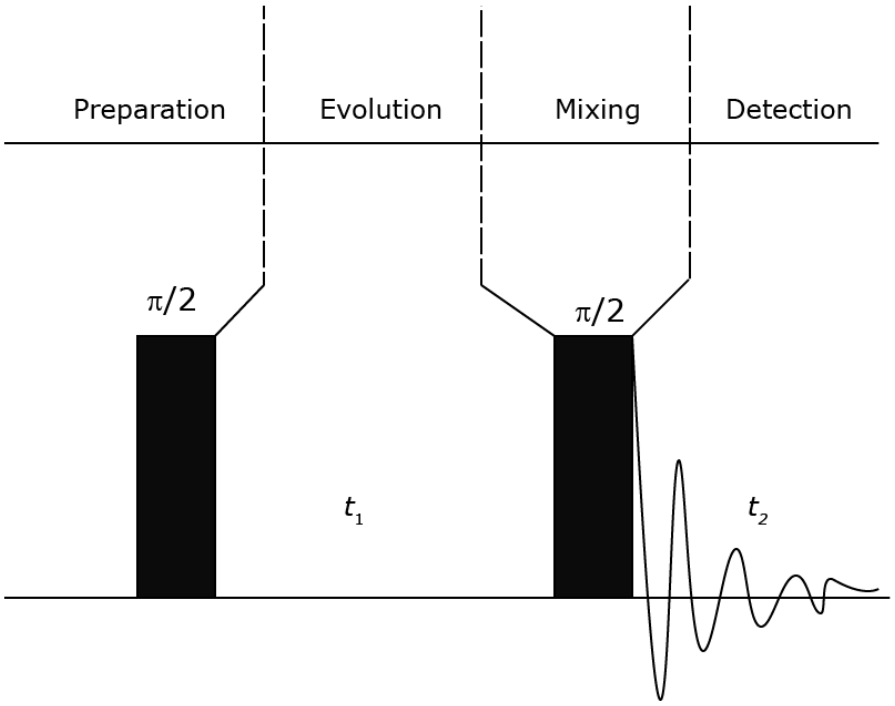

Figure 3.2: General scheme of a simple two-dimensional NMR experiment.

In general, a two dimensional NMR time-domain signal can be represented as:

$$S(t_1, t_2) = \exp(-ip\Omega t_1)\exp(-t_1 / T_2^{(1)})\exp(i\Omega t_2)\exp(-t_2 / T_2^{(2)}). \quad (3.6)$$

where p represents the coherence order in t_1 and $T_2^{(1)}$, and $T_2^{(2)}$ are the transverse relaxation times acting during the t_1 and t_2 evolution periods, respectively.

Experiments can be constructed either using a phase-modulated or amplitude-modulated scheme depending on the coherence transfer pathway, which is selected using phase cycling of the *rf* pulses and the receiver. When p = +1 in t_1, then Equation 3.6 becomes:

$$S_{pm}(t_1, t_2) = \exp(-i\Omega t_1)\exp(-t_1 / T_2^{(1)})\exp(i\Omega t_2)\exp(-t_2 / T_2^{(2)}), \quad (3.7)$$

where *pm* indicates that the signal is phase modulated with respect to the offset Ω in t_1.

A 2D frequency-domain spectrum with both indirect and direct frequency axes, ω_1, and ω_2, is generated by first Fourier transforming the signal in Equatio3.7 with respect to t_2.

$$S_{pm}(t_1, \omega_2) = \exp(-i\Omega t_1)\exp(-t_1 / T_2^{(1)})(A_2^+ - iD_2^+), \tag{3.8}$$

where A_2^+ and D_2^+ correspond to the absorptive and dispersive lineshapes centred at frequency $\pm\Omega$ in the ω_2 dimension. Fourier transformation of Equation 3.8 with respect to t_1 then yields:

$$S_{pm}(\omega_1, \omega_2) = (A_1^- - iD_1^-)(A_2^+ - iD_2^+)$$

$$= (A_1^- A_2^+ - D_1^- D_2^+) - i(A_1^- D_2^+ + D_1^- A_2^+). \tag{3.9}$$

It is clear from the Equation 3.9 that sign discrimination can be achieved by carrying out a two-dimensional experiment using a phase-modulated sequence, i.e., all the terms in the ω_1 dimensions are negative, and all the terms associated with the ω_2 dimension are positive. However, the spectrum contains a mixture of two-dimensional absorption and dispersion components, represented by the term $A_1^- A_2^+ - D_1^- D_2^+$ and results in phase twist lineshapes in the two-dimensional spectrum. Such phase twist lineshapes are much broader compared to absorptive lineshapes. In order to avoid such undesirable lineshapes, it is better to use an amplitude-modulated scheme for recording a two-dimensional spectrum.

2D experiments can be phase cycled in such a way that both $p = \pm 1$ are observed in the indirect dimension. The signal *S*(t) is then amplitude modulated with respect to t_1 and can be represented as:

$$S_{am,\cos}(t_1, t_2) = (\exp(-i\Omega t_1) + \exp(+i\Omega t_1))\exp(-t_1 / T_2^1)\exp(+i\Omega t_2)\exp(-t_2 / T_2^2)$$

$$S_{am,\cos}(t_1, t_2) = (\exp(-i\Omega t_1) + \exp(+i\Omega t_1))\exp(-t_1 / T_2^1)\exp(+i\Omega t_2)\exp(-t_2 / T_2^2)$$

$$= (2\cos(+\Omega t_1))\exp(-t_1 / T_2^1)\exp(+i\Omega t_2)\exp(-t_2 / T_2^2). \tag{3.10}$$

Fourier transformation with respect to t_2 gives:

$$S_{am,\cos}(t_1, \omega_2) = (\exp(-i\Omega t_1) + \exp(+i\Omega t_1))\exp(-t_1 / T_2^1)(A_2^+ - iD_2^+). \tag{3.11}$$

A hypercomplex Fourier transformation is required to achieve a two-dimensional absorptive peak. This separates the real and imaginary components before performing the Fourier transformation in t_1:

$$S^{\mathrm{Re}}_{am,\cos}(\omega_1,\omega_2) = \left[(A_1^- - iD_1^-) + (A_1^+ - iD_1^+)\right]A_2^+$$

$$= (A_1^- + A_1^+)A_2^+ - i(D_1^- + D_1^+)A_2^+ . \qquad (3.12)$$

$$S^{\mathrm{Im}}_{am,\cos}(\omega_1,\omega_2) == (A_1^- + A_1^+)D_2^+ - i(D_1^- + D_1^+)D_2^+ . \qquad (3.13)$$

The above Equations demonstrate that the real part leads to a pure absorptive lineshape in both the indirect and direct dimensions. However, sign discrimination has been lost in the ω_1 dimension because resonances are seen at both positive (A_1^+) and negative (A_1^-) frequencies in the indirect dimension. In order to restore sign discrimination in the 2D spectra, methods like States, TPPI, or by States-TPPI have to be employed by which two consecutive experiments are performed, phase shifting the first pulse (or block of pulses) by 90º/*p*, where *p* corresponds to the order of the coherence evolving in t_1. Consider a simple 2D experiment with $p = \pm 1$, the first signal takes the form of Equation 3.11 and the second is obtained by shifting the phase of the preparation pulse by 90º giving sine modulation in t_1:

$$S_{\sin}(t_1,t_2) = i\left[\exp(-i\Omega t_1) - \exp(+i\Omega t_1)\right]\exp(-t_1/T_2^{(1)})\exp(+i\Omega t_2)\exp(-t_2/T_2^{(2)})$$

$$= 2\sin(\Omega t_1)\exp(-t_1/T_2^{(1)})\exp(+i\Omega t_2)\exp(-t_2/T_2^{(2)}) . \qquad (3.14)$$

The cosine modulated signal in Equation 3.11 is now written as $S_{\cos}$. Both signals in Equation 3.11 and 3.14 are first Fourier transformed with respect to t_2:

$$S_{\cos}(t_1,\omega_2) = 2\cos(\Omega t_1)\exp(-t_2/T_2^{(1)})(A_2^+ - iD_2^+) \qquad (3.15)$$

$$S_{\sin}(t_1,\omega_2) = 2\sin(\Omega t_1)\exp(-t_2/T_2^{(2)})(A_2^+ - iD_2^+) . \qquad (3.16)$$

The real and imaginary components are combined to generate the States signal, S_{States}:

$$S_{states}(t_1,\omega_2) = \mathrm{Re}(S_{\cos}(t_1,\omega_2)) + i\,\mathrm{Re}(S_{\sin}(t_1,\omega_2))$$

$$= 2\exp(\Omega t_1)\exp(t_1 / T_2^{(1)})A_2^+ . \quad (3.17)$$

Fourier transforming again in t_1 gives:

$$S_{states}(\omega_1, \omega_2) = 2(A_1^+ - iD_1^+)A_2^+ = 2A_1^+A_2^+ - 2iA_2^+D_1^+ . \quad (3.18)$$

It is clear from the above Equation that the States method generates a 2D spectrum with purely an absorptive lineshape in the real part, with sign discrimination in both the direct and indirect dimensions. Another method to achievg0n discrimination in the 2D is the TPPI (time proportional phase incrementation) method, where only one signal is recorded for each value of t_1 and $\Delta t_1 = 1/2$ SW_1, where SW_1 is the spectral width of the indirect dimension in Hz and the phase of the preparation pulses is shifted by $90^o/p$ for each t_1 increment. Sign discrimination is achieved by modulating the coherence order by a phase that is dependent upon the t_1 increment. Throughout this thesis, all the two-dimensional experiments were recorded using State-TPPI method, which combines the principles of both methods. In this method both cosine and sine modulated signals are recorded as discussed before, and the phase of the preparation pulse is inverted by a phase change of $180^o/p$ for each successive Δt_1.

3.3 Phase Cycling

Coherences of different order can be excited by applying an *rf* pulse to nuclear spins, as described in Chapter 2. Coherence can be classified according to the values of Δm, i.e., the difference in the magnetic quantum numbers of the energy levels that are linked in the coherence. Application of *rf* pulses can generate many different orders of coherence depending on the number of eigenstates; however the only observable coherence in NMR are in-phase single quantum coherences ($\Delta m = \pm 1$). The selection of specific coherences is required to probe different interactions, which have a dependency on the particular spin coherence. For instance, a dipolar coupling between two spin ½ nuclei can generate double quantum coherence, but this is not the case for isolated spin ½ nuclei. NMR experiments can be constructed to generate and observe coherences of a different order, so to extract specific information about the interactions between the spins. The selection of desired coherences can be achieved by phase cycling the *rf* pulses and the receiver between successive acquisitions of the FID.

The 'Key Rules' of phase cycling[73] are:

- If the phase of a pulse is shifted by $\Delta\phi$, then a coherence undergoing a change in coherence order of Δp experiences a phase shift of $-\Delta p.\Delta\phi$.

- If a phase cycle uses $360^{o}/N$ steps, then in addition to the coherence change of Δp, additional coherences of the order $\Delta p \pm nN$ are also selected, where n= 1,2,3,…

The first rule implies that coherence pathways with different Δp acquire different phase shifts, and it is possible to differentiate pathways. Practically, this is done by repeating an NMR experiment with a specific change of one or more *rf* pulses and of the phase of the receiver. Experiments are performed many times, with different values of $\Delta\phi$, and upon combining the signals, the overall result is to cancel out the signals from the unwanted pathways. Receiver phases are usually limited to multiples of 90^{o}, whereas the phases of the pulses generated by the spectrometer can take any values. The phase of the receiver has to be adjusted in such a way so that it follows the overall phase acquired by the desired coherence.

It is clear from the second rule that it is not possible to completely remove all the pathways except the desired one. For example, double quantum coherence of order $p = 2$ is generated between spin pairs of coupled nuclei and all the higher-order coherences except ±6, ±10 ... are removed. It should be noted that the initial and final coherence point of any NMR pulse sequence is fixed since the system is at thermal equilibrium and corresponding to zero coherence ($p = 0$) at the initial state. Similarly, at the end of the experiment the only observable coherence is $p = -1$ (due to quadrature detection), hence only $n - 1$ *rf* pulse events need to be phase cycled.

Many complex NMR experiments require multiple changes in coherence; for such cases, a nested phase cycling is required. When designing a nested phase cycle, the phases of the individual pulses are chosen according to the key rules of phase cycling, and the receiver phase is calculated as the sum of individual receiver phases specified for each coherence change. For example, a full phase cycle for a two-dimensional double quantum experiment is shown in Figure 3.3 is given in Table 3.1.

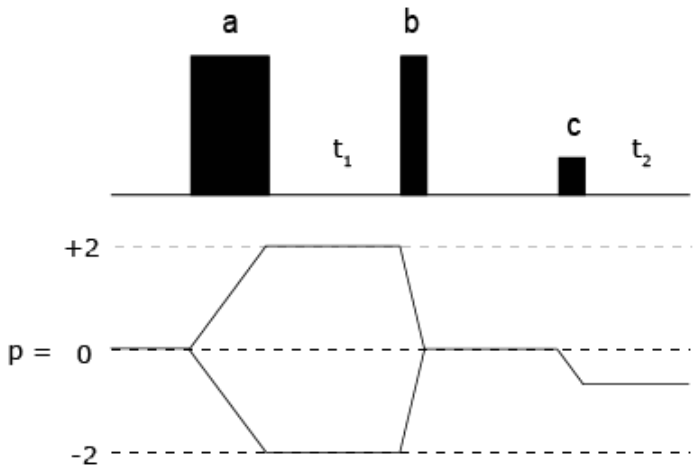

Figure 3.3: A pulse sequence and coherence transfer pathway for a two-dimensional double quantum (DQ)- single quantum (SQ) correlation experiment.

To excite double quantum coherence that evolves in t_1, a four-step phase cycle is applied to pulse a, to select $\Delta p = \pm 2$. All the coherences of the order $\pm 2 + 4n$ are also selected, but contributions from the higher-order coherences can be safely neglected. The final pulse is also subjected to a 4-step phase cycle to achieve a change in coherence order, $\Delta p = -1$. According to the second rule, the receiver phase is the sum of the individual receiver phase changes for pulses a and c, as listed in Table 3.1.

Table 3.1: Phase cycle for the DQ-SQ experiment presented in Figure 3.3.

Step number	ϕ_a	$-\Delta\phi_a.\Delta p=-2\phi_a$	ϕ_c	$-\Delta\phi_c.\Delta p = \phi_c$	Receiver Phase[a]
1	0	0	0	0	0
2	90	180	0	0	180
3	180	0	0	0	0
4	270	180	0	0	180
5	0	0	90	90	90
6	90	180	90	90	270
7	180	0	90	90	90
8	270	180	90	90	270
9	0	0	180	180	180
10	90	180	180	180	0
11	180	0	180	180	180
12	270	180	180	180	0
13	0	0	270	270	270
14	90	180	270	270	90
15	180	0	270	270	270
16	270	180	270	270	90

[a]Receiver phase $= \phi_{tot} = -\Delta\phi_a.\Delta p - \Delta\phi_c.\Delta p$

3.4 Experimental Methods

3.4.1 Dipolar Decoupling

As noted in Chapter 2, solid-state NMR has to deal with various anisotropic interactions such as chemical shift anisotropy, hetero-and homo-nuclear dipolar coupling, and quadrupolar coupling. To average out these interactions, it is necessary to manipulate either the spatial or spin part of the relevant Hamiltonian. We have already seen in Section (2.5.7) that the spatial part can be manipulated by spinning the sample at an angle of 54.7° (the magic angle) with respect to B_0. In order to manipulate the spin part, an *rf* pulse method has to be employed, which results in either removal or retention of the interactions. The removal of specific spin interactions is termed decoupling, which improves the resolution and sensitivity of the NMR spectrum. Decoupling can be either heteronuclear or homonuclear and will be briefly described in the following Sections.

3.4.2 Heteronuclear Decoupling

Heteronuclear spin decoupling is very critical in solid-state NMR, especially in the observation of dilute spins which are strongly coupled to the surrounding ^{1}H nuclei. There has been notable progress in the development of heteronuclear decoupling, since the first use of continuous wave irradiation to decouple heteronuclear interactions[60, 77]. A representation of what heteronuclear spin decoupling achieves is shown in Figure 3.4.

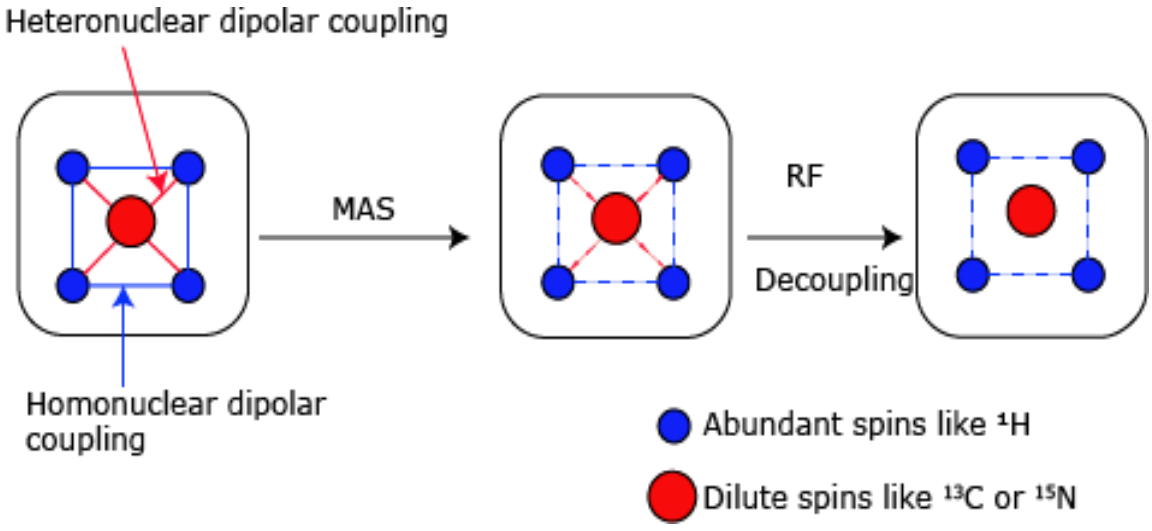

Figure 3.4: Schematic representation of heteronuclear decoupling, based on Ref[77]. Rare spins can be observed without any coupling using a combination of MAS and suitable decoupling techniques.

Typically, heteronuclear decoupling is applied to an abundant spin species by means of continuous, high rf nutation frequency irradiation. The most commonly used decoupling scheme until the mid-1990 was CW (continuous) decoupling. In this method, a strong *rf* irradiation was applied on the ^{1}H channel, and the signal is acquired on the X or rare spin channel, leading to highly resolved spectrum. Increasing the *rf* amplitude at a particular spinning frequency increases the spectral resolution by decreasing the line width and increasing the line intensity. The efficiency of the CW method under a given *rf* amplitude decreases upon increasing the spinning rate because homonuclear dipolar decoupling among the ^{1}H spins becomes less efficient with increasing the spinning frequency and results in residual splitting under CW irradiation.

In order to average out the heteronuclear dipolar coupling, the magnitude of the *rf* nutation frequency must be at least three times greater than the maximum H-X dipolar coupling magnitude[73]. For instance, an *rf* nutation frequency of 100 kHz is required to largely average out a directly bonded ^{1}H-^{13}C bonded coupling of about 23 kHz. The effect of continuous *rf* irradiation at a nutation frequency is to excite continuous transition between α and β states in a ^{1}H spin. If the *rf* nutation frequency is sufficiently high, then the timescale of these transitions will be fast relative to the heteronuclear dipolar coupling, and thus averages the heteronuclear dipolar coupling.

The limitations of the CW method led to the development of more improved phase modulated, and amplitude modulated decoupling schemes[77]. Some of the phase-modulated schemes are TPPM (two-pulse phase modulation)[78], FMPM (frequency modulated and phase-modulated)[79], AMPM (amplitude modulated TPPM)[80], and SPINAL (small phase incremental alteration)[81]. Experiments carried out in this thesis use TPPM or SPINAL-64.

3.4.3 Homonuclear Decoupling

^{1}H chemical shifts are very sensitive to interactions like intermolecular hydrogen bonding, and π-π interactions, hence they are very critical to solids. The magnitude of ^{1}H-^{1}H dipolar coupling is much higher in dense ^{1}H network systems, and therefore the chemical information from ^{1}H spectra may be limited. MAS alone is not sufficient to average out such large couplings, hence there is a need to apply homonuclear decoupling scheme to manipulate the spins. There are many schemes which can be used in conjunction with MAS. Lee-Goldburg (LG)[36] decoupling was the first proposed scheme for narrowing ^{1}H spectral lines. Later a combination of multiple pulses and MAS to remove CSA and homonuclear dipolar couplings was developed, which is known as CRAMPS[39] (combined rotation and multiple-pulse spectroscopy). A wide variety of sequences are based on the LG condition, where the pulses are off-resonance, such that $\omega_1 / \Omega = \sqrt{2}$ and

the effective field experienced by the spins is oriented at the magic angle with respect to a static B_0. Simple LG decoupling only suppresses the dipolar line broadening to the lowest order; in order to suppress higher order terms more effectively a frequency-switched (FSLG) scheme can be used, whereby a train of off resonance 360° pulses are applied continuously during the decoupling period. A full rotation of the bulk magnetisation about this effective field using a 2π pulse then averages the spin components of the dipolar Hamiltonian, thus eliminating the anisotropic effect.

Some experiments presented in this thesis utilise homonuclear decoupling based on the DUMBO (decoupling using mind boggling optimisation) scheme[43]. The DUMBO family uses constant-amplitude and phase-modulated *rf* irradiation along with the MAS to achieve homonuclear decoupling; this can be either in a windowed or windowless fashion. Three important DUMBO schemes are DUMBO-1[43], experimentally optimised schemes, eDUMBO-1_{22}[44], and eDUMBO-plus-1[82]. The design of these schemes is based on a Fourier series explaining the shape of the phase modulation.

One of the unavoidable consequences of using homonuclear decoupling in an experiment is the scaling effect on the spectrum, which occurs due to the evolution of magnetisation outside the transverse plane. This process scales the chemical shift information into a reduced spectral width. Hence, it is important to correct the effect via a scaling factor before extracting the chemical shift information from the spectra. If the decoupling is perfect, the chemical shift scaling factor will be equal to $\frac{1}{\sqrt{3}} = 0.58$[75]. The scaling faction will deviate from 0.58 if ideal decoupling is not attained. However, the scaling factor is susceptible to experimental factors. In this work, scaling factors are calculated by comparing the ^{1}H chemical shift, acquired with and without homonuclear decoupling, for a pair of well-resolved ^{1}H resonance in a fast MAS spectrum.

3.4.4 Recoupling Techniques

As mentioned in Section 2.5.7 and 3.4.2, both MAS and decoupling techniques act to average out the dipole coupling to zero. However the $1/r^3$ dependence of dipolar coupling can provide valuable structural information like internuclear distances between the nuclei. Hence, techniques for reintroducing, i.e., recoupling, these coupling under MAS during selected periods of time during experiments have been developed, where the nuclear spins evolve under dipolar coupling in a controlled fashion and provide a way to measure and probe internuclear distances experimentally. Some experiments in this thesis have used homonuclear and heteronuclear recoupling.

Dipolar recoupling was first applied in the heteronuclear context in the early 1980s, where heteronuclear dipolar couplings are restored by applying continuous *rf* field on one species[45]. The method was named as 'rotary resonance' and needed the amplitude of the *rf* field to be chosen so that the frequency of MAS is an integer multiple of the frequency of nutation:

$$\omega_1 = n\omega_R . \tag{3.19}$$

ω_R is the spinning frequency, and *n* relies on the particular spin introduction to be reintroduced.

Historically, the first homonuclear recoupling scheme was introduced by Earl and Meir, followed by the development of DRAMA (Dipolar Recovery At the Magic Angle)[46] by Tycko *et al*. Later several recoupling sequences have been developed such as a chemical shift compensated version of DRAMA (MELODRAMA)[83], Back to Back (BABA)[49], Radio Frequency Driven Recoupling (RFDR)[47], a windowless version of DRAMA (DRAWS)[84], Homonuclear rotary resonance (HORROR)[85], Dipolar Recoupling Enhance by Amplitude modulation (DREAM)[86], symmetry bases CN sequence, C7[87]. All these pulse sequences differ in their *rf* pulse requirements, excitation bandwidths, and their ability to compensate for pulse imperfection and perturbing interactions, and hence, not all schemes are suitable for dipolar recoupling. For instance, the sequences developed by Levitt *et al*., C7 and its variant Post C7, are among the best performing sequence under a moderately spinning frequency of 10-15 kHz. Experimentally, it is not possible to apply this scheme for MAS greater than 25 kHz, because it requires *rf* strength of $\omega_{RF} = 7\omega_R$, i.e., 245 kHz for 35 kHz MAS, which is beyond the technical capacity of a conventional MAS probe. To overcome this other problem, symmetry-based sequences can be used, which require lower *rf* nutation frequencies. However, most of the ^{1}H MAS experiments performed nowadays use the Back to Back (BABA) recoupling sequence, which is robust and straightforward and is discussed in detail in Section 3.4.9. As illustrated in this thesis, fast MAS in combination with a recoupling technique provides solid-state NMR with a unique opportunity to investigate molecular structure and dynamics in solid materials.

HMQC spectra presented in this thesis employ the above described rotary resonance recoupling (R^3) to recouple heteronuclear dipolar coupling. The solid-state ^{14}N-^{1}H HMQC experiment of Gan *et al.*, uses R^3 at $n = 2$. Such condition has been shown to effectively recouple the heteronuclear dipolar couplings while decoupling the powerful ^{1}H-^{1}H homonuclear dipolar couplings. At $n = 1$ all anisotropic interactions are reintroduced, and hence both homo and heteronuclear dipolar couplings are recoupled. However, only homonuclear dipolar couplings are reintroduced at $n = ½$

and are referred as Horror condition, which was used for homonuclear double quantum and correlation experiments under MAS[88].

3.4.5 Cross Polarization under Magic Angle Spinning (CPMAS)

The naturally abundant ^{1}H and ^{19}F nuclei have a high gyromagnetic ratio which is one main factor that determines the sensitivity of an NMR experiment; hence these nuclei have the highest sensitivity of all the naturally occurring spins. In 1962, Hartmann and Hahn showed that polarization transfer could be caused to occur between such abundant nuclei and so-called rare nuclei (e.g., ^{13}C and ^{15}N) when they are locked with radiofrequency nutation frequencies of the same amplitude[51], later Waugh *et al.* used this technique for increasing the sensitivity of rare spins[53]. Also, the relaxation times of the dilute spin (rare spins) will be long due to the absence of homonuclear dipolar interaction that induces relaxation transitions. The separation between the α (spin-up) and β (spin down) energy level of the proton exceeds the splitting for ^{13}C in the presence of magnetic field. Hence the polarization of ^{1}H is larger than the ^{13}C polarization. The achievable sensitivity enhancement for rare nuclei is given by order of their gyromagnetic ratios, i.e., γ_I/γ_s ($\gamma_{1H}/\gamma_{13C} \approx 4$). It is not possible to transfer the longitudinal magnetization from an abundant spin to a rare spin. Hence an *rf* field is applied, which helps to vary the energy difference between the spin state (α and β) individually, which makes the transfer of transverse magnetization possible. The resonance between the abundant and rare nuclei occurs if they satisfy the Hartmann-–Hahn condition:

$$\gamma_{1H} B_1(^1H) = \gamma_X B_1(X) \qquad X=^{13}C, ^{15}N \tag{3.20}$$

The cross-polarization experiments are more complicated compared to the direct excitation experiments, however, there are advantages. The recycle delay in CP experiments can be shorter compared to the direct excitation method, since it depends on T_1 of the ^{1}H magnetisation and not that of the dilute X nuclei, i.e., it depends on T_1^{H} and not T_1^{X}. Thus, the pulse sequence can be repeated very quickly compared to direct excitation on the X nucleus and this increases the signal to noise ratio and reduces the experimental time. A cross polarisation pulse sequence is shown in Figure 3.5. During t_2, heteronuclear decoupling (introduced in Section 3.4.1) is applied. A 90º pulse is applied to rotate the magnetisation to the transverse plane, followed by a 90º-phase-shifted ^{1}H pulse to spinlock the magnetisation while a pulse is applied simultaneously at the X channel – this is referred to as the contact pulse. When the Hartmann-Match condition is reached, the magnetization is transferred from the ^{1}H nuclei to the X nuclei, and the signal is measured during the acquisition time. Under MAS, the Hartmann-Hahn condition (3.20) is modified as:

$$\gamma_{^1H} B_1(^1H) = \gamma_X B_1(X) \pm n\nu_R, \tag{3.21}$$

where ν_R corresponds to the spinning frequency and n = 1, 2, …. Experimentally, to improve CP transfer under MAS conditions, a ramped pulse is used[89]; this allows there to be CP for a broadened Hartmann-Hahn condition and also enhances the intensity of the signal. Magnetisation transfer is achieved through the dipolar coupling between the spins and hence the rate of magnetisation transfer will be fast for the close proximity nuclei, whereas larger dipolar couplings require longer contact time. The length of the contact pulse can be varied experimentally. Typically in organic solids, a contact time of few milliseconds (usually 0.5 to 5ms) is enough to transfer polarisation effectively, however, some cases require longer contact time. Anything which affects the dipolar coupling can also disrupt CP transfer. For instance, motional effects in a molecule average the dipolar coupling, and this reduces the rate of cross polarisation transfer, in such cases a longer contact time is required.

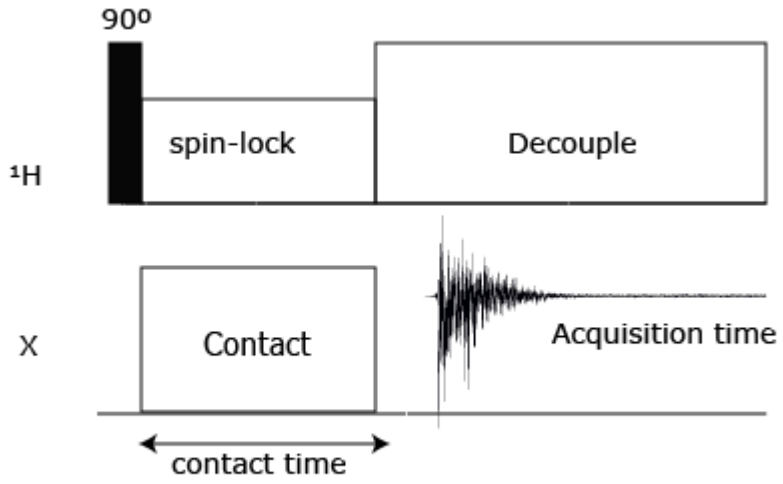

Figure 3.5: Schematic representation of a cross polarisation pulse sequence.

3.4.6 CP-HETCOR (Heteronuclear Correlation)

A two-dimensional heteronuclear experiment can be used from which one can extract ^{1}H-X correlations and identify proton chemical shifts with or without any homonuclear decoupling sequence during the t_1 evolution. This experiment is quite straightforward and works in a manner analogous to the above described CP experiment, with an additional t_1 evolution period for the ^{1}H spins. The pulse sequence is depicted in Figure 3.6.

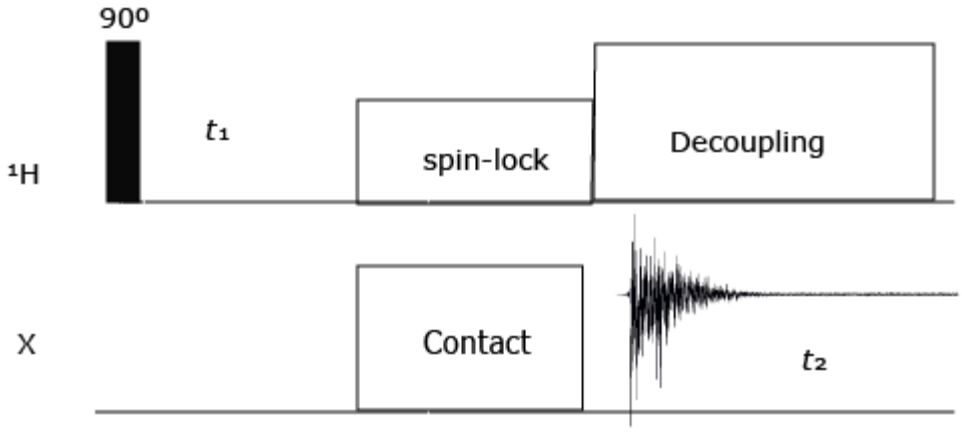

Figure 3.6: The pulse sequence for a two-dimensional CP HETCOR experiment.

Often, due to the strong dipolar interaction, the proton spectra can be broad. Hence to attain high proton resolution, homonuclear decoupling like FSLG or LG schemes described in Section 3.4.3, are applied after the initial 90º *rf* pulse.

3.4.7 Refocused INEPT (Insensitive Nuclei Enhancement by Polarisation Transfer) Experiment

In 1979, Morrison and Freeman developed an INEPT pulse sequence for solution-state NMR to enhance the spectral intensity for low gyromagnetic ratio nuclei by transferring polarization from a *J*-coupled high gyromagnetic ratio nucleus [61]. In solid-state NMR spectroscopy, the INEPT technique was first introduced for an inorganic material to study through−bond transfer between coupled nuclei [90]. The pulse sequence for a solid-state NMR refocused INEPT experiment was taken from the original solution-state NMR experiment by adding homonuclear proton decoupling discussed in Section 3.4.3, during the time τ and τ' to remove the effects of proton-proton dipolar couplings[64]. This decoupling of the proton-proton dipolar interaction can be achieved with several variant eDumbo continuous phase modulation schemes[44, 82], as shown in Figure 3.7. If the decoupling is sufficient enough during those delays, and the effect of chemical shift anisotropy and heteronuclear dipolar couplings are removed by the fast magic angle spinning, then the scalar couplings along with the isotropic chemical shift are preserved (only J_{CH} affects coherence transfer). The simultaneous 180º pulses on proton and carbon refocus the isotropic chemical shift after 2τ and $2\tau'$. During the first τ-π-τ period, antiphase proton coherence is created which is

converted to antiphase carbon coherence by the two simultaneous pulses. This carbon antiphase coherence is then refocused during the second time period into observable in-phase signal [64, 91].

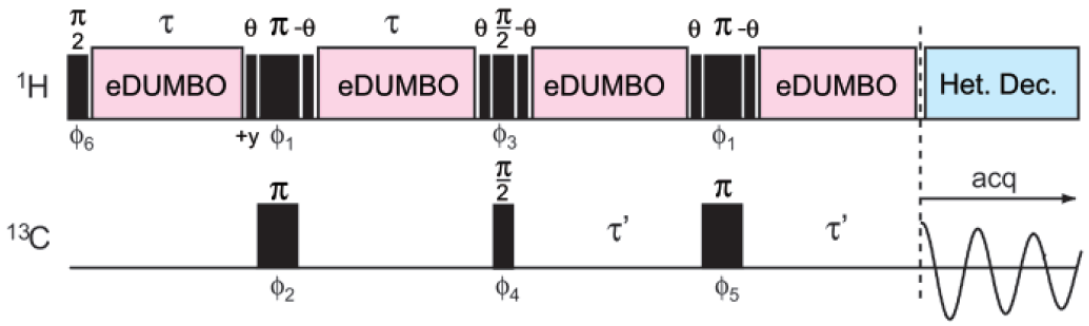

Figure 3.7: The pulse sequence for a solid-state refocused INEPT experiment taken from Ref[64].

3.4.8 Two Dimensional ^{1}H-^{1}H Spin Diffusion Experiment

Spatial proximity between different proton environments can be probed using a spin diffusion experiment. It is essentially the same as the NOESY (nuclear Overhauser spectroscopy) experiment in solution NMR. An initial 90º pulse creates transverse magnetisation that evolves during t_1, followed by another 90º pulse which places the magnetisation along z for a fixed time termed the mixing time (τ_{mix}). A schematic representation of the spin diffusion pulse sequence is presented in Figure 3.8. In solid-state NMR, spin diffusion experiments are used to determine distinct phases in a sample.

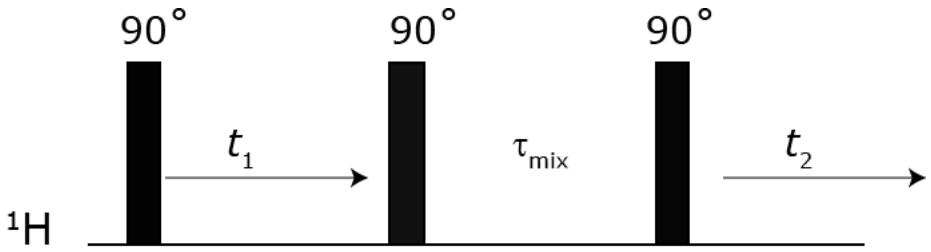

Figure 3.8: A pulse sequence for a ^{1}H-^{1}H spin diffusion experiment.

3.4.9 ^{1}H-^{1}H Double Quantum BABA Spectroscopy

For coupled spins, only energy transitions that change the quantum number, *m*, of the spin by ±1 are directly observable. They correspond to transverse magnetization and are called single-quantum (SQ) coherences. Multiple-quantum coherences notably double-quantum coherence

cannot be directly observed but can be indirectly probed by multi-dimensional NMR[71]. As discussed in Section 2.5.6, the dipolar coupling interaction, being dependent on the distance between the coupled spins, can provide information on, e.g., internuclear distances. However, for obtaining chemical shift resolution the line broadening caused by the dipolar coupling needs to be removed, for example, using magic angle spinning.

It is possible to excite double quantum (DQ) coherence in any system with strongly dipolar coupled spins. Pulse sequences have been developed which rely on the fact that the excitation efficiency for the DQ coherence, for isolated spin pairs, depends upon the strength of the dipolar coupling. The dipolar recoupling scheme mentioned in Section 3.4.4, Back to Back (BABA)[92-93] is used in all DQ/ SQ MAS experiments presented within this thesis for both excitation and reconversion of DQ coherence. Laboratory-frame pulse sequences for excitation/reconversion of multiple-quantum coherences are composed of 90° radiofrequency pulses. The basic BABA is made up of four pulses per rotor period (τ_R), as shown in Figure 3.9a. The BABA cycle can be repeated over several rotor periods to achieve longer dipolar recoupling times. The timing of the back-to-back sequence is set for full synchronization to the sample rotation for generating a pure DQ Hamiltonian, which leads to its maximum strength[94-101]. Rotor synchronization has two extra advantages: first, the experimental time of a two-dimensional experiment is reduced (since t_1 increments are reduced), second, increased sensitivity (due to the folding of signals from the sidebands into centre bands)[59].

In the DQ dimension, resonances are present at the sum of the single-quantum (SQ) frequencies of the nuclei involved, a schematic representation of DQ/SQ MAS spectrum for two spins A and B are presented in Figure 3.9b. A diagonal peak indicates couplings between spins with the same chemical shift, for example, spins (AA) with a single peak at frequencies ($2\omega_A$, ω_A) in the F_1 and F_2 dimension, respectively. The intensity due to DQ coherences between two peaks with different SQ chemical shifts (spins A and B) is split, in the SQ dimension, into a pair of cross-peaks symmetrically arranged on each side of the diagonal, at frequencies ($\omega_A + \omega_B$, ω_A) and ($\omega_A + \omega_B$, ω_B). The intensity of each peak is proportional to the number of spin-pairs giving rise to the DQ coherence and the dipolar coupling. This experiment is typically sensitive up to about 3.5Å[94].

(a)

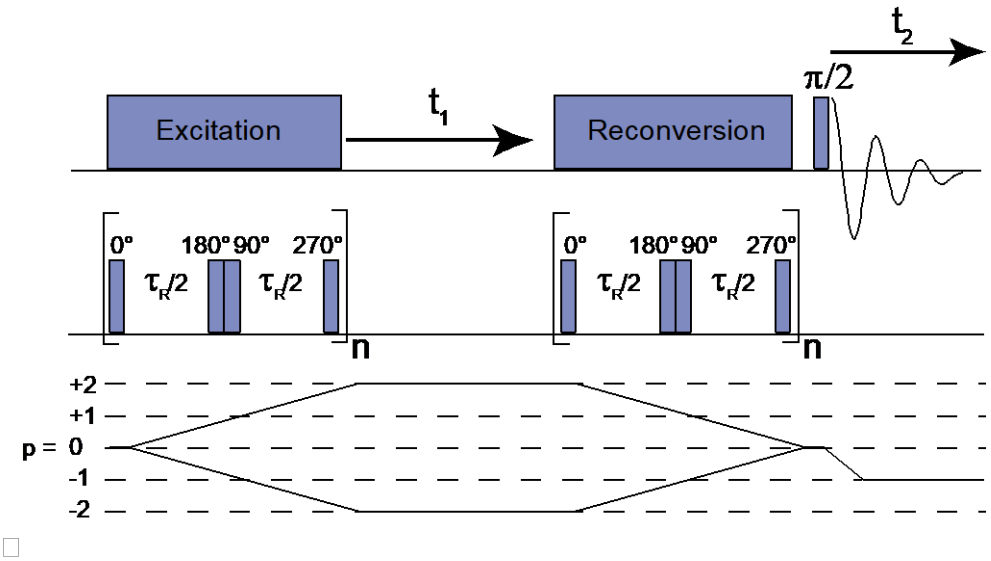

(b)

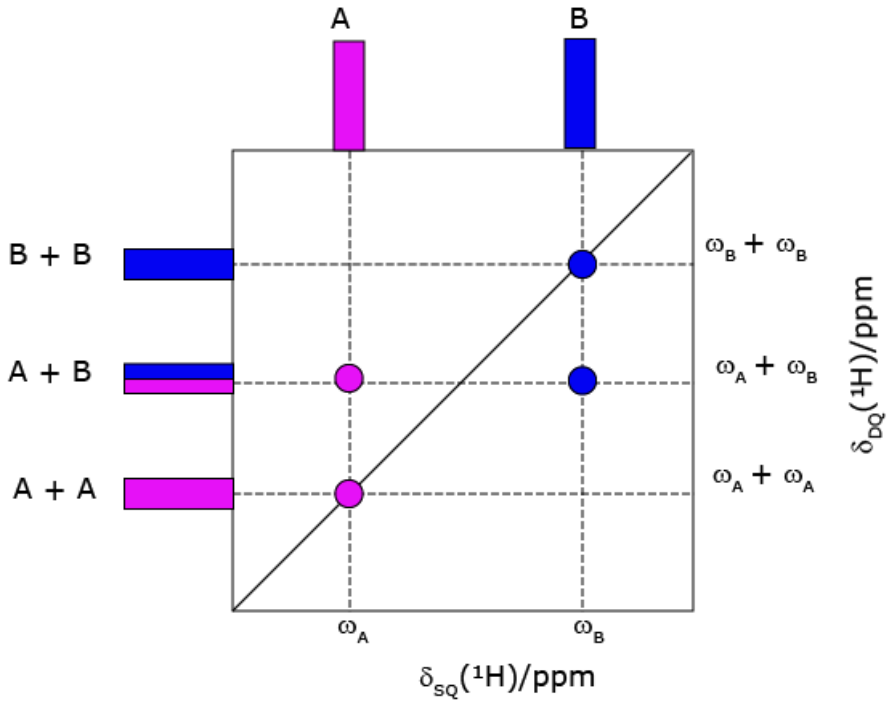

Figure 3.9: (a) General scheme for a BaBa ^{1}H DQ experiment and the corresponding coherence transfer pathway diagram. (b) Schematic representation of a two-dimensional double quantum

(DQ) single quantum (SQ) spectrum for two spins A and B which are dipolar coupled with each other and with themselves.

3.4.10 Heteronuclear Multiple–Quantum Correlation (HMQC) Experiment

This two-dimensional experiment provides information about the correlation between two different nuclear spins, e.g., ^{14}N-^{1}H. Direct detection occurs on the higher γ ^{1}H nucleus since ^{14}N solid-state NMR is challenging due to its quadrupolar nature and low gyromagnetic ratio:

$$\frac{\gamma^{14}N}{\gamma^{1}H} = 0.07\,.$$

The basic pulse sequence for a HMQC solid-state NMR experiment is taken from the original solution-state experiment, where the magnetisation transfer is achieved either via *J* couplings, while transfer can occur via heteronuclear dipolar couplings in the solid state. Specifically, a HMQC experiment consists of three main steps. In the first step, *I* (^{1}H) transverse magnetization is excited and is allowed to become anti-phase under evolution due to a ^{14}N-^{1}H coupling. This antiphase magnetization is converted into heteronuclear multiple-quantum coherence, which then evolves for a time period t_1. The multiple-quantum coherence is then converted back into observable magnetization on the *I* spin, the coupling is allowed to rephase and then the signal is acquired. This experiment benefits from fast MAS because of the line narrowing detected in the ^{1}H dimension. As discussed in Section 3.4.2, heteronuclear couplings are averaged to zero under MAS, hence the dipolar coupling has to be reintroduced in a controlled manner in order to probe the heteronuclear correlations. The HMQC experiment presented in this thesis uses rotary resonance recoupling (R^3) to recouple the heteronuclear dipolar couplings. A schematic representation of the solid-state ^{14}N–^{1}H HMQC pulse sequence and the corresponding coherence transfer pathway used in this thesis is presented in Figure 3.10. The recoupling scheme uses an *rf* field ω_1 matching twice the MAS frequency ω_R, which is called the n = 2 rotary resonance condition, as discussed in Section 3.4.2. The ^{14}N-^{1}H HMQC experiment is helpful for studying NH…X and XH…N intermolecular hydrogen bonding interactions, which are essential to small molecules and pharmaceuticals.

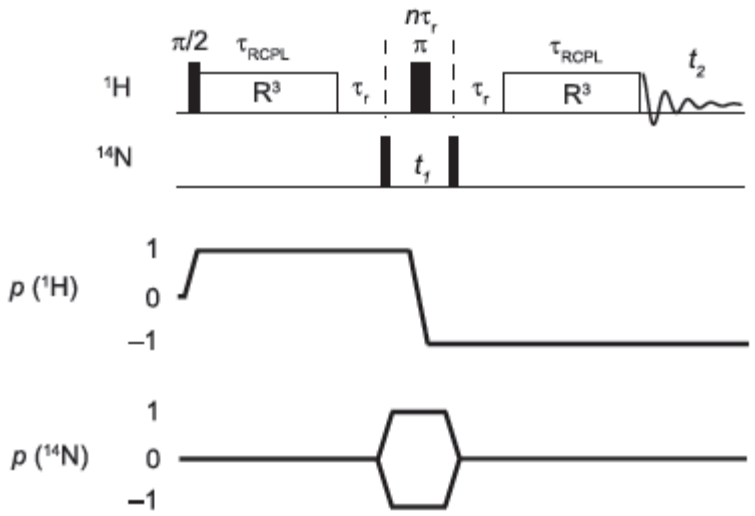

Figure 3.10: General scheme for a HMQC experiment and coherence transfer pathway. Taken from Ref[76].

3.4.11 Referencing

In all experiments, ^{1}H and ^{13}C chemical shifts are referenced using adamantane (higher ppm ^{1}H resonance, 1.85 ppm and ^{13}C resonance at 38.48 ppm) corresponding to TMS at 0 ppm[102] and ^{7}Li is referenced to lithium chloride at 0 ppm[103-104]. ^{31}P was referenced to 85% H_3PO_4[105-106] at 0 ppm using Ammonium dihydrogen phosphonate (ADP) at 0.99 ppm. ^{29}Si was referenced to Kaolinite at $\delta = -91.5$ ppm with respect to TMS [107]. ^{14}N is referenced using the dipeptide β- AspAla (^{14}N of NH_3 peak at −284 ppm at this magnetic field strength), corresponding to liquid CH_3NO_2 at 0 ppm[76].

Chapter 4

As mentioned in Chapter 1, valuable information can be gained by combining experimental results with computational methods. In this thesis, density functional theory (DFT) that uses the electron density as the fundamental variable is employed as a means for calculating NMR parameters. Here, electronic structure calculations at the DFT level of theory is briefly outlined before discussing the calculation of NMR parameters. This Chapter is based on a book entitled NMR crystallography[68] and two reviews[67, 108].

4.1 Electronic Structure Calculations

The DFT approach begins by considering Schrödinger's Equation under the Born-Oppenheimer approximation[109]: for a system of electrons and nuclei, the electronic Hamiltonian H(*R*) depends on the nuclear positions (*R*) and describes the kinetic energy of the electrons together with their electrostatic interaction:

$$H(R)\Psi(r;R) = E(R)\Psi(r;R), \tag{4.1}$$

where Ψ (*r*; *R*) is the many-body wave function of the coordinates of the electron *r* and nuclei *R* in the system. *E* is the total energy which provides a way to compare the relative stability of different phases of a material.

The fundamental theorem of DFT was proposed by Hohenberg and Kohn in 1964[110], where they proved that the total energy of a system could be determined from the electron density. This principle is much simpler than the full many-body wave function of the Schrödinger Equation because the electron density is a function of position. Kohn and Sham noted that the many-body problem of the Schrödinger problem could be described in terms of a set of non-interacting fictitious particles[111]. In this formalism, the charge density is obtained from a sum of occupied states which is identical to the total energy of the real system:

$$\rho(r) = \sum_i n_i \left|\Psi_i(r)\right|^2, \tag{4.2}$$

where n_i is the occupation number of the eigenstate which is represented by each one-particle wave function Ψ_i (*r*). The Kohn-Sham Equations for the electronic eigenstates are defined as follows:

$$-\frac{\hbar^2}{2m}\nabla^2\Psi^i(r) + V_{eff}(r)\Psi^i(r) = \varepsilon_i\Psi^i(r), \tag{4.3}$$

where

$$V_{eff} = V_{nuc} + V_{hartree}[\rho] + V_{xc}[\rho]. \tag{4.4}$$

($\frac{\hbar^2}{2m}\nabla^2$) corresponds to the kinetic energy of the non-interacting electrons, V_{nuc} is the electrostatic interaction with the nuclei, and $V_{hartree}[\rho]$ is the mean field electrostatic interaction with the other particle in the system. All of these can be computed except the V_{xc} term, which is the exchange-correlation function. The true functional form of the exchange-correlation function is still unknown, and assumptions have to be made based on physical constraints. The simplest estimate of the exchange-correlation function is the local density approximation (LDA)[111], which takes a piecewise strategy. In the LDA approximation, the contribution was made by each point of space, being equivalent to the exact exchange-correlation of a uniform electron gas. There are some noticeable drawbacks for the LDA[111], e.g., it overestimates the binding energy and underestimates lattice constants by 1-3%. The introduction of the generalized gradient approximation (GGA)[112] made the results of many properties better by introducing terms which are dependent on the gradient of density into the functional. An implementation of GGA proposed by Perdew, Burke, and Ernzerhof (PBE)[113], has been widely applied in the context of GIPAW NMR calculations, including those in this thesis.

Most solids possess translational symmetry meaning that one only needs to consider the unit cell with periodic boundary conditions and thus reduce the number of atoms or electrons to a reasonable number. If the nuclei are arranged in a periodically repeating pattern, then the potential acting on the electron will also be periodic and hence also the density:

$$\rho(r + L) = \rho(r), \tag{4.5}$$

where L is any lattice vector. However, while the charge density is periodic, the wavefunction must be treated carefully due to its complexity. The magnitude of the wavefunction can be periodic, whereas the phase may not. According to Bloch's theorem[114], such a wave function is termed as quasi-periodic:

$$\Psi_k(r) = e^{ik.r} U_k(r), \tag{4.6}$$

where

$$U_k(r) = U_k(r + L). \tag{4.7}$$

This incorporates the periodicity of the unit cell, and $e^{ik.r}$ is an arbitrary phase factor. The values of *k* lie within the reciprocal unit cell, which is defined by convention as the Brillouin zone (BZ). The BZ can be mapped out by a series of continuous *k*-points. In principle, for a continuous distribution of *k*-points, an infinite number of calculations must be carried out to calculate the electronic potential because, at each *k*-point, only the occupied state contributes to the electron density. However, most of the properties in a solid vary smoothly across the BZ. Hence a single *k*-point is enough to describe the electronic wave function of a small BZ. For a larger BZ, the *k*-point is divided into a set of regularly spaced points. The Monkhorst and Pack scheme[115] is applied for integrating over *k* space in the Brillouin zone for the evaluation of the density and electronic potential.

4.1.1 Basis Sets

A basis set needs to be chosen in order to implement the Kohn-Sham Equation as a computer program algorithm. Hence, the wavefunctions and charge density are expressed as a linear combination of simple mathematical functions, which can be truncated to achieve an appropriate level of accuracy. A set of localized atomic centred orbitals such as Gaussian-type orbitals or Slater-type orbitals has been commonly employed for periodic simulations[112, 114]. However, the GIPAW method uses a set of plane waves as the basis function, that is:

$$\Psi_k^n = \sum_G c_n^{k+G}(G)\, e^{i(k+G)r}, \tag{4.8}$$

where *G* is the set of reciprocal lattice vectors defined by $G \cdot l = 2\pi m$ where *l* is a lattice vector of the crystal and *m* is an integer. For example, if the cell is longer in one direction, then the wave vector along that direction will be shorter.

In order to reproduce the spatial dependence of the wavefunction, precisely an infinite number of plane waves would have to be used. However, the co-efficient c_n^G will become increasingly insignificant with higher *G* value. Therefore a cut off *G* wave vector can be defined by G_{cut}, which truncates the basis set and is defined by the maximum kinetic energy of the waves it corresponds to:

$$E^{cut} = \frac{\hbar^2}{2m}\left|G\right|^2. \tag{4.9}$$

The error introduced during basis set truncation can be eliminated by converging the parameter of interest with respect to the cut-off energy, which is controllable. The optimum value of E^{cut} primarily depends upon both the atomic species and the form of the pseudopotential as explained below.

4.1.2 Pseudopotentials

The pseudopotential approximation has been introduced to simplify the wavefunction so that it can be described in terms of a small number of waves. There were two main issues with regards to the core electron and the oscillation of the valence wavefunction close to the nucleus, which led to the development of this approximation[114]. The core electrons are those which are more tightly bound to the nucleus, whereas the valence electrons are quite extended. It is the valence electrons that generally define most of the properties of a material, while the core electrons are inert and are not involved in any interaction. Two key approximations applied to the core region increase the accuracy of the calculation. The first method is the frozen core approximation[116], which assumes that core electrons do not take part in chemical bonding. This approximation is complicated because it is not always straightforward to separate core and valence states.

The oscillation of the valence electrons due to the strong nuclear Coulomb potential and the interaction between the core and valence electrons can be removed and replaced by a smooth, effective potential, which is known as a pseudopotential. The pseudopotential approximation is not a unique construction, and numerous schemes have been developed to construct pseudopotentials. In this thesis, all the calculations were carried out using the "ultrasoft potential" scheme developed by Vanderbilt[117], which is implemented in the CASTEP[118] quantum-mechanical plane-wave code.

For certain properties of a solid, particularly the NMR chemical shifts, the effect of electrons close to the nucleus is very significant. Van de Walle and Blochl introduced the projector augmented wave (PAW)[119] methods which reconstruct the all-electron wavefunction by introducing the core electron density before calculating the NMR properties. In this approach, a linear transformation (T) maps the valence pseudo wavefunctions onto all corresponding electron wave functions, $\left|\Psi\right\rangle = T\left|\Psi\right\rangle$ (see Equation 2.28 of Ref[108]):

$$T = 1 + \sum_{R,n} \left[\left| \phi_{R,n} \right\rangle - \left| \tilde{\phi}_{R,n} \right\rangle \right] \left\langle \tilde{P}_{R,n} \right| . \qquad (4.10)$$

where $\left|\phi_{R,n}\right\rangle$ and $\left|\tilde{\phi}_{R,n}\right\rangle$ are the all-electron and pseudo partial waves derived from an isolated atomic calculation and $\left|\tilde{P}_{R,n}\right\rangle$ are a set of projectors. In the PAW approach, two chemically identical sites in a molecular system should have the same calculated magnetic shielding value. For an infinite basis set, this does not cause any problem, whereas for the finite basis set the two sites will eventually have different calculated values. This is referred to as the 'gauge origin problem'[108]. The Gauge Including Projector Augmented Wave (GIPAW) approach is a key extension of the PAW method, which utilizes a field-dependent transformation operator T_B, which overcomes the gauge-origin problem of the PAW approach[120].

4.1.3 Geometry Optimisation

A typical GIPAW DFT based NMR calculation starts from a crystal structure obtained either from diffraction-based experiment or from a computationally generated crystal structure prediction approach. Geometry optimisation refines the geometry of a 3D periodic system to obtain a stable structure. It is carried out through an iterative process allowing the atomic positions and, in some cases, the cell parameters to vary until the total energy of the structure reaches its minimum. The total energy is then used to establish the forces on the ions, (F_I), according to:

$$F_I = -\nabla_R \left\langle E \right\rangle, \tag{4.11}$$

where I denote the ions of interest, E is the energy of the system, and R is the position of the ions. A standard minimisation algorithm is used to move the ions to a new position; in this thesis, all the structures were optimised using the Broyden-Fletcher-Goldfarb-Shanno scheme (BFGS)[121], as implemented in the CASTEP code.

The electronic configuration is reoptimized at each minimization step. The total energy for the new configuration and the forces are tested against the tolerance limits. If the structure is not optimised, a new position is generated, and the process continues until the forces reach the tolerance limit. The geometry optimised structure is then used as an input for the GIPAW calculation of the NMR tensors. It should be noted that carrying out a calculation in this way corresponds to a temperature of 0 K.

4.1.4 Chemical Shift Calculations

The GIPAW method calculates the absolute magnetic shielding tensor (σ). Magnetic shielding is defined as the induced field (B_{in}) experienced by a nuclear spin due to the interaction between the electrons and the external magnetic field (B_0)[122]:

$$B_{in} = -\sigma B_0 . \tag{4.12}$$

The induced magnetic field arises from the orbital current $j(r)$ and can be computed using perturbation theory:

$$B_{in}(r) = \frac{1}{c}\int d^3 r' \, j(r') \times \frac{r - r'}{|r - r'|^3} . \tag{4.13}$$

Diagonalization of the symmetric part of the shielding tensor reveals three principal components of the magnetic shielding tensor ($\sigma_{xx}, \sigma_{yy}, \sigma_{zz}$). The average of these components gives the isotropic magnetic shielding (σ_{iso}^{calc}), defined by:

$$\sigma_{iso}^{calc} = \frac{1}{3} Tr\{\sigma\} . \tag{4.14}$$

The calculated isotopic chemical shift (δ_{iso}^{calc}) (which can be compared to experimental chemical shielding) then follows from:

$$\delta_{iso}^{calc} = \frac{-(\sigma_{ref}^{calc} - \sigma_{ref})}{1 - \sigma_{ref}} . \tag{4.15}$$

where σ_{ref} is the reference magnetic shielding. In practice, there exist various approaches for referencing. One of the conventional approaches for calculating reference shielding is via linear regression where the calculated shielding σ_{i} is mapped against the observed shift (experimentally referenced chemical shift) δ_{i} for a series of compounds,

$$\delta_i = a\sigma_i + b , \tag{4.16}$$

where a and b are empirical parameters. This method corrects any systematic errors which are involved within the calculations. Beran and coworkers have reported sets of a and b parameters from a set of test compounds. These regression parameters have been used for predicting the

chemical shift of a new system which is not included in the test sets. The parameter takes a value of −1 in the absence of any errors and *b* will represent the absolute shielding of the reference compound[123-124].

Another approach for calculating the reference shielding is by plotting the experimental chemical shift against the calculated magnetic shielding. In an ideal condition, the gradient of the line is constrained to −1[125]. To allow comparison with the literature [126-129], this approach has been adopted for the GIPAW calculations presented in this thesis.

4.2 Simulations

Simulations are also used to supplement the experimental results and provide a more thorough study; to this aim, the SIMPSON[130] simulation package was used. This program uses density operator theory to produce FIDs and thus spectra from an input file that details the spin system, pulse sequence, and experimental parameters. A SIMPSON input consists of four parts to detail this information; 'spinsys' in which the nuclei involved are defined and their chemical shift and couplings (dipole, jcoupling, quadrupole) associated with the nuclear spins are detailed, 'par' defines the experimental parameters e.g. static field, B_0, MAS frequency as well as parameters that dictate how simulation works, e.g. crystal file and number of gamma angles, 'proc pulse' in which the pulse sequence and their implementations are described and finally 'proc main' where the FID storage and Fourier transform of the FID is dealt with in conjunction with any line broadening applied. This program allows easy and flexible implementation of complex solid-state experiments and has a high level of freedom over the spin system compared to the real NMR experiment. The SIMPSON input file used to simulate the ^{14}N Form I spectrum presented in Figure 5.8 is listed here :

```
spinsys {

channels          14N

 nuclei  14N

 shift  1  -123.47606105p  52.76349494p  0.57518572  -100.68409795  82.56683955  -
127.04707014

 quadrupole       1 2 -4266165.96173644 0.38237417 141.15917056 71.20537969 -36.47752999

}
```

```
par {
   spin_rate        60000
   start_operator   I1x
   detect_operator  I1p
   gamma_angles     18
   crystal_file     rep320
   proton_frequency 600e6
   np               8192
   sw               30000
   verbose          1101
}

proc pulseq {}l {
  global par
   acq
for {set i 1} {$i < $par(np)} {incr i} {
   delay [expr 1e6/$par(sw)]
   acq
}
}

proc main {} {
  global par
```

```
    set f [fsimpson]
    fsave $f $par(name).fid
    fzerofill $f 2048
    faddlb $f 2000 0
    fft $f
    fsave $f $par(name).spe
    funload $f
}
```

The spin system used to simulate the ^{14}N Form II spectrum is:

```
spinsys {
channels          14N
 nuclei  14N
 shift     1 -116.5p -70.0p 0.7 -47.1 89.4 -22.8
 quadrupole       1 2 -3711291.4 0.5 -107.3 107.4 -8.0
}
```

4.3 Linear regression model[131]

A linear regression analysis of the calculated against the experimentally observed changes in chemical shifts is presented in Chapter 5b, whereby the coefficient of determination is determined to test the efficiency of the scoring function. The following Equation can be used to express a simple linear relationship between two variables x and y.

$$y = \beta x + \alpha + e\,, \tag{4.17}$$

where y is the dependent variable and x is the independent variable, β represents the slope of the line and α is the y-intercept and e is known as the random error and is assumed to be a random variable having mean 0. In statistics, the determination co-efficient or goodness of fit (R^2), is a metric that measures a model's ability to predict or describe a linear regression result. A high R^2 value means that the model fits the data well and the minimum R^2 value is 0. The coefficient of

determination (R^2), is the proportion of one variable explained by other variables in the regression and this determines the strength of the relationship in the regression. The coefficient of determination is expressed as:

$$R^2 = 1 - \frac{\sum_{i=1}^{n}\left(y_i - \hat{y}_i\right)^2}{\sum_{i=1}^{n}\left(y_i - \bar{y}\right)^2}, \tag{4.18}$$

where $\hat{y}_i$ represents the value of the objective variable(y) predicted by regression for the ith data point. The Linear regression with only one explanatory factor (x) is mathematically equal to the square of the coefficient of correlation r between x and the objective variable y. Then the residual sum of squares $\sum_{i=1}^{n}\left(y_i - \hat{y}_i\right)^2$ is:

$$\sum_{i=1}^{n}\left(y_i - \hat{y}_i\right)^2 = \sum_{i=1}^{n}\left(y_i - \bar{y}\right)^2 - \frac{\left\{\sum_{i=1}^{n}\left(x_i - \bar{x}\right)\left(y_i - \bar{y}\right)\right\}^2}{\sum_{i=1}^{n}\left(x_i - \bar{x}\right)^2}, \tag{4.19}$$

where x_i and y_i in Equation 4.18 and 4.19 represent the values of the two variables of the ith data point and n represent the sample size. $\bar{x}$ and $\bar{y}$ denote the means of x and y respectively.

Substitutiong Equation 4.19 into Equation4.18 yields:

$$R^2 = \frac{\left\{\sum_{i=1}^{n}\left(x_i - \bar{x}\right)\left(y_i - \bar{y}\right)\right\}^2}{\left\{\left(\sum_{i=1}^{n}\left(x_i - \bar{x}\right)^2\right)\left(\sum_{i=1}^{n}\left(y_i - \bar{y}\right)^2\right)\right\}}, \tag{4.20}$$

Mathematically, Coefficient of determination = (correlation coefficient, (r))^2

$$\text{where } r = \frac{\left\{\sum_{i=1}^{n}\left(x_i - \bar{x}\right)\left(y_i - \bar{y}\right)\right\}}{\left\{\left(\sum_{i=1}^{n}\left(x_i - \bar{x}\right)\right)\left(\sum_{i=1}^{n}\left(y_i - \bar{y}\right)\right)\right\}} \qquad (4.21)$$

Chapter 5: (a) An NMR Crystallography Characterisation of Two Polymorphs of Tolfenamic acid, (b) Conformations in Solution and in Solid-State Polymorphs: Correlating Experimental and Calculated Chemical Shits for Tolfenamic acids.

5a.1 Introduction

Pharmaceutical APIs are crystalline and can exhibit polymorphism, which is the existence of a crystal structure in more than one form. There are many definitions for a polymorph based on their physical properties and arrangement. The word polymorph is derived from Greek, where poly means many and morph means forms. It has different meanings and definitions based on the field of study. McCrone defined a polymorph as "a solid crystalline phase of a given compound resulting from the possibility of at least two different arrangements of the molecules of that compound in the solid-state"[132].

The development of MAS in combination with CP has made solid-state NMR a powerful method for application to pharmaceuticals. Solid-state NMR can reveal much crystallographically-relevant information about an organic solid; for example, small changes in conformation and local electronic structure can be observed via the chemical shift. The number of molecules in the asymmetric unit of the polymorphs can be extracted by looking at the ^{13}C CPMAS spectra of the sample: The NMR peaks split according to the number of molecules in the asymmetric unit, and with a finger print spectra for every polymorphic form[133]. For instance, Masuda *et al.* were able to distinguish the molecular conformation of α- and γ-polymorphs of indomethacin using ^{13}C CPMAS where the ^{13}C spectra of the α form showed splitting for the three conformationally different molecules in the asymmetric form[134]. Most of the polymorphic studies involve CPMAS experiments focussing on ^{1}H, ^{13}C, or ^{15}N nuclei, following the first reported use of ^{13}C CPMAS to investigate organic polymorphs by Ripmeester[135]. Two-dimensional NMR, particularly heteronuclear experiments such as ^{1}H-^{13}C refocussed INEPT, HETCOR, ^{1}H-^{14}N HMQC, and homonuclear NOESY, like spin diffusion experiments or ^{1}H single quantum-double quantum experiments have been widely used to investigate hydrogen bonding, π-π, and CH-π interactions at the molecular level. Homonuclear proton experiments allow one to define the structural network and measure the distance between neighbouring protons[59, 136]. The application of solid-state NMR to the development of pharmaceuticals development is expected to continue evolving. Nowadays, experimental and calculated (GIPAW) NMR chemical shifts are being increasingly used along with CSP for validation of polymorph trial structures and complete structures determinations.

For organic molecules, ^{1}H and ^{13}C NMR play an essential role because ^{1}H chemical shifts are sensitive to long-range electrostatic effects and ^{13}C NMR can provide information on local structure and conformation. For instance, Yates *et al.* probed the structure of flurbiprofen combining experimental and computational solid-state NMR[137]. Following this, Harris *et al*. reported a series of examples of this method to consider a large number of compounds which are of pharmaceutical interest, because the characterisation of polymorphism and solvate formation

is a crucial challenge for the pharmaceutical industry[133, 138-143]. For example, seven forms of cabamazine and terbutaline sulfate were studied by comparing GIPAW calculated and experimental solid-state NMR chemical shifts. The studies were able to clearly distinguish all seven forms of carbamazine from the ^{13}C calculated and experimental chemical shifts and differentiate the hydrogen bonding network in different forms of terbutaline sulfate[141-142]. In the latter case, two polymorphs differ in their torsion angle which altered the hydrogen bonding in both forms and it was possible to distinguish the two forms due to the sensitivity of ^{13}C isotropic chemical shifts to the torsion angle[140].

Yates *et al*. combined GIPAW calculated and experimental NMR chemical shifts to evaluate C-H···O hydrogen bonding interactions in anomeric forms of the disaccharide maltose[144]. The hydrogen bonding was investigated by comparing the change in GIPAW calculated NMR chemical shifts between the full crystal structure and isolated molecules. A substantial change (up to 2 ppm) in the ^{1}H chemical shift was observed for a short CH··O distance and angle nearer to linearity corresponding to optimal weak hydrogen bonding. Likewise, the structure of D-galactose[145], disaccharides[146], campho [2,3-c] pyrazole[147], indomethacin[128], the structure of 5 aminofulvene-1-aldimines and deoxy guanosine derivatives[148], uracil[149], 4-cyano-4'-ethynylbiphenyl[129], and glycine HCl[150], have been investigated using the calculated NMR parameters to probe intermolecular interactions such as hydrogen bonding or π-π stacking. This method has been extended to supramolecular assemblies, which examine the hydrogen bonding that is responsible for self-assembly. For example, intermolecular hydrogen bonding is probed in guanosine self-assemblies by combining GIPAW calculations and ^{1}H double quantum experiments[151-153]. Similar examples include the consideration of tautomerism of isocytosine, water clusters[154], and the reaction pathway for dehydration of 10-hydroxy-10,9-boroxophenanthrene[155]. For carbon nanotubes[156], the presence of water in the carbon nanotubes are investigated with GIPAW, calculations whereby a relatively large (ca. −23 ppm) upfield for the ^{1}H chemical shift relative to the bulk liquid water was observed due to large anisotropic magnetic fields induced in the carbon nanotubes[157]. Recently, Tatton *et al.* demonstrated NMR crystallography as a beneficial tool for checking the structure of piroxicam, for which there are two structures solved from PXRD with different R factors[158].

This Chapter presents the solid-state NMR characterisation of two forms of tolfenamic acid, (Form I and Form II), and the results are compared with the information extracted from GIPAW calculations as introduced in Chapter 4. This enables the assignment of all ^{1}H and ^{13}C resonances of both forms. Additionally, a comparison of chemical shifts for an isolated molecule and the full

crystal provides information about crystal packing via intermolecular hydrogen bonding. Tolfenamic acid (TFA, 2-[2-methyl-3chlorophenyl)amino]benzoic acid) which is also known by the trade name clotam, is a non-steroidal anti-inflammatory drug that belongs to the fenamate family which inhibits the biosynthesis of prostragladin[159]. There are at least five known polymorphs of anhydrous TFA. The most prominent among those are Form I (CSD-KAXXAI01), and Form II (CSD-KAXXAI)[54, 160], and exhibiting conformational polymorphism. The chemical structure of tolfenamic acid is shown in Figure 5.1, and the structural details of Form I and Form II are summarised in Table 5.1.

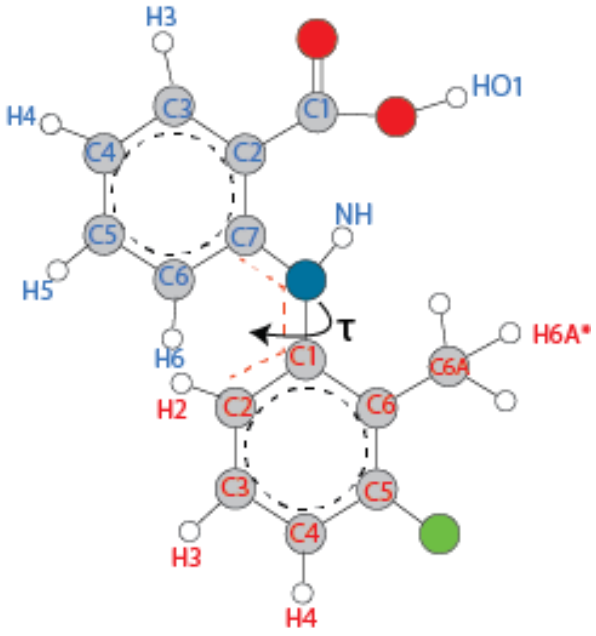

Figure 5.1: Structure of tolfenamic acid.

Table 5.1: Properties of the crystal structures of Forms 1 and II of TFA[160].

	Form I	Form II
Unit cell type	monoclinic	monoclinic
Space group	P21/c	P21/n
Unit cell lengths a, b, c / Å	4.826, 32.128, 8.041	3.836, 21.997, 14.205
Unit cell Angles (alpha, beta, gamma) /°	90, 104.88, 90	90, 94.11, 90

The overlay of a single molecule of Form I and Form II is represented in Figure 5.2, and it is clear that the main variation in conformation is in the torsion angle C7-N-C1-C6. The acid and N-H groups of both forms are very nearly planar (~ 171º) with a torsion angle being approximate to zero.

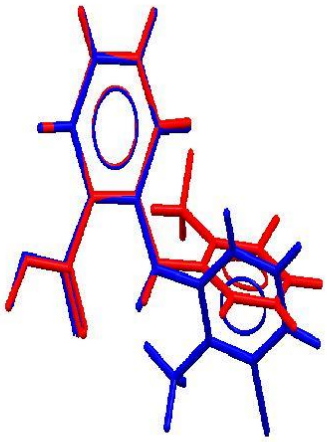

Figure 5.2: Overlay of Form I (CSD-KAXXAI01, red) and Form II (CSD-KAXXAI, blue) of TFA.

5a.2 Computational Details

DFT calculations were carried out using CASTEP[118, 161] which implements DFT within a generalized gradient approximation and employs the plane-wave pseudopotential approach. For geometry optimisation, the starting structure is the crystal structure determined from single-crystal XRD[160] data, in which the positions of all the atoms in the asymmetric unit were relaxed by keeping the unit cell dimensions fixed. NMR chemical shielding calculations were carried out on the geometry optimized structures using the GIPAW[120, 162] approach to determine the shielding tensor for each nucleus in the crystal structure. The calculation used a plane-wave basis set with a maximum cut-off energy of 700 eV, with a minimum Monkhorst–pack grid[115] spacing of $2\pi \times 0.1$ Å. In order to compare the results with experimentally measured isotropic chemical shifts directly, the following Equation 5.1 was used:

$$\delta_{iso} = \sigma_{ref} - \sigma_{iso}\,, \qquad (5.1)$$

where σ_{iso} is the absolute isotropic shielding value generated from the CASTEP calculation. The reference shielding (σ_{ref}) was determined by fitting the experimental isotropic chemical shift and the mean value of the calculated shielding (slope fixed to -1[125]), giving σ_{ref} equal to 169.9 ppm and 30.0 ppm for ^{13}C and ^{1}H, respectively. The fit between the experimental chemical shift and GIPAW calculated absolute shielding of TFA Form I is shown in Figure 5.3.

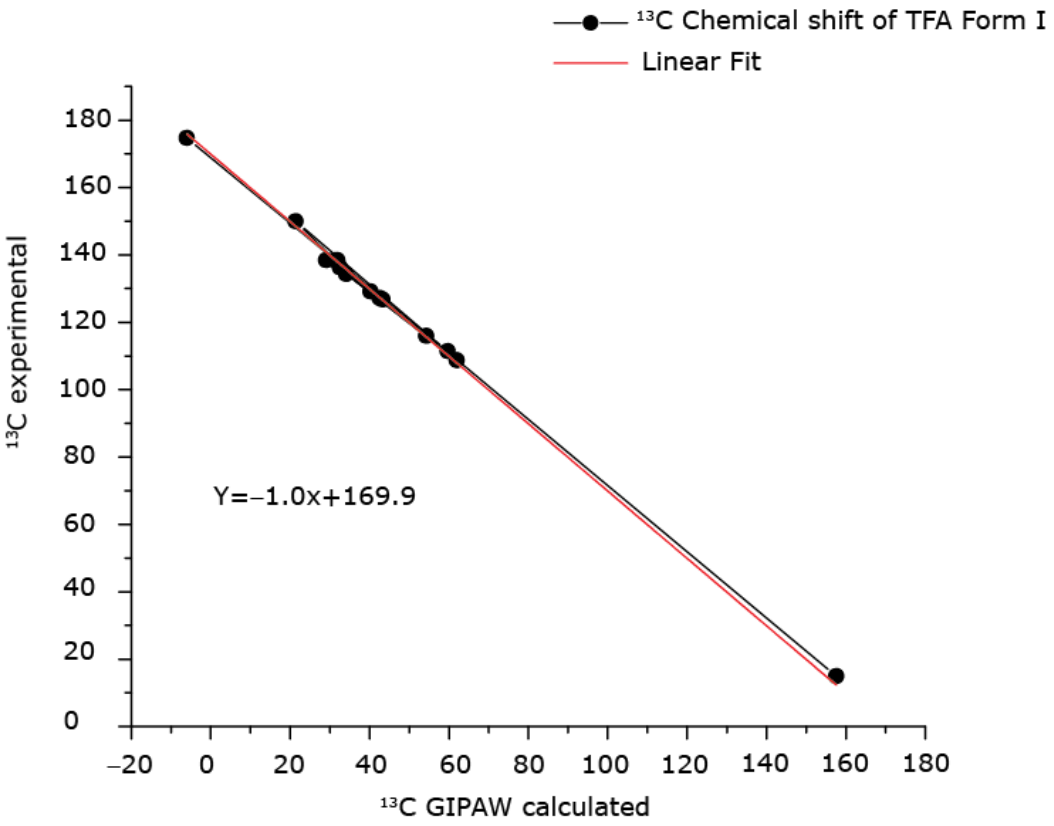

Figure 5.3: Comparison of experimental ^{13}C chemical shift (y-axis) and the GIPAW calculated absolute shielding (x-axis) of TFA Form I by fixing the gradient of the best fit to –1.

NMR calculations were also performed for an isolated single molecule, whereby a molecule was extracted from the geometry optimised crystal structure and placed into a periodically repeating unit cell with dimensions: Form I, 14.826 × 42.128 × 18.041 Å^3 and Form II, 13.836 × 31.997 × 24.205 Å^3 (such supercells can effectively eliminate the intermolecular interactions).

Calculated NMR shieldings were visualised and tabulated using Magresview[163] a visualization tool developed by CCP-NC (the collaborative computational project for NMR crystallography, www.ccpnc.ac.uk).

5a.3 Experimental Details

Both Form 1 and Form II TFA for solid-state NMR analysis, was provided from AstraZeneca, Macclesfield. TFA Form 1 was purchased from Sigma-Aldrich (Gillingam, UK) and Form II was prepared following the method by Du *et.al*[164]. All solid-state NMR experiments were carried out at room temperature using a Bruker Avance III and II+ spectrometer operating at a ^{1}H Larmor frequency of 500 MHz (11.7 T) and 600 MHz (14.1 T), respectively. A ^{1}H 90° pulse duration of 2.5 μs was used in all experiments.

^{1}H one-pulse MAS experiments were performed at a Larmor frequency of 600 MHz at 60 kHz MAS using a 1.3 mm HXY probe (in double resonance mode).^{13}C CPMAS spectra were acquired at a ^{1}H Larmor frequency of 500 MHz with a 4 mm HXY probe in double resonance mode and 12.5 kHz spinning frequency. Cross polarization was achieved by using a 90-100% amplitude ramp[89] on ^{1}H during a contact time of 1 ms. SPINAL-64[81] ^{1}H decoupling at a nutation frequency of 100 kHz was used. 1000 transients were co-added with a recycle delay of 60 s and an acquisition time of 40 ms.

^{1}H-^{13}C Refocused INEPT: A Refocused–insensitive nuclei enhancement using polarization transfer (INEPT) pulse sequence[64] was used with ^{1}H homonuclear decoupling (eDumbo-1_{22})[43-44] to attain high resolution in the indirect dimension and also to extend the coherence lifetimes during the spin-echo periods. 2D spectra were recorded with a spin-echo duration (τ-π-τ) of τ = 1.44 ms at a ^{1}H Larmor frequency of 500 MHz spectrometer and a spinning frequency of 12.5 kHz. For windowless eDumbo-1_{22}, the homonuclear decoupling was applied with a total cycle duration of 32 μs. Prepulses of duration 1.2 μs were used. 8 transients were co-added for each of 256 t_1 FIDs using the States TPPI method (to achieve sign discrimination), corresponding to a total experimental time of 19 hours.

^{1}H – ^{1}H Double Quantum (DQ) MAS[59]: DQ-SQ correlation spectra were acquired at a ^{1}H Larmor frequency of 600 MHz spectrometer with a 1.3 mm HXY probe (in double resonance mode). The MAS frequency was 60 kHz. Excitation and reconversion of DQ coherence were achieved using one rotor period of the BaBa (Back to Back) recoupling sequence [93, 165]. A 16-step phase cycle was used to select $\Delta p = \pm 2$ during excitation and $\Delta p = -1$ on the z-filter 90° pulse, where p is the coherence order. 8 transients were co-added for each of 144 (for Form I) or 160 (for Form II) t_1

FIDs, using the States method to achieve sign discrimination in F_1 with a rotor synchronized t_1 increment of 16.67 μs, corresponding to a total experimental time of 19 h (for Form I) or 21h (for Form II).

^{14}N-^{1}H HMQC experiments: Experiments were performed at a ^{1}H Larmor frequency of 600 MHz spectrometer using a 1.3 mm triple resonance probe (operating in double resonance mode) at a spinning frequency of 60 kHz. A ^{1}H 90° pulse of duration 2.5 μs was used, whereas a ^{14}N pulse of duration of 11 μs was used. The Optimum ^{14}N pulse length depends on the P_Q of a specific ^{14}N enviornment and nutation frequency. The employed 11 μs is a comprise for the range of typically encountered P_Q values for ^{14}N nuclei. The ^{14}N-^{1}H HMQC pulse sequence of Gan[88] utilizing rotary resonance recoupling (R^3)[45], which applies a ^{1}H RF nutation frequency of twice the spinning frequency, was used with an x-x phase inversion (every rotor period)[166]. The pulse sequence used is depicted in Figure 3.10. 8 transients were co-added for each of 144 t_1 FIDS with a recycle delay of 60 s. A short R^3 recoupling time of 133.33 μs was used to observe one bond NH correlations[76].

5a.4 Results and Discussions

The ^{13}C CP MAS spectra of both Form I and Form II exhibit 12 peaks with no splitting indicating the presence of one molecule in the asymmetric unit cell (see Figure 5.4). There is ambiguity in the overlap of C3 and C5 at 136.8 ppm and 138.9 ppm for Form I and C1 and C6 at 139.1 ppm and 126.1 ppm for Form II. As expected, ^{13}C chemical shifts vary markedly between the Forms, in particular, C2, C4, and C6 (see Tables 5. 2 and 5.3). This data is consistent with the previously published ^{13}C NMR spectra of Form I and Form II[159]. The purple stick spectra below the experimental spectra in Figure 5.4 correspond to the GIPAW calculated chemical shifts. A significant difference between the calculated and experimental OH1 proton chemical shift (~2 ppm) is seen, which can be explained by the strong temperature dependence of hydrogen-bonded resonances[167-169]. The experimental chemical shift at room temperature is expected to be at a lower ppm value compared to the calculated value corresponding to 0 K.

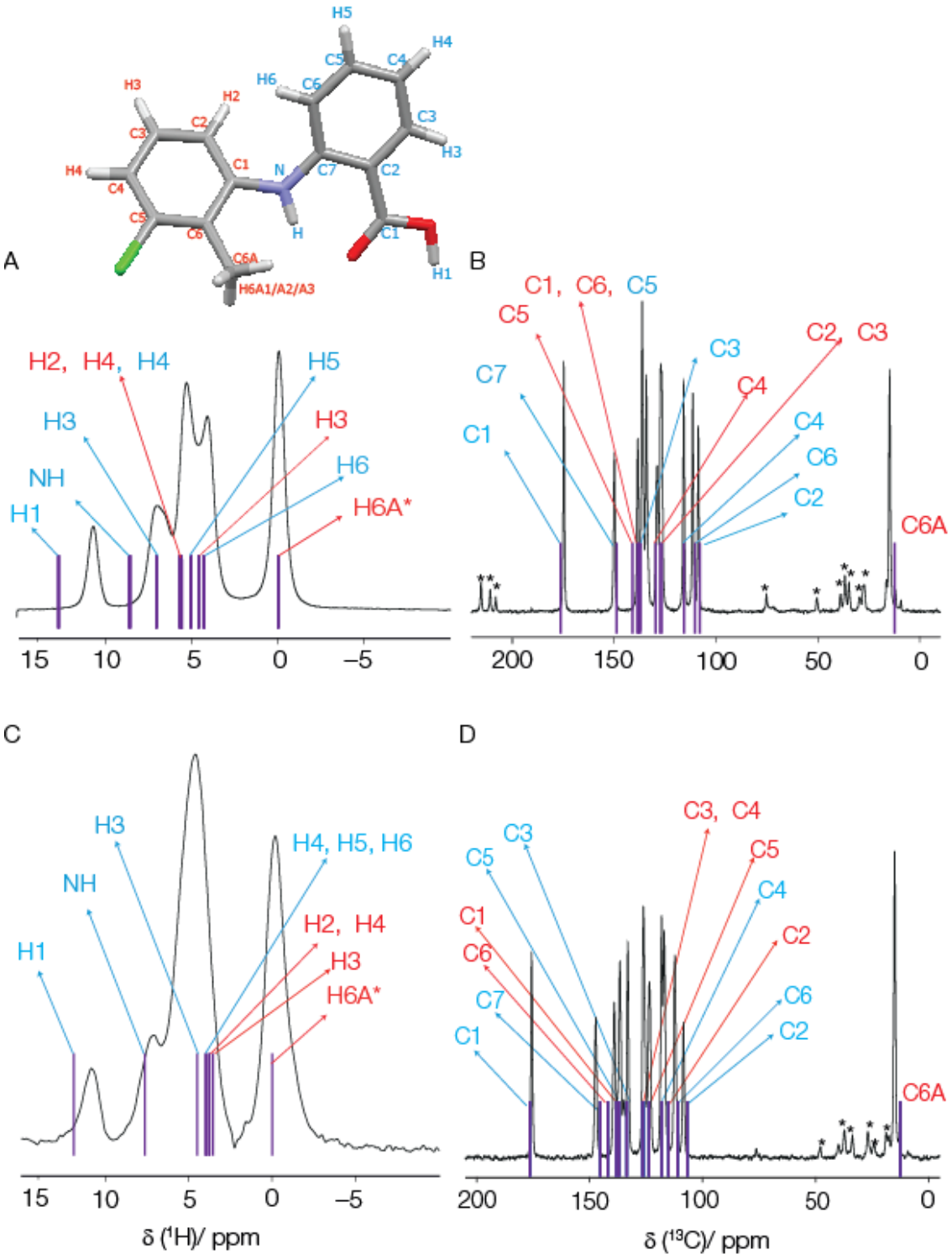

Figure 5.4: ^{1}H (600 MHz) MAS (60 kHz) and ^{1}H-^{13}C (125 MHz) CP MAS (12.5 kHz) spectra of Form I (a and b) and Form II (c and d). The stick spectra (in purple) correspond to GIPAW calculated chemical shifts (see Tables 5.2 and 5.3). * represents that the stated chemical shift is the average of the three protons of the CH_3 group.

Table 5.2: Comparison of experimental chemical shifts (in ppm) to GIPAW calculated chemical shifts (in ppm) for the full crystal and isolated molecule and experimental shift of TFA Form I.

Atom	$\delta_{crystal}$	$\delta_{mol(10Å)}$	$\Delta\delta^{cry-mol}$	δ_{exp} $^{1}H \pm 0.2$ $^{13}C \pm 0.1$
H1	14.0	6.1	7.9	12.6
H3	8.0	7.3	0.7	8.4
H4	6.6	5.7	0.9	6.7
H5	5.9	6.3	−0.4	6.1
H6	5.1	5.2	−0.1	5.6
NH	9.7	9.9	−0.2	9.0
H2	6.5	6.1	0.4	6.7
H3	5.5	6.4	−0.9	5.6
H4	6.6	6.3	0.3	6.7
H6A1/2/3	0.7[a]	1.1[a]	−0.4	1.2
C1	176.2	171.3	4.9	175.2
C2	107.9	104.8	3.1	109.2
C3	135.8	130.8	5.0	134.9
C4	115.7	113.8	1.9	116.5
C5	137.4	133.4	4.0	136.8
C6	110.2	111.0	−0.8	112.0
C7	148.6	148.8	−0.2	150.4
C1	138.6	139.4	−0.8	138.9
C2	126.7	124.4	2.3	127.8
C3	127.4	126.4	1.0	127.0
C4	129.7	126.7	3.0	129.4
C5	140.8	142.6	−1.8	138.9
C6	138.0	137.3	0.7	136.8
C6A	12.4	9.1	3.3	15.4

[a]The stated calculated isotropic ^{1}H chemical shift for the CH_3 group corresponds to the average for the three protons

Table 5.3: Comparison of experimental chemical shifts (in ppm) to calculated GIPAW chemical shifts (in ppm) for the full crystal and isolated molecule and experimental shift of TFA Form II.

Atom	$\delta_{crystal}$	$\delta_{mol(10Å)}$	$\Delta\delta^{cry-mol}$	δ_{exp} $^{1}H \pm 0.2$ $^{13}C \pm 0.1$
H1	14.3	6.2	8.1	12.8
H3	6.9	7.4	−0.5	7.0
H4	6.3	5.7	0.6	6.3
H5	6.4	6.3	0.0	6.3
H6	6.4	6.8	−0.4	6.3
NH	10.1	10.8	−0.7	9.2
H2	6.2	6.5	−0.4	6.2
H3	5.9	6.1	−0.2	6.1
H4	6.2	6.1	0.1	6.3
H6A1/2/3	1.4[a]	1.4[a]	0.0	1.9
C1	176.5	172.0	4.5	175.7
C2	106.7	106.3	0.4	108.5
C3	133.5	131.4	2.1	132.9
C4	118.1	114.3	3.8	117.9
C5	137.0	133.5	3.4	136.2
C6	111.0	109.7	1.2	112.0
C7	145.2	145.6	−0.4	147.3
C1	138.2	138.7	−0.5	139.1
C2	115.1	114.9	0.2	116.8
C3	126.1	124.2	1.9	126.1
C4	123.5	122.1	1.4	123.3
C5	142.0	142.3	−0.4	139.1
C6	126.4	128.7	−2.3	126.1
C6A	12.35	8.50	3.9	14.9

[a] The stated calculated isotropic ^{1}H chemical shift for the CH_3 group corresponds to the average for the three protons.

A series of two-dimensional experiments were performed to provide additional structural insight into packing effects such as hydrogen bonding interactions and π-π stacking. ^{1}H double quantum (DQ) – ^{1}H single quantum (SQ) spectra of Form I and Form II were recorded using one rotor period of BABA recoupling. The observation of a cross peak in the double quantum dimension of a DQ MAS spectrum indicates the close proximity (typically less than 3.5 Å) of a pair of two protons[59, 100]. The resolution of the DQ MAS spectra of Form I and Form II is sufficient to resolve many cross-peaks, as shown in Figure 5.5a and 5.5d. Tables 5.4 and 5.5 lists, for the NH and OH protons, H-H distances of the H atom (within 3.5 Å) which correspond to the observed double quantum peaks.

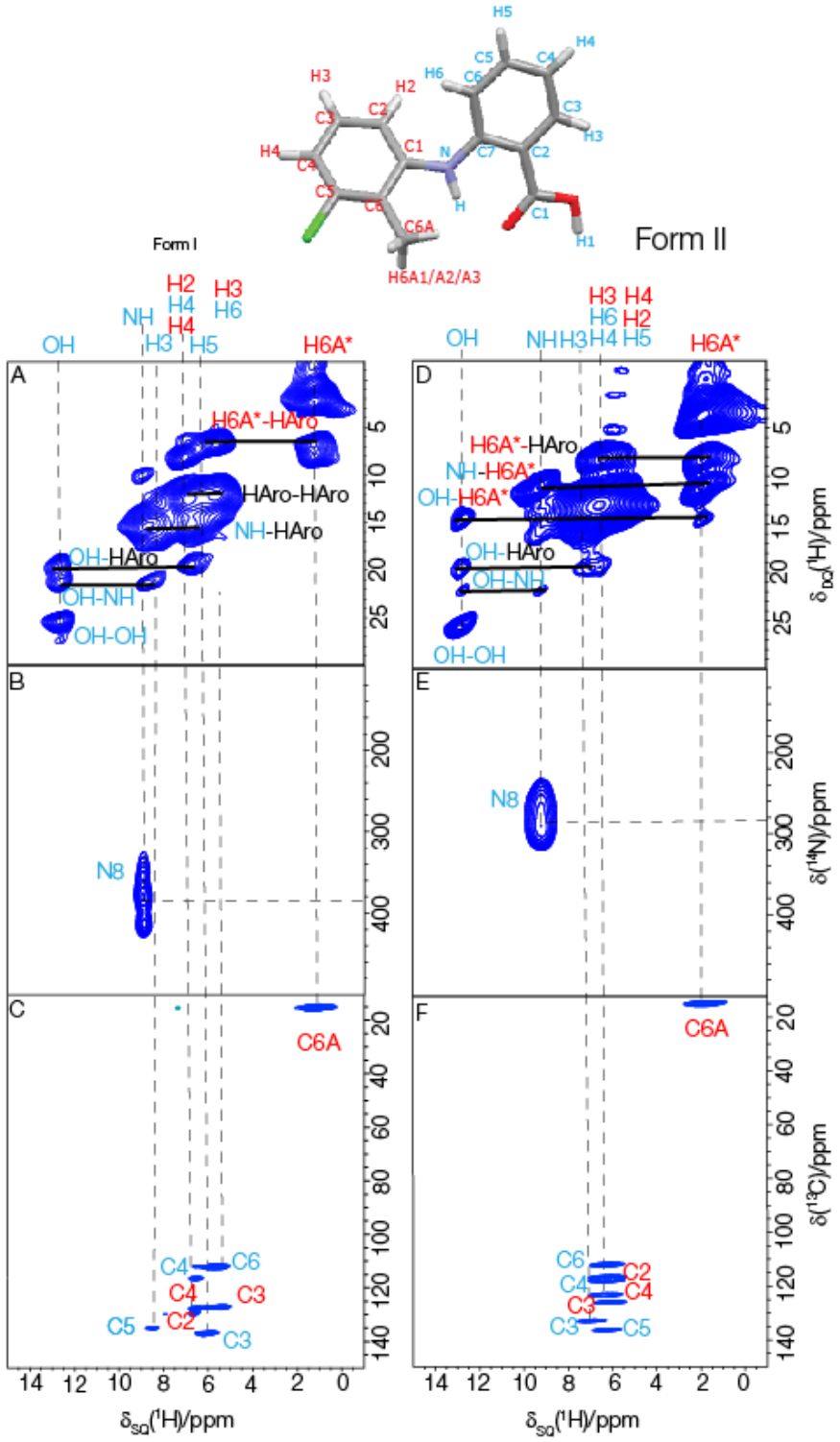

Figure 5.5: (a,and d) 2D ^{1}H (600 MHz) (DQ)–^{1}H (SQ) MAS (60 kHz, with 1 τ_R of BABA recoupling), (b, and e) 2D ^{14}N –^{1}H (600 MHz) HMQC MAS (60 kHz, τ_{RCPL} =133 μs) and (c, and f) 2D ^{1}H (500 MHz) –^{13}C refocused INEPT (12.5 kHz MAS, spin-echo duration of 1.44 ms)

spectra of Form I and Form II. Note that the $^{1}H–^{13}C$ spectrum is rotated 90º to allow better comparison with the other two spectra.

Double quantum peaks at δ_{DQ} = 12.6 +12.6 = 25.2 ppm and δ_{DQ} = 12.8 +12.8 = 25.6 ppm in both forms correspond to the intermolecular proximity between the two OH protons as expected for a hydrogen bonded dimer (see Figure 5.6). From the geometrically optimised crystal structures, the OH–OH distances (see Tables 5.4 and 5.5) are 2.27 Å and 2.28 Å for Form I and Form II, respectively. The pair of cross-peaks at δ_{DQ} = 21.1 ppm (Form I) and δ_{DQ} = 21.7 ppm (Form II), and at δ_{DQ} = 19.3 ppm (Form I) and δ_{DQ} = 19.5 ppm (Form II) correspond to the proximity of the OH proton to NH and aromatic protons, respectively. An additional DQ cross peak at 14.1 ppm is noted for Form II, which indicates the proximity of the OH proton to methyl protons (see Table 5.5). There are also short contacts between NH - CH_3 (δ_{DQ} =11 ppm, 2.14 Å) and between H6 and H2 (δ_{DQ} = 12.5 ppm, 2.33 Å) of Form II, whereas such short intramolecular distances between the NH –CH_3 and H6 and H2 are not seen in Form I.

However, there is a large number of overlapping peaks in the range 5.5 to 7 ppm, which corresponds to the aromatic protons and makes the assignment of the distinct protons from the ^{1}H DQ spectra not possible. The strong auto-peak observed at δ_{DQ} =1.25 +1.25 = 2.5, and δ_{DQ} = 1.85+1.85 = 3.70 occurs in both Form I and Form II, due to the close proximity of the methyl protons.

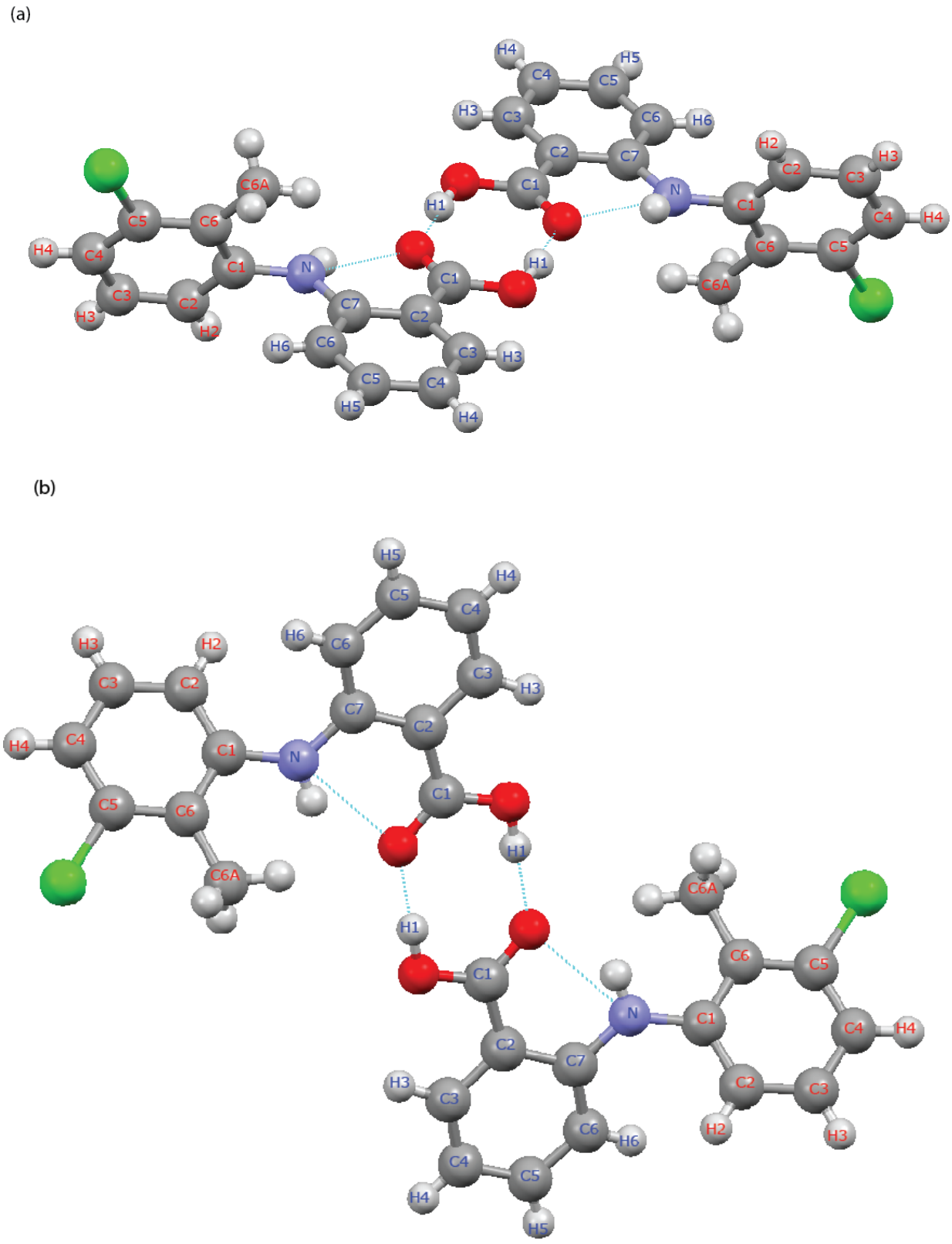

Figure 5.6: Geometry optimised crystal structure of TFA Form I (a) and Form II (b), highlighting the short hydrogen bond between two molecules forming a dimer (blue dotted lines).

Table 5.4: Distances of OH and NH proton to the nearest protons (within 3.5 Å) and corresponding ^{1}H DQ shifts in Form I.

Atom 1	Atom 2	Distance (Å)	δ_{SQ} (ppm)	δ_{DQ} (ppm)
OH	OH	2.27	12.6	25.2
12.6 ppm	H2 (aromatic)	2.80	6.7	19.3
	H4 (aromatic)	2.93	6.7	19.3
	NH	3.15	9.0	21.6
	H3 (aromatic)	3.23	8.4	21.0
	H3 (aromatic)	3.36	8.4	21.0
	NH	3.43	9.0	21.6
NH	H4 (aromatic)	2.53	8.4	17.4
9.0 ppm	H2 (aromatic)	2.78	6.7	15.7
	H2 (aromatic)	2.85	6.7	15.7
	H6A1 (CH_3)	3.06	1.2	10.2
	OH	3.15	12.6	21.6
	OH	3.43	12.6	21.6

Table 5.5: Distances of OH and NH proton to the nearest protons (within 3.5 Å) and corresponding ^{1}H DQ shifts in Form II

Atom 1	Atom 2	Distance (Å)	δ_{SQ} (ppm)	δ_{DQ} (ppm)
OH	OH	2.28	12.8	25.6
12.8 ppm	H6A1 (CH_3)	2.80	1.9	14.7
	NH	3.09	9.2	22.0
	H3 (aromatic)	3.33	7.0	19.8
	H3 (aromatic)	3.43	6.1	18.9
NH	H6A1 (CH_3)	2.09	1.9	11.1
9.2 ppm	H6A1 (CH_3)	2.49	1.9	11.1
	H6A2 (CH_3)	2.85	1.9	11.1
	H6A3 (CH_3)	3.00	1.9	11.1
	OH	3.09	12.8	22.0

^{1}H -^{13}C Refocused INEPT spectra show the correlations between directly bonded ^{13}C and ^{1}H nuclei in Form I and Form II. This is illustrated in Figure 5.5c and 5.5f and calculated and experimental ^{13}C, and ^{1}H chemical shifts for both forms are listed in Tables 5.2 and 5.3. The use of a short spin-echo duration τ = 1.44 ms ensures that no correlation peaks are observed for the carboxylic acid (quaternary carbon) group which was assigned in the ^{13}C CP MAS spectra (see Figure 5.4). Separate peaks are resolved for the CH_3 group and aromatic protonated ^{13}C resonances, thus allowing the experimental determination of the ^{13}C and ^{1}H chemical shifts. The observed chemical shifts are assigned utilizing GIPAW chemical shift calculations for the full

crystal structure. Expanded views of ^{1}H-^{13}C refocused INEPT spectra of Form I and Form II corresponding to the ^{13}C resonances of the aromatic carbons are illustrated in Figure 5.7 (red crosses in the spectra represents the GIPAW calculated chemical shift). Good (within the usual ~1% of the chemical shift range[125]) agreement is observed between the experimental and calculated ^{13}C and ^{1}H chemical shifts.

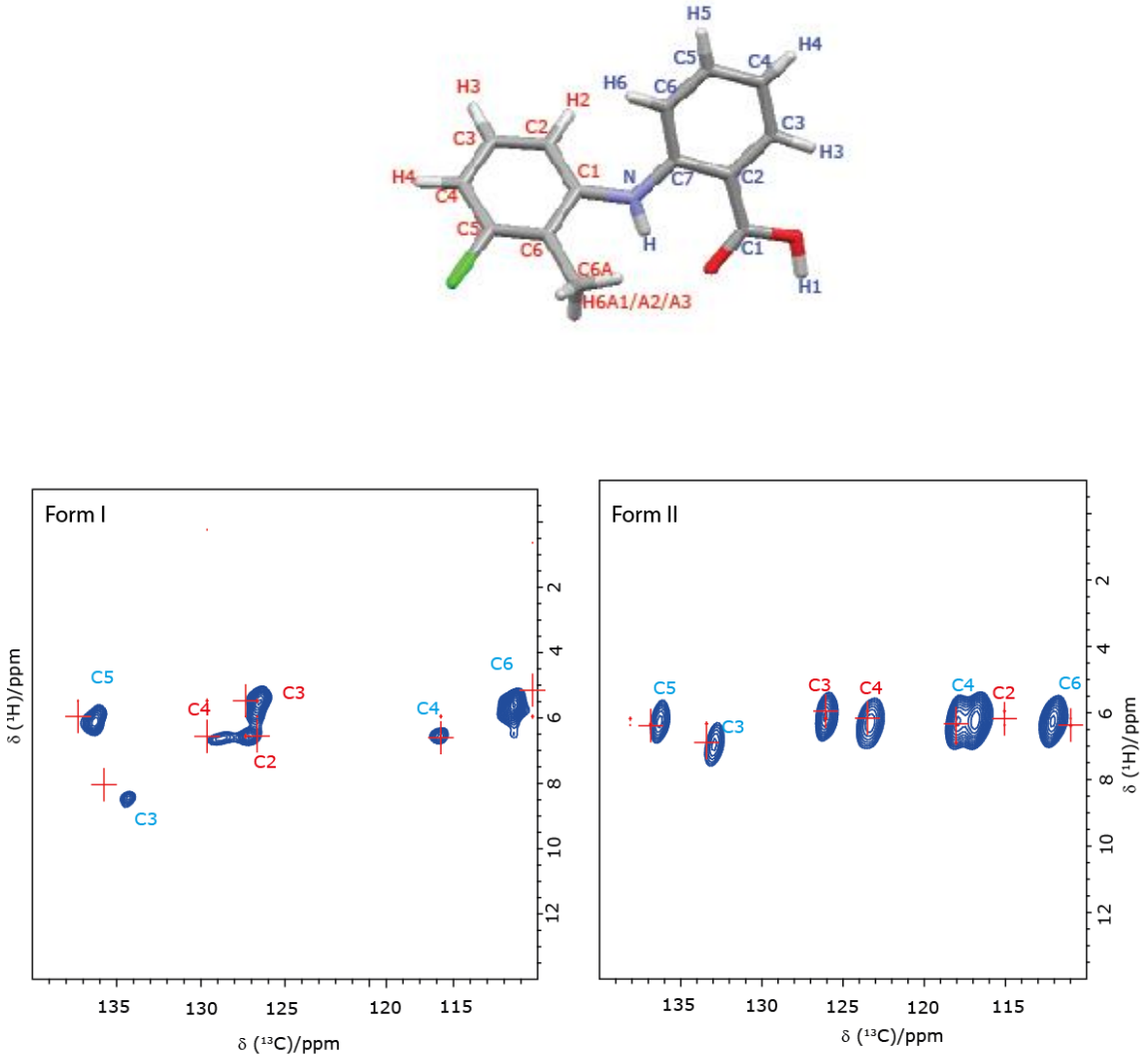

Figure 5.7: An expanded view of the aromatic region from 2D ^{1}H (500MHz)-^{13}C refocused INEPT spectra of Form I and Form II (the full spectral region is shown in Figure 5.5c and f). The red crosses represent the calculated (GIPAW) ^{1}H and ^{13}C chemical shifts.

The 2D ^{14}N -^{1}H HMQC experiment is a powerful probe to understand N-H proximities. ^{14}N -^{1}H spectra of both forms were recorded with a short recoupling time of 133.33 μs (shown in Figure 5.5b). As expected, a cross-peak is seen for the protonated nitrogen for both forms, but with

different ^{14}N line shapes. Figure 5.8 presents SIMPSON[130] simulated spectra for Form I and Form II using the GIPAW calculated quadrupolar parameters compared to the columns extracted from the ^{14}N-^{1}H HMQC spectra. This clearly shows the sensitivity of ^{14}N NMR to small changes in the environment (the C_Q of Form I is larger than that for Form II). GIPAW calculated ^{14}N shifts along with the quadrupolar parameters and experimental shifts are listed in Table 5.6. From the table, it is evident that there is a good agreement between experimental and GIPAW calculated ^{14}N shifts.

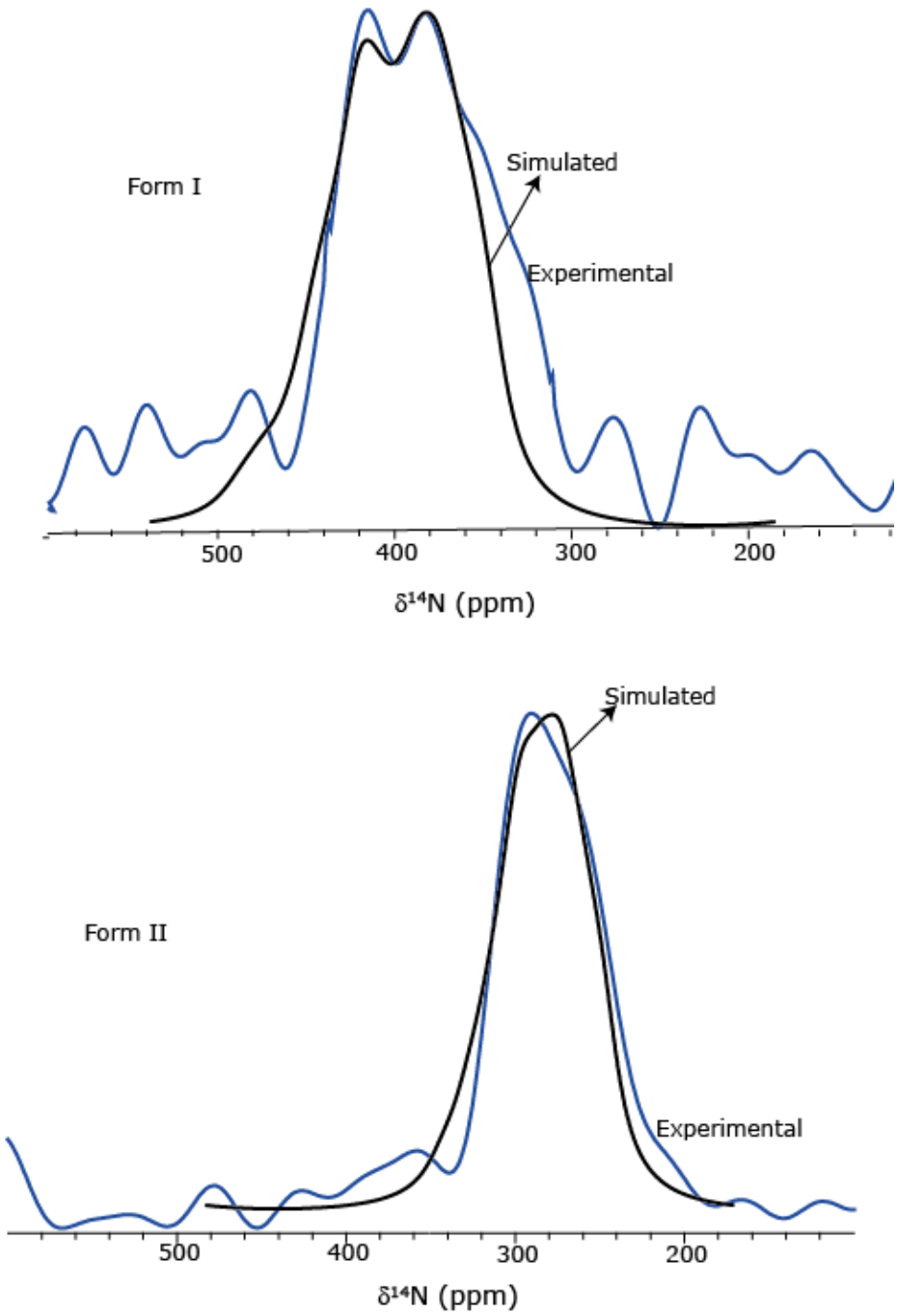

Figure 5.8: ^{14}N spectra were simulated using SIMPSON (for the GIPAW calculated quadrupolar parameters in Table 5.6) NMR and compared with the row extracted from the ^{14}N -^{1}H spectra (Figure 5.5b) at a ^{1}H chemical shift of 9.0 and 9.2 ppm for Form I and Form II, respectively. The pulse sequence and quadrupolar parameters used for the simulation is presented in Section 4.2.

Table 5.6: GIPAW calculated and experimental ^{14}N quadrupolar parameters and shifts.

	[a]C_Q/ MHz	[a]η_Q	[a,b]δ^{iso}_{CS}/ ppm	[a,c]$\delta^{Q}_{ISO}{}^{cal}$/ ppm	[c]$\delta(^{14}N)_{calc}$ / ppm=$\delta_{iso}{}^{calc}+\delta^{Q}_{ISO}{}^{cal}$/ppm	δ $(^{14}N)_{expt}$	δ $(^{1}H)_{expt}$
I	–4.3	0.4	–277.0	692	416	385	9.0
II	−3.7	0.5	−269.5	539	269	285	9.2

[a]where C_Q and η_Q represents the quadrupolar coupling constant and asymmetry. δ^{iso}_{CS} and δ^{Q}_{ISO} correspond to the isotropic chemical shift and the isotropic second-order quadrupolar shift, respectively (see Equations 2.144 and 2.145).

[b]Using σ_{ref} = −153 ppm. The σ_{ref} value is obtained by taking the sum of the experimental chemical shift and the GIPAW calculated chemical shielding.

[c]Using a scaling factor of 0.95 for C_Q to give best agreement with the experimental value and a ^{14}N Larmor frequency of 43.36 MHz, see Section 3.2 of reference[76].

5a.6 Molecule to Full Crystal Changes in Calculated Chemical Shifts.

Insight into intermolecular hydrogen bonding and aromatic π-π interactions is obtained by comparing the chemical shift calculations for a full crystal structure with those for an extracted isolated molecule[170-171]. Similar studies have been carried for a dithianon–pyrimenthanil cocrystal[172], guanosine derivatives [153], γ-indomethacin [128], and other organic compounds[127, 173-176]. As shown in Tables 5.2 and 5.3, the largest isolated molecule to crystal change in the calculated ^{1}H chemical shift is for the OH proton ($\Delta\delta_{crystal-mol}$ = 7.9 ppm for Form I and 8.1 ppm for Form II) of the carboxylic acid group that forms an intermolecular hydrogen bonded dimer. The carboxylic acid is almost coplanar with the phenyl group to which it is bonded (see Figures 5.9 and 5.10). The hydrogen bond distances and angle for both forms are listed in Table 5.7. From the table, it is clear that the geometry and strength of the hydrogen bonds are similar in both forms. The packing and conformation of Form II are distinctive compared to the Form I and have short contact between the chlorine and aromatic ring (see Figures 5.9 and 5.10).

Table 5.7: Distances and angles for OH…O hydrogen bonds extracted from the crystal structure of Forms I and II of TFA.

	d(O-O) / Å	d(H…O) / Å	∠OHO / °	$\Delta\delta^{crystal-mol}$/ ppm
Form I	2.26	1.02 1.60	174. 6	7.9
Form II	2.28	1.02 1.59	175.1	8.3

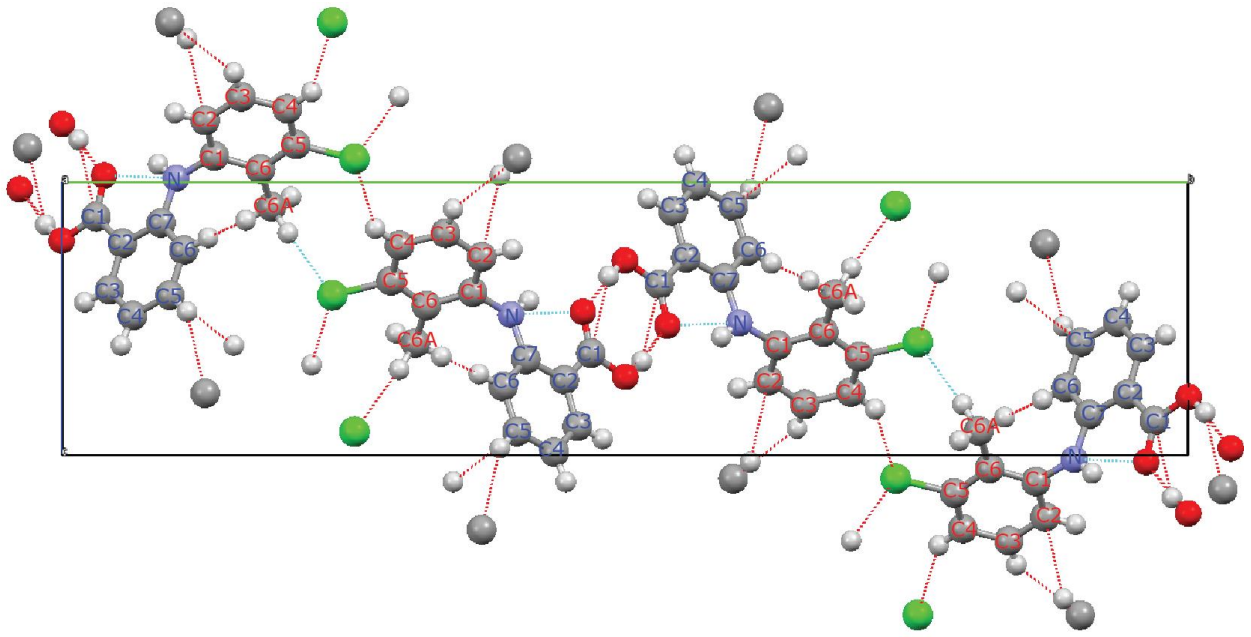

Figure 5.9: Packing of TFA Form I with short contacts and hydrogen bonds.

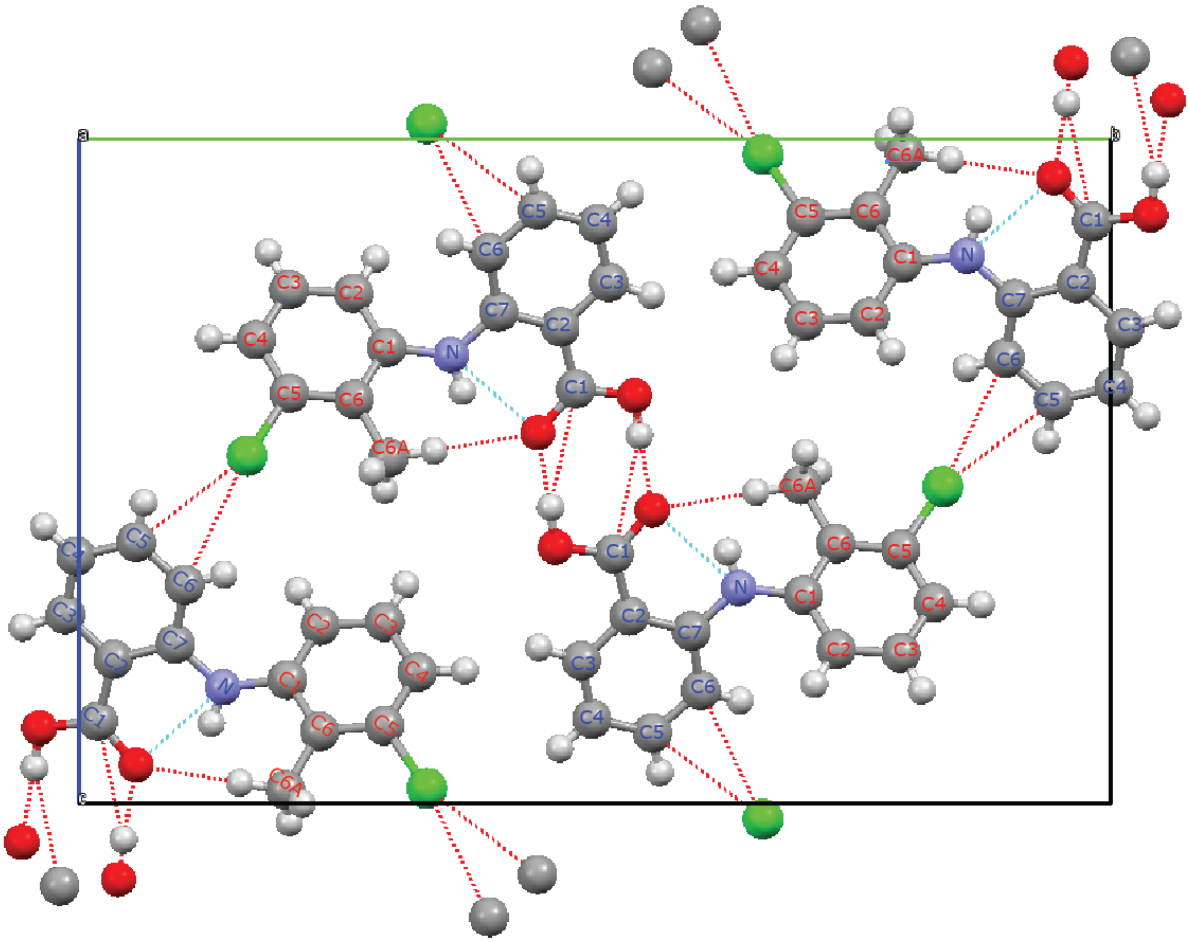

Figure 5.10: Packing of TFA Form II with short contacts and hydrogen bonds.

5a.7 Conclusions

The results presented in this subchapter show that ^{13}C CPMAS NMR experiment can be used to distinguish conformational polymorphs. ^{1}H and ^{13}C resonances are resolved and assigned with a high degree of accuracy and reliablility in both forms by comparing experimental data with the GIPAW calculated chemical shifts. Additionally, the comparison of calculated chemical shifts for the optimized full crystal structure and a molecule placed in a supercell allowed intermolecular interaction in both forms to be investigated. Two-dimensional ^{1}H-^{1}H DQ/SQ spectra recorded at 60 kHz MAS probe the intermolecular hydrogen bonding in both forms and also provide insight regarding other protons which are in close spatial proximity. Moreover, ^{13}C-^{1}H INEPT and ^{14}N-^{1}H HMQC spectra, together with the calculated chemical shifts, make the proton assignments in both forms easier.

5b.1 Introduction

Polymorphs may have different arrangements or conformations and thus possess different chemical and physical properties such as packing, thermodynamics, and spectroscopic, kinetic, interfacial, and mechanical properties[177]. Hence it is crucial to produce the same polymorph while manufacturing, particularly for pharmaceutical industries, because the properties of the API have a direct effect on the stability, dissolution, and bioavailability of the drug. For instance, consider the case of ritonavir, which is marketed as Norvir, for the treatment of Acquired Immune Deficiency Syndrome (AIDS). The company had to withdraw the drug from the market due to an unexpected change in the physical properties. This sudden change was due to the appearance of a new polymorph, which is thermodynamically stable and less soluble than form I[178]. Another famous example of polymorphism is 5-methyl-2[(2-nitrophenyl) amino]-3-thiophenecarbonitrile, an antipsychotic agent, which is commonly known as ROY, which is named for the colours Red, Orange, Yellow. ROY is an extraordinary system with 11 known polymorphs[179]. It is essential to make the appropriate polymorphic form, as the other form may not have the same effect. Klaproth (in 1788) was the first to observe polymorphism while crystallising calcium carbonate to calcite and aragonite, but often in literature, Mitscherlich is recognised as the first to report polymorphism in several arsenates and phosphates [180].

There are two types of polymorphism: packing and conformational polymorphism. In packing polymorphism, the molecules are packed differently by keeping the conformation more or less the same, whereas, in conformational polymorphism, the molecules can adopt different conformations, resulting in the formation of different conformers[181]. The two polymorphs of *p*-nitrophenol are a well-known example for the packing polymorphs where different types of intermolecular hydrogen bonding result in the formation of different structures[182]. ROY is a well-studied example for conformational polymorphism. Out of the 11 polymorphic forms, seven forms have been determined by X-Ray diffraction, with different torsion angles and conformations. Conformational polymorphs differ in their properties compared to the packing polymorphs because many physiochemical properties such as dipole moment, molecular shape and colours are conformation−dependent[132].

Understanding of crystal packing arrangements and intermolecular forces like hydrogen bonding, Van der Waals interaction, Coulombic interactions, steric repulsions, and weak interaction π-π stacking can help to identify the most stable polymorph while developing the product. These interactions can change the torsion angle and result in the formation of different conformations[179].

The two fundamental approaches used for the characterisation of an organic solid are X-ray diffraction and spectroscopy. X-ray diffraction (XRD), both powder (PXRD) and single crystal

(SXRD), reflect the differences in the crystal structure. Conventionally, PXRD is used to identify the number of phases and to solve the structure, whereas SXRD is employed for the detailed molecular and crystal structure analysis[132]. One of the main limitations of SXRD is its requirement of a suitable single crystal of appropriate size and quality, which is not always possible and hence the best approach for investigating the structural properties in such cases is to use PXRD. For instance, the structural properties of 1:1 cocrystal containing benzoic acid and pentafluorobenzoic acid have been studied directly from the PXRD data using the direct-space genetic algorithm approach for structure solution followed by Rietveld refinement[183].

Spectroscopy techniques include infrared, Raman, and solid-state NMR spectroscopy. Both infrared and Raman can give information about the vibrational modes, whereas solid-state NMR is needed to probe the environment of an atom, particularly to reveal molecular interactions at the atomic level[132, 180, 184], as mentioned in the introduction of subchapter 5a.

As detailed in the earlier paragraph, it is not always possible to get a sufficiently high-quality crystal for SXRD, which makes the characterisation of polymorphs very difficult. In such circumstances, a variety of techniques, including CSP[185-188], PXRD[189-190], and infrared spectroscopy[191] are used to characterise the powder sample. However, all these techniques are not enough for the detailed analysis of the atomic and molecular structure.

CSP methods can be used to generate possible crystal structures based solely on the molecular structure[185]; progress made in this field, for organic molecules, can be followed from a series of blind tests[192-196]. For pharmaceuticals, CSP has the potential to predict all possible polymorphs, noting that control of the crystallisation to produce phase pure samples in the licensed polymorphic form is essential for quality control. Importantly, CSP methods provide a way to calculate the crystal energy landscape, thus revealing the set of thermodynamically feasible structures[197]. It can be combined with other techniques such as XRD or solid-state NMR for structural verification. For instance, recently to determine the phase of glycine dehydrate, Xu *et al*. combined CSP with powder X-ray diffraction[198].

The CSP method itself is computationally expensive due to many interdependent variables, and hence, alternative methods were developed for structural refinement. In 2010, Salager *et al.* showed how ^{1}H chemical shifts, CSP, and GIPAW calculation could be used for structure elucidation in the case of thymol. In this approach, trial structures are generated using the Monte Carlo annealing method and a conformational search and optimisation based upon a molecular mechanics description for forces. The corresponding stable structures are then optimised via hybrid DFT/molecular mechanics approaches, and the structures are ranked according to their energy. The predicted structures were subjected to a periodic DFT GIPAW calculation, and a final

structure with an RMSD of 0.29 Å from the X-ray crystal structure is predicted by comparing the calculated and experimental ^{1}H chemical shifts, with the ability of spin diffusion ^{1}H MAS NMR to predict the correct structure being also tested[199]. This approach[200] has been used for the structure determination of cocaine, flutamide, flufenamic acid, theophylline, and 4-[4-(2-adamantylcarbamoyl)-5-tert-butyl-pyrazol-1-yl] benzoic acid[201].

Needs and Pickards introduced ab-initio random structure searching (AIRSS)[202], which produces a structure from randomised atomic coordinates and cell vectors, unlike crystal structure prediction techniques which depend upon force fields for geometry and energy minimisation[122]. The corresponding structures are optimised under quantum mechanical stresses and forces. A combination of AIRSS and GIPAW has been applied in battery[203] and mineral studies[204]. In 2017, Zilka *et al.* used an AIRSS search for the structure determination of two forms of m- amino benzoic acid, out of five known polymorphs, by generating 600 candidate structures[205]. Recently Thureau *et al.* elucidated a computationally less expensive approach for the structural screening of the theophylline molecule by combining the AIRSS method with solid-state ^{13}C-^{13}C double quantum experiments measured by DNP. Two candidate structures of theophylline were determined from a pool of structures by comparing the experimental and theoretical ^{13}C-^{13}C double quantum build-up curves[206].

An approach has been developed by Hofstetter *et al.* to quantify positional uncertainties in crystal structures by chemical shift-based NMR crystallography. The method established a correlation between the root square mean deviation of experimental and calculated chemical shift and the variance of atomic positions of individual atoms in structures determined by NMR crystallography. This approach was then tested in cocaine, flutamide, flufenamic acid, 4-[4-(2-adamantylcarbamoyl)-5-tert-butylpyrazol-1-yl]-benzoic acid, and the K salt of penicillin G[207]. Recently Paruzzo *et al.* developed a cost-effective machine learning framework to predict the chemical shifts in solids, which is based on the local environments of the individual atoms. These chemical shifts are predicted by training the model on a database constituted of a large number of GIPAW calculated chemical shifts for various reference crystal structures following geometry optimisation[208]. It is clear that the full potential of NMR crystallography has yet to be exploited and is still an active area of research[199].

Conformational polymorphism can be easily analysed using scalar coupling, residual dipolar coupling, and cross-relaxation data such as NOEs, which can be accessed from the solution NMR data. The chemical shift of resonance is highly dependent on the environment and hence is

conformation-dependent; however, extracting quantitative conformational information from the chemical shift is always challenging.

This subchapter builds upon the experimental and calculated chemical shifts of TFA Form I and Form II detailed in the previous subchapter 5a. The current subchapter describes a novel scoring function for ranking or predicting crystal structures of tolfenamic acid using solution- and solid-state NMR data in conjunction with DFT calculated chemical shift using the GIPAW approach. This method provides a way to reduce the number of alternative crystal structures in a crystal structure prediction campaign by introducing calculated and experimental solution-state data that probes conformations. Additionally, this approach can also distinguish polymorphs, at least in the case of TFA. We have also shown that the effects of packing and conformation on chemical shift can be deconvoluted using the scoring function. This Section of work was done in collaboration with C4X Discovery (Drs Charles Blundell, Hugh Dannatt, and Duncan Crick) and AstraZeneca (Drs Leslie Hughes and Helen Blade).

The methodology for this scoring function is divided into three stages:

1. Firstly, experimental ^{1}H and ^{13}C solid-state ($\delta_{Solid\ exp}$) and solution NMR data were measured ($\delta_{Solution\ exp}$).
2. Secondly, chemical shifts were calculated for TFA in solution from the ensemble of conformations generated using solution NMR data ($\delta_{Solutioncalc}$) and from the crystal structure of TFA form using the GIPAW approach ($\delta_{Solidcalc}$).
3. Finally, the scoring function is determined using Equation 5.2. Plotting the observed changes in the experimental ($\Delta\delta_{experimental}$) chemical shift against the changes in the calculated ($\Delta\delta_{calculated}$) chemical shift between the solution and the solid state gives a scoring function, which is shown here to be able to distinguish different polymorphs:

$$\Delta\delta_{\exp erimental} = \delta_{solid\,\exp} - \delta_{solution\,\exp}$$
$$\Delta\delta_{calculated} = \delta_{solidcalc} - \delta_{solutioncalc} \quad . \qquad (5.2)$$

A schematic representation of the scoring function is depicted in Figure 5.11.

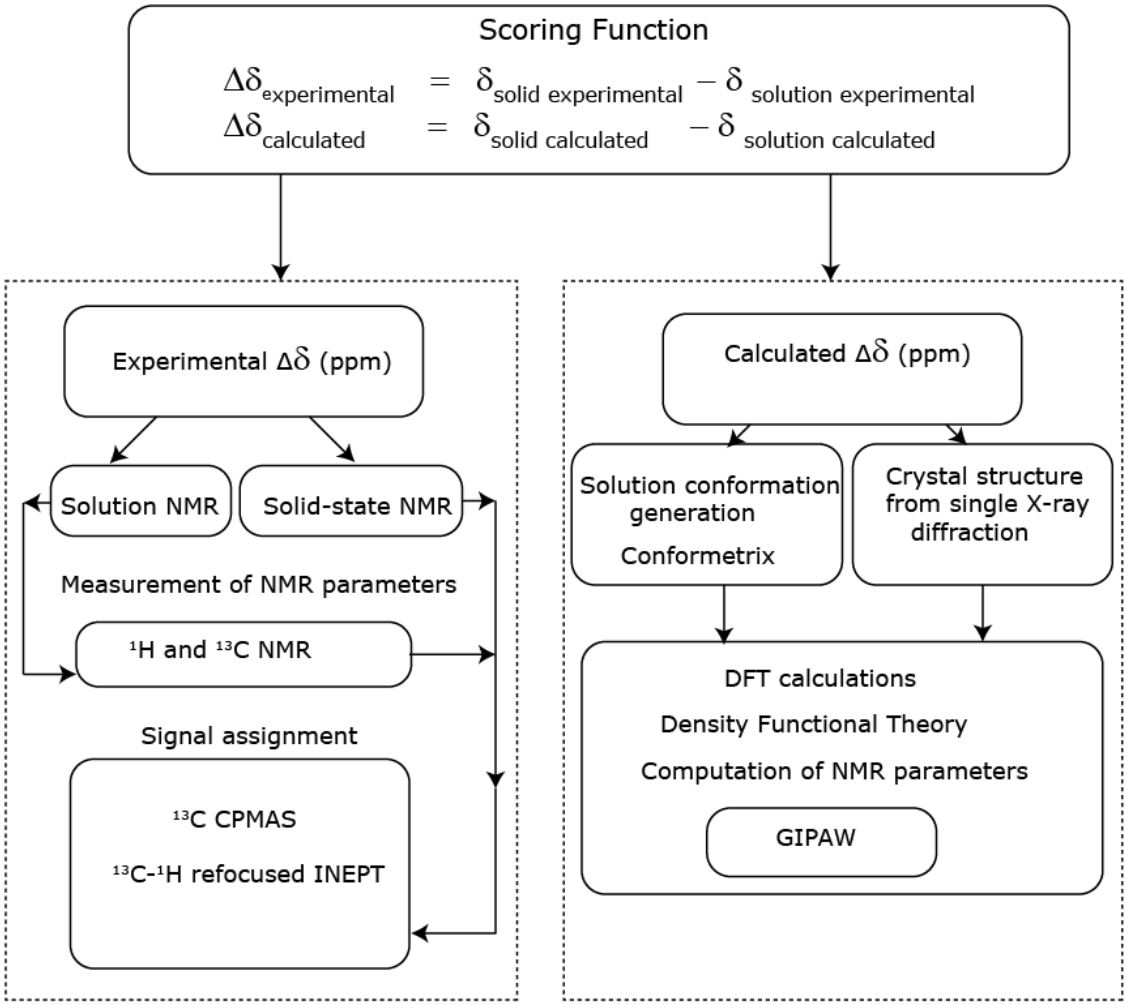

Figure 5.11: Schematic representation of the scoring function approach presented in this Chapter.

There are at least six or seven degrees of freedom in the TFA molecule (see Figure 5.12). However, it is clear from the overlaid image of Form I and II (see Figure 5.2) that the main difference in the conformation is due to the torsion 1 (C7-N-C1-C6).

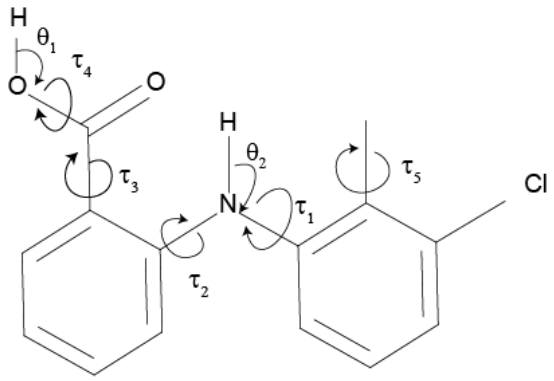

Figure 5.12: Possibles degrees of freedoms in a TFA molecule based on the figure presented in Ref[209].

5b.2 Sample

High-resolution structures of TFA Form I and Form 2 were determined (by Dr Charles Blundell, C4X Discovery) these were used as the base geometry for solution conformer generation. Structural information for all the polymorphs used in this study is presented in Table 5.8.

Table 5.8: Crystal structure information and torsion angle (C7-N-C1-C6) details of all the four forms of TFA from the SCXRD data.

Refcode	Space group	Z'	Torsion angle/º C7-N-C1-C6
Form I KAXXA101	$P2/_1c$	1	–74.91
High-resolution Form I	$P2/_1c$	1	–74.33
Form II KAXXAI	$P2_1/n$	1	–142.63
High-resolution Form II	$P2_1/n$	1	–142.94
Form III KAXXAI02	$P2/_1c$	2	(a) –138.37 (b) 126.78
Form IV KAXXAI03	P-1	3	(a) –115.85 (b) –125.92 (c) –134.14

5b.3 GIPAW Calculation of Solid-State NMR Chemical Shifts

The experimental and calculated ^{1}H and ^{13}C solid-state chemical shifts of Form 1 and Form II were presented in Chapter 5a (see Table 5.2 and Table 5.3). The calculated chemical shifts for the full crystal structure and the isolated molecules of two other forms of TFA, Form III (CSD refcode: KAXXAI02) and Form IV (CSD refcode: KAXXAI03) were obtained using the GIPAW approach.

5b.4 Experimental Solution NMR Chemical Shifts

Drs Charles Blundell and Duncan Crick (C4X Discovery, personal communication) recorded solution NMR chemical shifts of TFA using $CDCl_3$. A suitable deuterated solvent must be used, ensuring the same charge state in solution as the solid forms. Hence in the present study, deuterated chloroform was considered as a suitable solvent, which has no effect on the conformation of the solvent compared to deuterated benzene and toluene which can exert an aromatic ring current effect upon the TFA molecule.

5b.5 Calculation of Solution NMR Chemical Shifts

Drug molecules often have more than one rotatable bond and may adopt a large number of conformation in solutions. Separate sub-spectra for conformers cannot be observed in NMR because most of the conformational processes (interconversion between conformers) are rapid on the NMR time scale; however, a weighted average dependent on a mole fraction of each contributing species can be obtained[210]. It is well known that stereochemistry and conformation affect the physicochemical properties of a molecule like reactivity or solubility as well as the ability of a drug molecule to interact with a receptor. Hence, pharmaceutical chemists can aim to use conformational information to make better drug molecules. As described above, the conformation of a molecule can depend on what solvent it is dissolved in. NMR is a vital tool to probe conformational and stereochemistry studies because it can access different parameters which can determine the shape of a molecule such as NOEs and scalar coupling, residual dipolar couplings, and chemical shifts[210].

Three-dimensional (3D) model structures, can be derived using the structural constraints information obtained from solution NMR data. These 3D structures are an integral of all the intermolecular interactions it can form, hence several theoretical and computational techniques have been developed for generating such 3D structures[211]. One of the critical characteristics of a 3D dynamic structure model is that it describes all the conformations that a molecule can occupy in solution. Blundell *et al.* showed that a 3D dynamic model could be generated through two

principal steps: firstly, a 3D model is defined to represent a molecule and, secondly, the model is refined using a large amount of solution NMR data until the best fit is obtained[212].

According to Blundell's solution NMR approach, a single rotatable bond has conformers (macrostates or modes) around which local libration takes place and can be represented as a Gaussian distribution of microstates (conformations) around those macrostates (conformers/modes). Blundell *et al*. parameterise this behaviour against solution experimental NMR data using variables for the conformer position (Gaussian mean angle), its libration (Gaussian standard deviation) and its population relative to other conformers, producing a dynamic 3D structure that encapsulates the solution behaviour for each torsion. Such a 3D dynamic model has been published for streptomycin, and the conformations generated through the 3D model are consistent with the low-energy conformations seen in the solid state from X-ray diffraction[213]. For this study, Drs Charles Blundell and Hugh Dannatt (C4X Discovery, personal communication) provided such a dynamic 3D-structure for tolfenamic acid in the charged state in water. The conformer mean angles, librational amplitudes and populations are given in Table 5.9.

Table 5.9: Conformer mean angles, librational amplitudes, and populations of tolfenamic acid in water in the charged state (provided by Blundell and Dannatt) determined from solution NMR data according to the method of Blundell *et al.*[212].

Torsions	Mean angle (°)	Population %	Librations
O1–C1–C2–C7	0 ± 0 180 ± 0	50 ± 0 50 ± 0	5 ± 2 5 ± 2
C2–C7–N–C1	180 ± 0	100 ± 0	2 ± 2
C7–N–C1–C6	134.5 ± 2 –134.5 ± 2 69.8 ± 2 –69.8 ± 2	40.5 ± 4 40.5 ± 4 9.5 ± 4 9.5 ± 4	15 ± 4 15 ± 4 15 ± 4 15 ± 4

For the calculation of solution chemical shifts for tolfenamic acid, the initial step was to determine the solution conformations from the solution NMR data. The dynamic solution 3D structure confirmed that the torsion C7-N-C1-C6 (which was responsible for the overall conformation of TFA in solution) librates in 4 modes/conformers in two symmetrical pairs as shown in Table 5.9 and population for each mode is not identical. The mean angles are ± 135° and ± 70°, and each fluctuates around 15°. Blundell and Dannatt (C4X Discovery) derived the conformational behaviour of tolfenamic acid in solution, and this is shown in Figure 5.13. None of the other torsions contribute to the overall conformation of the molecule and therefore do not result in chemical shift perturbations. For example, O1–C1–C2–C7 is fixed at 0° (see Table 5.9).

In order to calculate the solution NMR chemical shifts, each conformer was placed in a large isolated box, which mimics the molecule in the gas state and the torsion angle C7-N-C1-C6 which

is responsible for the variation of the conformation is fixed. Then the structure was subjected to a GIPAW calculation to calculate the NMR shieldings. This was repeated for all the conformers, and the chemical shifts in solution were calculated by taking a weighted average of the respective chemical shifts for all the conformers.

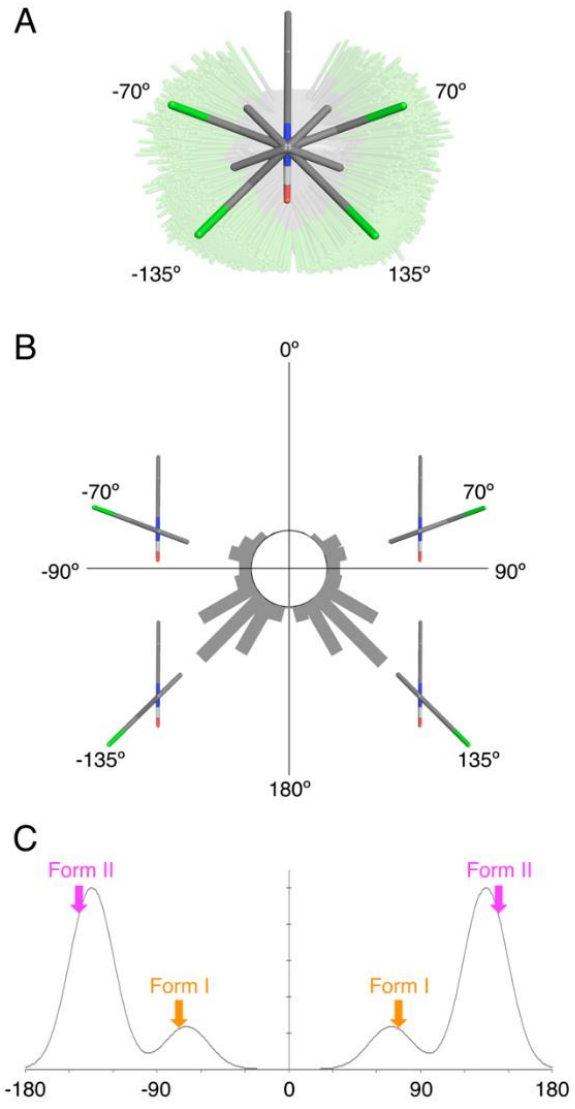

Figure 5.13: (A) Dynamic 3D structure of TFA with mean angle and its librations. (B) Circular histogram representing the distribution of the conformational population. (C) Graph representing the conformational distribution. This analysis was carried out by Drs Charles Blundell and Hugh Dannatt (C4X Discovery).

5b.6 Results and Discussion

Separate conformers were generated by setting the torsion angle C7-N-C1-C6 at 15° intervals using the base geometry (i.e., bond lengths, bond angles, and improper dihedrals) of both Form I and Form II. The chemical shifts were calculated for each conformer, as described in Section 5b.4. The calculated chemical shifts for all the solution conformers are presented in Tables 5.10, 5.11, and 5.12, and the variation of chemical shift with torsion angle are represented in Figures 5.14 and 5.15. The presented chemical shifts in Tables 5.10-5.12 are the mean calculated chemical shifts of the conformers generated using the geometry of high-resolution Form I and Form II.

Table 5.10: Mean calculated ^{1}H and ^{13}C chemical shifts using geometry symmetrised high-resolution structures of Form I and Form II of TFA varying the C7-N-C1-C6 torsion angle.

	The C7-N-C1-C6 torsion angle (°)							
	−180.00	−165.00	−150.00	−135.00	−120.00	−105.00	−90.00	−75.00
H1	4.83	4.85	4.82	4.80	4.77	4.75	4.73	4.77
H3	7.68	7.63	7.53	7.50	7.43	7.38	7.40	7.45
H4	5.90	5.93	5.87	5.82	5.77	5.73	5.72	5.78
H5	6.67	6.60	6.50	6.43	6.35	6.32	6.32	6.37
H6	7.22	7.30	7.15	6.78	6.15	5.45	5.05	5.25
NH	11.35	11.00	10.87	10.58	10.27	9.97	9.90	10.10
H2	6.93	6.92	6.72	6.55	6.32	6.22	6.17	6.15
H3	6.30	6.25	6.22	6.25	6.32	6.40	6.45	6.43
H4	6.03	6.07	6.08	6.18	6.30	6.43	6.50	6.43
H6A*	1.66	1.61	1.56	1.47	1.38	1.38	1.26	1.21
C1	170.32	170.38	170.37	170.35	170.40	170.42	170.33	170.22
C2	107.83	107.72	107.08	106.53	105.93	105.18	104.78	105.52
C3	133.52	132.93	132.68	132.38	132.03	131.70	131.65	131.95
C4	115.32	115.77	115.67	115.32	114.65	113.77	113.38	114.15
C5	135.22	134.68	134.40	134.28	134.30	134.27	134.30	134.37
C6	113.05	111.77	109.97	109.05	109.33	110.18	110.67	110.85
C7	146.28	145.78	145.95	147.13	149.18	150.93	151.37	150.05
C1	141.30	140.95	140.20	139.87	139.65	139.88	139.98	139.83
C2	110.62	110.93	113.85	118.38	123.70	127.62	128.25	124.92
C3	125.17	124.77	124.38	124.38	124.88	125.72	126.33	126.23
C4	120.58	121.17	122.23	123.80	125.70	127.55	128.50	127.38
C5	143.50	141.72	141.97	142.48	143.35	143.65	143.47	142.98
C6	126.27	125.88	127.17	129.98	134.03	138.13	140.48	138.25
C6A	8.50	9.10	8.72	8.72	8.88	9.02	8.92	9.23

Table 5.11: Mean calculated ^{1}H and ^{13}C chemical shifts using geometry symmetrised high-resolution structures of Form I and Form II of TFA varying the C7-N-C1-C6 torsion angle.

	The C7-N-C1-C6 torsion angle (°)							
	–60.00	–45.00	–30.00	–15.00	0.00	15.00	30.00	45.00
H1	4.80	4.78	4.80	4.80	4.75	4.80	4.80	4.80
H3	7.47	7.48	7.52	7.50	7.53	7.52	7.50	7.48
H4	5.82	5.85	5.85	5.87	5.82	5.85	5.87	5.83
H5	6.45	6.50	6.53	6.57	6.58	6.58	6.55	6.48
H6	5.42	5.63	5.90	6.23	1.75	6.23	5.88	5.62
NH	10.53	11.03	11.43	11.73	12.07	11.77	11.43	11.02
H2	6.05	6.02	6.00	5.97	6.03	5.97	5.97	6.05
H3	6.38	6.33	6.28	6.25	6.20	6.27	6.28	6.33
H4	6.32	6.23	6.12	6.05	6.03	6.07	6.13	6.22
H6A*	1.13	1.12	1.21	1.41	3.41	1.41	1.22	1.10
C1	170.22	170.43	170.67	170.80	170.88	170.82	170.67	170.42
C2	105.97	106.25	106.72	107.30	107.73	107.32	106.73	106.27
C3	131.97	131.83	131.80	131.97	132.58	131.95	131.77	131.83
C4	114.78	115.13	115.37	115.42	115.35	115.40	115.33	115.10
C5	134.10	133.68	133.35	133.28	133.83	133.27	133.30	133.68
C6	111.58	112.67	114.52	116.70	117.35	116.67	114.55	112.70
C7	147.95	146.33	145.20	144.52	144.52	144.53	145.20	146.32
C1	139.65	139.67	139.93	140.65	142.05	140.68	139.92	139.63
C2	121.78	119.88	118.98	119.02	119.82	119.03	118.95	119.78
C3	126.07	125.97	125.83	125.68	125.60	125.67	125.83	125.95
C4	125.55	123.78	122.43	121.63	121.50	121.65	122.42	123.80
C5	143.18	143.98	144.98	145.77	145.97	145.82	144.98	144.02
C6	133.75	128.87	124.18	120.28	118.02	120.30	124.20	128.88
C6A	11.30	13.77	15.87	17.52	18.63	17.55	15.85	13.77

Table 5.12: Mean calculated ^{1}H and ^{13}C chemical shifts using geometry symmetrised high-resolution structures of Form I and Form of TFA varying the C7-N-C1-C6 torsion angle.

The C7-N-C1-C6 torsion angle (°)									
·	60.00	75.00	90.00	105.00	120.00	135.00	150.00	165.00	180.00
H1	4.80	4.73	4.70	4.73	4.77	4.78	4.80	4.85	4.83
H3	7.45	7.43	7.38	7.40	7.43	7.47	7.53	7.63	7.68
H4	5.82	5.75	5.70	5.72	5.75	5.83	5.88	5.92	5.90
H5	6.45	6.37	6.30	6.32	6.37	6.43	6.50	6.60	6.67
H6	5.42	5.23	5.05	5.45	6.15	6.78	7.15	7.32	7.22
NH	10.52	10.10	9.90	9.97	10.25	10.55	10.87	11.00	11.35
H2	6.08	6.10	6.13	6.20	6.33	6.52	6.72	6.90	6.93
H3	6.38	6.45	6.47	6.43	6.32	6.25	6.22	6.25	6.30
H4	6.32	6.42	6.48	6.43	6.30	6.15	6.08	6.07	6.03
H6A*	1.13	1.19	1.26	1.31	1.36	1.48	1.54	1.66	1.66
C1	170.22	170.15	170.32	170.40	170.35	170.32	170.37	170.38	170.32
C2	105.92	105.43	104.77	105.20	105.88	106.55	107.10	107.70	107.83
C3	131.95	131.88	131.63	131.68	131.98	132.37	132.67	132.95	133.52
C4	114.73	114.10	113.35	113.73	114.60	115.30	115.65	115.77	115.32
C5	134.10	134.42	134.30	134.25	134.28	134.30	134.38	134.70	135.22
C6	111.52	110.82	110.68	110.18	109.33	109.07	109.95	111.75	113.05
C7	147.97	150.03	151.37	150.93	149.17	147.12	145.97	145.75	146.28
C1	139.65	139.78	139.97	139.87	139.62	139.88	140.20	140.92	141.30
C2	121.78	124.92	128.23	127.58	123.65	118.35	113.83	110.90	110.62
C3	126.05	126.20	126.35	125.70	124.87	124.38	124.35	124.73	125.17
C4	125.55	127.42	128.52	127.57	125.70	123.82	122.23	121.17	120.58
C5	143.18	142.97	143.48	143.68	143.33	142.43	141.98	141.73	143.50
C6	133.77	138.25	140.47	138.13	134.03	129.98	127.17	125.90	126.27
C6A	11.28	9.18	8.90	8.98	8.88	8.72	8.67	9.07	8.50

*The stated chemical shift for the methyl group correspond to the average chemical shift for the three protons.

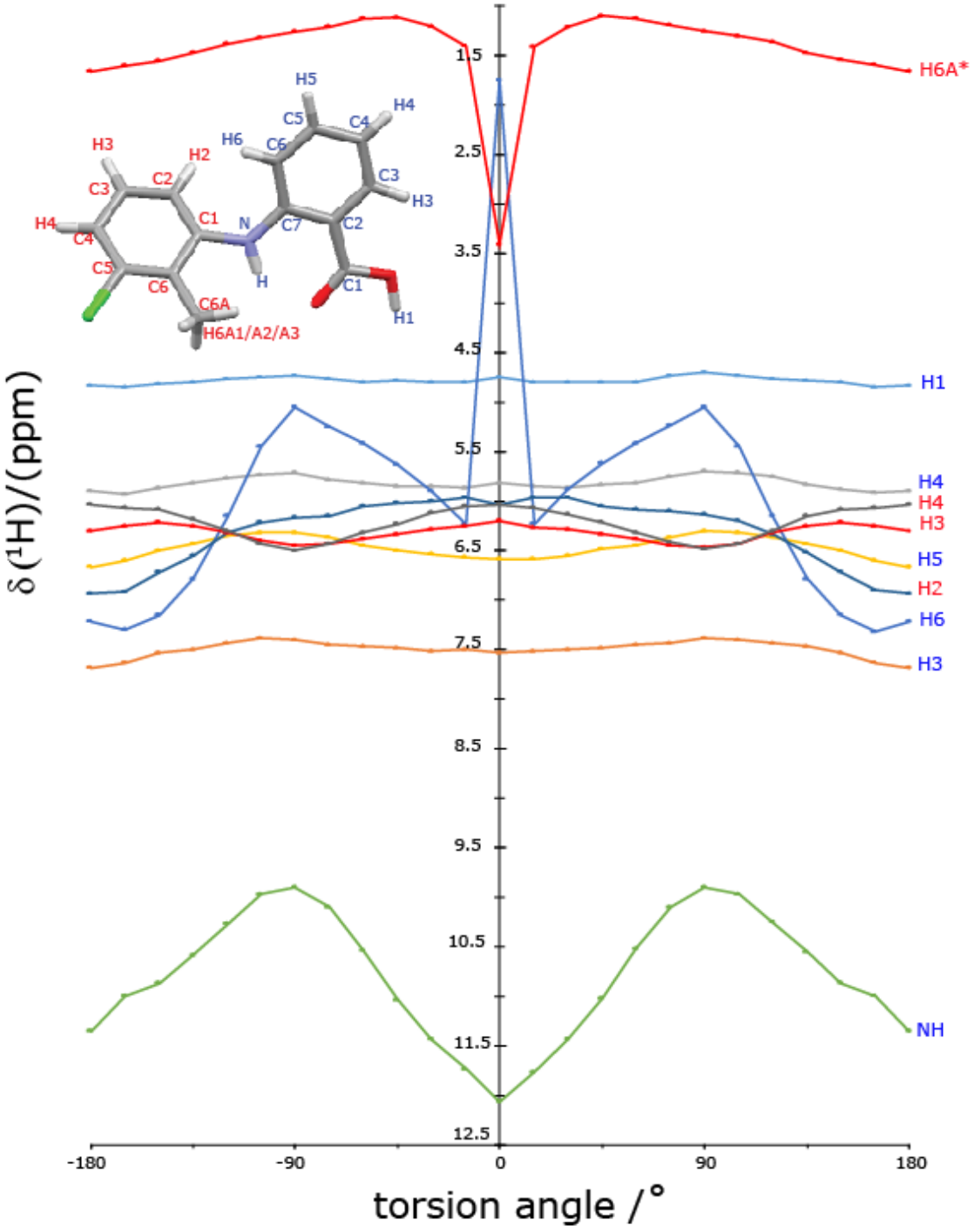

Figure 5.14: Variation of calculated ^{1}H chemical shifts for TFA with the torsion angle C7-N-C1-C6 (See Tables 5.10-5.12).

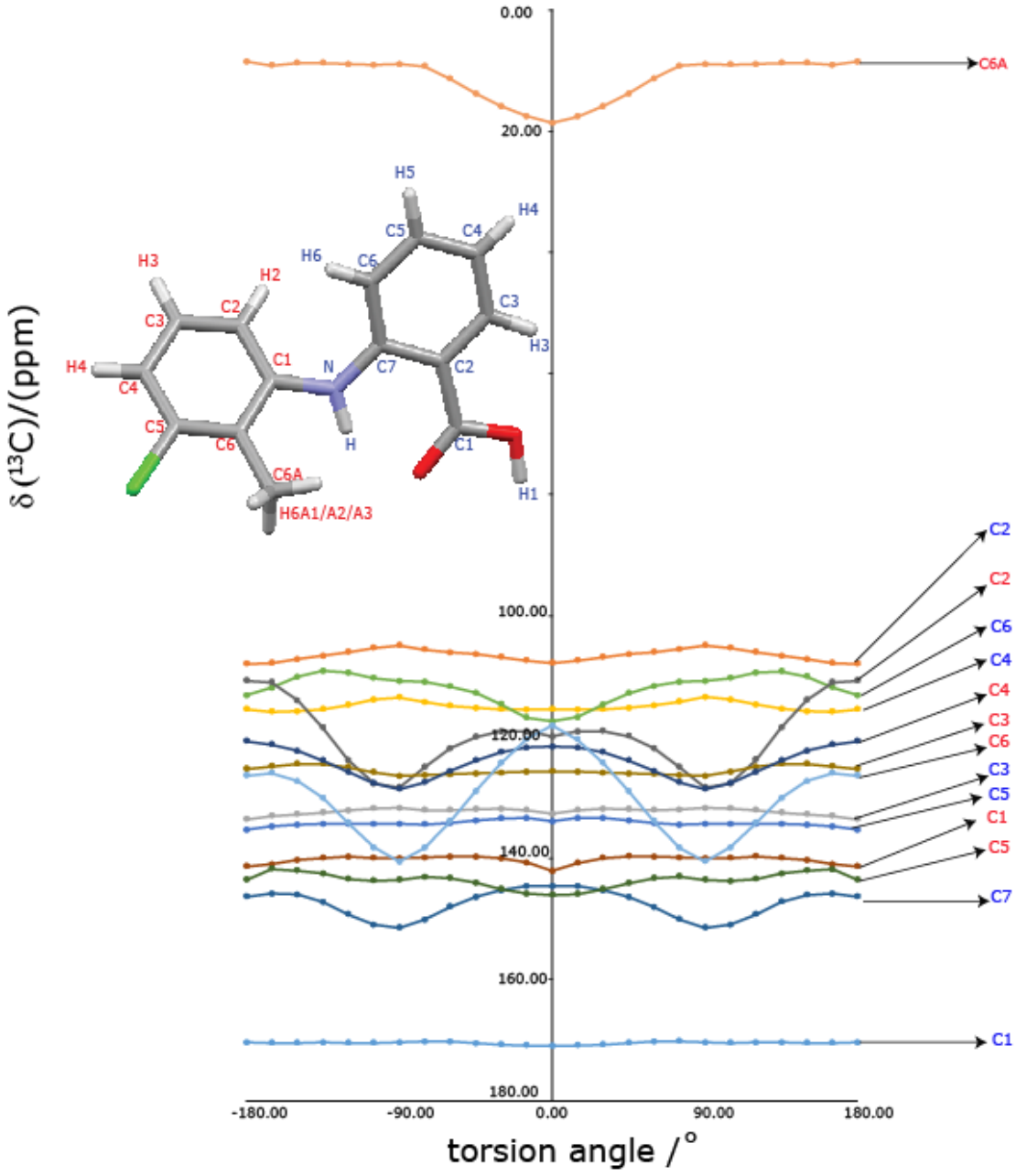

Figure 5.15: Variation of calculated ^{13}C chemical shifts for TFA with the torsion angle C7-N-C1-C6 (see Tables 5.10-5.12).

The ^{1}H and ^{13}C solid-state chemical shifts of Form I and Form II were determined from the ^{13}C CPMAS, and ^{1}H-^{13}C refocused INEPT spectra (see Figures 5.4 and 5.5) as described in Section 5a.5. The next step is to determine the calculated solid-state chemical shifts using the GIPAW approach, as described in Section 5a.2. The experimental and calculated ^{1}H, ^{13}C chemical shift values for both solution and solid forms are presented in Table 5.13. ^{1}H and ^{13}C solution NMR chemical shifts were obtained by C4X discovery. For Form III and Form IV, only calculated chemical shifts are presented. Note that average chemical shifts are taken since there are multiple conformations in the asymmetric unit (2 molecules for Form III and 3 molecules for Form IV). The conformations of the two molecules in the asymmetric unit of Form III have similar conformations as two of the three molecules in Form IV. Form V is not included in this study, due to its highly disordered nature[214]. Note that errors in experimental chemical shifts are calculated at one quarter of the observed linewidth of each resonance. For ^{13}C and ^{1}H in solid-state this approximates to ±0.1 and ±0.2 ppm , and for solution this is estimated to ±0.001 and ±0.02 ppm, respectively.

Table 5.13: Experimental and GIPAW calculated ^{1}H and ^{13}C chemical shifts (in ppm) for TFA in solution and for the solid-state forms.

Atoms	Experimentally measured δ(ppm)			GIPAW calculation				
	$\delta_{Solution\ expt}$	$\delta_{Solid\ expt}$		$\delta_{Solution\ calc}$	$\delta_{Solid\ calc}$			
	Solution[a] $CDCl_3$ ^{1}H±0.001 ^{13}C±0.02	Form I ^{1}H±0.2 ^{13}C±0.1	Form II ^{1}H±0.2 ^{13}C±0.1	Solution	Form I[b]	Form II[b]	Form III[c]	Form IV[c]
H1	[d]-	12.6	12.8	4.8	14.0	14.4	13.7	13.5
H3	8.043	8.4	7.0	7.5	8.0	6.9	8.0	7.7
H4	6.751	6.6	6.3	5.8	6.6	6.3	6.4	6.1
H5	7.330	6.1	6.3	6.4	5.9	6.4	4.8	4.3
H6	6.773	5.6	6.3	6.4	5.1	6.3	6.8	6.1
NH	9.188	9.0	9.2	10.5	9.7	10.1	10.7	9.8
H2	7.242	6.6	6.2	6.4	6.6	6.2	6.6	6.5
H3	7.148	5.6	6.1	6.3	5.4	6.0	5.6	4.8

H4	7.246	6.6	6.3	6.2	6.6	6.2	6.4	6.3
H6A[e]	2.335	1.2	1.9	1.4b	0.7[b]	1.5[b]	1.8b	1.0b
C1	172.75	175.2	175.7	170.3	176.3	176.5	175.9	175.4
C2	109.87	109.2	108.5	106.3	107.8	106.6	109.5	108.7
C3	132.48	134.9	132.9	132.2	135.8	133.3	134.1	133.2
C4	117.00	116.5	117.9	115.0	115.6	117.7	116.2	116.2
C5	135.34	136.9	136.2	134.3	137.5	136.9	137.6	136.4
C6	113.83	112.0	112.0	109.9	110.5	110.8	110.4	111.7
C7	149.40	150.4	147.3	147.8	148.8	145.0	148.9	149.1
C1	140.04	138.9	139.1	139.9	138.7	138.1	140.0	140.1
C2	123.64	127.8	116.8	119.8	126.8	115.2	122.6	124.7
C3	126.88	127.0	126.0	124.9	127.4	126.3	127.9	127.0
C4	126.26	129.4	123.3	124.5	129.8	123.5	126.4	125.8
C5	135.63	138.9	139.1	142.7	140.9	141.5	141.8	142.4
C6	132.20	136.8	126.1	131.7	138.2	126.4	132.1	134.6
C6A	15.20	15.4	14.9	9.1	12.2	12.5	13.5	12.5

[a]Solution NMR data were recorded by the C4X Discovery

[b] New high resolution structures are used for the calculation of Form I and Form II chemical shifts.

[b]For forms III and IV, the average over the two and the three molecules, respectively in the asymmetric unit cell is stated.

[c]Typically -OH proton does not appear in the solution NMR because it rapidly exchanged with the solvent.

[d]The stated chemical shift is the average chemical shifts of the three protons of the CH_3 group.

High-resolution structures of Form I and Form II were determined by Dr Charles Blundell (C4X Discovery, Personnel communication) to see whether this affects the calculated chemical shift. These high resolution structures are at ~0.5Å good enough to see the position of H atoms from the electron density compared to the original CSD structure. The NH group in the high resolution structure is moved slightly confirming the partial sp^2 character of N atom. Hence, these high resolution structures give lots of confidence in the geometries compared to the CSD published structures. It is clear from Table 5.14 that the difference in chemical shifts of the high-resolution structures of Form I and Form II are negligible compared to the previously published CSD structures KAXXA101 and KAXXAI.

Table 5.14: GIPAW calculated ^{1}H and ^{13}C chemical shifts of high resolution and published crystal structure of TFA Form I and Form II and their absolute difference.

Atoms	High resolution Form I	KAXXA101	Difference between the high resolution and KAXXAI01	High resolution Form II	KAXXAI	Difference between the high resolution and KAXXAI
H1	14.0	14.0	0.1	14.4	14.3	0.1
H3	8.0	8.0	0.0	6.9	6.3	–0.1
H4	6.6	6.6	0.0	6.3	6.3	0.0
H5	5.9	5.9	0.0	6.4	6.4	0.0
H6	5.2	5.1	0.0	6.3	6.4	0.0
NH	9.7	9.7	0.0	10.1	10.1	0.0
H2	6.6	6.5	0.0	6.2	6.2	0.1
H3	5.4	5.5	0.0	6.0	5.9	0.0
H4	6.6	6.6	0.0	6.2	6.2	0.0
H6A*	0.7	0.7	0.0	1.5	1.4	0.1
C1	176.3	176.2	0.1	176.5	176.5	0.0
C2	107.8	107.9	–0.1	106.6	106.7	–0.2
C3	135.8	135.8	0.0	133.3	133.5	–0.2
C4	115.6	115.7	–0.1	117.7	118.1	–0.4
C5	137.5	137.4	0.1	136.9	137	0.0
C6	110.5	110.2	0.2	110.8	111.0	–0.2
C7	148.8	148.6	0.2	145.0	145.2	–0.1
C1	138.7	138.6	0.0	133.3	133.5	–0.2
C2	126.8	126.7	0.1	115.2	115.1	0.2
C3	127.4	127.4	0.0	126.3	126.1	0.2
C4	129.8	129.7	0.1	123.5	123.5	–0.1
C5	140.9	140.9	0.0	141.5	142.0	–0.4
C6	138.2	138.0	0.2	126.4	126.4	0.0
C6A	12.2	12.4	–0.2	12.5	12.4	0.1

* The stated chemical shift is the average chemical shifts of the three protons of the CH_3 group.

These high-resolution structures were used as the base geometry for the generation of solution conformations and all subsequent calculations. To build the scoring function, experimentally measured change ($\Delta\delta_{exp}$) and the GIPAW calculated changes in chemical shift ($\Delta\delta_{calc}$) from solution to solid are presented in Table 5.15.

Table 5.15: Comparison of the experimental measured and DFT GIPAW calculated changes in NMR ^{1}H and ^{13}C (in ppm) chemical shifts for TFA upon passing from the solution state to the solid-state.

Atoms	Experimental[a,c]		GIPAW Calculated[b, c]								
	Form I	Form II	Form I	Form II	Form III			Form IV			
					1[d]	2[e]	Mean	1[f]	2[g]	3[h]	Mean
H1	-	-	9.2	9.6	9.2	8.6	8.9	8.6	8.6	8.8	8.7
H3	0.4	–1.0	0.5	–0.6	0.6	0.5	0.5	0.0	0.3	0.4	0.2
H4	–0.2	–0.5	0.8	0.5	0.6	0.5	0.5	0.3	0.4	0.4	0.3
H5	–1.2	–1.0	–0.5	–0.1	–1.5	–1.8	–1.6	–1.7	–2.4	–2.2	–2.1
H6	–1.2	–0.5	–1.2	–0.1	0.4	0.4	0.4	–0.5	–0.1	–0.3	–0.3
NH	–0.2	0.0	–0.8	–0.4	0.0	0.4	0.2	–0.6	–0.7	–0.9	–0.7
H2	–0.6	–1.0	0.1	–0.3	0.4	–0.1	0.1	–0.5	0.5	0.2	0.0
H3	–1.5	–1.0	–0.9	–0.3	–1.1	–0.2	–0.7	–0.5	–1.6	–2.4	–1.5
H4	–0.6	–0.9	0.3	–0.1	0.1	0.1	0.1	–0.3	0.5	–0.1	0.0
H6A*	–1.1	–0.4	–0.7	0.1	0.4	0.4	0.4	–0.5	–0.3	–0.5	–0.5
C1	–0.4	0.1	6.0	6.2	5.7	5.5	5.6	5.3	4.6	5.4	5.1
C2	–3.3	–4.0	1.5	0.3	3.8	2.5	3.2	2.1	0.9	1.2	0.9
C3	–0.4	–2.4	3.6	1.1	2.3	1.5	1.9	0.8	0.9	1.2	0.9
C4	–3.2	–1.8	0.7	2.7	1.8	0.7	1.2	0.4	1.8	1.6	1.3
C5	–1.2	–1.9	3.2	2.6	2.7	3.9	3.3	2.5	2.5	1.2	2.1
C6	–4.5	–4.5	0.6	0.9	2.3	–1.2	0.5	0.3	2.6	2.5	1.8
C7	–1.7	–4.8	0.9	–2.8	1.4	0.8	1.1	1.4	1.4	1.0	1.2
C1	–3.9	–3.7	–1.2	–1.8	0.4	–0.3	0.0	–0.5	0.4	0.8	0.2
C2	1.4	–9.6	7.0	–4.5	2.3	3.3	2.8	6.0	5.9	2.9	4.9
C3	–2.7	–3.7	2.5	1.4	2.8	3.2	3.0	1.4	2.6	2.4	2.1
C4	0.4	–5.7	5.3	–1.0	1.8	2.0	1.9	1.1	1.5	1.4	1.3
C5	0.5	0.7	–1.9	–1.2	0.2	–2.0	–0.9	0.7	0.2	–1.8	–0.3
C6	0.9	–8.8	6.5	–5.3	–0.1	0.9	0.4	4.0	2.6	2.0	2.9
C6A	–2.5	–3.0	3.1	3.4	3.6	5.2	4.4	3.6	3.7	2.9	3.4

[a]Experimentally measured change (ppm) $\Delta\delta_{expt} = \delta_{expt\ solid} - \delta_{expt\ solution}$.

[b]GIPAW calculated change (ppm) $\Delta\delta_{calc} = \delta_{calcsolid} - \delta$ isolated solution.

[c] Individual experimental and GIPAW calculated chemical shifts are listed in Table 5.13.

[d-h]represents each molecule in the asymmetric unit of the full crystal structure of Form III and Form IV.

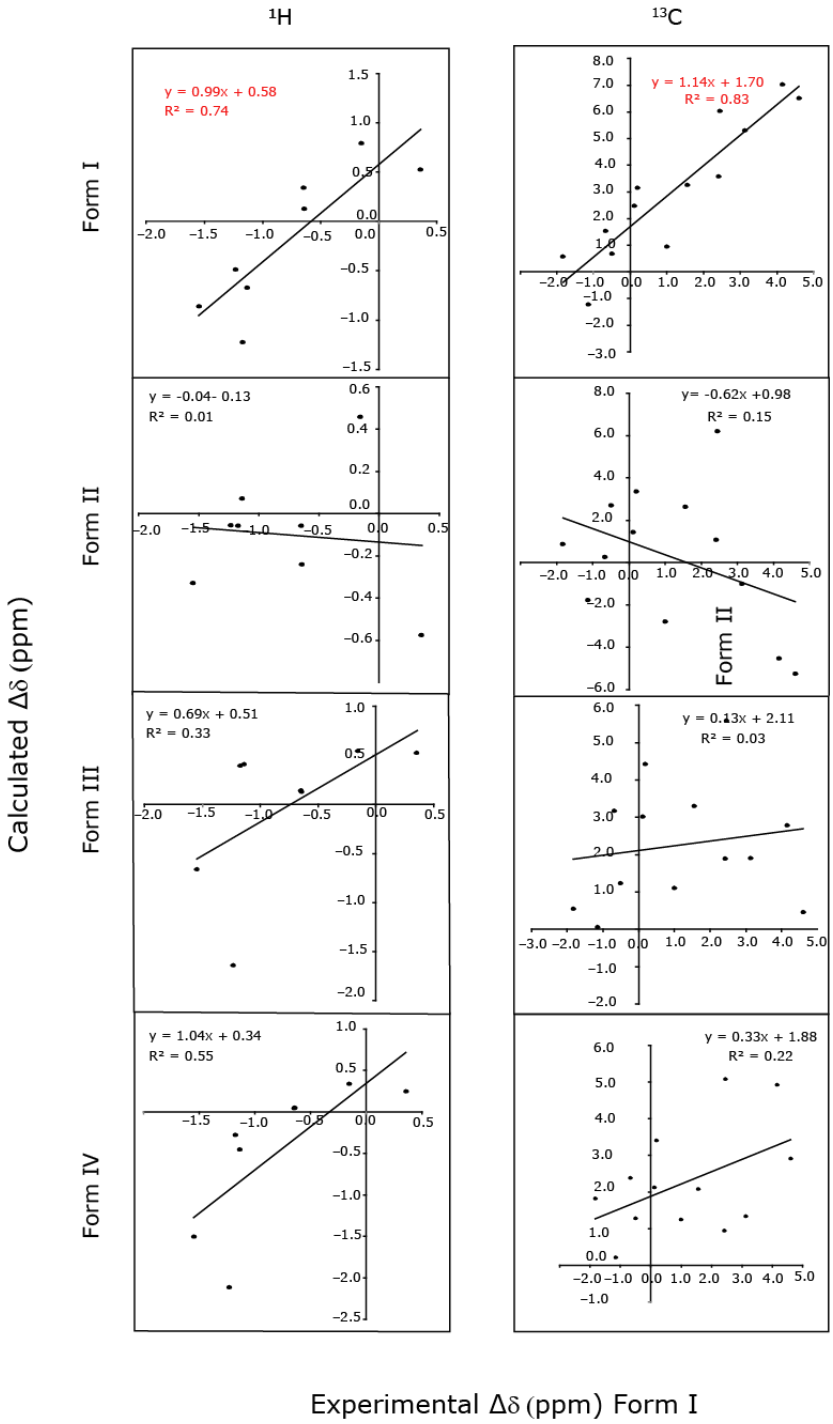

Figure 5.16: Experimentally measured changes ($\Delta\delta_{experimental}$) for Form I against the calculated changes ($\Delta\delta_{calculated}$) for Form I, II, III, and IV of TFA for both ^{1}H and ^{13}C chemical shifts showing how well the scoring function discriminates Form I (R^2 = 0.74 and 0.83, respectively) from the other three forms. The error bars for the experimental chemical shifts were estimated to be very small and are omitted.

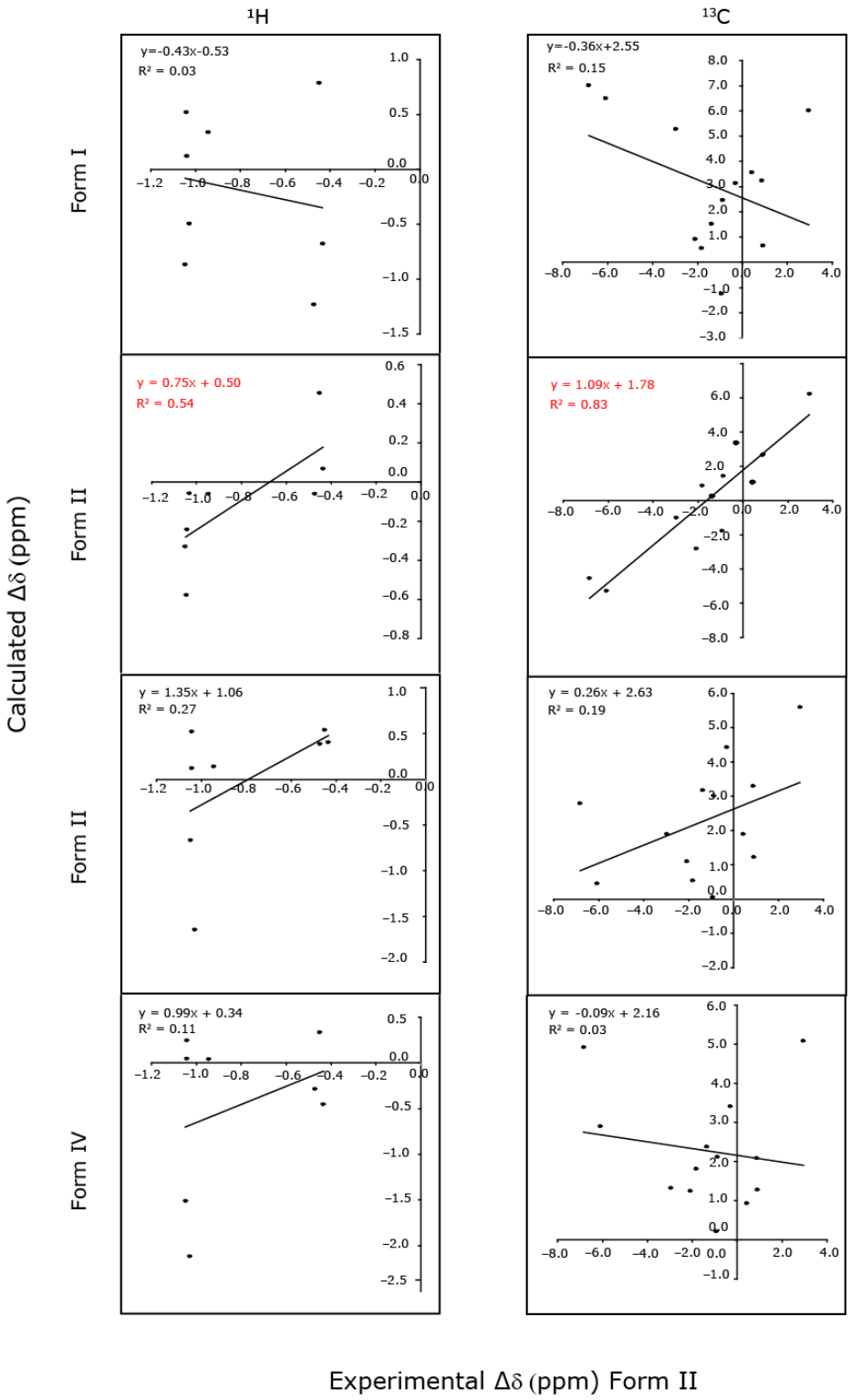

Figure 5.17: Experimentally measured changes ($\Delta\delta_{experimental}$) for Form II against the calculated changes ($\Delta\delta_{calculated}$) for Form I, II, III, and IV of TFA for both ^{1}H and ^{13}C chemical shifts showing

how well the scoring function discriminates Form II (R^2 =0.54 and 0.83, respectively) from the other three forms.

In order to investigate how well the scoring function discriminates different forms of a crystal structure, our approach is to plot $\Delta\delta_{experimental}$ against $\Delta\delta_{calculated}$. The data in each plot were then fitted using a linear function, and the goodness of fit was determined. To obtain a good fit, the chemical shift changes for NH was removed from the ^{1}H plots, because it is was clearly residual, probably due to the solvent exchange affecting the solution chemical shift. In the same way, C5 was removed from the ^{13}C plots because the calculated chemical shift is apparently inaccurate due to the Cl attached to it. Figure 5.16 shows plots of $\Delta\delta_{experimental}$ of Form I against $\Delta\delta$calculated for Forms I, II, III, and IV. From the figure, it is apparent that the ^{1}H and ^{13}C experimental changes of Form I fit well with calculated changes of Form I with an R^2 value of 0.74 and 0.83 respectively, whereas the correlations are inadequate for all the other three forms.

Similarly, Figure 5.17 plots $\Delta\delta_{experimental}$ of Form II against the calculated changes in chemical shift of Form I, II, III, and IV. The best fit is between the calculated changes in Form II against the experimental changes in Form II with an R^2 value of 0.54 and 0.83 for ^{1}H and ^{13}C. These results indicate that the scoring function can distinguish between forms using the experimental and calculated chemical shifts.

Table 5.16: The goodness of the fit R^2 from the scoring function plots of both Form I and Form II of TFA on passing from solution to solid (see Figure 5.16 and 5.17).

$\Delta\delta_{calculated}$	$\Delta\delta_{experimental}$	
	Form I	Form II
^{1}H		
Form I	0.74	0.03
Form II	0.01	0.54
Form III		
mean	0.33	0.27
1	0.42	0.26

2	0.20	0.25
Form IV		
mean	0.55	0.11
1	0.41	0.11
2	0.46	0.08
3	0.60	0.12
^{13}C		
Form I	0.83	0.16
Form II	0.16	0.83
Form III		
mean	0.02	0.19
1	0.01	0.32
2	0.11	0.08
Form IV		
mean	0.22	0.03
1	0.44	0.09
2	0.19	–0.14
3	0.00	0.08

The highlighted red values in Table 5.16 implies that the ^{1}H and ^{13}C experimentally measured chemical shift changes of Form I only fit with calculated changes of Form I under the scoring function. Likewise, experimental changes for Form II fit only with the calculated changes of Form II chemical shifts. Thus, the scoring function provides a way for ranking crystal structure by

discriminating the correct crystal structure from several conformationally similar structures, with ^{13}C being observed to be the best nucleus for discriminating structure.

5b.6.1 What Happens if we do not have Calculated and Experimental Solution Chemical Shifts?

Figure 5.18 and 5.19 shows the calculated chemical shifts of all the four forms against the experimental solid-state chemicals shifts of Form I and Form II. It is clear from the figure that it is not plausible to discriminate between forms using solid-state chemical shifts alone. Hence, a key observation is that the solution NMR chemical shifts have to be included to distinguish forms.

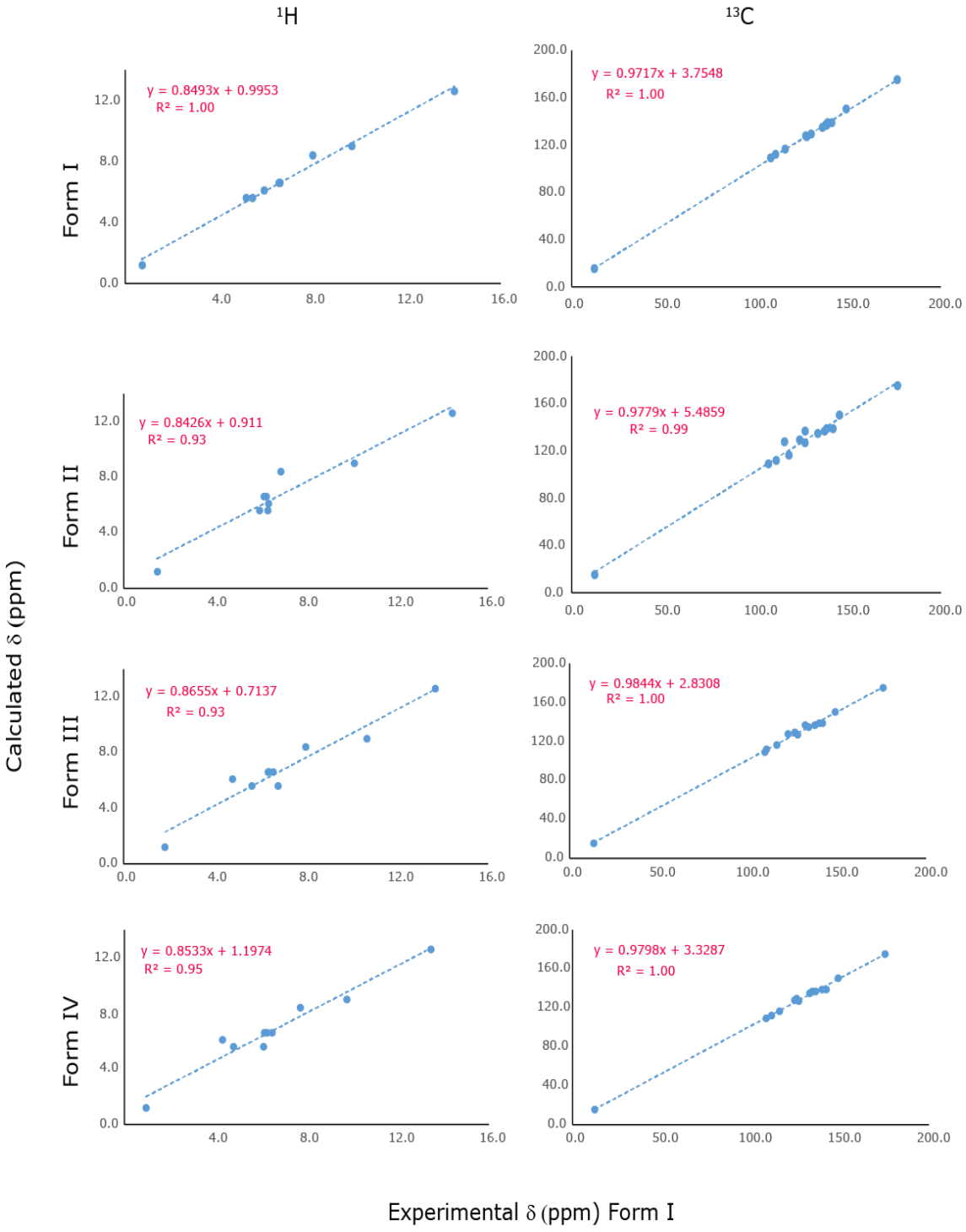

Figure 5.18: $\delta_{\text{Solid expt}}$ for Form I against $\delta_{\text{Solid calc}}$ for Forms I, II, III, and IV of TFA for both ^{1}H and ^{13}C.

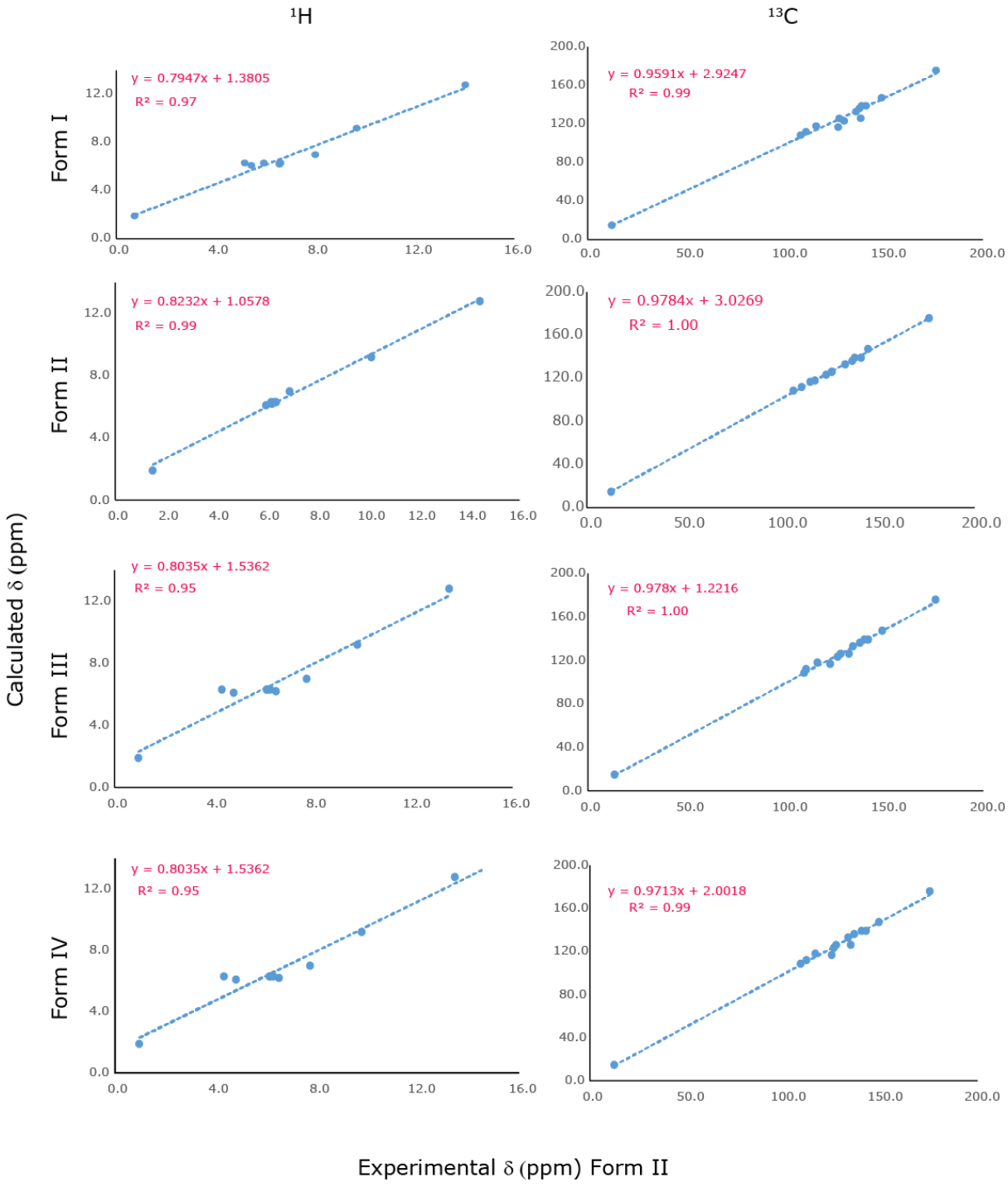

Figure 5.19: $\delta_{\text{Solid expt}}$ for Form II against $\delta_{\text{Solid calc}}$ for Forms I, II, III, and IV of TFA for both ^{1}H and ^{13}C.

5b.6.2 Does Packing have any Effect on the Scoring Function?

The contribution of conformation and packing effect on the chemical shift is proved by calculating the chemical shifts of an isolated molecule $\delta_{\text{isolated calc}}$ for all the four forms so that the effect of intermolecular interactions are removed. The $\delta_{\text{solidccalc}}$ in Equation 5.2 is now replaced with $\delta_{\text{isolated calc}}$. Therefore Equation 5.2 now becomes:

$$\Delta\delta_{\text{exp}erimental} = \delta_{solid\,\text{exp}} - \delta_{solution\,\text{exp}}$$
$$\Delta\delta_{calculate-isolated} = \delta_{isolatedsolid} - \delta_{solutioncalc} \quad . \qquad (5.3)$$

For example, Figure 5.20 represents the experimentally measured changes of Form I against the changes in the isolated chemical shift for isolated crystal conformation of Form I, II, III, and IV. Table 5.17 presents the R^2 values on passing from solution to solid state for experimentally measured changes of Form I and Form II against the calculated isolated crystal conformations of Form I, II, III, and IV. It is evident from the table that the plots for ^{13}C can still discriminate Form I ($R^2 = 0.46$) and Form II ($R^2 = 0.78$) from the other forms, whereas plots for ^{1}H fail to discriminate the correct form. This implies that the ^{1}H chemical shift is more sensitive to packing, whereas the ^{13}C chemical shift is more sensitive to conformation. However, it is still possible to discriminate forms through the scoring function even, if packing effects are removed as stated in Section 5b.1.

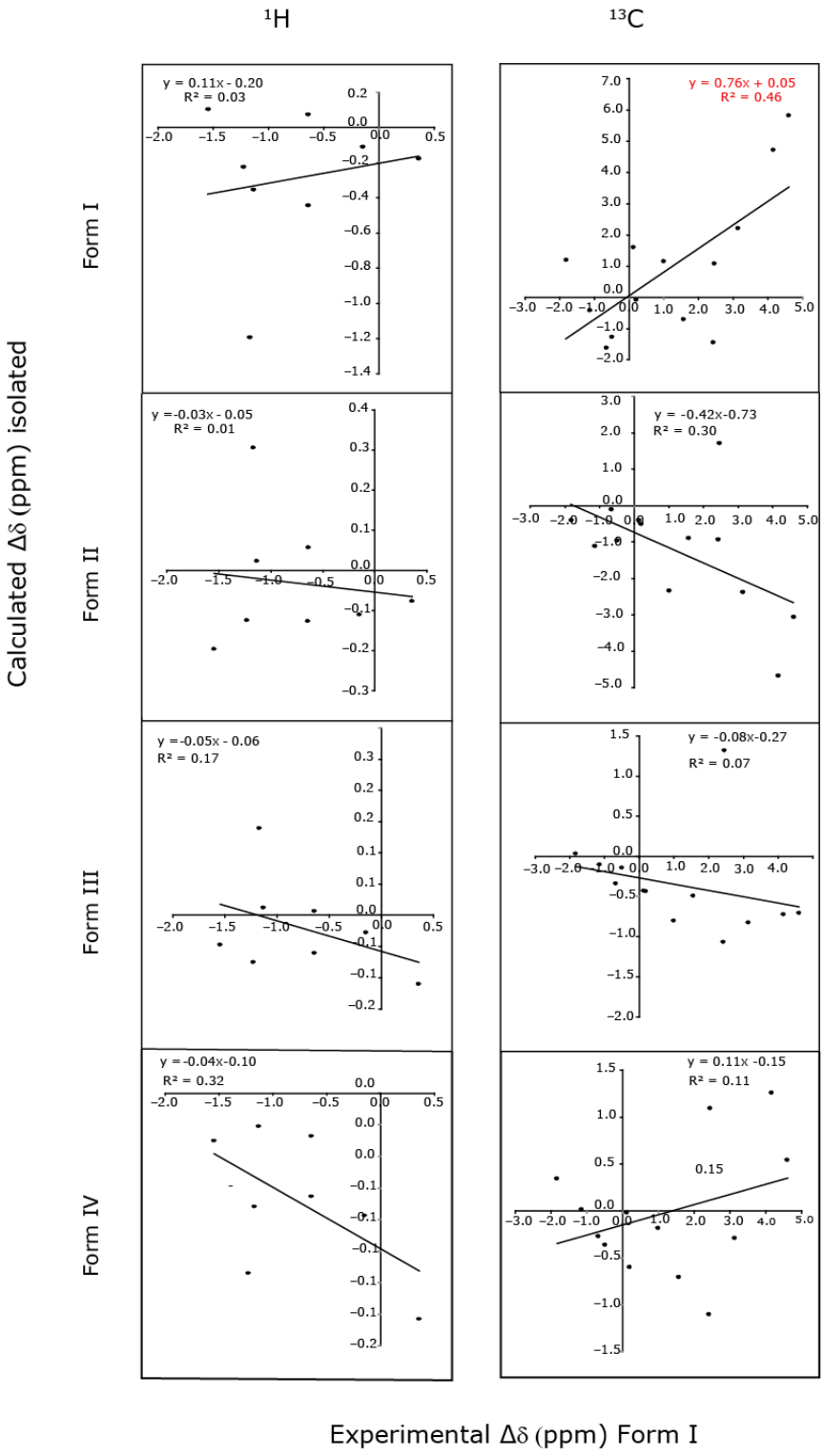

Figure 5.20: Plots of experimentally measured changes ($\Delta\delta_{experimental}$) for Form I against the calculated changes in the chemical shifts for isolated crystal conformations ($\Delta\delta_{\ isolated\ calculated}$) for Form I, II, III, and IV of TFA.

Table 5.17*:* Fit parameter (R^2) from graphs of $\Delta\delta_{Calculated\text{-}Isolated}$ against $\Delta\delta_{Experimental}$ (i.e., with $\delta_{Solid\ calc}$ replaced with $\delta_{Isolated\ calc}$, a calculation for an isolated molecule extracted from the crystal structure) on passing from solution to solid state for combinations of calculated (Form I, II, III and IV) and experimentally measured (Form I and II) changes in chemical shift for isolated crystal conformations.

$\Delta\delta_{calculated}$	$\Delta\delta_{experimental}$	
	Form I	Form II
^{1}H		
Form I	0.03	0.23
Form II	0.01	0.26
Form III		
mean	0.17	0.41
1	0.40	0.37
2	0.00	0.33
Form IV		
mean	0.32	0.10
1	0.40	0.30
2	0.06	0.11
3	0.01	0.06

^{13}C		
Form I	0.46	0.64
Form II	0.30	0.78
Form III		
mean	0.07	0.30
1	0.01	0.27
2	0.24	0.09
Form IV		
mean	0.11	0.50
1	0.01	0.42
2	0.42	0.55
3	0.05	0.10

5b.6.3 Can we Predict the Conformation without the Crystal Structure?

To investigate whether this scoring method can predict conformation without a crystal structure, ^{13}C chemical shifts for isolated conformations with torsion angle C6 - C1 - N - C7 varied at 15° intervals and calculated their changes in chemical shift, giving a set of $\Delta\delta_{Calculated\text{-}Isolated\ conformation\ at\ specific\ 15°\ angle}$ (from Tables 5.10-5.12) are plotted against the experimentally measured chemical shifts (from Table 5.15) of Form I and Form II. Note that now $\delta_{Solid\ calc}$ in Equation 5.2 is replaced by $\delta_{Isolated\ conformation\ at\ specific\ 15°\ angle}$ for each 15° angle. The respective fit parameters (slope m, and coefficient of determination R^2 values) were then determined as before. Note that it has already shown that the chemical shift does change with conformation (see Tables 5.10 –5.12 and Figures 5.14, and 5.15)

Table 5.18: Fit parameters (slope m and R^2 values) for isolated conformation for Form I and Form II experimental ^{13}C chemical shift data. Conformations differ by 15° intervals at torsion angle C6 - C1 - N - C7.

Torsion/ °	Form I R^2	Form I m	Form I R^2*sign(m)	Form II R^2	Form II m	Form II R^2*sign(m)
–180	0.64	–1.32	–0.64	0.61	0.97	0.61
–165	0.65	–1.24	–0.65	0.69	0.96	0.69
–150	0.57	–0.77	–0.57	0.78	0.68	0.78
–135	0.30	–0.17	–0.30	0.75	0.20	0.75
–120	0.60	0.50	0.60	0.70	–0.41	–0.70
–105	0.55	1.04	0.55	0.79	–0.94	–0.79
–90	0.55	1.25	0.55	0.79	–1.13	–0.79
–75	0.52	0.82	0.52	0.79	–0.76	–0.79
–60	0.10	0.16	0.10	0.44	–0.25	–0.44
–45	0.30	–0.49	–0.30	0.09	0.20	0.09
–30	0.44	–1.09	–0.44	0.20	0.56	0.20
–15	0.47	–1.58	–0.47	0.21	0.80	0.21
0	0.46	–1.84	–0.46	0.22	0.95	0.22
15	0.48	–1.6	–0.48	0.22	0.82	0.22
30	0.44	–1.1	–0.44	0.21	0.57	0.21
45	0.29	–0.5	–0.29	0.09	0.21	0.21
60	0.11	0.17	0.11	0.44	–0.25	–0.44
75	0.53	0.84	0.53	0.80	–0.77	–0.80

90	0.56	1.28	0.56	0.80	–1.15	–0.80
105	0.57	1.07	0.57	0.71	–0.95	–0.71
120	0.62	0.51	0.62	0.76	–0.41	–0.76
135	0.31	–0.17	–0.31	0.79	0.21	0.79
150	0.58	–0.75	–0.58	0.79	0.69	0.79
165	0.66	–1.26	–0.66	0.70	0.98	0.70
180	0.66	–1.35	–0.66	0.62	0.98	0.98

The higher R^2 value with positive slope (m) shows a reasonable fit with experimental data for a given conformation. In order to find the best conformation, the correlation coefficient, *r* is determined from the trial structures, by taking the square root of R^2 *sign(m) from the ^{13}C plots and are plotted against the torsion angle as shown in Figure 5.21. The correlation co-efficient is the measure of linear relationship between two variables. The conformations which fit best with the experimental data are those which have the highest points in the graph. From Figure 5.21, it is clear that conformations which fit best with the experimental Form I are 75° and 120° and with experimental Form II are 135° and 180°. The torsion angles observed in Form I (±74.9°) and Form II (±142.6°) do indeed fall in these ranges. This implies that the conformation of a crystal structure can be predicted using solid-state and solution NMR data.

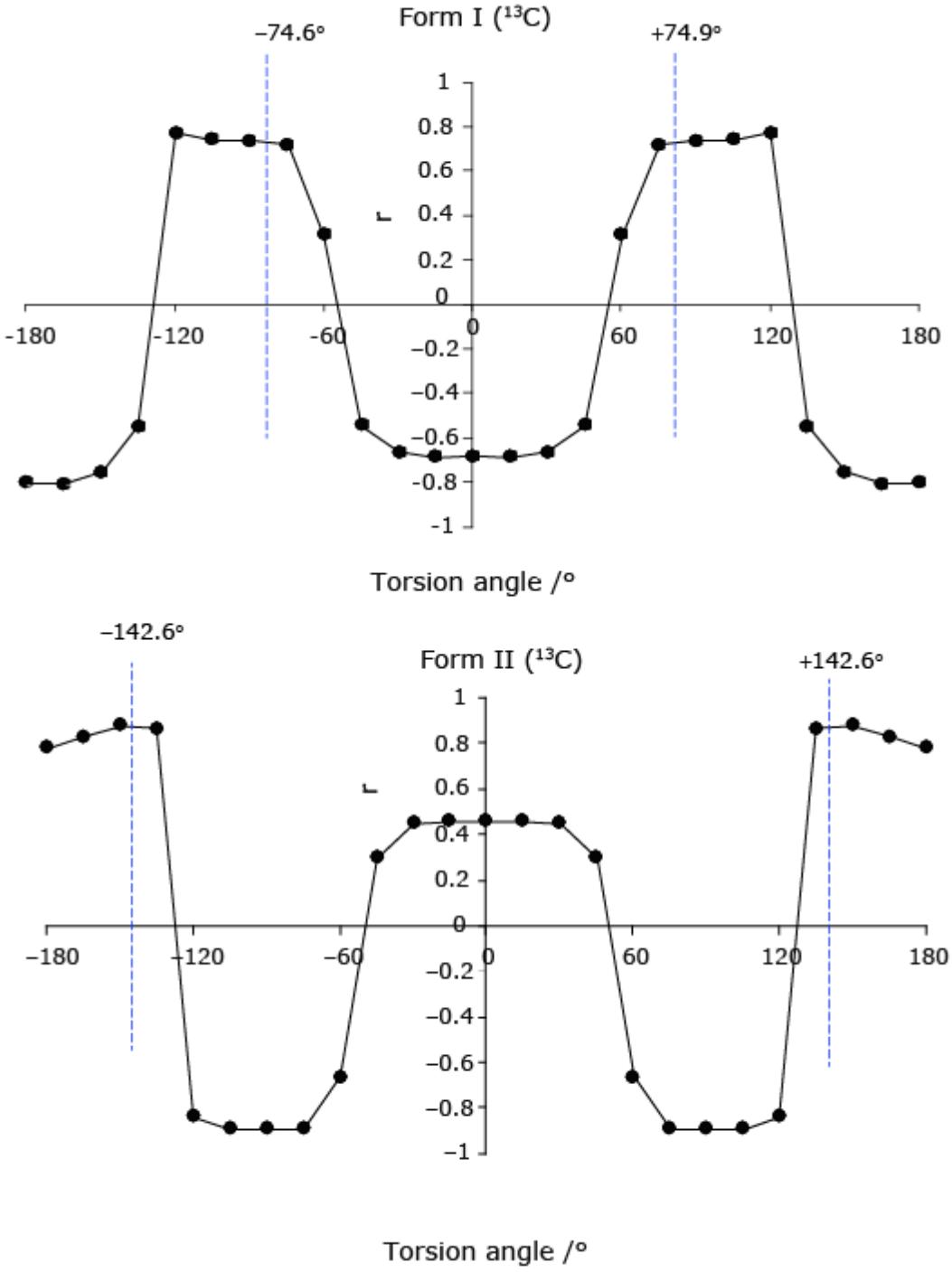

Figure 5.21: Correlation co-efficient, *r*, for ^{13}C against the torsion angle to find the best trial structure for both Form I and II of TFA.

5b.7 Conclusions

This work was done in collaboration with Drs Leslie Hughes and Helen Blade at AstraZeneca and Drs Charles Blundell, Hugh Dannatt, and Duncan Crick at C4X Discovery to create a robust scoring function by combining solution and solid-state NMR data, and first principle DFT calculations for analyzing polymorphs and solving crystal structures. The scoring function was successfully tested on four polymorphs of tolfenamic acid, of which Form II, III and IV have conformational similarities. To establish this scoring function, we measured ^{1}H and ^{13}C experimental solid-state chemical shifts for Form I and Form II ($\delta_{Solid\ expt}$) and the corresponding solution-state NMR chemical shifts ($\delta_{Solution\ expt}$). Similarly, the NMR chemical shifts were calculated for both TFA in solid ($\delta_{Solid\ calc}$) and in solution ($\delta_{Solution\ calc}$), using the DFT GIPAW approach. We have then shown that a good correlation exists between calculated ($\Delta\delta_{Calculated}$) and measured ($\Delta\delta_{Experimental}$) changes in chemical shifts between TFA in solution and the solid-state, to clearly distinguish the polymorphs from each other. For example, the experimental changes (solution and solid-state) of Form I agrees well with the calculated changes (solution and solid-state) of Form I, whereas the correlation of experimental changes of Form I with the calculated changes of the other three forms were very poor.

It is also demonstrated that calculated and experimental solid-state NMR chemical shifts alone cannot differentiate polymorphs from each other; hence, solution NMR data (both experimental and calculated) is essential to achieve excellent discrimination.

This novel approach also provides a way to predict the conformation of a new polymorphic form in the absence of a crystal structure, and thus, this approach is suitable for many cases where crystal structure cannot be generated. Moreover, we have shown that the scoring function can discriminate forms even if the packing effects are removed and ^{13}C seems to be the most discriminating nucleus.

This scoring function can be used in combination with tools like CSP and other techniques like PXRD to solve intractable crystal structures. One can use the scoring function at the beginning of a CSP study to predict the most favorable conformation of a crystal structure; this reduces the number of candidate structures. The scoring function can also be used for a second time to identify the correct structure from the CSP predicted structure by incorporating experimental NMR data. Therefore, the combination of experimental and DFT calculated chemical shifts could considerably simplify the analysis of a large pool of candidate structures.

Note that this method works only in cases where the chemical shifts are sensitive to conformational changes arising from the change in torsion angle. The findings from this particular study can be a valuable addition to the emerging field of NMR crystallography and crystal structure prediction.

Chapter 6: Solid-State NMR Characterisation of iPMPA Loaded SBA-15.

6.1 Introduction

Since their discovery during the 1990's[215-217], mesoporous silica materials have gained much recognition due to their ordered pore structure, high surface areas[218-219], and adjustable pore diameters. The capability to functionalise these mesoporous silicas with different organic functional groups has increased their application in pharmaceuticals[220-221], catalysis[222-224], sensor design[225-227], chromatography[228], separation[229-230], nuclear industry[231-232], and in diverse areas such as electronic devices[233-234], environmental protection[235-236], and bioanalysis[237-238]. Numerous studies have been carried out on mesoporous silica functionalised in acid catalysed reactions with organic groups such as amines[229], carboxylic acids[239-241], phosphonic acids[242-245], and sulfonic acid[246-247]. Such acid functionalised mesoporous silica materials are good solid supports for proton conductivity in fuel cells[248-250]. Functionalisation may be performed either by co-condensation or via grafting of the organic groups into the surface silica[251-254]. SBA-15 has received considerable attention among all the mesoporous silica due to its hexagonal pores with a two-dimensional array, where the diameter varies from 5 to 30 nm depending upon the synthetic method[255-256]. The properties of functionalised mesoporous silica vary according to the nature and concentration or loading of the organic group and its interaction with the surface and organic groups themselves[255].

In the Chapter, we have investigated the local environment of SBA-15 loaded with isopropyl methyl phosphonic acid (iPMPA) using magic-angle spinning (MAS) solid-state NMR spectroscopy. iPMPA is a simulant of isopropyl methylphosphonofluoridate, otherwise known as sarin, one of the many nerve agents accountable for destruction in numerous countries[257]. Nerve agents are potent acetylcholinesterase active agents which cause vomiting of blood and choking due to their organophosphorus structure. On hydrolysis, sarin produces iPMPA and hydrofluoric acid and slowly converts into methyl phosphonic acid through the loss of isopropanol[258]. The structures of sarin and iPMPA are depicted in Figure 6.1a and 6.1b, respectively. iPMPA is a well-known contaminant of the groundwater at the Rocky Mountain Arsenal due to the production of sarin from 1953 to 1957[257-258]. Bossle *et al*. have identified the C-P bond which is highly resistant to thermal decomposition, hydrolysis, and chemical decomposition[259] and Munno *et al.* reported that iPMPA has a half-life of 1,990 years at a pH of 1[258]. It is essential to understand the behaviour and interaction of iPMPA with soil, thus motivating this study of the synthesised iPMPA adsorbed on SBA-15.

Solid-state NMR has been widely applied for the characterisation of organic group functionalised silica materials[247]. ^{13}C and ^{29}Si magic angle spinning (MAS) NMR has been used to confirm the presence of the organic moiety and to probe the silica network in systems like SBA-15 containing

primary amines and sulfonic acid[260], ibuprofen[261], 3-((3-(trimethoxysilyl)propyl)thio)propane-1-sulfonic acid, and propylphosphonic acid[255].

Phosphonic acid is amphoteric in nature; hence, it can act both as a hydrogen bond acceptor and the donor through the P=O or P−OH bond. For instance, Lyssenkko *et al.* reported that the P=O moiety could form up to three hydrogen bonds at the same time in the crystal state[262]. These interactions can be easily probed using ^{1}H and ^{31}P MAS NMR. It is well known that higher proton chemical shifts are observed for acidic protons involved in hydrogen bonding depending on the strength of hydrogen bonds[100]. For instance, ^{1}H chemical shifts of 11.8 and 17.4 ppm have been reported for hydrogen-bonded carbamic acid in amine functionalised SBA-15[263], and for the proton involved in intra ligand hydrogen bonding in diethyl (2-oxo-2((3-(triethoxysilyl)propyl)amino)ethyl) phosphonate functionalised SBA-15[264], respectively. Aliev *et al.* were the first to report the synthesis of phosphonic acid or phosphonate functionalised mesoporous silica and its characterisation using solid-state NMR techniques. Two peaks are observed in the ^{31}P spectra of the phosphonic acid functionalised mesoporous silica. The higher chemical shift (δ = 34 ppm) was assigned to free phosphonic acid, while the resonance at 23 ppm was assigned to phosphonic acid engaged in hydrogen bonding with the surface Si-OH groups of the mesoporous silica[242]. Following this, various researchers have carried out studies of different types of phosphonic acid functionalised mesoporous silica, notably SBA-15[243, 245, 255-256, 265-269]. Pan *et al.*[268] confirmed Aliev *et al.*'s observation by incorporating DFT calculations, whereas Lee *et al.*[270] hypothesised that the lower chemical shift is due to the formation of a phosphonic acid anhydride.

In contrast, Bibent *et al.*[255] speculated that the lower chemical shift peak is characteristic of phosphonic acid groups engaged in hydrogen bonding through P=O to the adjacent phosphonic acid and not with the surface Si− OH. Recently, Uribe *et al.* investigated acetamide diethyl phosphonate functionalised SBA-15, which is an excellent solid-state candidate for the adsorption of actinides and lanthanides, using single pulse ^{1}H NMR, and ^{31}P–^{31}P Double Quantum- based Dipolar Recoupling Effects Nuclear Alignment Reduction (DQ-DRENAR)[271] NMR to probe the dipolar coupling between the phosphorus atoms. Two distinct resonances were observed in the ^{31}P MAS NMR spectra at 23 ppm and 15 ppm, where the lower chemical shift was assigned to the deprotonated P−O^{-}which then forms either P−O−H····O-P or P-O−H····O−Si type hydrogen bonds. The DQ-DRENAR method revealed that the deprotonated phosphonic acid ligand engaged in hydrogen bonding has a higher ^{31}P–^{31}P dipolar coupling as compared to the free phosphonic acid ligand[264, 272].

As noted above, most of the phosphonic acid functionalised mesoporous silica prepared to date have employed either co-condensation or post-synthesis grafting techniques for the functionalisation. Both methods connect the organic groups covalently to the silica network[273] . Here, we have prepared iPMPA loaded mesoporous silica samples using a facile method, where the organic groups are connected to the surface silanol through hydrogen bonding interactions. The structure of iPMPA and Sarin is shown in Figure 6.1. These samples constitute an excellent model system for understanding the binding of iPMPA to a soil surface. This Chapter presents a solid-state MAS NMR study of iPMPA adsorbed SBA-15 using one and two-dimensional techniques, notably heteronuclear experiments involving ^{1}H, ^{13}C, ^{29}Si, and ^{31}P to provide insight into local order and the interactions. The relative mobility and dynamic nature of the phosphonic acid within the mesoporous silica are probed using MAS NMR spectroscopy.

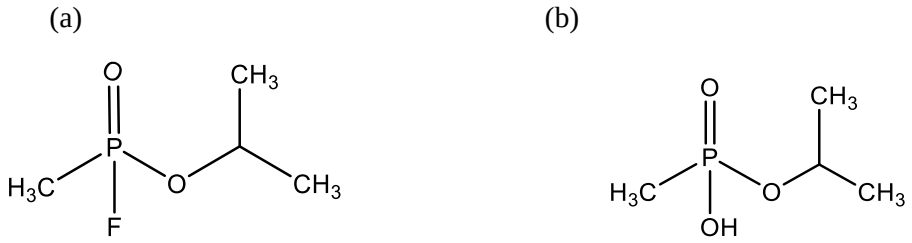

Figure 6.1: Structure of (a) Sarin and (b) its breakdown product, isopropyl methyl phosphonic acid (iPMPA), the latter being studied in this Chapter.

6.2 Sample Preparation

SBA-15 with surface area and pore size of 450-550 m^2/g and 8 nm, respectively, was purchased from Sigma-Aldrich. iPMPA was synthesised by Rebecca William, DSTL. iPMPA was dissolved in 20 ml of DCM at room temperature. The mixture was stirred for 2 hrs, and the resulting slurry was then mixed with SBA-15. The material was filtered and vacuum dried at 100℃. Four samples were prepared with different loadings, namely 1.28, 0.64, 0.32, and 0.16 g/g of iPMPA to SBA-15. These samples are referred to as SBA-15:iPMPA_1.28, SBA-15:iPMPA_0.64, SBA-15:iPMPA_0.32, and SBA-15:iPMPA_0.16.

6.3 Experimental NMR Details

Solid-state NMR experiments were performed (unless otherwise stated) using a Bruker Avance III spectrometer operating at a ^{1}H Larmor frequency of 500.1 MHz, 125.8 MHz (for ^{13}C), 202.5 MHz (for ^{31}P) and 99.3 MHz (for ^{29}Si) and a 4 mm triple resonance probe operating in double

resonance mode at a MAS frequency of 12.5 kHz. A ^{1}H 90° pulse of duration 2.5 μs and a recycle delay of 8 s was used. The nutation frequency, ν_1, was equal to 100 kHz for heteronuclear ^{1}H decoupling. 16 transients were co-added for both ^{1}H and ^{31}P one pulse experiment. A Bruker Avance II spectrometer operating at ^{1}H Larmor frequency of 400 MHz was used to record ^{31}P solution NMR spectra of both SBA:iPMPA_1.28 g/g and SBA:iPMPA_0.64 g/g samples. Samples were prepared by dissolving the samples in $CDCl_3$.

6.3.1 ^{13}C, ^{31}P, and ^{29}Si Detected CPMAS NMR:

In ^{1}H–^{13}C, ^{1}H–^{31}P, and ^{1}H–^{29}Si cross polarisation (CP) MAS experiments, CP was achieved using a ramp[89] of 80 to 100% efficiency on the ^{1}H channel for a contact time of 2, 4, and 8 ms for ^{13}C, ^{31}P, and ^{29}Si, respectively. SPINAL-64[81] ^{1}H heteronuclear decoupling was applied with a pulse duration of 5.8 μs for an acquisition time of 46, 54, and 93 ms for ^{13}C, ^{31}P, and ^{29}Si, respectively. 2048 (for ^{13}C), 256 (for ^{31}P), and 1024 (for ^{29}Si) transients were co-added, corresponding to a total time of 4 hrs 55 mins, 1 hr 14 mins, and 2 hrs 28 mins, respectively.

6.3.2 2D CP ^{1}H–^{13}C, ^{1}H–^{31}P, and ^{1}H–^{29}Si Heteronuclear Correlation MAS NMR:

2D CP HETCOR[274] spectra for the SBA-15: iPMPA_1.28 and 0.64 g/g samples were recorded with no homonuclear ^{1}H decoupling during the t_1 period. 16 (for ^{31}P), or 512 (for ^{29}Si) transients were co-added for each of 128 (for ^{31}P) or 32 (for ^{29}Si) t_1 FIDs, using the States–TPPI method to achieve sign discrimination in the F_1 dimension with a rotor synchronised t_1 increment of 80 μs. A 90-100% amplitude ramp on ^{1}H was employed for a CP contact time of 500 μs for ^{13}C, or 2 ms for both ^{31}P and ^{29}Si. For ^{1}H–^{13}C CP HETCOR experiments, 16 (for the SBA15: iPMPA_1.28) or 32 (for SBA15: iPMPA_0.64) transients were co-added for each of 256 (for the SBA15: iPMPA_1.28) or 160 (for SBA15: iPMPA_0.64) t_1 FIDs. The pulse sequence for the 2D CP HETCOR experiment is depicted in Figure 3.6. The following phase cycling was employed: ^{1}H 90° pulse (90°, 270°), X CP contact pulse (0°), receiver (0°, 180°, 180°, 0°, 90°, 270°, 270°, 90°), where X = ^{13}C, ^{31}P, or ^{29}Si.

6.3.3 Variable Temperature Experiments

^{1}H MAS and ^{31}P CPMAS spectra were acquired for the 1.28, and 0.64 g/g loaded samples between 308 K and 263 K, at 5 K increments. The stated temperature corresponds to the input gas temperature. The experiment was conducted both for decreasing and increasing the temperature, a waiting period of 90 s was used for temperature equilibration, with a recycle delay of 8 s.

In all experiments, the ^{13}C and ^{1}H chemical shifts are referenced to neat tetramethylsilane (TMS) at 0 ppm, using adamantane as a secondary reference, setting the ^{1}H and ^{13}C of the CH_2 peak at 1.8 and 38.5 ppm, respectively[102, 275]. ^{31}P was referenced to 85% H_3PO_4[105-106] at 0 ppm using Ammonium dihydrogen phosphonate (ADP) at 0.99 ppm. ^{29}Si was referenced to Kaolinite at δ = –91.5 ppm with respect to TMS [107].

6.4 Results

Multinuclear solid-state MAS NMR experiments were conducted on four samples of SBA-15 with different loadings of iPMPA to characterise and study the interaction of iPMPA with the silica surface.

Figure 6.2a compares ^{1}H MAS NMR one-pulse spectra for the four SBA-15: iPMPA samples with a ^{1}H MAS spectrum of SBA-15 alone. For SBA-15, a sharp peak centred at 3.8 ppm is observed together with two broad shoulder peaks around 6.5 ppm and 1.8 ppm. Five resonances are observed for SBA-15: iPMPA_1.28. A peak at 9.4 ppm with a shoulder peak at 10.5 ppm (peaks are zoomed and shown in Figure 6.2a) is seen for the 1.28 g/g loaded sample, corresponding to hydrogen bonded protons. This peak is shifted to 8.4 ppm for the 0.64g/g sample, and the shoulder peak is absent. The hydrogen bonded P-OH resonance and the shoulder peaks are absent for lower loadings. A peak at 4.6 ppm and two peaks at 1.3 and 1.2 ppm are observed for both the 1.28 g/g and 0.64 g/g loaded samples, which correspond to the CH and two CH_3 groups of the iPMPA molecule. In lower loading samples, two peaks can be seen, one at 4.5 ppm and another at 1.04 ppm, which are assigned to the OH group in exchange with water or silanol and methyl groups, respectively.

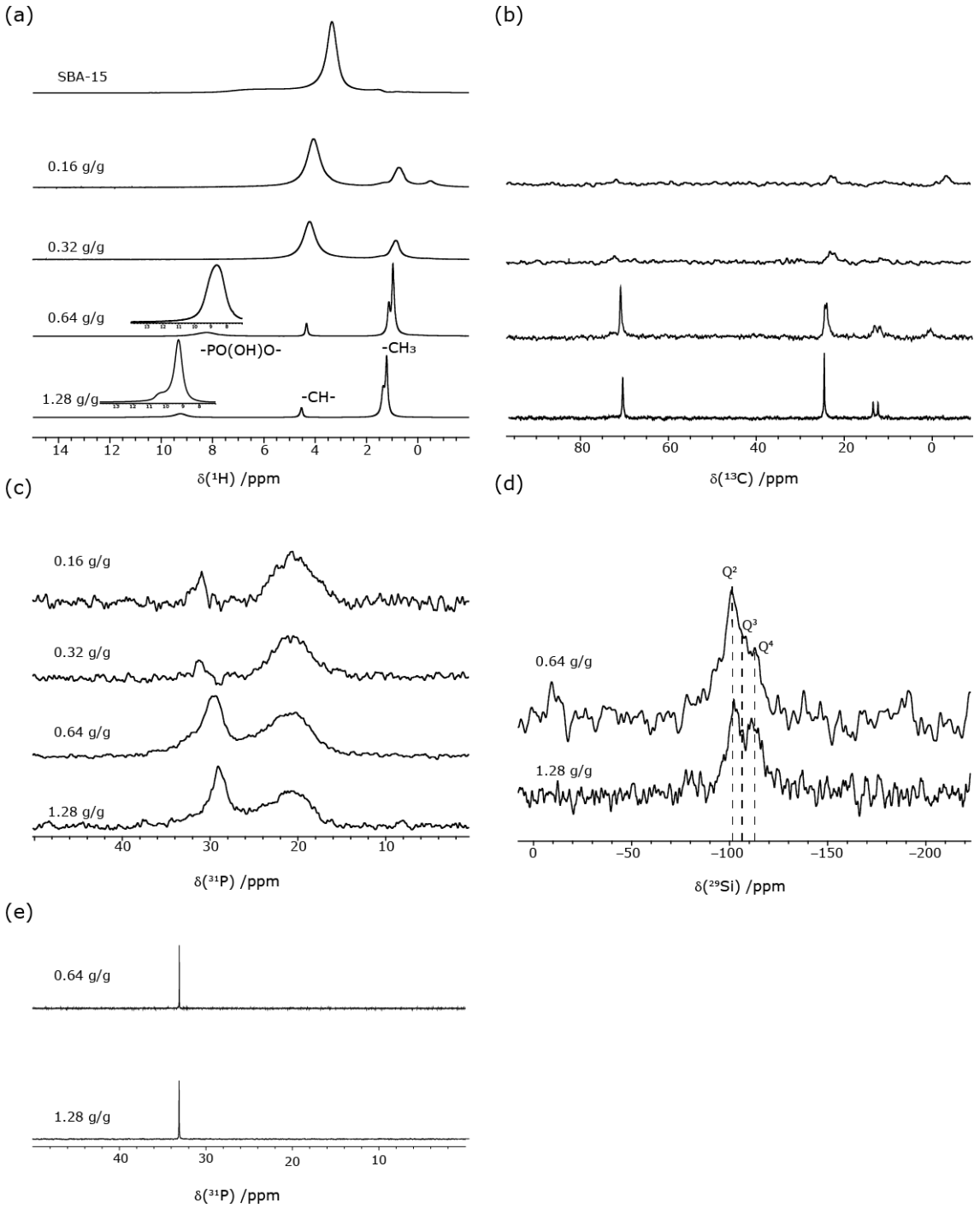

Figure 6.2: One-dimensional MAS (12.5 kHz) NMR spectra of SBA-15 with four different loadings of iPMPA: (a) ^{1}H one-pulse; (b) ^{1}H–^{13}C CPMAS; (c) ^{1}H–^{31}P CPMAS; (d) ^{1}H–^{29}Si CPMAS, (e) ^{31}P solution NMR. All experiments were performed at a ^{1}H Larmor frequency of 500 MHz except the one-pulse ^{1}H MAS NMR spectrum of SBA-15, which is presented at the top of (a), that was recorded at a ^{1}H Larmor frequency of 600 MHz and the solution NMR spectra were recorded at a ^{31}P Larmor frequency of 161.98 MHz.

^{13}C CPMAS NMR experiments have been widely used to confirm the presence of organic groups in functionalised mesoporous silica[273]. ^{13}C CPMAS NMR spectra of all four SBA-15: iPMPA samples are shown in Figure 6.2b. Four distinct peaks are resolved at 70.7, 24.4, 13.2, and 12.1 ppm which can be assigned to the CH and three non-equivalent methyl groups of iPMPA, respectively.

^{31}P one-pulse MAS NMR spectra of the samples exhibit a single line at ~30 ppm with a weak shoulder peak (Figure 6.3), whereas ^{31}P CPMAS NMR spectra in Figure 6.2c of the adsorbed samples show two peaks at ~30 and ~21 ppm; these are assigned to free phosphonic acid and a hydrogen bonded P-OH, respectively. The ^{31}P chemical shift of the assigned free phosphonic acid increases with decreasing loading from: δ = 29.0 ppm for 1.28 g/g, δ = 29.8 ppm for 0.64 g/g loading, to 31.2 ppm for both 0.32 g/g and 0.16 g/g samples, while no evident change in the ^{31}P chemical shift of the broad hydrogen-bonded phosphorus peak (20.5 ppm) is observed across the four samples.

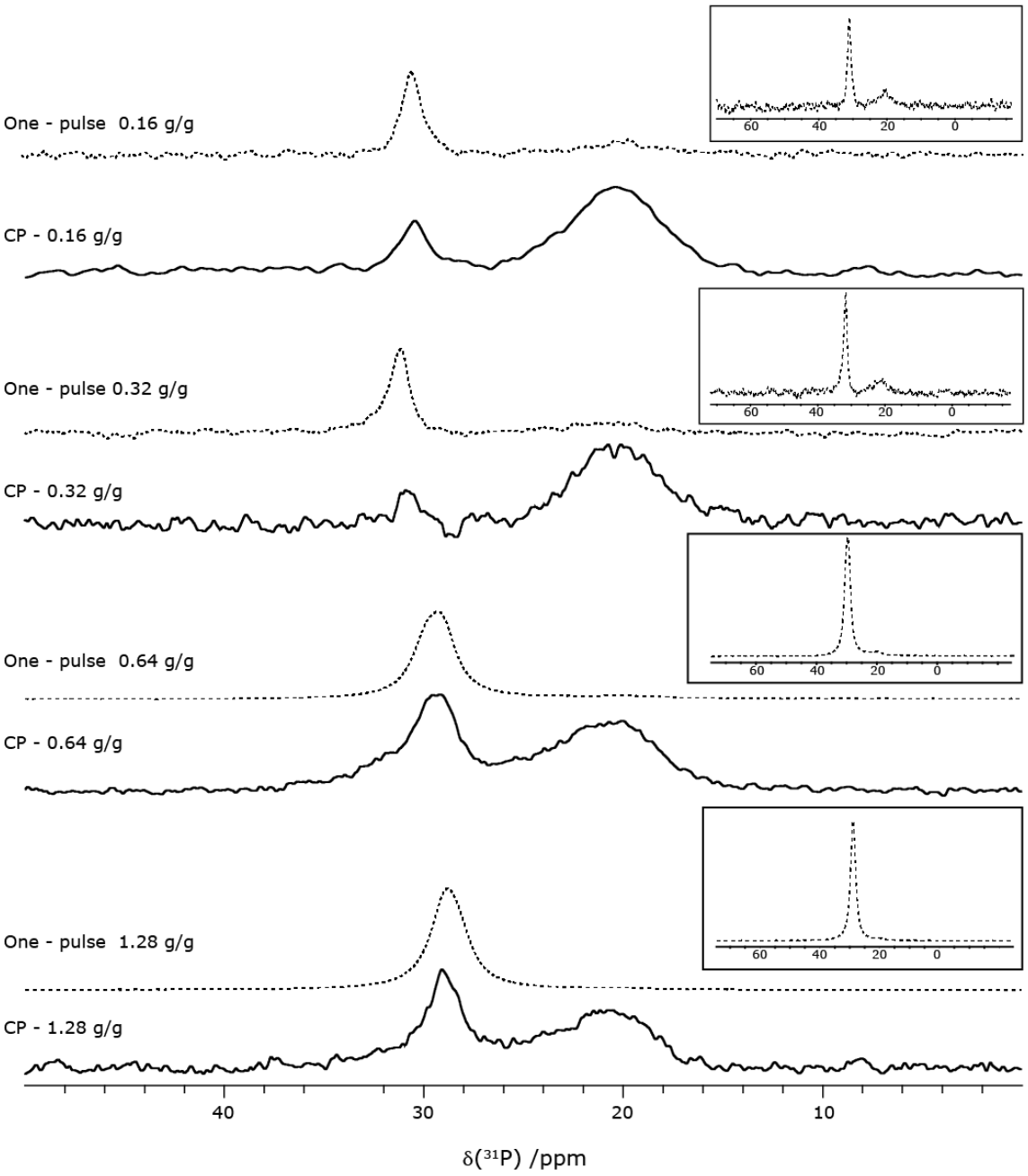

Figure 6.3: ^{31}P CPMAS and one-pulse spectra of SBA-15 with four different loadings of iPMPA. The one-pulse spectrum is zoomed out and is represented in a square box on the top of each spectrum.

^{29}Si CPMAS MAS spectra for the 1.28 g/g and 0.64 g/g samples are presented in Figure 6.2d. Silica networks are assigned based on Q^n and T^m sites, for which chemical shifts range from –80 to –120 ppm and –50 to –80 ppm, respectively[276]. Q^n represents the possible siloxane species and refers to $[Si(OSi)_n(OH)_{4-n})]$ where n = 0, 1, 2, 3, 4, while the T^m notation describes

$[RSi(OSi)_m(OH)_{4-n}]$ species where m = 0,1,2, 3, i.e., corresponding to Si species bonded to an organic moiety[255]. The ^{29}Si CPMAS spectra show no evidence for T sites, demonstrating, as expected, that the iPMPA is not chemically bonded to the SBA-15 via a Si-C bond. Three resonances were resolved for the 1.28 g/g and 0.64 g/g samples which correspond to Q^4 (~–108 ppm), Q^3 (~–100 ppm), and Q^2 (~–95 ppm) species.

$^1H–^{13}C$ CP HETCOR spectra were recorded with a $^1H–^{13}C$ CP contact time of 500 μs, shown in Figure 6.4 (top) to probe C-H proximities. In the ^1H-^{13}C spectra of 1.28 g/g and 0.64 g/g samples, a cross peak is observed between the ^1H resonance at 4.5 ppm and ^{13}C peak at 70.7. Also, cross-peaks correlating ^1H resonance at 1.3 ppm and three methyl carbons are seen. This confirms the assignments of ^1H and ^{13}C spectra. 2D $^1H–^{31}P$ CP HETCOR MAS NMR spectra for both 1.28 g/g and 0.64 g/g loadings were recorded with a CP contact time of 2 ms to probe $^1H–^{31}P$ proximities and are presented in Figure 6.4 (middle spectra). Clear correlation peaks are observed between the OH, CH, methyl protons, and the free phosphonic acid site. For the lower chemical shift phosphorus site, a correlation is observed only with the methyl protons in both samples.

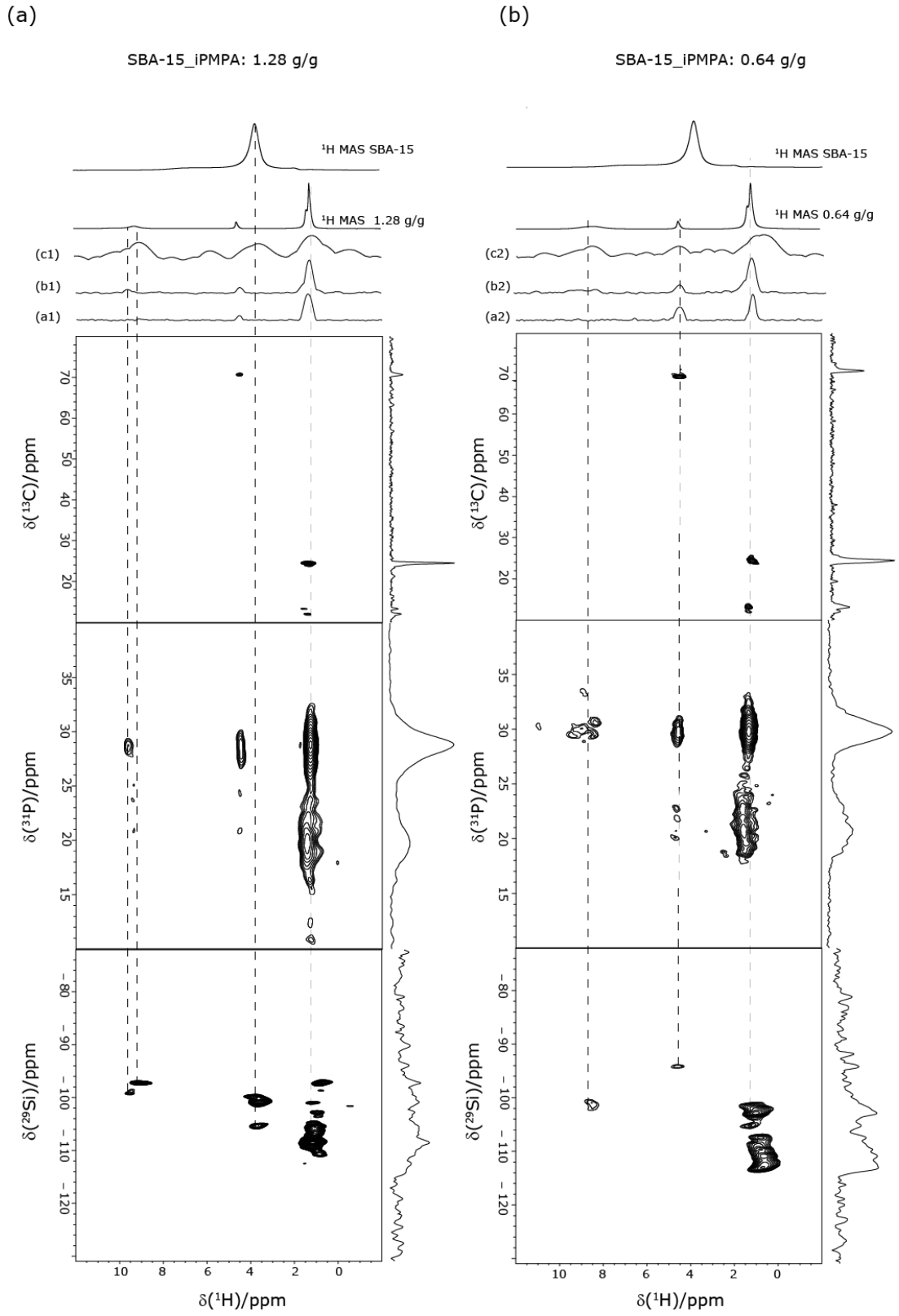

Figure 6.4: Two-dimensional CP HETCOR MAS (12.5 kHz) NMR spectra of (a) SBA-15: iPMPA_1.28 (b) SBA-15: iPMPA_0.68 recorded at a ^{1}H Larmor frequency of 500 MHz: top

$^{1}H–^{13}C$, middle $^{1}H–^{31}P$, and bottom $^{1}H–^{29}Si$. ^{1}H MAS spectra of both samples are shown at the top along with F_1 and F_2 projections. The base contour level as a percentage of the maximum intensity is ($^{1}H–^{13}C$) 12% for 1.28 g/g and 16% for 0.64 g/g, ($^{1}H–^{31}P$) 12% for 1.28 g/g and 16% for 0.64 g/g, ($^{1}H–^{29}Si$) 59% for 1.28 g/g and 56% for 0.64 g/g.

Clear evidence for the proximity between the iPMPA and surface silica is obtained from the $^{1}H–^{29}Si$ CP HETCOR MAS NMR spectra of both 1.28, and 0.64 g/g loaded samples which are shown in Figure 6.4. In the 1.28 g/g loaded sample, strong correlations are seen between the ^{1}H resonance at ~9.4 ppm and Q^2 (~97 ppm) species. There are also cross-peaks between methyl proton and Q^3 species. In addition, cross-peaks correlating the ^{1}H resonance at around 3.6 ppm and Q3 species are observed. For the 0.64 g/g loaded sample, the correlation between the hydrogen bonded proton resonance (~8.4 ppm) and Q^3 site is seen. There are also cross-peaks between the Q sites (-Q^3 and Q^4) and the proton resonance at around 1.8 ppm (isolated silanol) and methyl proton (1.2 ppm). The ^{1}H resonance at 4.5 ppm due to -CH proton shows a correlation to the Q^2 species (~94 ppm) of the SBA-15

VT one-pulse ^{1}H MAS NMR experiments were performed over the temperature range of 258-308 K at 12.5 kHz MAS. As shown in Figure 6.5, as the temperature is increased, continuous and significant line narrowing is observed for the peaks at 9.4 ppm and 10.5 ppm for the 1.28 g/g loading and at 8.5 ppm for the 0.64 g/g loading (see Figure 6.5b), while only negligible changes in linewidth are observed for the CH and methyl protons in 1.28 g/g sample. One of the methyl peaks in the 0.64 g/g loaded sample has broadened with decreasing temperature. There is no noticeable change in the chemical shift of the proton resonance of the CH and methyl peak for both samples. The zoomed spectra of ^{1}H MAS of 1.28 and 0.68 g/g sample at 308 and 258 K is presented in Figure 6.8.

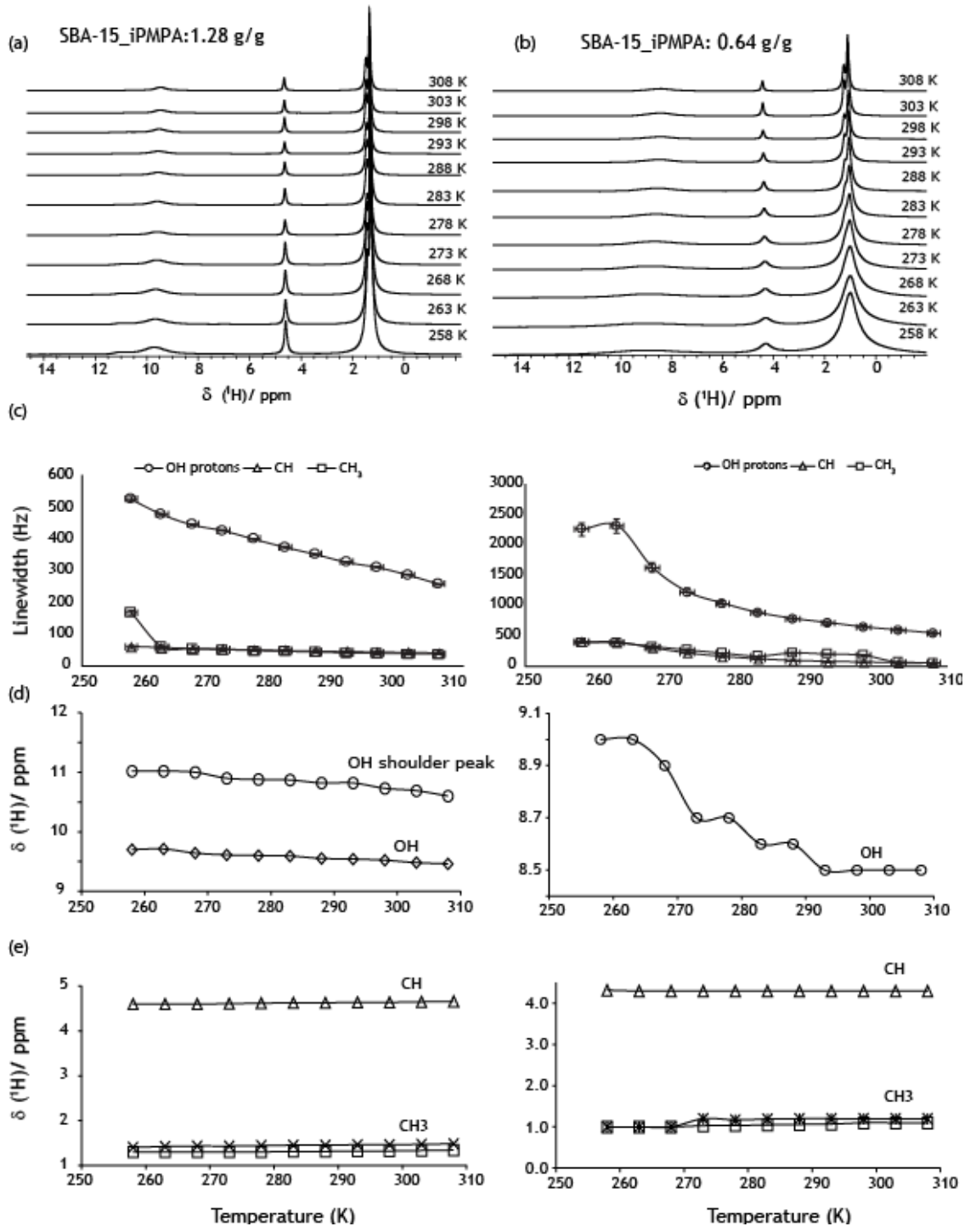

Figure 6.5: VT ^{1}H (500 MHz) MAS (12.5 kHz) NMR spectra of (a) SBA-15: iPMPA_1.28 (b) SBA-15: iPMPA_0.68. The effect of temperature on the (c) linewidths of the OH, CH, CH_3 resonances and the (d) OH and CH, and (e) CH_3 ^{1}H chemical shifts for the SBA-15: iPMPA_1.28 (left), and SBA-15: iPMPA_0.68 (right) samples. Lines linking the points in (c) to (e) are included

as guides to the eye. The estimated error in the measured linewidth (c) is of 5% and for chemical shift (d, e) is ± 0.1 ppm, and is not shown because it is smaller than the symbol height.

The ^{31}P resonance of the P-OH group in both samples is shifted to lower ppm values with increasing temperature. Variable temperature ^{1}H–^{31}P CPMAS acquired at 12.5 kHz are shown in Figure 6.6. As the temperature increases, the phosphorus site involved in hydrogen bonding starts to emerge and is seen as a separate peak at 308 K.

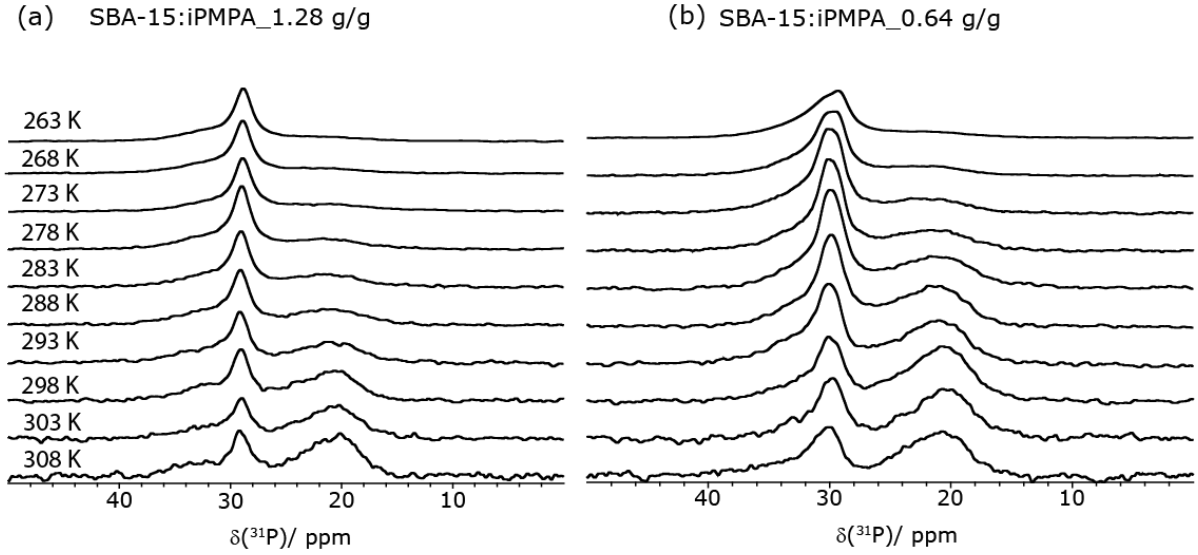

Figure 6.6: Variable temperature ^{1}H (500 MHz)–^{31}P CP MAS (12.5 kHz) NMR spectra of (a) SBA-15: iPMPA_1.28 and (b) SBA-15: iPMPA_0.68.

6.5 Discussion

SBA-15 contains hexagonal arrays of uniformly sized cylindrical pores of 8 nm and has an exceptionally high inner surface area due to the high pore density and small pore diameter. Hence, these silica materials are well suited for adsorbing guest molecules. Figure 6.7 schematically shows the potential interactions that occur upon loading with iPMPA. The silanol groups on the surface of SBA-15 are shown in Figure 6.7f, as well as their interaction with water molecules in Figure 6.7e. On loading, the adsorbed iPMPA molecules will first interact with the OH protons of the silanol groups which are located on the surface (see Figure 6.7a and 6.7b). Some of the iPMPA molecules may remain free (as shown in Figure 6.7a and 6.7e) along with water molecules confined in the core of the pores of the mesoporous silica. As the iPMPA loading increases, there

is the possibility for iPMPA molecules to hydrogen bond to themselves away from the surface (see Figure 6.7c).

Considering the ^{1}H MAS NMR spectrum of pristine SBA-15, the very broad peak at 6.5 ppm in SBA-15 is assigned to water clusters situated in the pores and surfaces or to hydrogen bonded silanols[277-279] as shown in Figure 6.7g. We assign the sharp peak at around 3.8 ppm as due to the fast exchange of silanol and water molecule, and the small peak at 1.8 ppm to isolated silanol (see Figure 6.7f)[279].

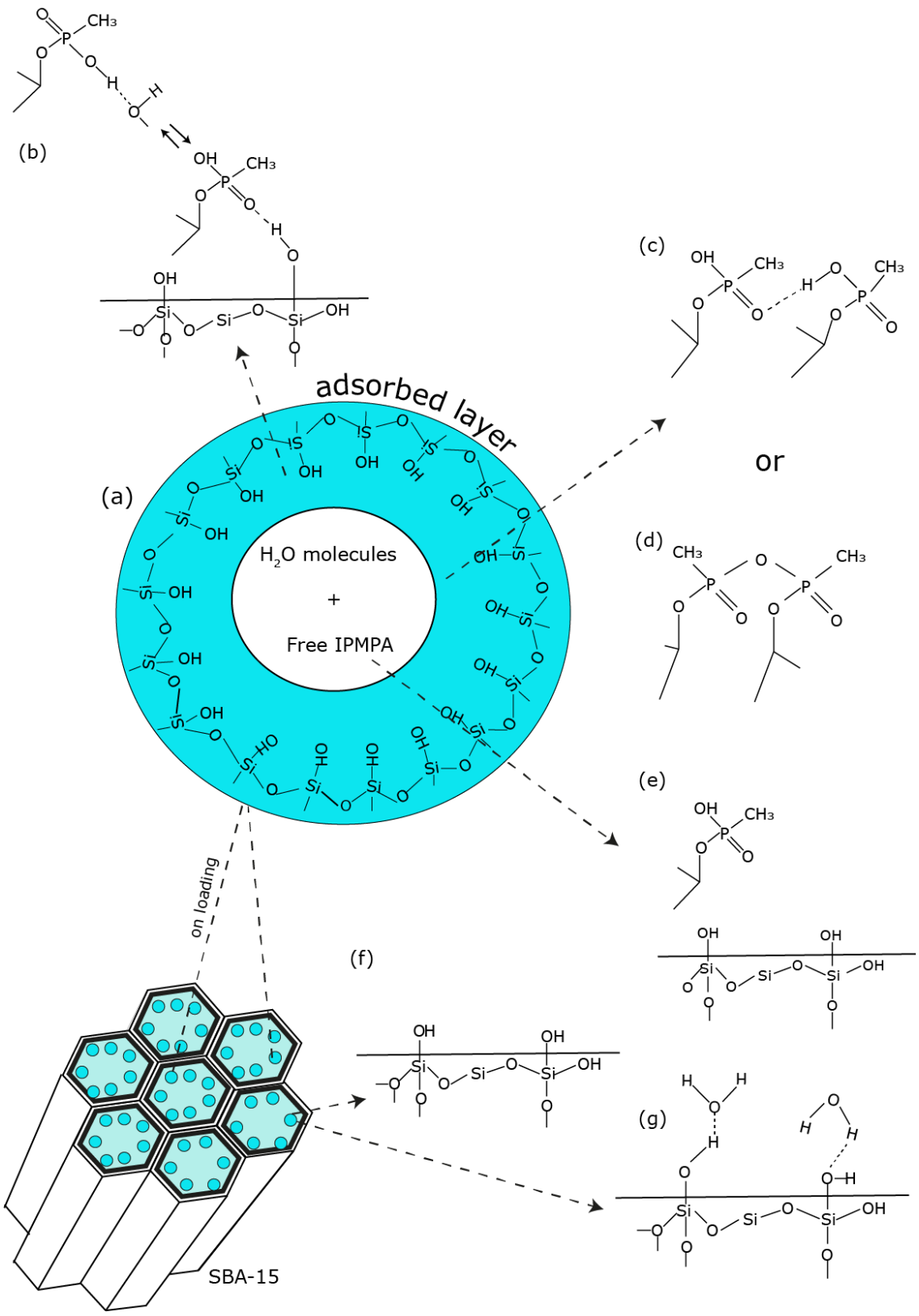

Figure 6.7: Schematic representation of the adsorbed layers of SBA-15 pore on iPMPA loading and possible hydrogen bonding motifs between iPMPA and SBA-15.

A phosphonic acid group can form a strong P−OH−O=P type hydrogen bond with a bond strength of 10 kcal/mol and can form even stronger bonds of the type P−O−H···O-P with an energy of approximately 20 kcal/mol[280-282]. Hence, each phosphonic acid group can act as a hydrogen acceptor for one or two hydrogen bond donors through its P=O, while the P−OH group can act as both an acceptor and donor[255]. Higher proton chemical shift is observed for systems containing strong hydrogen bonding[270], and hence the peaks at 9.4 ppm and 10.5 ppm in SBA: iPMPA_1.28 suggest the existence of various types of hydrogen bonding as shown in 6.7b, and 6.7c. A higher proton chemical shift around 9 ppm is not seen in the ^{1}H spectra of 0.32 and 0.16, g/g loaded samples. The existence of hydrogen bonding is further confirmed through the ^{31}P CPMAS spectra. The presence of two peaks in the ^{31}P CPMAS NMR spectra of the SBA-15: iPMPA samples indicates that there are two distinct phosphorus environments in the loaded samples. The higher ppm chemical shift is assigned to free phosphonic acid, and the lower chemical shift is assigned to a phosphorus site involved in hydrogen bonding[242-243, 255-256, 264, 268, 270, 272].

As mentioned above, the peak observed at 20.5 ppm is either due to the hydrogen bonding between the phosphonic acid and Si-OH species on the surface or adjacent iPMPA or due to phosphonic acid anhydride (see Figure 6.7b, 6.7c, and 6.7d) in the adsorbed layer. In a ^{31}P solution NMR spectrum of a sample with P-O-P bond, two signals are expected with a coupling between them of about 17-22 Hz due to the coupling between two phosphorus centres[283]. The solution NMR ^{31}P spectra of 1.28 g/g and 0.64 g/g samples presented in Figure 6.2e showed only a narrow peak at 33 ppm, which rules out the formation of a P-O-P bond. Hence the possibility for the formation of phosphonic anhydride (Figure 6.7d) is ruled out for SBA-15 loading by iPMPA.

A chemical shift value of less than 5 ppm in the ^{1}H spectra is consistent with the chemical shift value reported for the non-hydrogen bonded carbamic acid in amine functionalised SBA-15[263]. Hence the peak at 4.4 ppm in the lower loaded samples could be due to free phosphonic acid or with the OH group of the iPMPA is undergoing fast exchange with the water molecules situated in the core. These results are consistent with the ^{31}P CPMAS spectra of the 0.32 and 0.16 g/g samples. In the 0.32 and 0.16 g/g loaded samples, surprisingly, the signal intensity of the free phosphonic acid decreased, and the linewidth and intensity of the lower chemical shift phosphorus site increased. Hence, at a lower concentration, the amount of iPMPA is less compared to the water molecules situated in the pores. This suggests that the iPMPA molecules either form a

hydrogen bond with the Si-OH group or undergo fast exchange between the OH and water molecule.

A detailed analysis was carried out for 1.28 g/g, and 0.64 g/g loaded samples using two-dimensional experiments, as is evidenced from the ^{13}C CPMAS spectra where the signal amplitudes for the 0.32 g/g and 0.16 g/g samples are significantly less compared to the samples with higher loadings. From Figure 6.4, it is evident that there are clear correlations between the high ppm phosphorus site (which was assigned for the free phosphonic acid) with the methyl, CH, and –OH protons. In contrast, the low ppm phosphorus site, assigned to the phosphorus involved in hydrogen bonding, shows no correlation to either the CH proton or the hydrogen bonded proton. The correlation observed between the 30 ppm phosphorus site, and the hydrogen-bonded proton indicates that the high ppm ^{31}P site is due to the phosphorus involved in hydrogen bonding between the adjacent phosphonic acid in the adsorbed layer as shown in Figure 6.7c. This confirms that the hydrogen bond between the phosphonic acid is rigid within the timescale of the NMR experiment. The high ppm phosphorous environment can also be due to free phosphonic acid (Figure 6.7e) as mentioned in the previous studies[242, 255, 284]; unfortunately, none of the authors have recorded a 2D ^{31}P HETCOR spectrum for phosphonic acid functionalised mesoporous silica. Correlation peaks between the hydrogen bonded peak and the low chemical shift phosphorus environment are barely detected in the ^{1}H–^{31}P HETCOR spectra of both 1.28 and 0.64 g/g sample. It is suggested that the lower ppm phosphorus environment is due to the phosphorus involved in hydrogen bonding between the surface silanol, as shown in Figure 7b. This peak could also be due to fast exchange between hydrogen-bonded phosphonic acid in the adsorbed layer (Figure 6.7b) and free phosphonic or water molecule situated in the core, which reduces the dipolar interaction because of their higher mobility. This explains the disappearance of cross-peaks between the hydrogen-bonded protons and the 20.5 ppm phosphorus site.

These results, along with ^{1}H–^{29}Si HETCOR spectra, strongly suggest that iPMPA is in very close proximity to the silica surface. In 1.28 g/g loaded samples, the correlation peak between the ^{1}H resonance at 3.6 ppm (peak assigned due to the fast exchange between the Si-OH and the water molecule in the SBA-15) and the Q^3 species implies that the -OH group of the Q^3 environment is undergoing fast exchange with either the OH proton of the iPMPA or water molecule. Q^2 show correlation peaks with both hydrogen bonded proton and isolated silanol proton resonance (~ 0.8 ppm). In contrast, for the 0.64 g/g loaded sample, the Q^2 species show cross-peaks with the -CH proton, whereas the Q^3 species show correlations with the hydrogen bonded resonance and the

methyl and isolated silanol group. It is clear from the ^{1}H-^{29}Si HETCOR spectra that, at higher loading, iPMPA is forming hydrogen bonds with the silicon species situated on the walls of the pores (Q^2 and Q^3). Q^4 species, which are found on the walls of the mesoporous silica, are not exhibiting any hydrogen bonding. ^{1}H-^{29}Si spectra of both 1.28 g/g and 0.64 g/g samples confirm the hydrogen bonding interaction between the iPMPA and Si-OH of the silica surface, further supporting the conclusions derived from the ^{1}H-^{31}P HETCOR spectra.

The continuous decrease in linewidth and shifting of the chemical shift to lower ppm on raising the temperature, as shown in Figure 6.5, is attributed to proton mobility. ^{1}H MAS spectra of the 1.28 and 0.64 g/g sample at 308 and 258 K are presented in Figure 6.8. These results reveal that at ambient temperature, there is a change in the population between the free phosphonic (situated in the core) and hydrogen bonded phosphonic acid (Figure 6.7b in the adsorbed layer). Similar results have been reported for different organic systems[285-288].

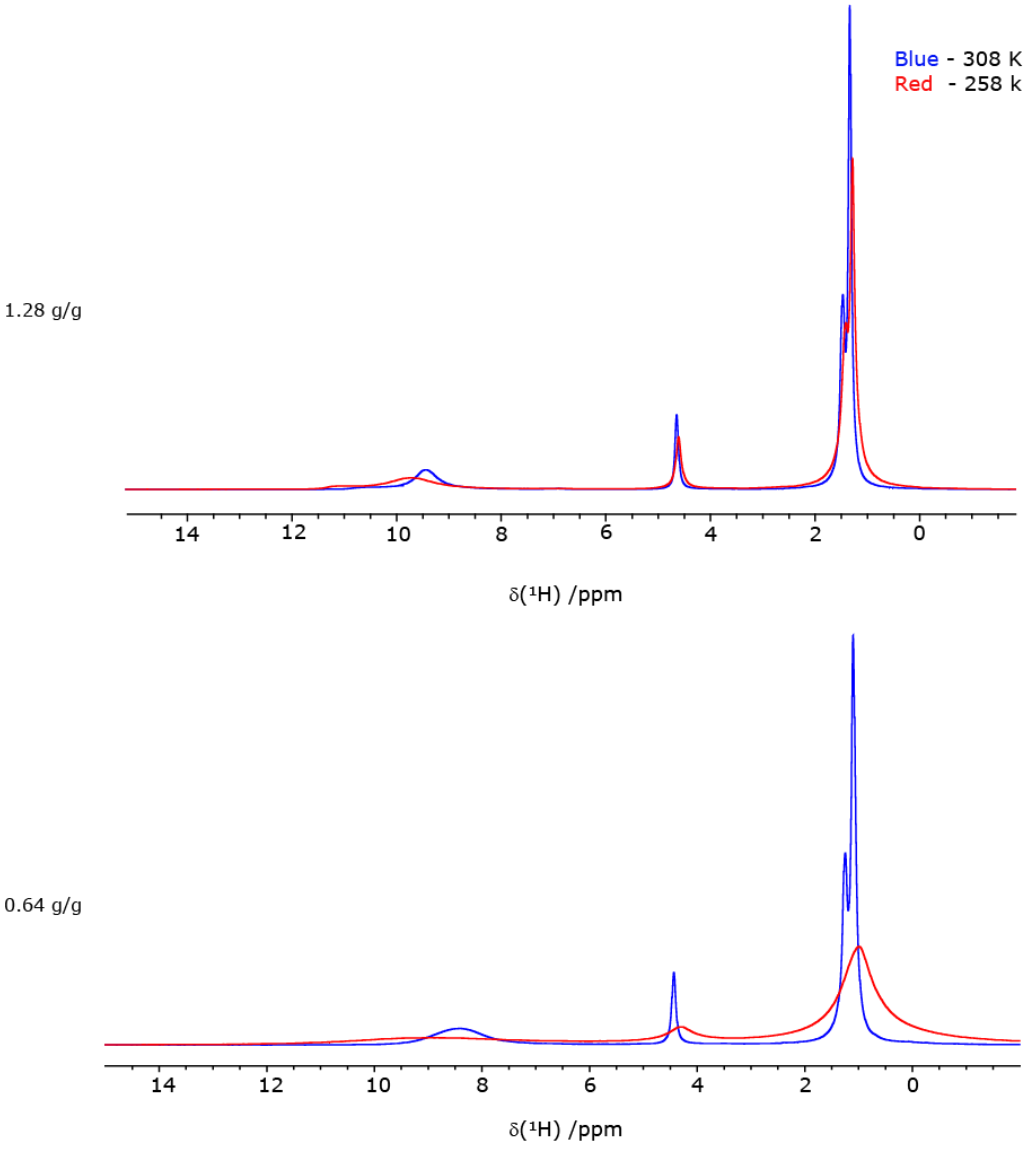

Figure 6.8: ^{1}H (500 MHZ) MAS (12.5 kHz) spectra of SBA-15: iPMPA_1.28 and SBA-15: iPMPA_0.64 g/g samples at 308 and 258 K.

All the above results are consistent with the acid proton exchanging between a hydrogen-bonded and a free state:

$$RPOOH \cdots\cdots HOOPR \underset{kb}{\overset{kf}{\rightleftharpoons}} 2RPOOH,$$

where k_f and k_b are rate constants of the forward and backward reaction and K is the equilibrium constant $K = k_f/k_b$. The exchange rate (k) can be described as fast, intermediate, and slow according to the NMR timescale of motion, relative to the frequency difference between the resonances in

exchange, $\Delta\nu$[288]. Similar observations are seen for the carboxylic acid protons being in exchange between a hydrogen bonded and free state[286]. In the slow exchange limit ($k << \Delta\nu$), two separate peaks can be observed arising from each species, whereas, in the fast exchange limit ($k >> \Delta\nu$); a single resonance is observed at the population-weighted average chemical shift of each species. In the slow exchange regime, the rate constant k is calculated for the 1.28, and 0.64 g/g loaded SBA-15: iPMPA samples using the below Equation:

$$R_2^{observed} = R_2^0 + k\,, \tag{6.1}$$

where R_2^0 is the transverse relaxation rate in the absence of exchange and $R_2^{observed}$ is estimated from the linewidth to be Linewidth*π.

Figure 6.9 shows the linear dependence of the line width (OH resonance) on the inverse temperature, and an activation energy of 9.09 and 20.21 kJ/mol is determined for the SBA-15: iPMPA_1.28 and SBA-15: iPMPA_0.68 samples, respectively, by fitting to the Arrhenius Equation:

$$k = Ae^{\frac{-Ea}{RT}}\,. \tag{6.2}$$

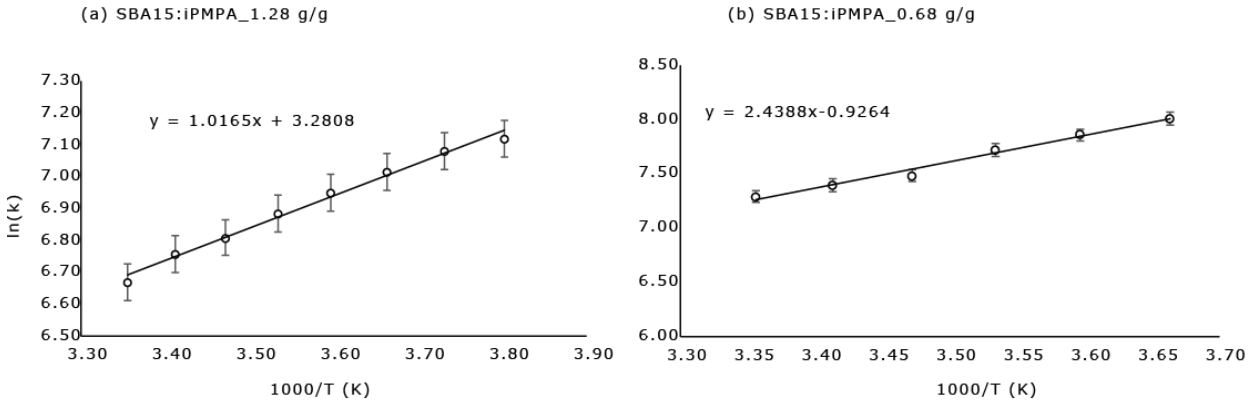

Figure 6.9: The linewidth of the OH resonance at 9.4 and 8.4 ppm for the SBA-15: iPMPA_1.28 and 0.64 samples as a function of inverse temperature. The error in linewidth measurement is estimated to be 5%. The linear region between x and y was used for the Arrhenius analysis.

The variable-temperature ^{31}P NMR results agree well with the observations of the ^{1}H MAS variable temperature spectra. At 308 K, two separate environments are seen, which are attributed to the hydrogen bonding between adjacent phosphonic acid or free phosphonic acid and hydrogen bonded phosphonic acid between surface silanol. At lower temperatures, the linewidth of the high ppm phosphorus environment increases, and the phosphorus site at 20.5 ppm has disappeared or broadened. This change in ^{31}P linewidth is likely due to the fast exchange associated with the hydrogen bonded phosphonic acid in the adsorbed layer and the free phosphonic acid in the core.

6.6 Conclusions

In this chapter, a multinuclear solid-state MAS NMR spectroscopic study of the model system, SBA 15: iPMPA has been carried out with the motivation of understanding the interactions of iPMPA in soil. The samples were prepared using DCM as the transport agent with different iPMPA loading amounts. The ^{13}C, ^{31}P, and ^{29}Si MAS NMR results confirm that the loading of SBA-15 with isopropyl methyl phosphonic acid was successful. The ^{1}H NMR spectra of the higher loaded samples showed evidence for two types of hydrogen bonding. The presence of hydrogen bonding was further confirmed by ^{31}P CP MAS NMR, which showed two distinct peaks implying two different phosphorus environments. Previous reports have assigned these peaks to free phosphonic acid and a hydrogen bonded environment. Our 2D ^{1}H–^{31}P HETCOR results confirm that the higher ^{31}P chemical shift environment is likely due to the hydrogen bonding between the adjacent phosphonic acid, which is adsorbed into the pores. The lower ^{31}P chemical shift environment corresponds to the phosphonic acid involved in hydrogen bonding with the surface silanol groups of the SBA-15 and is relatively mobile. ^{1}H–^{29}Si confirmed that the iPMPA molecule is in close proximity to the silica network and is involved in hydrogen bonding with the silica surface and phosphonic acid. The OH group of the iPMPA in the lower loaded samples undergoes rapid exchange with the water molecules situated in the pore and hence the chemical shift is shifted to a higher field. VT ^{1}H and ^{31}P spectra confirmed that the hydrogen-bonded proton is in exchange with the free phosphonic situated in the pore.

Chapter 7: Solid-State NMR Characterisation of Organic Components of Solid-Electrolyte Interphase of Lithium Ion Batteries.

7.1 Introduction

This chapter is based on the recent publication "Identifying the components of the solid-electrolyte interphase in Li-ion Batteries"[289]. Rechargeable lithium-ion batteries (LIBs) have become the primary energy source for electronic devices and electrical vehicles[290]. However, due to the continuous increase in energy consumption, efforts have been made to develop new materials which can supply high energy densities and long-life times. Thus, traditional batteries like Ni-Cd, alkaline, and lead-acid batteries have been replaced by LIBs due to their higher voltage and gravimetric specific energy[290]. A typical battery cell is composed of two electrodes and an ion-conducting electrolyte. It is the redox potential of the electrodes, and the amount of charge that it can store that determines the energy density of a system and lifetime of the battery or number of cycles. The electrolytes used are typically a $LiPF_6$ salt dissolved in a mixture of organic carbonates which contain high dielectric ingredients such as ethylene carbonates (EC) and low viscosity ingredients such as dimethyl carbonates (DMC), diethyl carbonates (DEC), and ethyl methyl carbonates (EMC)[291]. Conventionally graphite material is used as the active material in the anode[292-293], and the cathode comprises oxides of transition metals[294] or phosphates[295]. The commonly used materials are $LiCoO_2$[296-297], $LiMn_2O_4$[298], and $LiFePO_4$[299]. Since Li is thermodynamically unstable when in contact with an organic solvent, the cycling stability relies on all the side reactions involved with the electrolyte components. Li-ions shuttle back and forth between the anode and the cathode during the first cycle and hence the state of art of Li-ion battery is also known as a 'rocking chair'[300].

Electrolytes undergo reduction during the first charge and form a passive layer consisting of inorganic and organic electrolyte decomposition products. This passive layer is known as a solid-electrolyte interphase[301](SEI), which prevents further electrolyte degradation by blocking electron transport and allowing Li-ions to pass through. Until today, the SEI is still regarded as the most vital and least understood area of Li-ion batteries.

Lithiated carbons are less stable in the air; hence, these are always left in their discharged state, either with graphite or lithiated positively charged materials. It is well known that the organic SEI component primarily comes from the electrochemical reduction of EC[302]. For example, $LiPF_6$ in a mixture of carbonate solvents, including EC, dialkyl carbonates, forms a mixture of reduction products and lithium ethylene carbonate (LEDC, ($CH_2COCO_2Li_2$)). Other reported components include lithium methyl carbonate (LMC) $(CH_3OCO_2Li)_2$, lithium ethylene mono carbonate (LEMC), lithium ethyl carbonate (LEC), $CH_3CH_2OCO_2Li$, Li_2CO_3, CH_3OLi, CH_3CH_2OLi, $LiOCH_2CH_2OLi$, Li_2O, LiF and $Li_xPF_yO_z$[290]. The SEI is very sensitive to temperature, thus

affecting the performance of the battery. There has been much debate regarding the composition of the SEI layer. The composition and thickness of the SEI change throughout the cycling and contains inorganic salts like LiF[303-304] and Li_2CO_3[305-307] and degraded carbonate molecules[305, 308-310]. This layer imparts kinetic stability to the electrolyte against further reductions in the following cycles. The onset potential of SEI formation varies due to the nature and composition of the electrolyte and the additives used in the electrolyte. The performance of the battery depends on the properties of the SEI, which lead to irreversible charge loss occurring due to the solvent reduction, a detrimental process during storage[308].

As stated above, the SEI is comprised of the degradation products of the salt and partial or complete reduction products of the electrolyte[290, 302, 311]. EC is commonly believed to generate LEDC[305, 310, 312] as the primary product on reduction, which is established through the following Equation.

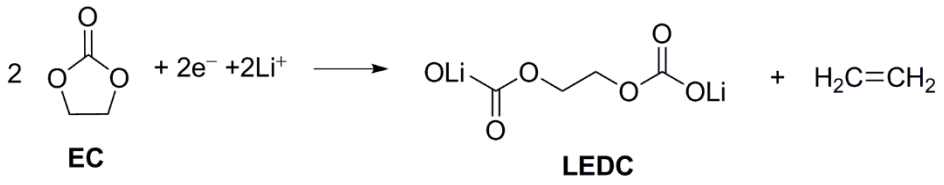

(7.1)

This has been studied by various techniques such as X-ray photoelectron spectroscopy[305, 313-314], Fourier transform infrared spectroscopy[305, 310, 312, 315], and solid-state and solution NMR[313, 316-318]. Conventionally, experimental results from the SEI layer have been compared to the spectra of standard LEDC prepared by four different laboratories[318-321] to understand the composition of the SEI. These laboratories encountered insolubility problems during the synthesis, which leads to kinetic limitations in the carbonate formation process.

The synthetic standard obtained in all the reported literature is lithium ethylene mono-carbonate and not LEDC. Eichhorn's lab is believed to be the first to synthesize LEDC, and the synthetic scheme is described below (see Figure 7.1). This Chapter describes the analysis of the standard compounds LEDC, LMC, LEMC, and the SEI layer generated on graphite electrode by X-ray diffraction and solid-state NMR.

Solid-state NMR spectroscopy is an excellent approach for studying electrochemical processes in the bulk of electrodes[322-324]. It is an ideal tool for identifying or investigating the compositions of SEIs at an atomic level. For LIBs, both ^{7}Li (I= 3/2, 93% abundance) abundance and ^{6}Li (I=1, 7% abundance) have been utilized in many studies to investigate the SEI layer. ^{6}Li NMR experiments are insensitive compared to ^{7}Li, due to its low natural abundance (7%), smaller quadrupole moment, and longer relaxation time. Apart from ^{6}Li or ^{7}Li, NMR active nuclides like ^{19}F, ^{13}C, and

^{1}H have also been widely applied in studies of SEI layers. Most of the NMR studies focus on the determination of the composition of the SEI, which can be probed using ^{1}H, ^{13}C, $^{6,7}Li$, ^{19}F, ^{23}Na, and using ^{17}O NMR. Table 7.1 summarises the main organic components of the SEI layer and reported ^{1}H, ^{13}C, and ^{7}Li chemical shift in the literature.

Table 7.1: Common Interphases and their reported chemical shifts.

Year	Author	Compound	Chemical Shift (ppm)			Reference
			^{7}Li	^{1}H	^{13}C	
2013	Leskes *et al*.	Li_2CO_3	0		167 - 170	325
2016	Michan *et al*.					317
2013	Leskes *et al*.	LiOH	1	-1 to -1.5		325
2005	Meyer *et al*.	Li_2O	2.6 to 2.8			326
2016	Michan *et al*.	Ethylene carbonate		4.6	67, 155.9-160	317
2016	Michan *et al*.	Dimethyl carbonate		3.8	55, 156	317
2013	Leskes *et al*.	HCO_2Li		8		325
2016	Michan *et al*.	CH_3OLi		3.5	56	317
2013	Hu *et al*.					327
2016	Michan *et al*.	Lithium ethyl carbonate		3.5	62, 161	317
2016	Michan *et al*.	$ROCH_2CH_2OR^1$			61-70	317
2016	Michan *et al*.	CH_3OCO_2Li (LMC)			53, 160	317

In this Chapter, the solid-state NMR results and the applicability of NMR crystallography to investigate the structure of three SEI organic model compounds and the SEI layer are detailed. This complements other experimental findings that are discussed and detailed in reference[289]. Multinuclear (^{7}Li, ^{13}C, ^{1}H) solid-state magic angle spinning (MAS) NMR experiments were performed at a high magnetic field of 20.0 T (for ^{7}Li and ^{1}H) and of 11.7 T for ^{13}C.

7.2 Experimental Details

All the samples studied were prepared and provided by the Eichhorn group, University of Maryland. The synthesis method is explained in Ref[289], and the scheme used for the preparation of the model compounds (LEDC, LEMC, and LMC) is presented in Figure 7.1. Single crystal structures of LEMC and LMC are also given for the DFT calculation.

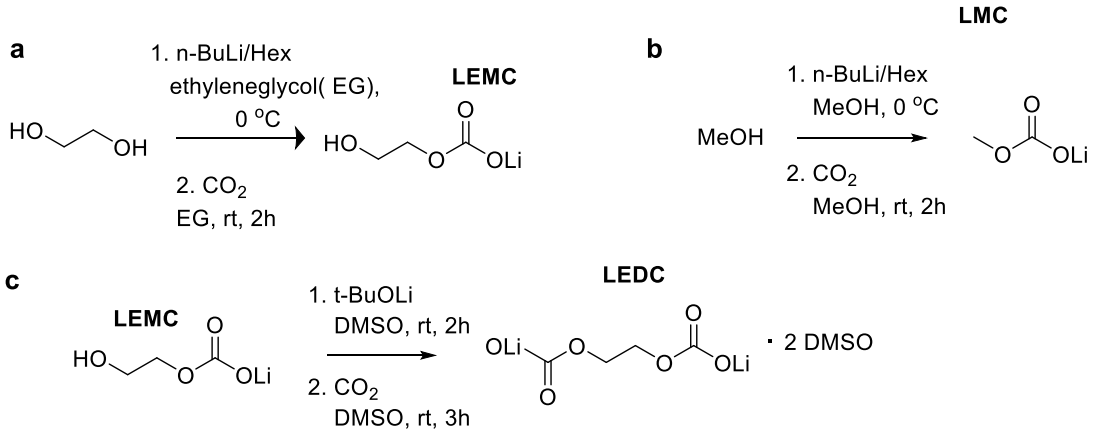

Figure 7.1: Synthesis scheme used for LEMC, LMC, and LEDC, taken from Ref[289].

To prepare a SEI layer, a graphite electrode was cycled from 0.7 – 2.0 V *vs* Li foil using a copper current collector and 1M $LiPF_6$ in EC/DMC (v: v = 1: 1) for 3 times. The electrode was recovered in its charged state, rinsed with anhydrous DMC and vacuumed to remove volatile solvents. The SEI layers @ graphite powder were carefully scratched off from the Cu current collector with a blade in an inert atmosphere. The SEI layers @ graphite powder, along with chemical standards (LMC, LEMC, and LEDC·2DMSO) were all packed in a glove box under nitrogen atmosphere to reduce the amount of exposure of the samples to air and moisture.

All solid-state NMR experiments were recorded on a Bruker Avance III HD 850 MHz spectrometer operating at a Larmor frequency of 850.2 MHz for ^{1}H and 330.4 MHz for ^{7}Li except for ^{13}C, using a 1.3 mm triple resonance probe operating in double resonance mode at a MAS frequency of 60 kHz (unless specified). A ^{1}H 90° pulse duration of 1.5 µs which corresponds to a

nutation frequency of 167 kHz and a recycle delay of 3 s was used in all experiments. The ^{7}Li pulse duration was 2.5 μs for a nutation frequency of 100 kHz.

7.2.1 ^{13}C CPMAS

^{13}C CPMAS experiments were carried out at room temperature using an 11.7 T (^{1}H Larmor frequency, 500 MHz) Bruker Avance II+ spectrometer equipped with a Bruker 1.3 mm HXY probe, operating in double resonance. ^{13}C magnetization was generated by cross-polarization with a 90 to 100 % ramp[89] on the ^{1}H channel for a contact time of 1.5 ms. SPINAL-64[81] heteronuclear decoupling with a pulse duration of 45 μs was employed throughout a t_2 acquisition time of 40 ms. 512 (LEDC, LMC) or 1024 (LEMC) transients were co-added, with a recycle delay of 3 s delay.

7.2.2 ^{1}H – ^{1}H Double Quantum (DQ) MAS

For DQ using BABA recoupling, 16 transients were co-added for each of 160 (for LMC and LEDC.2DMSO) or 128 (for LEMC) t_1 FIDs, using the States – TPPI method to achieve sign discrimination in F_1 with a rotor synchronized t_1 increment of 16.67 μs, corresponding to a total experimental time of 1 h 9 mins (for LMC and LEDC.2DMSO) or 1 h 26 mins (for LEMC).

7.2.3 Li – ^{1}H Heteronuclear Single Quantum Correlation (HMQC) Experiments

A ^{7}Li -^{1}H HMQC pulse sequence utilizing rotary resonance recoupling (R^3)[45], which applies a ^{1}H RF nutation frequency equal to twice the spinning frequency, pulse sequence of Gan[88] *et al.* was used with a phase inversion (every rotor period) of the R^3 pulses[166]. ^{1}H 90° pulse of duration 1.5 μs and ^{7}Li pulses of duration of 2.5 μs were used. 16 transients were co-added for each of 128 t_1 FIDS, using states – TPPI method with a rotor synchronized t_1 increment of 16.67 μs corresponding to a maximum t_1 delay of 1.1 ms (Note that the ^{7}Li FID is thus truncated in comparison to the case for the 1D spectra which were recorded with 20 ms acquisition time, hence explaining the observed broader linewidths in the 2D spectra). A R^3 recoupling time of 400 μs was used to observe one bond Li-H correlations. The pulse sequence is depicted in Figure 3.10.

7.3 Density Functional Theory (DFT) Calculations on Solid-State NMR Spectra

Calculations were performed for the crystal structure of LEMC and LMC using the CASTEP code[161] (academic release version 16.1). The crystal structures of LMC and LEMC were geometry optimized by keeping the unit cell dimensions fixed. NMR shielding calculations were carried out using the GIPAW[120] method to find out the shielding tensor for each nucleus in the crystal structure. Both geometry optimization and NMR shielding calculations used a plane-wave basis

set and the PBE exchange-correlation functional[113] using an ultrasoft pseudopotential[162], with a maximum cut-off energy of 700 eV, with a minimum Monkhorst-pack grid[115] spacing of $2\pi \times 0.1$ $Å^{-1}$. To compare the results with experimentally measured isotropic chemical shifts directly, the below Equation is used:

$$\delta_{iso} = \sigma_{ref} - \sigma_{iso} . \quad (7.2)$$

σ_{ref} values for ^{1}H, ^{13}C, ^{7}Li were 30.0, 170.0 and 90.9 ppm, respectively, as obtained by plotting the experimental chemical shift against the absolute the GIPAW calculated absolute shielding (by fixing the slope to −1)[125-126]. The GIPAW calculated NMR shieldings are viewed and tabulated through the Magres view[163], a visualization tool developed by CCP-NC (the collaborative computational project for NMR crystallography, www.ccpnc.ac.uk).

7.4 Results and Discussion

The solid-state structures of LMC and LEMC were determined from single-crystal XRD by collaborators in reference 288. LMC is monoclinic and consists of two molecules in the asymmetric unit. The crystal structure of LMC is depicted in Figure 7.2. The structure of LMC is disordered; hence, it is divided into two layers of the crystal lattice. Both layers contain double sheets of LMC molecules with LiO_4 tetrahedra at the inner layer, and methyl groups are pointed to the outside. Two LMC molecules are connected through the terminal oxygen of the carbonate. Both layers are very similar, apart from the positional disorder in one of the layers.

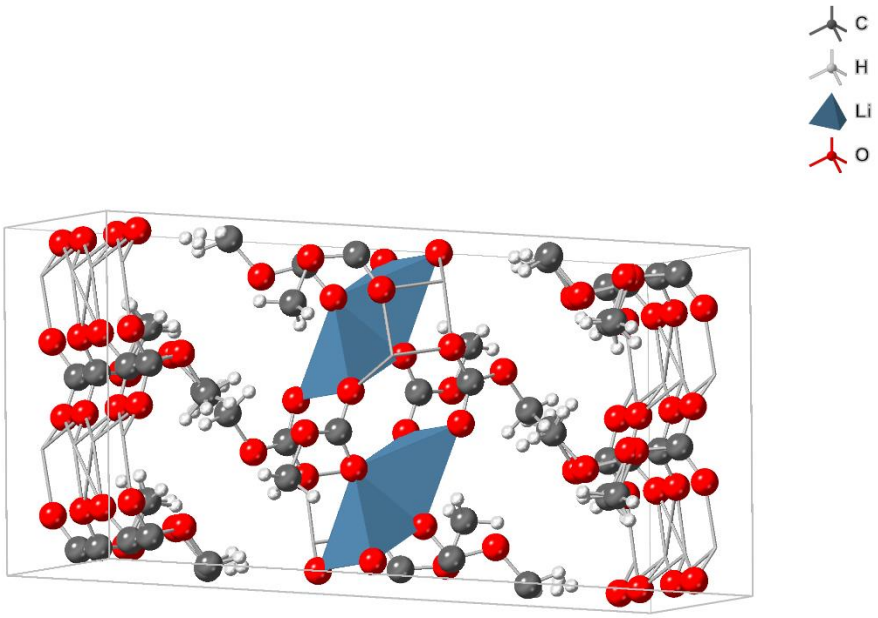

Figure 7.2: Crystal structure of LMC (CCDC 1847785), as determined by co-workers in Ref[289].

LEMC is orthorhombic and has a single molecule in the asymmetric unit. A depiction of the crystal structure of LEMC is presented in Figure 7.3. The structure consists of two layers of LEMC molecules, with a 5 coordinated Li^+ ions shared between three oxygens of the terminal carbonate oxygen, one alkyl carbonate and with a hydroxyl group.

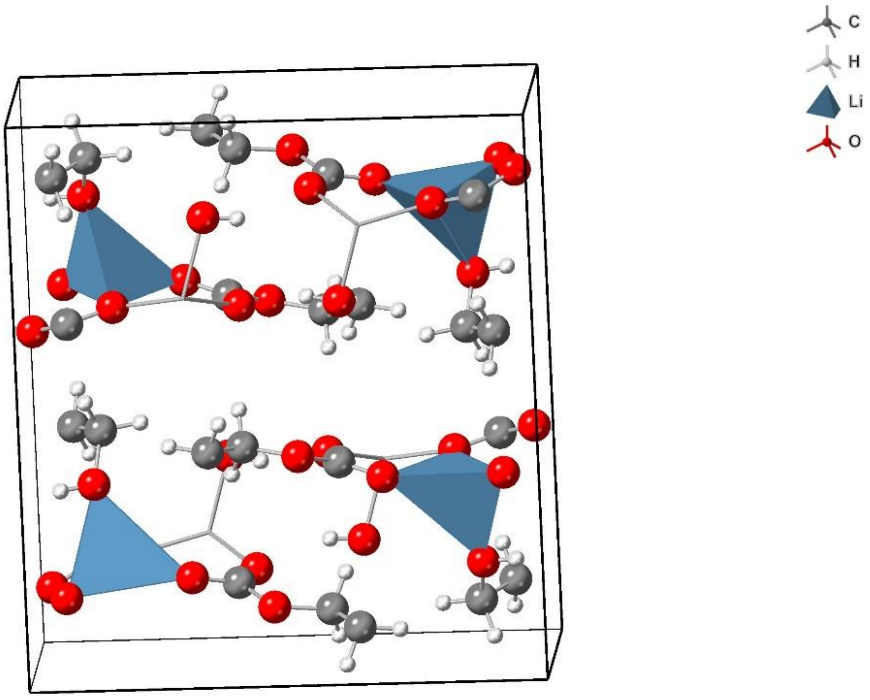

Figure 7.3: Crystal structure of LEMC (CCDC 1847784), as determined by co-workers in Ref[289].

Single-pulse ^{7}Li MAS NMR spectra of the SEI model compounds are shown in Figure 7.4. A single narrow ^{7}Li resonance is centred at approximately 0.25, 0.26, or − 0.35 ppm for LEDC.2DMSO, LEMC, and LMC, respectively. The experimental spectra for LEMC and LMC are consistent with the GIPAW calculated spectra, see Figure 7.4.

^{1}H spectra of LEDC.2DMSO, LEMC, and LMC are shown in Figure 7.4. The ^{1}H spectrum of LEDC.2 DMSO exhibits a very broad shoulder peak at 3.5 ppm, which is assigned to the two CH_2 groups along with a peak at 2.6 ppm for the lattice DMSO. For LEMC, two peaks are observed at 5.2 ppm and 3.3 ppm respectively, which correspond to the OH and two CH_2 protons, respectively, whereas in LMC a peak at 3.4 ppm is seen which corresponds to the CH_3 group. In the ^{1}H spectra of LMC, an additional peak at 1.2 ppm is observed, which is due to an impurity from the synthesis. The GIPAW calculated chemical shifts for LMC and LEMC are compared with the experimental spectra in Figure 7.5. The experimental spectra are consistent with the GIPAW calculated spectra.

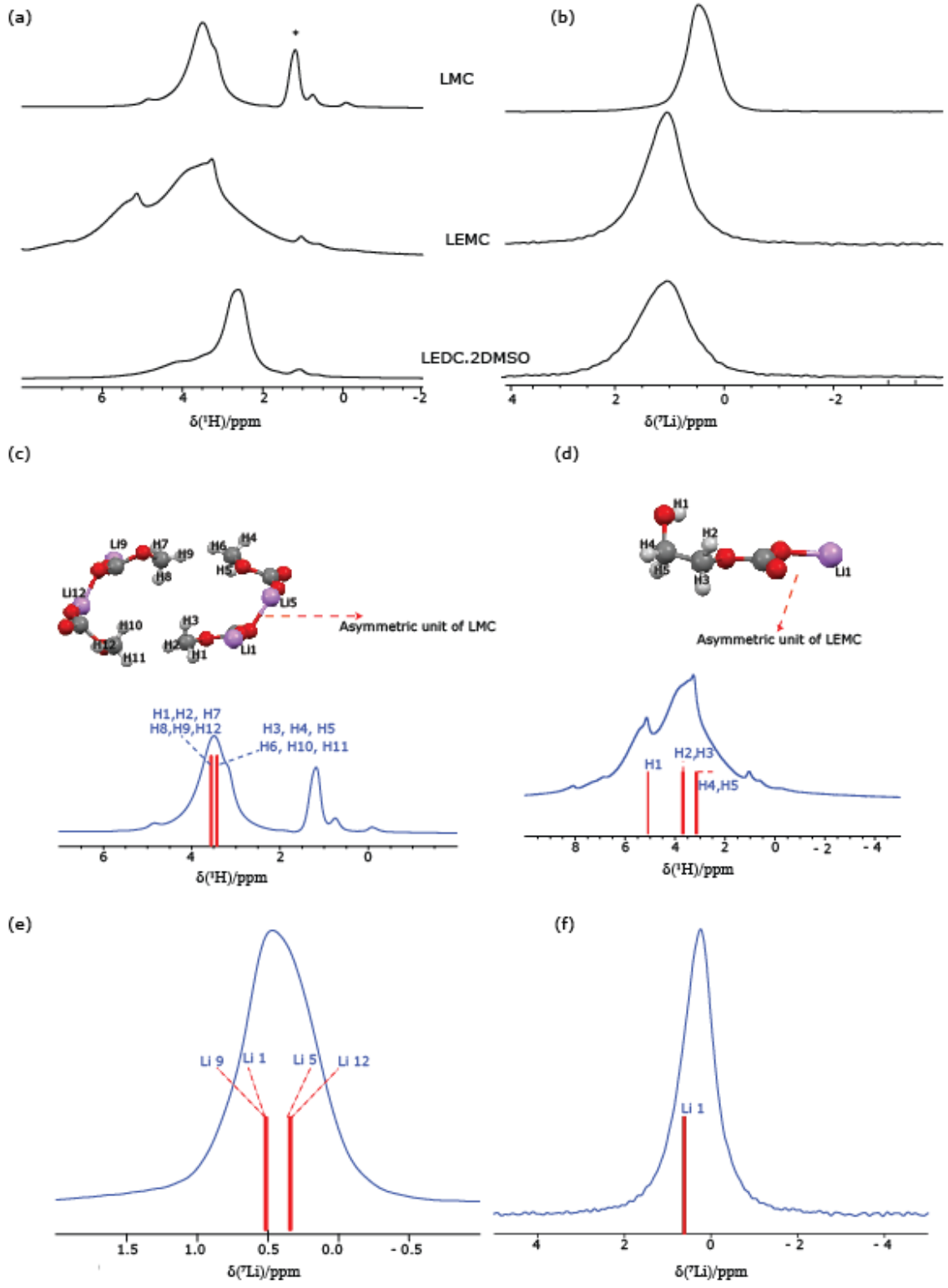

Figure 7.4: 1D solid-state NMR spectra. (a) ^{1}H (850 MHz) and (b) ^{7}Li (330 MHz) one pulse MAS NMR spectra of LMC, LEMC, and LEDC·2DMSO. ^{1}H (c,d) (850 MHz) and ^{7}Li (d, e) MAS (60 kHz) NMR spectra of (c) LMC and (d) LEMC, together the stick spectra corresponding to the

GIPAW calculated chemical shifts for the geometry optimized (CASTEP) crystal structure. An impurity (hydrolysis) due to sample preparation is noted with an asterisk.

^{13}C CPMAS spectra of LEDC. 2DMSO, LEMC, and LMC are shown in Figure 7.5. Two resonances at 64 and 155 ppm for ethylene and carbonate carbons are observed in the LEDC.2DMSO spectrum with an additional two peaks around 40 ppm which correspond to the lattice DMSO[328]. Three resonances at 160.2, 67.4, and 59.4 pm for carbonate and the two ethylene carbons in LEMC are observed. The chemical shifts for LEMC are consistent with previously reported chemical shifts of LEDC[329-330]. For LMC, a peak at 162.5 and two peaks at 53.9 and 54.5 ppm are seen which is consistent with the chemical shifts reported by Grey and coworkers[330]. The highest resonance is attributed to the carbonate. The two peaks at around 55 ppm correspond to the methyl group of the two asymmetric units. The experimental spectra of both LEMC and LMC are consistent with the GIPAW calculated spectra and are shown in Figure 7.5.

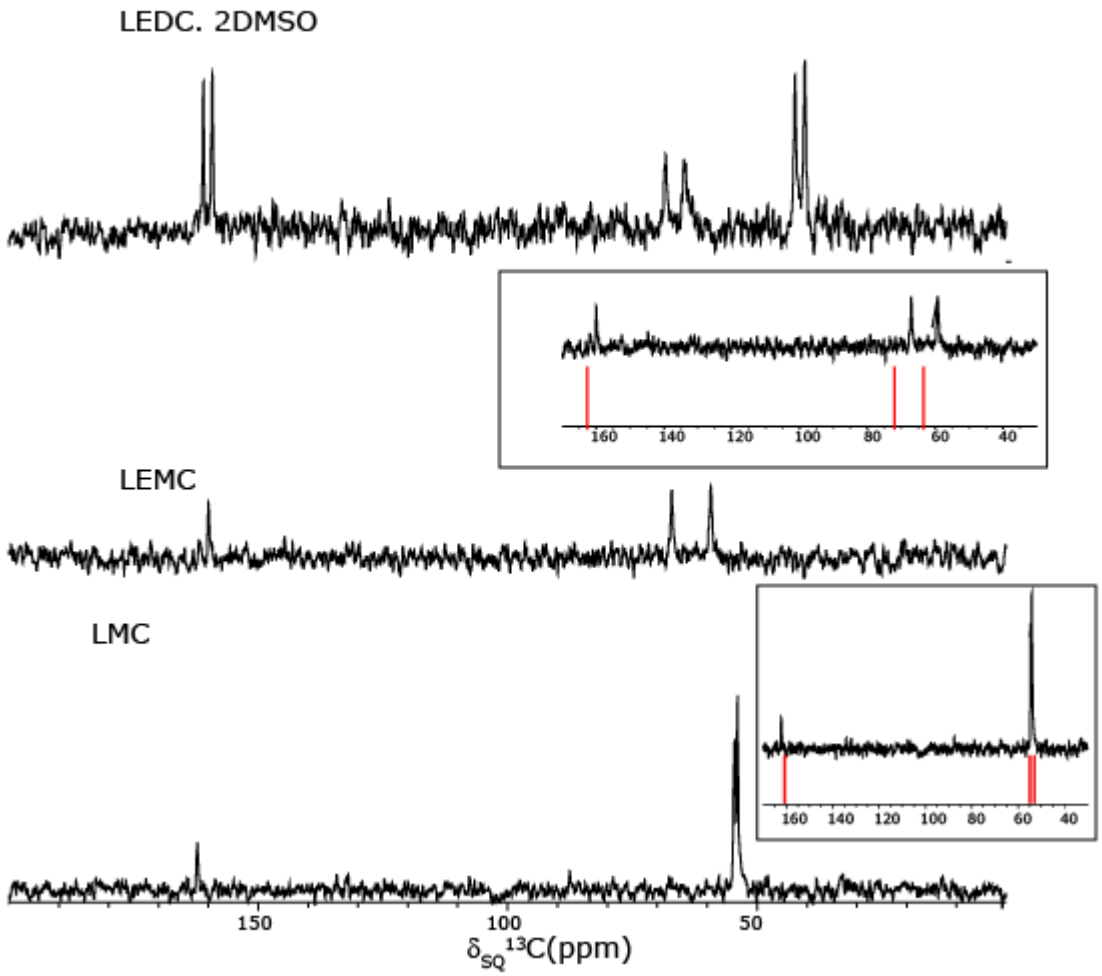

Figure 7.5: ^{1}H-^{13}C (125.3 MHz) CP-MAS (60 kHz) NMR spectra of LMC, LEMC, and LEDC.2DMSO, together with stick spectra (red) in a box which corresponds to the GIPAW calculated chemical shifts for the geometry optimized LEMC and LMC.

^{1}H and ^{7}Li one-pulse MAS NMR spectra of a SEI layer generated on graphite are shown in Figure 7.6 and exhibit very broad lines which are likely due to the paramagnetic nature of the electrode.The experiments were repeated at a ^{1}H Larmor frequency of 100 MHz spectrometer at a spinning frequency of 60 kHz, but the spectrum was still broad. In diamagnetic materials, lithium NMR has a relatively small range of chemical shifts typically about 5 ppm, whereas lithium NMR spectra for a bulk electrode exhibit resonances of several 10s or 100's of ppm due to the Knight and paramagnetic shifts[324]. layer

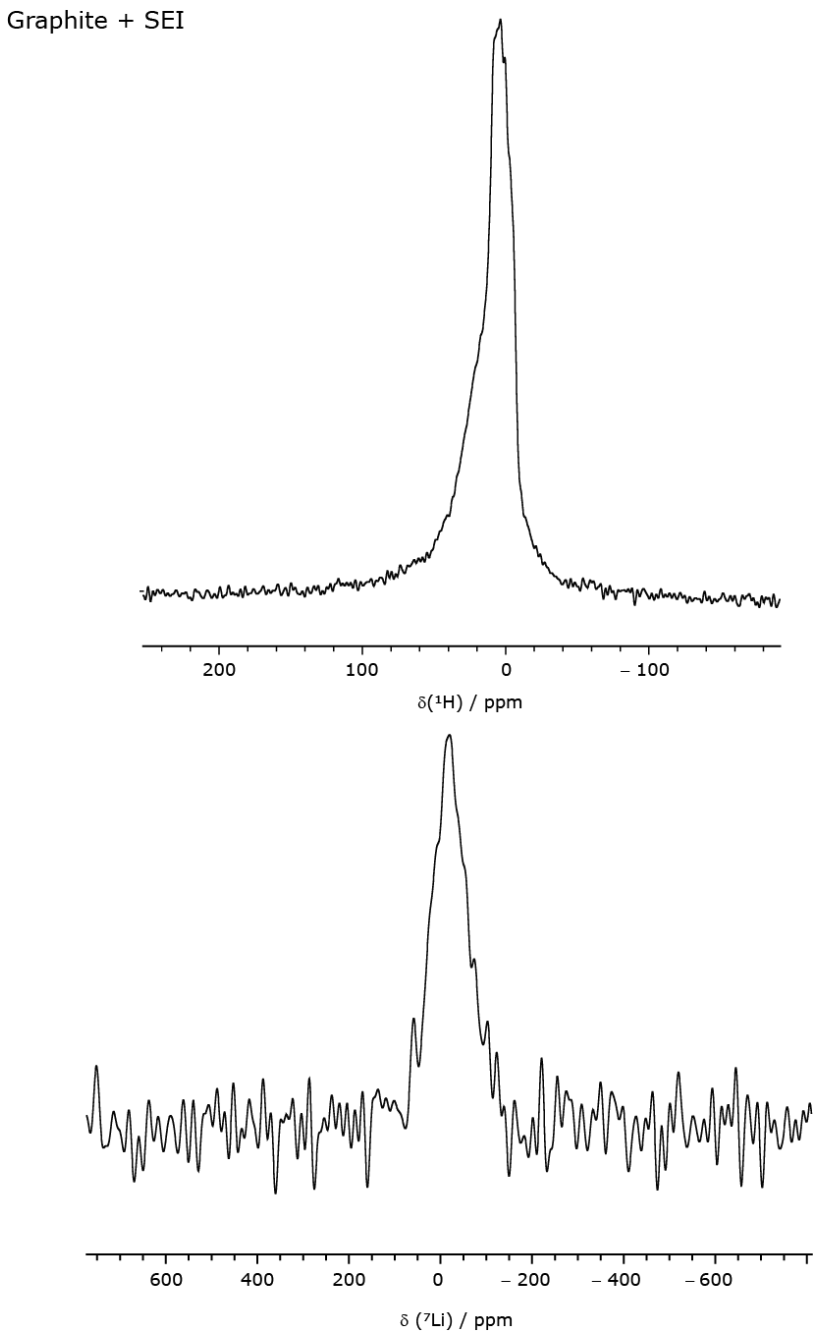

Figure 7.6: ^{1}H and ^{7}Li One–pulse MAS NMR spectra of the SEI generated on the graphite layer, recorded at 20.0 T and 40 kHz MAS.

The proximities between Li-H and H-H in the standard compounds and SEI generated on the graphite electrode have been studied using ^{1}H (double quantum) – ^{1}H (single quantum), and ^{7}Li-^{1}H HMQC MAS NMR experiments that are presented in Figure 7.7. A ^{7}Li-^{1}H HMQC MAS NMR spectrum of LEDC.2DMSO confirms that the Li-ions are in close proximity with both the ethylene

and lattice DMSO protons. Similarly, a ^{7}Li-^{1}H HMQC MAS NMR of LEMC shows that the Li-ion is close to the ethylene protons and the -OH proton. Separate peaks can be seen for the OH proton and ethylene protons in the ^{1}H DQ MAS NMR spectrum of LEMC.

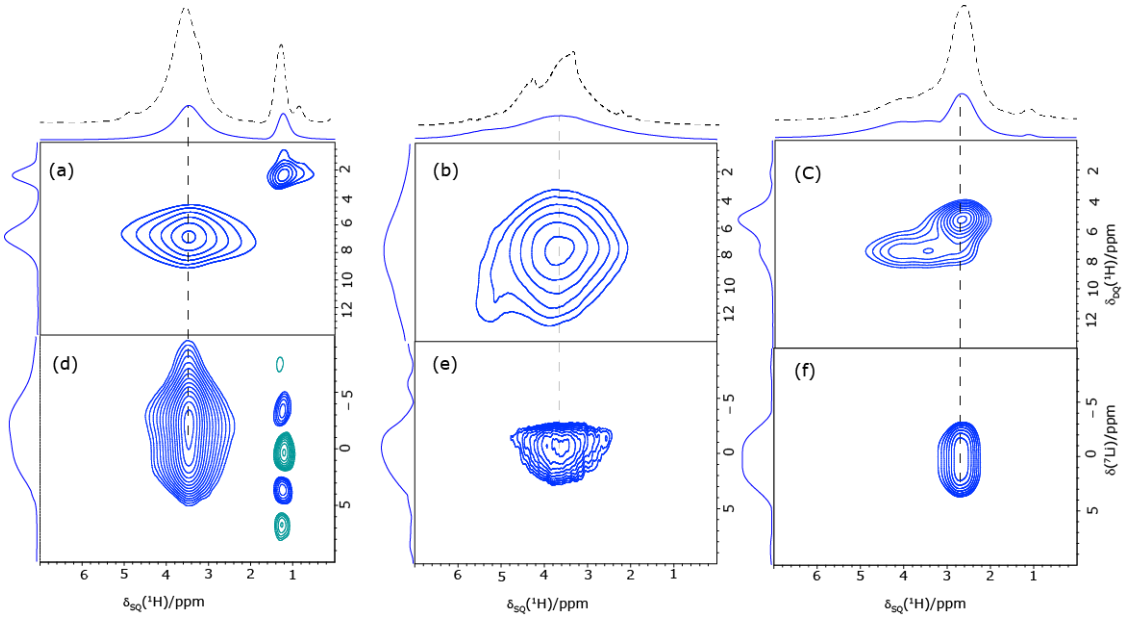

Figure 7.7: (a, b and c) 2D ^{1}H (850 MHz) (DQ)-^{1}H (SQ) MAS (60 kHz, with 1 τ_R of BABA recoupling), and (d, e and f) 2D ^{7}Li-^{1}H (850 MHz) HMQC MAS (60 kHz, τ_{RCPL}= 400 μs) NMR spectra of (a) LMC, (b) LEMC and (c) LEDC·2DMSO. For the 2D spectra, skyline projections are presented; in addition, at the top 1D one-pulse ^{1}H MAS NMR spectra (dashed) are presented. The base contour levels are at 4% and 14% of the maximum peak intensity in (a) and (d) for LMC, 38% and 44% in (b) and e) for LEMC, 22% and 20% for (c) and (f) for LEDC·2DMSO, respectively.

Figure 7.8 presents an overlay of spin diffusion spectra for all four samples. Two-dimensional ^{1}H-^{1}H spin diffusion MAS NMR spectra can be used to reveal the number of phases present in a sample. From Figure 7.8, it is clear that at an intermediate mixing time of 33 ms, all the protons within the samples experience polarisation transfer to and from all the other proton environments, thus confirming a single phase. However, it is difficult to predict whether LEMC or LEDC is the primary product in the SEI from the solid-state NMR results.

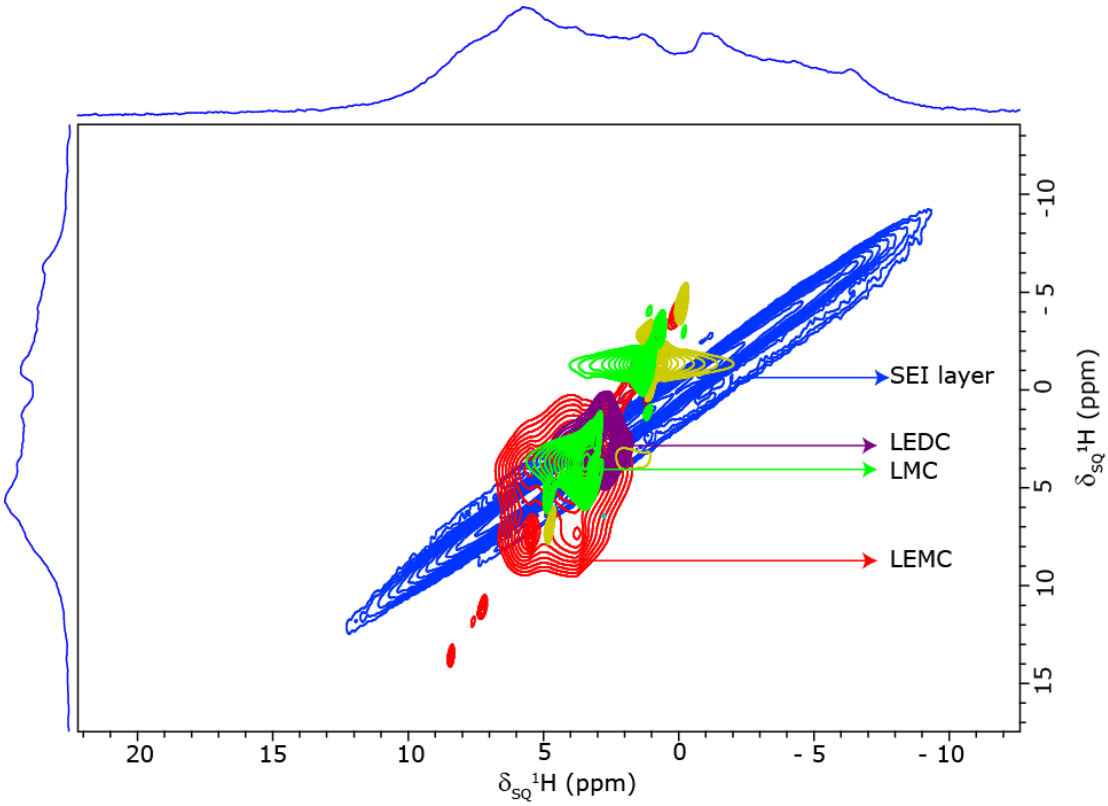

Figure 7.8: An overlay of ^{1}H (850 MHz) -^{1}H NOESY like spin diffusion MAS (60 kHz) NMR spectra of LEMC, LEDC, LMC, and a SEI generated on a graphite electrode.

7.5 Conclusions

This chapter has presented a multinuclear NMR approach for the characterisation of solid electrolyte interphase model compounds and SEI layer on the graphite electrode. The experimental and calculated solid-state NMR results for LEMC are consistent with the results reported for LEDC, which suggested that all the previous results were characterising LEMC and not LEDC[289]. A better understanding of the peak splitting and assignment of LEMC and LMC was achieved by combining experiment with first principles (GIPAW) chemical shift calculation. Proton-proton and proton-lithium proximities are probed using two-dimensional NMR experiments. However, it is not possible to identify the major component of the SEI layer using solid-state NMR. To overcome this issue, solid-state NMR techniques must be coupled with solution NMR, XPS, and FTIR as reported in Ref[289], which suggested that the LEMC, instead of LEDC, is likely the major organic component in the SEI. In conclusion, solid-state NMR in combination of other techniques, can provide detailed molecular-level insight into the composition of the electrode-electrolyte interphase, which will enable a full understanding of battery chemistries.

Chapter 8: Thesis Summary

This thesis covers a diverse area of research where structural and dynamic information is probed using multi-nuclear solid-state MAS NMR experiments. Notably, two dimensional homonuclear and heteronuclear experiments which utilise through-space proximities or through-bond connectivities are used in conjunction with GIPAW calculated chemical shifts (for systems where SXRD data is available) to provide insight into intermolecular packing and interactions.

The first part of chapter 5 involves the NMR crystallographic characterisation of two polymorphs of TFA, which are relevant to pharmaceuticals. The structure of both Form I and Form II TFA was probed using first-principles DFT calculations and solid-state NMR spectra. The experimental chemical shifts are found to be in good agreement with the GIPAW calculated chemical shifts. ^{1}H-^{13}C directly bonded pairs are identified using ^{1}H-^{13}C refocused INEPT MAS NMR spectra and aided the assignment of ^{1}H and ^{13}C chemical shifts. Long- and short–range ^{1}H-^{1}H proximities are determined using ^{1}H-^{1}H double quantum MAS NMR spectra. Moreover, the comparison of calculated GIPAW chemical shifts for the full crystal and an isolated molecule allowed quantitative analysis of intermolecular interactions, notably hydrogen bonding.

Following this, Chapter 5 introduces a novel scoring function that can be employed for ranking/solving putative crystal structures, based on combining experimentally measured chemical shifts and GIPAW calculated NMR chemical shifts on going from solution to solid-state. The approach has been applied to four polymorphic forms of TFA. Experimental solid-state chemical shifts for Form I and II were taken from subchapter 5a. Solution NMR of TFA was carried out by C4X discovery. Solution and solid-state chemical shifts were calculated for four polymorphic forms of TFA. To calculate solution NMR chemical shifts, an ensemble of conformations were generated from the solution NMR data, and chemical shifts for each conformer were calculated using the GIPAW approach by fixing the torsion angle. Both experimental and calculated changes in the chemical shifts from the solution state to the solid-state were determined. Subsequently, a plot of the observed against the calculated changes in chemical shifts provides a scoring function that identifies and effectively discriminates between the various TFA polymorphs. Importantly, the scoring function offers a way to identify specific conformations for a new polymorphic form for which experimental NMR information is available, but there is no information on the crystal structure.

In addition, we have shown that this approach provides a means to separately consider the impact of packing and conformation on chemical shifts, at least for TFA polymorphs. Chapter 5 demonstrates an approach to improve the effectiveness and precision of CSP by reducing the number of feasible alternative structures by combining solution-state NMR conformational and

chemical shift information. The scoring function also offers a technique to evaluate how well a suggested structure matches the chemical shifts of the observed solid-state NMR. The implementation of solid-state NMR information in conjunction with both measured and calculated changes in NMR chemical shifts from solution to crystal-state offers the extra advantage of a sensitive scoring function to discriminate against four comparable TFA polymorphs. It is observed that the ^{13}C chemical shift is more sensitive than the ^{1}H chemical shift to conformational changes

Chapter 6 considers SBA-15 loaded with various amounts of iPMPA(isopropyl methyl phosphonic acid), the first degradation product of the chemical warfare agent Sarin. SBA-15:iPMPA samples are considered as a model system to understand how the presence of the degradation product will affect the soil. The nature and interactions of iPMPA with the silica surface are investigated using multinuclear MAS NMR experiments.

^{13}C CPMAS confirmed that the loading has been successful. ^{1}H MAS NMR showed evidence for various hydrogen bonding interactions as further confirmed by ^{31}P CPMAS NMR spectra. Both ^{31}P one-pulse and ^{31}P CPMAS NMR revealed two distinct environments at ~30 ppm and ~20. Previous reports have assigned these to free phosphonic and hydrogen bonded phosphorus sites. Therefore, the lower ppm chemical shift seen in the ^{31}P CPMAS NMR is assigned to a hydrogen –bonded phosphorus site. The observation in the ^{31}P CPMAS spectra that the intensity of the hydrogen bonded phosphorus site increased in a lower loaded sample compared to a higher loading could be due to the fast exchange between the hydrogen bonded phosphonic acid and water molecules in the core. Two dimensional ^{1}H-^{31}P and ^{1}H-^{29}Si CP HETCOR experiments were performed on the two high loading samples to investigate the nature of the hydrogen bonding. The HETCOR spectra revealed that the higher ppm (30 ppm) phosphorus site is due to the hydrogen bonding between the phosphonic acid molecules adsorbed in the pores. Phosphonic acid can form more complex hydrogen bonded structures due to its hydrogen bond donor and acceptor character. The lower chemical shift phosphorus site is due to the hydrogen bonding between the phosphonic acid and silanol groups or from the exchange undergoing with the water molecules situated in the pores. This explains the increased intensity of the ~20 ppm peak for the lower loaded samples. Variable temperature ^{1}H MAS and ^{31}P MAS spectra revealed that at ambient temperature, hydrogen bonded phosphonic acid is undergoing fast exchange with free phosphonic acid.

As of January 2019, about 97% of the stockpiles declared by the Chemical Weapons Convention (CWC) nations have been verifiably destroyed. However, there are concerns that some countries have undeclared stockpiles and that non-state actors are becoming increasingly threatening[331]. Chemical warfare agents (CWAs) undergo degradation in the presence of water. Hence their

presence in the environment can be easily detected via their corresponding degradation product. It is therefore equally or more necessary to analyze the degradation products than the initial parent agent. We believe that our study has particular relevance, especially for the chemical weapons defense centres, to identify the presence of the CWA in the environment and to determine the material concerned.

The final set of materials investigated were the primary organic components of the solid electrolyte interphase (SEI) layer of Li-ion batteries. The SEI is still considered the most important but least understood element in Li-ion rechargeable batteries, although considerable attempts have been made to clarify its structure and function. The SEI contains inorganic salts (e.g., Li_2CO_3 and LiF) and degraded carbonate molecules (semi-carbonates and polymers) and prevents further solvent degradation as an electronic insulator while facilitating the transportation of Li+. It is well known that the organic SEI element originates mainly from the electrochemical reduction of ethylene carbonate (EC). EC reduction through a single electron pathway is widely thought to generate lithium ethylene dicarbonate (LEDC). Typically, SEI spectroscopic signatures are compared to the spectra collected from synthetic LEDC standards, which have been independently reported by four separate laboratories. Unfortunately, in the method of carbonate formation, these synthetic processes for LEDC synthesis suffer from issues of insolubility that lead to kinetic constraints. Eichhorn's Maryland group found that the` synthetic standard is not LEDC but is lithium ethylene mono-carbonate (LEMC); LEDC was not prepared before this work. Major organic components of the SEI, namely, LEDC, LEMC, and LMC, were characterised using ^{1}H, ^{13}C, and ^{7}Li solid-state NMR spectra. The experimental solid-state NMR chemical shifts of LEMC and LMC were consistent with the GIPAW calculated chemical shifts. ^{1}H-^{1}H and ^{1}H -^{7}Li proximities were probed using two-dimensional MAS NMR experiments. ^{13}C and ^{1}H MAS NMR spectra of LEMC were consistent with the previously reported chemical shifts of LEDC. This confirmed that the previously synthesised primary standard “LEDC” is LEMC. This work also attempted to characterize the components of the SEI generated on the graphite layer. Unfortunately, both ^{1}H and ^{7}Li MAS NMR spectra were very broad, probably due to paramagnet effect. It was, therefore, challenging to define the SEI element using solid-state MAS NMR alone. However, solid-state NMR is a powerful tool to understand the composition of SEI when coupled with other techniques like FTIR, solution NMR, PXRD, and XPS.

Recent developments in solid-state NMR have included pulse sequence improvements, specifically advanced forms of decoupling and recoupling (both homo- and heteronuclear) applicable at higher MAS rates (e.g., ~150 kHz is now accessible[65]). This leads to substantial

resolution improvements in the solid-state spectra. For instance, Emsley *et al.* have obtained a high-resolution spectrum (about 30% narrower than in the one-pulse spectra) of β-AspAla in less than 10 min using constant time acquisition in the indirect dimension of a two-dimensional experiment at 111 kHz MAS[332].

One of the main constraints of NMR spectroscopy is its low sensitivity due to the only small difference in nuclear spin populations at room temperature. This motivates the design and manufacture of stronger magnetic field spectrometers to increase the sensitivity of the NMR experiments. The development of alternative techniques for enhancing solid-state NMR signal based on the hyperpolarization of nuclear spin states like DNP (dynamic nuclear polarisation) has also received significant attention recently. The ideal DNP enhancement is γ_e/γ_n, where γ_e and γ_n are the respective gyromagnetic ratios of the electron and the polarized nucleus, which means that enhancement factors up to ~ 650 can be obtained theoretically for $^1H^3$. DNP NMR takes advantage of this to increase the intensity of the signal considerably and to reduce the experimental time, and hence has gained widespread attention. In the future, many scientific fields will consider solid-state NMR as a comprehensive technique, which provides novel information.

In conclusion, this thesis has demonstrated the power of solid-state NMR for the structural studies of a wide array of systems, including pharmaceuticals, mesoporous materials, and energy materials. It has also been shown that solid-state NMR is capable of providing crystal structure information and chemical shift assignments when combined with other techniques such as DFT calculations, solution-NMR (as was seen in Chapter 5b) and diffraction techniques (as was seen in Chapter 5a and 7).

References

1. Becker, E. D., A brief history of nuclear magnetic resonance. *Anal. Chem.* **1993,** *65*, A295-A302.

2. Andrew, E. R.; Szczesniak, E., A historical account of NMR in the solid state. *Prog. Nucl. Magn. Reson. Spectrosc.* **1995,** *28*, 11-36.

3. Ashbrook, S. E.; Griffin, J. M.; Johnston, K. E., Recent Advances in Solid-State Nuclear Magnetic Resonance Spectroscopy. *Annu. Rev. Anal. Chem.* **2018,** *11*, 485-508.

4. Emsley, J. W.; Feeney, J., Forty years of Progress in Nuclear Magnetic Resonance Spectroscopy. *Prog. Nucl. Magn. Reson. Spectrosc.* **2007,** *50*, 179-198.

5. Gerlach, W., Stern , O., Der experimentelle Nachweis der Richtungsquantelung im Magnetfeld. *Zeitschrift fur Physik* **1922,** *9*, 349-352.

6. Kellogg, J. M. B., Rabi, I. I, Ramsey, N. F, Zacharias, J. R, The Magnetic Moments of the Proton and the Deuteron. The Radiofrequency Spectrum of H_2 in Various Magnetic Fields. *Phys. Rev.* **1939,** *56*, 728-743.

7. Rabi, I. I., Millman, S, Kusch, P, Zacharias, J. R., The molecular beam resonance method for measuring nuclear magnetic moments. the magnetic moments of $_3Li^6$, $_3Li^7$ and $_9F^{19}$. *Phys. Rev.* **1939,** *55*, 526-535.

8. Gorter, C. J., Broer, L. J. F., Negative result of an attempt to observe nuclear magnetic resonance in solids. *Physica* **1942,** *9*, 591.

9. Purcell, E. M., Torrey, H. C, Pound, R. V., Resonance Absorption by Nuclear Magnetic Moments in a Solid. *Phys. Rev.* **1946,** *69*, 37-38.

10. Bloch, F., Hansen, W. W, Packard, M, Nuclear Induction. *Phys. Rev.* **1946,** *69*, 127-127.

11. Rollin, B. V., Nuclear Magnetic Resonance and Spin Lattice Equilibrium. *Nature* **1946,** *669-670*.

12. Rollin, B. V., Hatton, J., Nuclear Magnetic Resonance at Low Temperatures. *Nature* **1947,** *159*, 201.

13. Pake, G. E., Nuclear Resonance Absorption in Hydrated Crystals: Fine Structure of the Proton Line. *J. Chem. Phys.* **1948,** *16*, 327.

14. Andrew, E. R., Bersohn, R., Nuclear magnetic resonance line shape for a triangular configuration of nuclei. *J. Chem. Phys.* **1950,** *18*, 159-161.

15. Van Vleck, J. H., The Dipolar Broadening of Magnetic Resonance Lines in Crystals. *Phys. Rev.* **1948,** *74*, 1168-1183.

16. Arnold, J. T., Dharmatti, S. S, Packard, M. E., Chemical Effects on Nuclear Induction Signals from Organic Compounds. *J. Chem. Phys.* **1951,** *19*, 507-507.

17. Gutowsky, H. S., McCall, D. W., Nuclear Magnetic Resonance Fine Structure in Liquids. *Phys. Rev.* **1951,** *82*, 748-749.

18. Ramsey, N. F., Purcell, E. M., Interactions between Nuclear Spins in Molecules. *Phys. Rev.* **1952,** *85*, 143-144.

19. Gutowsky, H. S., Nuclear magnetic resonance multiplets in liquids. *J. Chem. Phys.* **1953,** *21*, 279-292.

20. McConnell, H. M., Reaction rates by nuclear magnetic resonance. *J. Chem. Phys.* **1958,** *28*, 430-431.

21. Hahn, E. L., Spin Echoes. *Phys. Rev.* **1950,** *80*, 580-594.

22. Torrey, H. C., Transient Nutations in Nuclear Magnetic Resonance. *Phys. Rev.* **1949,** *76*, 1059-1068.

23. Lowe, I. J., Norberg, R. E., Free-Induction Decays in Solids. *Phys. Rev.* **1957,** *107*, 46-61.

24. Andrew, E. R.; Bradbury, A.; Eades, R. G., Nuclear Magnetic Resonance Spectra from a Crystal rotated at High Speed. *Nature* **1958,** *182*, 1659-1659.

25. Andrew, E. R.; Bradbury, A.; Eades, R. G., Removal of Dipolar Broadening of Nuclear Magnetic Resonance Spectra of Solids by Specimen Rotation. *Nature* **1959,** *183*, 1802-1803.

26. Lowe, I. J., Free Induction Decays of Rotating Solids. *Phys. Rev. Lett.* **1959,** *2*, 285-287.

27. Andrew, E. R., Magic angle spinning in solid state n.m.r. spectroscopy. *Philos. Trans. R. Soc. London Ser., A* **1981,** *299* 505-520.

28. Mansfield, P.; Ware, D., Nuclear resonance line narrowing in solids by repeated short pulse r.f. irradiation. *Phys. Lett.* **1966,** *22*, 133-135.

29. Ostroff, E. D.; Waugh, J. S., Multiple Spin Echoes and Spin Locking in Solids. *Phys. Rev. Lett.* **1966,** *16*, 1097-1098.

30. Burum, D. P.; Rhim, W. K., Analyisis of multiple pulse NMR in solids. *J. Chem. Phys.* **1979,** *71*, 944-956.

31. Waugh, J. S.; Huber, L. M.; Haeberlen, U., Approach to high-resolution NMR in Solids. *Phys. Rev. Lett.* **1968,** *20*, 180-182.

32. Rhim, W. K.; Elleman, D. D.; Vaughan, R. W., Analysis of multiple pulse NMR in solids. **1973,** *59*, 3740-3749.

33. Haeberlen.U, *High resolution NMR in solids-selective Averaging*. Adv. Magn. Reson. Academic Press,: New York, **1976**.

34. Vega, S., *Floquet theory*. Wiley: London, **1995**.

35. Goldburg, W. I.; Lee, M., Nuclear Magnetic Resonance Line Narrowing by a Rotating rf Field. *Phys. Rev. Lett.* **1963,** *11*, 255-258.

36. Lee, M.; Goldburg, W. I., Nuclear-Magnetic-Resonance Line Narrowing by a Rotating rf Field. *Phys. Rev.* **1965,** *140*, A1261-A1271.

37. Mehring, M.; Waugh, J. S., Magic-Angle NMR Experiments in Solids. *Phys. Rev. B.* **1972,** *5*, 3459-3471.

38. Levitt, M. H.; Kolbert, A. C.; Bielecki, A.; Ruben, D. J., High-resolution ^{1}H NMR in solids with frequency-switched multiple-pulse sequences. *Solid State Nucl. Magn. Reson.* **1993,** *2*, 151-163.

39. Vinogradov, E.; Madhu, P. K.; Vega, S., High-resolution proton solid-state NMR spectroscopy by phase-modulated Lee–Goldburg experiment. *Chem. Phys. Lett.* **1999,** *314*, 443-450.

40. Gerstein, B. C., High-resolution n.m.r. in solids with strong homonuclear dipolar broadening: combined multiple-pulse decoupling and magic angle spinning. *Philos. Trans. R. Soc. London, Ser. A* **1981,** *299*, 521-546.

41. Scheler. G, H. U., Rosenberger. H, High-resolution ^{1}H NMR in solids with multiple-pulse sequences and magic-angle sample spinning at 270 MHz. *J. Magn. Reson.* **1981,** *44*, 134-144.

42. Harris, R. K.; Jackson, P.; Merwin, L. H.; Say, B. J.; Hagele, G., Perspectives in high resolution solid-state nuclear magnetic resonance. with emphasis on combined rotation and multiple pulse spectroscopy. *J. Chem. Soc. Faraday Trans.* **1988,** *84*, 3649-3672.

43. Sakellariou, D.; Lesage, A.; Hodgkinson, P.; Emsley, L., Homonuclear dipolar decoupling in solid-state NMR using continuous phase modulation. *Chem. Phys. Lett.* **2000,** *319*, 253-260.

44. Elena, B.; de Paepe, G.; Emsley, L., Direct spectral optimisation of proton-proton homonuclear dipolar decoupling in solid-state NMR. *Chem. Phys. Lett.* **2004,** *398*, 532-538.

45. Oas, T. G.; Griffin, R. G.; Levitt, M. H., Rotary resonance recoupling of dipolar interactions in solid-state nuclear magnetic resonance spectroscopy. *J. Chem. Phys.* **1988,** *89*, 692-695.

46. Tycko, R.; Dabbagh, G., Measurement of nuclear magnetic dipole-dipole couplings in magic angle spinning NMR. *Chem. Phys. Lett.* **1990,** *173*, 461-465.

47. Bennett, A. E.; Griffin, R. G.; Ok, J. H.; Vega, S., Chemical shift correlation spectroscopy in rotating solids: Radio frequency-driven dipolar recoupling and longitudinal exchange. *J. Chem. Phys.* **1992,** *96*, 8624-8627.

48. Hohwy, M.; Jakobsen, H. J.; Edén, M.; Levitt, M. H.; Nielsen, N. C., Broadband dipolar recoupling in the nuclear magnetic resonance of rotating solids: A compensated C7 pulse sequence. *J. Chem. Phys.* **1998,** *108*, 2686-2694.

49. Feike, M.; Demco, D. E.; Graf, R.; Gottwald, J.; Hafner, S.; Spiess, H. W., Broadband multiple-quantum NMR spectroscopy. *J. Magn. Reson., Ser. A* **1996,** *122*, 214-221.

50. Schaefer, J.; Stejskal, E. O., ^{13}C Nuclear magnetic resonance of polymers spinning at magic angle *J. Amer. Chem. Soc.* **1976,** *98*, 1031-1032.

51. Hartmann, S. R., Hahn, E.L, Nuclear double resonance in the rotating frame'. *Phys. Rev.* **1962,** *128*, 2042-2050.

52. Pines, A.; Waugh, J. S.; Gibby, M. G., Proton-enhanced nuclear induction spectroscopy ^{13}C chemical shielding anisotropy in some organic solids *Chem. Phys. Lett.* **1972,** *15*, 1776-1777.

53. Pines, A.; Gibby, M. G.; Waugh, J. S., Proton-enhanced NMR of dilute spins in solids. **1973,** *59*, 569-590.

54. Jeener, J: Reminiscences about the Early Days of 2D NMR. In *eMagRes, 10.1002/9780470034590.emrhp0087* 2007.

55. Ernst, R. R.: The Success Story of Fourier Transformation in NMR. In *eMagRes, 10.1002/9780470034590.emrhp0051*.

56. Ernst, R. R., Two-dimensional spectroscopy". *Chimia* **1975,** *29*, 179.

57. Hatanaka, H.; Terao, T.; Hashi, T., Excitation and detection of coherence between forbidden levels in 3-level spin system by multistep processes. *J. Phys. Soc. Jpn.* **1975,** *39*, 835-836.

58. Vega, S.; Shattuck, T. W.; Pines, A., Fourier-Transform double quantum NMR in solids. *Phys. Rev. Lett.* **1976,** *37*, 43-46.

59. Brown, S. P., Probing proton-proton proximities in the solid state. *Prog. Nucl. Magn. Reson. Spectrosc.* **2007,** *50*, 199-251.

60. Mote, K. R.; Agarwal, V.; Madhu, P. K., Five decades of homonuclear dipolar decoupling in solid-state NMR: Status and outlook. *Prog. Nucl. Magn. Reson. Spectrosc.* **2016,** *97*, 1-39.

61. Morris, G. A.; Freeman, R., Enhancement of nuclear magnetic resonance signals by polarisation transfer *J. Amer. Chem. Soc.* **1979,** *101*, 760-762.

62. Lesage, A.; Sakellariou, D.; Steuernagel, S.; Emsley, L., Carbon-proton chemical shift correlation in solid-state NMR by through-bond multiple-quantum spectroscopy. *J. Amer. Chem. Soc.* **1998,** *120*, 13194-13201.

63. Lesage, A.; Emsley, L., Through-Bond Heteronuclear Single-Quantum Correlation Spectroscopy in Solid-State NMR, and Comparison to Other Through-Bond and Through-Space Experiments. *J. Magn. Reson.* **2001,** *148*, 449-454.

64. Elena, B.; Lesage, A.; Steuernagel, S.; Bockmann, A.; Emsley, L., Proton to carbon-13 INEPT in solid-state NMR spectroscopy. *J. Amer. Chem. Soc.* **2005,** *127*, 17296-17302.

65. Lin, Y. L.; Cheng, Y. S.; Ho, C. I.; Guo, Z. H.; Huang, S. J.; Org, M. L.; Oss, A.; Samoson, A.; Chan, J. C. C., Preparation of fibril nuclei of beta-amyloid peptides in reverse micelles. *Chem. Commun.* **2018,** *54*, 10459-10462.

66. Bragg, W. L., The Diffraction of Short Electromagnetic Waves by a Crystal. *Proc. Cambridge Philos. Soc* **1913,** *17*, 43-57.

67. Ashbrook, S. E.; Hodgkinson, P., Perspective: Current advances in solid-state NMR spectroscopy. *J. Chem. Phys.* **2018,** *149*, 040901.

68. Harris, R. K., Wasylishen, R. E., Duer, M. J., *NMR crystallography*. Wiley-Blackwell Chichester, **2009**.

69. Martineau, C.; Senker, J.; Taulelle, F., NMR Crystallography. *Annu. Rep. NMR. Spectrosc.*, **2014**; 82, 1-57.

70. Bryce, D. L., NMR crystallography: structure and properties of materials from solid-state nuclear magnetic resonance observables. *IUCrJ* **2017,** *4*, 350-359.

71. Keeler, J., *Understanding NMR spectroscopy*. John Wiley & Sons: Chichester, **2005**.

72. Hore, P. J., Jones , J. A, Wimperis, S, *NMR: The Toolkit: How pulse sequences work*. Oxford University Press: Oxford, **2015**.

73. Duer, J. M., *Intoduction to solid state NMR*. Blackwell publishing Ltd: Oxford, **2004**.

74. Levitt, M. H., *Spin dynamics: Basics of nuclear magnetic resonance*. Wiley-Blackwell: Chichester, **2008**.

75. Apperley, C. A., Hodgkinson, P., Harris, R. K., *Solid state NMR: Basic principles & practice*. Momentum Press: New York, **2012**.

76. Tatton, A. S.; Bradley, J. P.; Iuga, D.; Brown, S. P., ^{14}N-^{1}H Heteronuclear Multiple-Quantum Correlation Magic-Angle Spinning NMR Spectroscopy of Organic Solids. *Phys. Chem. Chem. Phys.* **2012,** *226*, 1187-1203.

77. Madhu, P. K., Heteronuclear Spin Decoupling in Solid-State Nuclear Magnetic Resonance: Overview and Outlook. *Isr. J. Chem.* **2014,** *54*, 25-38.

78. Bennett, A. E.; Rienstra, C. M.; Auger, M.; Lakshmi, K. V.; Griffin, R. G., Heteronuclear decoupling in rotating solids. *J. Chem. Phys.* **1995,** *103*, 6951-6958.

79. Gan, Z. H.; Ernst, R. R., Frequency- and phase-modulated heteronuclear decoupling in rotating solids. *Solid State Nucl. Magn. Reson.* **1997,** *8*, 153-159.

80. Takegoshi, K.; Mizokami, J.; Terao, T., ^{1}H decoupling with third averaging in solid NMR. *Chem. Phys. Lett.* **2001,** *341*, 540-544.

81. Fung, B. M.; Khitrin, A. K.; Ermolaev, K., An improved broadband decoupling sequence for liquid crystals and solids. *J. Magn. Reson.* **2000,** *142*, 97-101.

82. Salager, E.; Dumez, J. N.; Stein, R. S.; Steuernagel, S.; Lesage, A.; Elena-Herrmann, B.; Emsley, L., Homonuclear dipolar decoupling with very large scaling factors for high-resolution ultrafast magic angle spinning ^{1}H solid-state NMR spectroscopy. *Chem. Phys. Lett.* **2010,** *498*, 214-220.

83. Sun, B. Q.; Costa, P. R.; Griffin, R. G., Heteronuclear polarization transfer by radiofrequency driven dipolar recoupling under magic angle spinning. *J. Magn. Reson., Ser. A* **1995,** *112*, 191-198.

84. Gregory, D. M.; Mitchell, D. J.; Stringer, J. A.; Kiihne, S.; Shiels, J. C.; Callahan, J.; Mehta, M. A.; Drobny, G. P., Windowless dipolar recoupling- The detection of weak dipolar couplings between spin 1/2 nuclei with large chemical shift anisotropies. *Chem. Phys. Lett.* **1995,** *246*, 654-663.

85. Nielsen, N. C.; Bildsoe, H.; Jakobsen, H. J.; Levitt, M. H., Double-quantum homonuclear rotary resonance -efficient dipolar recovery in magic angle spinning nuclear magnetic resonance. *J. Chem. Phys.* **1994,** *101*, 1805-1812.

86. Verel, R.; Ernst, M.; Meier, B. H., Adiabatic dipolar recoupling in solid-state NMR: The DREAM scheme. *J. Magn. Reson.* **2001,** *150*, 81-99.

87. Lee, Y. K.; Kurur, N. D.; Helmle, M.; Johannessen, O. G.; Nielsen, N. C.; Levitt, M. H., Efficient dipolar recoupling in the NMR of rotating solids- A sevenfold symmetrical radiofrequency pulse sequence. *Chem. Phys. Lett.* **1995,** *242*, 304-309.

88. Gan, Z.; Amoureux, J. P.; Trébosc, J., Proton-detected ^{14}N MAS NMR using homonuclear decoupled rotary resonance. *Chem. Phys. Lett.* **2007,** *435*, 163-169.

89. Metz, G.; Wu, X. L.; Smith, S. O., Ramped amplitude cross-polarization in magic angle spinning. *J. Magn. Reson., Ser. A* **1994,** *110*, 219-227.

90. Fyfe, C. A.; Wongmoon, K. C.; Huang, Y.; Grondey, H., INEPT experiments in solid-state NMR. *J. Amer. Chem. Soc.* **1995,** *117*, 10397-10398.

91. Brus, J.; Jegorov, A., Through-bonds and through-space solid-state NMR correlations at natural isotopic abundance: Signal assignment and structural study of simvastatin. *J. Phys. Chem. A.* **2004,** *108*, 3955-3964.

92. Sommer, W.; Gottwald, J.; Demco, D. E.; Spiess, H. W., Dipolar heteronuclear multiple quantum NMR spectroscopy in rotating solids. *J. Magn. Reson., Ser. A* **1995,** *113*, 131-134.

93. Schnell, I.; Lupulescu, A.; Hafner, S.; Demco, D. E.; Spiess, H. W., Resolution enhancement in multiple-quantum MAS NMR spectroscopy. *J. Magn. Reson.* **1998,** *133*, 61-69.

94. Brown, S. P.; Spiess, H. W., Advanced solid-state NMR methods for the elucidation of structure and dynamics of molecular, macromolecular, and supramolecular systems. *Chem. Rev.* **2001,** *101*, 4125-4155.

95. Gottwald, J.; Demco, D. E.; Graf, R.; Spiess, H. W., High-resolution double-quantum NMR spectroscopy of homonuclear spin pairs and proton connectivities in solids *Chem. Phys. Lett.* **1995,** *243*, 314-323.

96. Spiess, H. W., Double-quantum NMR spectroscopy of dipolar coupled spins under fast magic-angle spinning. *eMagRes*, **2012**, *10.1002/9780470034590.emrstm0133.pub2*.

97. Saalwaechter, K.; Lange, F.; Matyjaszewski, K.; Huang, C.-F.; Graf, R., BaBa-xy16: Robust and broadband homonuclear DQ recoupling for applications in rigid and soft solids up to the highest MAS frequencies. *J. Magn. Reson.* **2011,** *212*, 204-215.

98. Feike, M.; Graf, R.; Schnell, I.; Jager, C.; Spiess, H. W., Structure of crystalline phosphates from ^{31}Pdouble-quantum NMR spectroscopy. *J. Amer. Chem. Soc.* **1996,** *118*, 9631-9634.

99. Graf, R.; Demco, D. E.; Gottwald, J.; Hafner, S.; Spiess, H. W., Dipolar couplings and internuclear distances by double-quantum nuclear magnetic resonance spectroscopy of solids. *J. Chem. Phys.* **1997,** *106*, 885-895.

100. Brown, S. P., Applications of high-resolution ^{1}H solid-state NMR. *Solid State Nucl. Magn. Reson.* **2012,** *41*, 1-27.

101. Madhu, P. K., High-resolution solid-state NMR spectroscopy of protons with homonuclear dipolar decoupling schemes under magic-angle spinning. *Solid State Nucl. Magn. Reson.* **2009,** *35*, 2-11.

102. Morcombe, C. R.; Zilm, K. W., Chemical shift referencing in MAS solid state NMR. *J. Magn. Reson.* **2003,** *162*, 479-486.

103. Liang, Y.; Bohme, B.; Ormeci, A.; Borrmann, H.; Pecher, O.; Haarmann, F.; Schnelle, W.; Baitinger, M.; Grin, Y., A Clathrate-I Phase with Li-Ge Framework. *Chem. Eur. J.* **2012,** *18*, 9818-9822.

104. Poppler, A. C.; Walker, D.; Brown, S. P., A combined NMR crystallographic and PXRD investigation of the structure-directing role of water molecules in orotic acid and its lithium and magnesium salts. *Crystengcomm* **2017,** *19*, 224-236.

105. Guerry, P.; Smith, M. E.; Brown, S. P., ^{31}P MAS Refocused INADEQUATE Spin-Echo (REINE) NMR Spectroscopy: Revealing J Coupling and Chemical Shift Two-Dimensional Correlations in Disordered Solids. *J. Amer. Chem. Soc.* **2009,** *131*, 11861-11874.

106. MacKenzie, K. J. D., Smith, M. E., *Multinuclear Solid State NMR of Inorganic Materials*. Pergamon: Oxford, **2002**.

107. Magi, M.; Lippmaa, E.; Samoson, A.; Engelhardt, G.; Grimmer, A. R., Solid-state high-resolution silicon-29 chemical shifts in silicates. *J. Phys. Chem.* **1984,** *88*, 1518-1522.

108. Bonhomme, C.; Gervais, C.; Babonneau, F.; Coelho, C.; Pourpoint, F.; Azais, T.; Ashbrook, S. E.; Griffin, J. M.; Yates, J. R.; Mauri, F.; Pickard, C. J., First-Principles Calculation of NMR Parameters Using the Gauge Including Projector Augmented Wave Method: A Chemist's Point of View. *Chem. Rev.* **2012,** *112*, 5733-5779.

109. Martin, R. M., *Electronic Structure: Basic Theory and Practical Methods.* Cambridge University Press: Cambridge **2004**.

110. Hohenberg, P., Kohn, W., Inhomogeneous electron gas. *Phys. Rev. B.* **1964,** *136*, 864.

111. Kohn, W., Sham, L. J., Self-consistent Equations including exchange and correlation effects. *Phys. Rev.* **1965,** *140*, 1133.

112. Koch, W., Holthausen, M. C., *A chemist's guide to Density Functional Theory* Wiley-VCH: New York, **2000**.

113. Perdew, J. P.; Burke, K.; Ernzerhof, M., Generalized gradient approximation made simple. *Phys. Rev. Lett.* **1996,** *77*, 3865-3868.

114. Kohanoff, J., *Electronic structure calculation of solids and molecules: Theory and computational methods;*. Cambridge University Press: New York, **2006**.

115. Monkhorst, H. J.; Pack, J. D., Special points for brillouin-zone integrations *Phys. Rev. B.* **1976,** *13*, 5188-5192.

116. Gregor, T.; Mauri, F.; Car, R., A comparison of methods for the calculation of NMR chemical shifts. *J. Chem. Phys.* **1999,** *111*, 1815-1822.

117. Vanderbilt, D., Soft self-consistent pseudopotentials in a generalised eigenvalue formalism. *Phys. Rev. B.* **1990,** *41*, 7892-7895.

118. Clark, S. J.; Segall, M. D.; Pickard, C. J.; Hasnip, P. J.; Probert, M. J.; Refson, K.; Payne, M. C., First principles methods using CASTEP. *Z .Kristallogr. Cryst. Mater* **2005,** *220*, 567-570.

119. Van De Walle, C. G.; Blochl, P. E., Ist Principles calculations of hyperfine parameters. *Phys. Rev. B.* **1993,** *47*, 4244-4255.

120. Pickard, C. J.; Mauri, F., All-electron magnetic response with pseudopotentials: NMR chemical shifts. *Phys. Rev. B.* **2001,** *63*, 245101.

121. Nocedal, J., Wright, S., *Numerical optimization*. Springer: New York, **2006**.

122. Ashbrook, S. E.; McKay, D., Combining solid-state NMR spectroscopy with first-principles calculations - a guide to NMR crystallography. *Chem. Commun.* **2016,** *52*, 7186-7204.

123. Hartman, J. D.; Kudla, R. A.; Day, G. M.; Mueller, L. J.; Beran, G. J. O., Benchmark fragment-based ^{1}H, ^{13}C, ^{15}N and ^{17}O chemical shift predictions in molecular crystals. *Phys. Chem. Chem. Phys* **2016,** *18*, 21686-21709.

124. Beran, G. J. O.; Hartman, J. D.; Heit, Y. N., Predicting Molecular Crystal Properties from First Principles: Finite Temperature Thermochemistry to NMR Crystallography. *Acc. Chem. Res.* **2016,** *49*, 2501-2508.

125. Harris, R. K.; Hodgkinson, P.; Pickard, C. J.; Yates, J. R.; Zorin, V., Chemical shift computations on a crystallographic basis: some reflections and comments. *Magn. Reson. Chem.* **2007,** *45*, S174-S186.

126. Reddy, G. N. M.; Cook, D. S.; Iuga, D.; Walton, R. I.; Marsh, A.; Brown, S. P., An NMR crystallography study of the hemihydrate of 2', 3'-O-isopropylidineguanosine. *Solid State Nucl. Magn. Reson.* **2015,** *65*, 41-48.

127. Webber, A. L.; Emsley, L.; Claramunt, R. M.; Brown, S. P., NMR Crystallography of Campho[2,3-c]pyrazole (Z' = 6): Combining High-Resolution ^{1}H-^{13}C Solid-State MAS NMR Spectroscopy and GIPAW Chemical-Shift Calculations. *J. Phys. Chem..A* **2010,** *114*, 10435-10442.

128. Bradley, J. P., Velaga, S. P, Antzutkin, N. A., Brown, S . P, Probing intermolecular crystal packing in γ-indomethacin by high-resolution ^{1}H solid-state NMR spectroscopy. *Cryst. Growth Des.* **2011,** *11*, 3463-3471.

129. Uldry, A.-C.; Griffin, J. M.; Yates, J. R.; Perez-Torralba, M.; Maria, M. D. S.; Webber, A. L.; Beaumont, M. L. L.; Samoson, A.; Claramunt, R. M.; Pickard, C. J.; Brown, S. P., Quantifying weak hydrogen bonding in uracil and 4-cyano-4 '-ethynylbiphenyl: A combined computational and experimental investigation of NMR chemical shifts in the solid state. *J. Amer. Chem. Soc.* **2008,** *130*, 945-954.

130. Bak, M.; Rasmussen, J. T.; Nielsen, N. C., SIMPSON: A general simulation program for solid-state NMR spectroscopy. *J. Magn. Reson.* **2000,** *147*, 296-330.

131. Ross, A., Willson, V,L., *Linear Regression. In: Basic and Advanced Statistical Tests*. SensePublishers: Rotterdam, 2017.

132. Bernstein, J., *Polymorphism in molecular crystals*. Oxford University Press: Oxford, **2002**.

133. Harris, R. K., NMR studies of organic polymorphs & solvates. *Analyst* **2006,** *131*, 351-373.

134. Masuda, K.; Tabata, S.; Kono, H.; Sakata, Y.; Hayase, T.; Yonemochi, E.; Terada, K., Solid-state ^{13}C NMR study of indomethacin polymorphism. *Int. J. Pharm.* **2006,** *318*, 146-153.

135. Ripmeester, J. A., Application of solid-state ^{13}C NMR to the study of polymorphs, clatharates, and complexes. *Chem. Phys. Lett.* **1980,** *74*, 536-538.

136. Dudek, M. K.; Kazmierski, S.; Kostrzewa, M.; Potrzebowski, M. J., Solid-State NMR Studies of Molecular Crystals. *Annu. Rep. NMR. Spectrosc* **2018,** *95*, 1-81.

137. Yates, J. R.; Dobbins, S. E.; Pickard, C. J.; Mauri, F.; Ghi, P. Y.; Harris, R. K., A combined first principles computational and solid-state NMR study of a molecular crystal: flurbiprofen. *Phys. Chem. Chem. Phys* **2005,** *7*, 1402-1407.

138. Harris, R. K., Applications of solid-state NMR to pharmaceutical polymorphism and related matters. *J. Pharm. Pharmacol.* **2007,** *59*, 225-239.

139. Harris, R. K.; Cadars, S.; Emsley, L.; Yates, J. R.; Pickard, C. J.; Jetti, R. K. R.; Griesser, U. J., NMR crystallography of oxybuprocaine hydrochloride, Modification II. *Phys. Chem. Chem. Phys* **2007,** *9*, 360-368.

140. Harris, R. K.; Ghi, P. Y.; Hammond, R. B.; Ma, C. Y.; Roberts, K. J.; Yates, J. R.; Pickard, C. J., Solid-state NMR and computational studies of 4-methyl-2-nitroacetanilide. *Magn. Reson. Chem.* **2006,** *44*, 325-333.

141. Harris, R. K.; Ghi, P. Y.; Puschmann, H.; Apperley, D. C.; Griesser, U. J.; Hammond, R. B.; Ma, C. Y.; Roberts, K. J.; Pearce, G. J.; Yates, J. R.; Pickard, C. J., Structural studies of the polymorphs of carbamazepine, its dihydrate, and two solvates. *Org. Process Res. Dev.* **2005,** *9*, 902-910.

142. Harris, R. K.; Hodgkinson, P.; Larsson, T.; Muruganantham, A.; Ymen, I.; Yufit, D. S.; Zorin, V., Characterization of polymorphs and solvates of terbutaline sulfate. *Cryst. Growth Des.* **2008,** *8*, 80-90.

143. Harris, R. K.; Joyce, S. A.; Pickard, C. J.; Cadars, S.; Emsley, L., Assigning carbon-13 NMR spectra to crystal structures by the INADEQUATE pulse sequence and first principles computation: a case study of two forms of testosterone. *Phys. Chem. Chem. Phys* **2006,** *8*, 137-143.

144. Yates, J. R.; Pham, T. N.; Pickard, C. J.; Mauri, F.; Amado, A. M.; Gil, A. M.; Brown, S. P., An investigation of weak CH···O hydrogen bonds in maltose anomers by a combination of calculation and experimental solid-state NMR spectroscopy. *J. Amer. Chem. Soc.* **2005,** *127*, 10216-10220.

145. Kibalchenko, M.; Lee, D.; Shao, L.; Payne, M. C.; Titman, J. J.; Yates, J. R., Distinguishing hydrogen bonding networks in alpha-D-galactose using NMR experiments and first principles calculations. *Chem. Phys. Lett.* **2010,** *498*, 270-276.

146. Brouwer, D. H.; Langendoen, K. P.; Ferrant, Q., Measurement and calculation of C-13 chemical shift tensors in alpha-glucose and alpha-glucose monohydrate. *Can. J. Chem.* **2011,** *89*, 737-744.

147. Webber, A. L.; Emsley, L.; Claramunt, R. M.; Brown, S. P., NMR Crystallography of Campho 2,3-c pyrazole (Z '=6): Combining High-Resolution ^{1}H-^{13}C Solid-State MAS NMR Spectroscopy and GIPAW Chemical-Shift Calculations. *J. Phys. Chem. A.* **2010,** *114*, 10435-10442.

148. Joyce, S. A.; Yates, J. R.; Pickard, C. J.; Brown, S. P., Density functional theory calculations of hydrogen-bond-mediated NMR J coupling in the solid state. *J. Amer. Chem. Soc.* **2008,** *130*, 12663-12670.

149. Hung, I.; Uldry, A.-C.; Becker-Baldus, J.; Webber, A. L.; Wong, A.; Smith, M. E.; Joyce, S. A.; Yates, J. R.; Pickard, C. J.; Dupree, R.; Brown, S. P., Probing Heteronuclear ^{15}N-^{17}O and ^{13}C-^{17}O Connectivities and Proximities by Solid-State NMR Spectroscopy. *J. Amer. Chem. Soc.* **2009,** *131*, 1820-1834.

150. Stievano, L.; Tielens, F.; Lopes, I.; Folliet, N.; Gervais, C.; Costa, D.; Lambert, J.-F., Density Functional Theory Modeling and Calculation of NMR Parameters: An ab Initio Study of the Polymorphs of Bulk Glycine. *Cryst. Growth Des.* **2010,** *10*, 3657-3667.

151. Webber, A. L.; Masiero, S.; Pieraccini, S.; Burey, J. C.; Tatton, A. S.; Iuga, D.; Pham, T. N.; Spada, G. P.; Brown, S. P., Identifying Guanosine Self Assembly at Natural Isotopic Abundance by High-Resolution ^{1}H and ^{13}C Solid-State NMR Spectroscopy. *J. Amer. Chem. Soc.* **2011,** *133*, 19777-19795.

152. Reddy, G. N. M.; Cook, D. S.; Iuga, D.; Walton, R. I.; Marsh, A.; Brown, S. P., An NMR crystallography study of the hemihydrate of 2 ', 3 '-O-isopropylidineguanosine. *Solid State Nucl. Magn. Reson.* **2015,** *65*, 41-48.

153. Reddy, G. N. M.; Marsh, A.; Davis, J. T.; Masiero, S.; Brown, S. P., Interplay of Noncovalent Interactions in Ribbon-like Guanosine Self-Assembly: An NMR Crystallography Study. *Cryst. Growth Des.* **2015,** *15*, 5945-5954.

154. Dracinsky, M.; Jansa, P.; Ahonen, K.; Budesinsky, M., Tautomerism and the Protonation/Deprotonation of Isocytosine in Liquid- and Solid-States Studied by NMR Spectroscopy and Theoretical Calculations. *Eur. J. Org. Chem.* **2011**, 1544-1551.

155. Carnevale, D.; del Amo, V.; Philp, D.; Ashbrook, S. E., Detecting solid-state reactivity in 10-hydroxy-10,9-boroxophenanthrene using NMR spectroscopy. *Tetrahedron* **2010,** *66*, 6238-6250.

156. Marques, M. A. L.; d'Avezac, M.; Mauri, F., Magnetic response and NMR spectra of carbon nanotubes from ab initio calculations. *Phys. Rev. B.* **2006,** *73*, 125433.

157. Huang, P.; Schwegler, E.; Galli, G., Water Confined in Carbon Nanotubes: Magnetic Response and Proton Chemical Shieldings. *J. Phys. Chem. C* **2009,** *113*, 8696-8700.

158. Tatton, A. S.; Blade, H.; Brown, S. P.; Hodgkinson, P.; Hughes, L. P.; Lill, S. O. N.; Yates, J. R., Improving Confidence in Crystal Structure Solutions Using NMR Crystallography: The Case of beta-Piroxicam. *Cryst. Growth Des.* **2018,** *18*, 3339-3351.

159. Gaglioti, K.; Chierotti, M. R.; Grifasi, F.; Gobetto, R.; Griesser, U. J.; Hasa, D.; Voinovich, D., Improvement of the water solubility of tolfenamic acid by new multiple-component crystals produced by mechanochemical methods. *Crystengcomm* **2014,** *16*, 8252-8262.

160. Andersen, K. V.; Larsen, S.; Alhede, B.; Gelting, N.; Buchardt, O., Characterization of two polymorphic forms of tolfenamic acid, N-(2-methyl-3-chlorophenyl)anthranilic acid: their crystal structures and relative stabilities. *J. Chem. Soc.* **1989**, 1443-1447.

161. Segall, M. D.; Lindan, P. J. D.; Probert, M. J.; Pickard, C. J.; Hasnip, P. J.; Clark, S. J.; Payne, M. C., First-principles simulation: ideas, illustrations and the CASTEP code. *J.Phys.Condens.Matter* **2002,** *14*, 2717-2744.

162. Yates, J. R.; Pickard, C. J.; Mauri, F., Calculation of NMR chemical shifts for extended systems using ultrasoft pseudopotentials. *Phys. Rev. B.* **2007,** *76*, 024401.

163. Sturniolo, S.; Green, T. F. G.; Hanson, R. M.; Zilka, M.; Refson, K.; Hodgkinson, P.; Brown, S. P.; Yates, J. R., Visualization and processing of computed solid-state NMR parameters: MagresView and MagresPython. *Solid State Nucl. Magn. Reson.* **2016,** *78*, 64-70.

164. Du, W.; Cruz-Cabeza, A. J.; Woutersen, S.; Davey, R. J.; Yin, Q., Can the study of self-assembly in solution lead to a good model for the nucleation pathway? The case of tolfenamic acid. *Chemical Science* **2015,** *6*, 3515-3524.

165. Sommer, W.; Gottwald, J.; Demco, D. E.; Spiess, H. W., Dipolar heteronuclear multiple-quantum NMR spectroscopy in rotating solids. *J. Magn. Reson., Ser. A* **1995,** *113*, 131-134.

166. Costa, P. R.; Gross, J. D.; Hong, M.; Griffin, R. G., Solid-state NMR measurement of Ψ in peptides: a NCCN 2Q-heteronuclear local field experiment. *Chem. Phys. Lett.* **1997,** *280*, 95-103.

167. Webber, A. L.; Elena, B.; Griffin, J. M.; Yates, J. R.; Pham, T. N.; Mauri, F.; Pickard, C. J.; Gil, A. M.; Stein, R.; Lesage, A.; Emsley, L.; Brown, S. P., Complete ^{1}H resonance assignment of beta-maltose from ^{1}H-^{1}H DQ-SQ CRAMPS and ^{1}H (DQ-DUMBO)-^{13}C SQ refocused INEPT 2D solid-state NMR spectra and first principles GIPAW calculations. *Phys. Chem. Chem. Phys* **2010,** *12*, 6970-6983.

168. Brown, S. P.; Zhu, X. X.; Saalwachter, K.; Spiess, H. W., An investigation of the hydrogen-bonding structure in bilirubin by ^{1}H double-quantum magic-angle spinning solid-state NMR spectroscopy. *J. Amer. Chem. Soc.* **2001,** *123*, 4275-4285.

169. Dumez, J. N.; Pickard, C. J., Calculation of NMR chemical shifts in organic solids: Accounting for motional effects. *J. Chem. Phys.* **2009,** *130*, 104701.

170. Yates, J. R.; Pham, T. N.; Pickard, C. J.; Mauri, F.; Amado, A. M.; Gil, A. M.; Brown, S. P., An investigation of weak CH ...O hydrogen bonds in maltose anomers by a combination of calculation and experimental solid-state NMR spectroscopy. *J. Amer. Chem. Soc.* **2005,** *127*, 10216-10220.

171. Schmidt, J.; Hoffmann, A.; Spiess, H. W.; Sebastiani, D., Bulk chemical shifts in hydrogen-bonded systems from first-principles calculations and solid-state-NMR. *J. Phys. Chem. B* **2006,** *110*, 23204-23210.

172. Poppler, A. C.; Corlett, E. K.; Pearce, H.; Seymour, M. P.; Reid, M.; Montgomery, M. G.; Brown, S. P., Single-crystal X-ray diffraction and NMR crystallography of a 1:1 cocrystal of dithianon and pyrimethanil. *Acta Crystallogr., Sect. C: Cryst. Struct. Commun.* **2017,** *73*, 149-156.

173. Gowda, C. M.; Vasconcelos, F.; Schwartz, E.; Van Eck, E. R. H.; Marsman, M.; Cornelissen, J.; Rowan, A. E.; de Wijs, G. A.; Kentgens, A. P. M., Hydrogen bonding and chemical shift assignments in carbazole functionalized isocyanides from solid-state NMR and first-principles calculations. *Phys. Chem. Chem. Phys* **2011,** *13*, 13082-13095.

174. Mafra, L.; Santos, S. M.; Siegel, R.; Alves, I.; Paz, F. A. A.; Dudenko, D.; Spiess, H. W., Packing Interactions in Hydrated and Anhydrous Forms of the Antibiotic Ciprofloxacin: a Solid-State NMR, X-ray Diffraction, and Computer Simulation Study. *J. Amer. Chem. Soc.* **2012,** *134*, 71-74.

175. Dudenko, D. V.; Williams, P. A.; Hughes, C. E.; Antzutkin, O. N.; Velaga, S. P.; Brown, S. P.; Harris, K. D. M., Exploiting the Synergy of Powder X-ray Diffraction and Solid-State NMR Spectroscopy in Structure Determination of Organic Molecular Solids. *J. Phys. Chem. C* **2013,** *117*, 12258-12265.

176. Dudenko, D. V.; Yates, J. R.; Harris, K. D. M.; Brown, S. P., An NMR crystallography DFT-D approach to analyse the role of intermolecular hydrogen bonding and π-π interactions in driving cocrystallisation of indomethacin and nicotinamide. *CrystEngComm* **2013,** *15*, 8797-8807.

177. Cruz-Cabeza, A. J.; Bernstein, J., Conformational Polymorphism. *Chem. Rev.* **2014,** *114*, 2170-2191.

178. Bauer, J., Polymorphism—a critical consideration in pharmaceutical development manufacturing, and stability. *J. Valid Technol.* **2008,** *5*, 15-23.

179. Gushurst, K. S.; Nyman, J.; Boerrigter, S. X. M., The PO13 crystal structure of ROY. *Crystengcomm* **2019,** *21*, 1363-1368.

180. Haleblian, J., McCrone. W.,, Pharmaceutical Applications of Polymorphism. *J. Pharm. Sci.* **1969,** *58*, 911-929.

181. Vippagunta, S. R.; Brittain, H. G.; Grant, D. J. W., Crystalline solids. *Adv. Drug Delivery Rev.* **2001,** *48*, 3-26.

182. Kulkarni, G. U.; Kumaradhas, P.; Rao, C. N. R., Charge density study of the polymorphs of p-nitrophenol. *Chem. Mater* **1998,** *10*, 3498-3505.

183. Albesa-Jove, D.; Kariuki, B. M.; Kitchin, S. J.; Grice, L.; Cheung, E. Y.; Harris, K. D. M., Challenges in direct-space structure determination from powder diffraction data: A molecular material with four independent molecules in the asymmetric unit. *ChemPhysChem* **2004,** *5*, 414-418.

184. Brog, J. P.; Chanez, C. L.; Crochet, A.; Fromm, K. M., Polymorphism, what it is and how to identify it: a systematic review. *Rsc Adv.* **2013,** *3*, 16905-16931.

185. Price, S. L., Predicting crystal structures of organic compounds. *Chem. Soc. Rev.* **2014,** *43*, 2098-2111.

186. Price, S. L., Control and prediction of the organic solid state: a challenge to theory and experiment. *Proc. Royal Soc. A* **2018,** *474*, 20180351.

187. Day, G. M., Current approaches to predicting molecular organic crystal structures. *Crystallogr. Rev.* **2011,** *17*, 3-52.

188. Stephen, A. D.; Nidhin, P. V.; Srinivasan, P., Ab initio Prediction of the Stable Polymorphs of 4-amino-3,5-dinitrobenzamide (DOPLOL). *Croat. Chem. Acta* **2017,** *90*, 87-98.

189. Lim, G. K.; Fujii, K.; Harris, K. D. M.; Apperley, D. C., Structure Determination from Powder X-ray Diffraction Data of a New Polymorph of a High-Density Organic Hydrate Material, with an Assessment of Hydrogen-Bond Disorder by Rietveld Refinement. *Cryst. Growth Des.* **2011,** *11*, 5192-5199.

190. Thakral, N. K.; Zanon, R. L.; Kelly, R. C.; Thakral, S., Applications of Powder X-Ray Diffraction in Small Molecule Pharmaceuticals: Achievements and Aspirations. *J. Pharm. Sci.* **2018,** *107*, 2969-2982.

191. Bauer, J.; Spanton, S.; Henry, R.; Quick, J.; Dziki, W.; Porter, W.; Morris, J., Ritonavir: An extraordinary example of conformational polymorphism. *Pharm. Res.* **2001,** *18*, 859-866.

192. Lommerse, J. P. M.; Motherwell, W. D. S.; Ammon, H. L.; Dunitz, J. D.; Gavezzotti, A.; Hofmann, D. W. M.; Leusen, F. J. J.; Mooij, W. T. M.; Price, S. L.; Schweizer, B.; Schmidt, M. U.; van Eijck, B. P.; Verwer, P.; Williams, D. E., A test of crystal structure prediction of small organic molecules. *Acta Crystallogr., Sect. B: Struct. Sci* **2000,** *56*, 697-714.

193. Motherwell, W. D. S.; Ammon, H. L.; Dunitz, J. D.; Dzyabchenko, A.; Erk, P.; Gavezzotti, A.; Hofmann, D. W. M.; Leusen, F. J. J.; Lommerse, J. P. M.; Mooij, W. T. M.; Price, S. L.; Scheraga, H.; Schweizer, B.; Schmidt, M. U.; van Eijck, B. P.; Verwer, P.; Williams, D. E., Crystal

structure prediction of small organic molecules: a second blind test. *Acta Crystallogr., Sect. B: Struct. Sci* **2002,** *58*, 647-661.

194. Day, G. M.; Cooper, T. G.; Cruz-Cabeza, A. J.; Hejczyk, K. E.; Ammon, H. L.; Boerrigter, S. X. M.; Tan, J. S.; Della Valle, R. G.; Venuti, E.; Jose, J.; Gadre, S. R.; Desiraju, G. R.; Thakur, T. S.; van Eijck, B. P.; Facelli, J. C.; Bazterra, V. E.; Ferraro, M. B.; Hofmann, D. W. M.; Neumann, M. A.; Leusen, F. J. J.; Kendrick, J.; Price, S. L.; Misquitta, A. J.; Karamertzanis, P. G.; Welch, G. W. A.; Scheraga, H. A.; Arnautova, Y. A.; Schmidt, M. U.; van de Streek, J.; Wolf, A. K.; Schweizer, B., Significant progress in predicting the crystal structures of small organic molecules - a report on the fourth blind test. *Acta Crystallogr., Sect. B: Struct. Sci* **2009,** *65*, 107-125.

195. Day, G. M.; Motherwell, W. D. S.; Ammon, H. L.; Boerrigter, S. X. M.; Della Valle, R. G.; Venuti, E.; Dzyabchenko, A.; Dunitz, J. D.; Schweizer, B.; van Eijck, B. P.; Erk, P.; Facelli, J. C.; Bazterra, V. E.; Ferraro, M. B.; Hofmann, D. W. M.; Leusen, F. J. J.; Liang, C.; Pantelides, C. C.; Karamertzanis, P. G.; Price, S. L.; Lewis, T. C.; Nowell, H.; Torrisi, A.; Scheraga, H. A.; Arnautova, Y. A.; Schmidt, M. U.; Verwer, P., A third blind test of crystal structure prediction. *Acta Crystallogr., Sect. B: Struct. Sci* **2005,** *61*, 511-527.

196. Reilly, A. M.; Cooper, R. I.; Adjiman, C. S.; Bhattacharya, S.; Boese, A. D.; Brandenburg, J. G.; Bygrave, P. J.; Bylsma, R.; Campbell, J. E.; Car, R.; Case, D. H.; Chadha, R.; Cole, J. C.; Cosburn, K.; Cuppen, H. M.; Curtis, F.; Day, G. M.; DiStasio, R. A.; Dzyabchenko, A.; van Eijck, B. P.; Elking, D. M.; van den Ende, J. A.; Facelli, J. C.; Ferraro, M. B.; Fusti-Molnar, L.; Gatsiou, C. A.; Gee, T. S.; de Gelder, R.; Ghiringhelli, L. M.; Goto, H.; Grimme, S.; Guo, R.; Hofmann, D. W. M.; Hoja, J.; Hylton, R. K.; Iuzzolino, L.; Jankiewicz, W.; de Jong, D. T.; Kendrick, J.; de Klerk, N. J. J.; Ko, H. Y.; Kuleshova, L. N.; Li, X. Y.; Lohani, S.; Leusen, F. J. J.; Lund, A. M.; Lv, J.; Ma, Y. M.; Marom, N.; Masunov, A. E.; McCabe, P.; McMahon, D. P.; Meekes, H.; Metz, M. P.; Misquitta, A. J.; Mohamed, S.; Monserrat, B.; Needs, R. J.; Neumann, M. A.; Nyman, J.; Obata, S.; Oberhofer, H.; Oganov, A. R.; Orendt, A. M.; Pagola, G. I.; Pantelides, C. C.; Pickard, C. J.; Podeszwa, R.; Price, L. S.; Price, S. L.; Pulido, A.; Read, M. G.; Reuter, K.; Schneider, E.; Schober, C.; Shields, G. P.; Singh, P.; Sugden, I. J.; Szalewicz, K.; Taylor, C. R.; Tkatchenko, A.; Tuckerman, M. E.; Vacarro, F.; Vasileiadis, M.; Vazquez-Mayagoitia, A.; Vogt, L.; Wang, Y. C.; Watson, R. E.; de Wijs, G. A.; Yang, J.; Zhu, Q.; Groom, C. R., Report on the sixth blind test of organic crystal structure prediction methods. *Acta Crystallogr., Sect. B: Struct. Sci* **2016,** *72*, 439-459.

197. Price, S. L., From crystal structure prediction to polymorph prediction: interpreting the crystal energy landscape. *Phys. Chem. Chem. Phys* **2008,** *10*, 1996-2009.

198. Xu, W. Q.; Zhu, Q.; Hu, C. H., The Structure of Glycine Dihydrate: Implications for the Crystallization of Glycine from Solution and Its Structure in Outer Space. *Angew. Chem. Int. Ed.* **2017,** *56*, 2030-2034.

199. Salager, E.; Day, G. M.; Stein, R. S.; Pickard, C. J.; Elena, B.; Emsley, L., Powder Crystallography by Combined Crystal Structure Prediction and High-Resolution H-1 Solid-State NMR Spectroscopy. *J. Amer. Chem. Soc.* **2010,** *132*, 2564-2566.

200. Baias, M.; Widdifield, C. M.; Dumez, J. N.; Thompson, H. P. G.; Cooper, T. G.; Salager, E.; Bassil, S.; Stein, R. S.; Lesage, A.; Day, G. M.; Emsley, L., Powder crystallography of pharmaceutical materials by combined crystal structure prediction and solid-state ^{1}H NMR spectroscopy. *Phys. Chem. Chem. Phys* **2013,** *15*, 8069-8080.

201. Baias, M.; Dumez, J. N.; Svensson, P. H.; Schantz, S.; Day, G. M.; Emsley, L., De Novo Determination of the Crystal Structure of a Large Drug Molecule by Crystal Structure Prediction-Based Powder NMR Crystallography. *J. Amer. Chem. Soc.* **2013,** *135*, 17501-17507.

202. Pickard, C. J.; Needs, R. J., Ab initio random structure searching. *J.Phys.Condens.Matter* **2011,** *23*, 053201.

203. See, K. A.; Leskes, M.; Griffin, J. M.; Britto, S.; Matthews, P. D.; Emly, A.; Van der Ven, A.; Wright, D. S.; Morris, A. J.; Grey, C. P.; Seshadri, R., Ab Initio Structure Search and in Situ ^{7}Li NMR Studies of Discharge Products in the Li-S Battery System. *J. Amer. Chem. Soc.* **2014,** *136*, 16368-16377.

204. Moran, R. F.; McKay, D.; Pickard, C. J.; Berry, A. J.; Griffin, J. M.; Ashbrook, S. E., Hunting for hydrogen: random structure searching and prediction of NMR parameters of hydrous wadsleyite. *Phys. Chem. Chem. Phys* **2016,** *18*, 10173-10181.

205. Zilka, M.; Dudenko, D. V.; Hughes, C. E.; Williams, P. A.; Sturniolo, S.; Franks, W. T.; Pickard, C. J.; Yates, J. R.; Harris, K. D. M.; Brown, S. P., Ab initio random structure searching of organic molecular solids: assessment and validation against experimental data. *Phys. Chem. Chem. Phys* **2017,** *19*, 25949-25960.

206. Thureau, P.; Sturniolo, S.; Zilka, M.; Ziarelli, F.; Viel, S.; Yates, J. R.; Mollica, G., Reducing the computational cost of NMR crystallography of organic powders at natural isotopic abundance with the help of ^{13}C-^{13}C dipolar couplings. *Magn. Reson. Chem.* **2019,** *57*, 256-264.

207. Hofstetter, A.; Emsley, L., Positional Variance in NMR Crystallography. *J. Amer. Chem. Soc.* **2017,** *139*, 2573-2576.

208. Paruzzo, F. M.; Hofstetter, A.; Musil, F.; De, S.; Ceriotti, M.; Emsley, L., Chemical shifts in molecular solids by machine learning. *Nat. Commun.* **2018,** *9*, 4501.

209. Uzoh, O. G.; Cruz-Cabeza, A. J.; Price, S. L., Is the Fenamate Group a Polymorphophore? Contrasting the Crystal Energy Landscapes of Fenamic and Tolfenamic Acids. *Cryst. Growth Des.* **2012,** *12*, 4230-4239.

210. Sharman, G. J., Conformation and Stereochemical Analysis of Drug Molecules. *Emagres* **2015,** *4*, 105-115.

211. Habgood, M., Conformational ensemble comparison for small molecules in drug discovery. *J. Comput.-Aided Mol. Des.* **2018,** *32*, 841-852.

212. Blundell, C. D.; Nowak, T.; Watson, M. J., Chapter Two - Measurement, Interpretation and Use of Free Ligand Solution Conformations in Drug Discovery. *Prog. Med. Chem.*, **2016**, 55, 45-147.

213. Blundell, C. D.; Packer, M. J.; Almond, A., Quantification of free ligand conformational preferences by NMR and their relationship to the bioactive conformation. *Bioorg. Med. Chem.* **2013,** *21*, 4976-4987.

214. Lopez-Mejias, V.; Kampf, J. W.; Matzger, A. J., Polymer-Induced Heteronucleation of Tolfenamic Acid: Structural Investigation of a Pentamorph. *J. Amer. Chem. Soc.* **2009,** *131*, 4554-4555.

215. DiRenzo, F.; Cambon, H.; Dutartre, R., A 28-year-old synthesis of micelle-templated mesoporous silica. *Microporous Mater* **1997,** *10*, 283-286.

216. Beck, J. S.; Vartuli, J. C.; Roth, W. J.; Leonowicz, M. E.; Kresge, C. T.; Schmitt, K. D.; Chu, C. T. W.; Olson, D. H.; Sheppard, E. W.; McCullen, S. B.; Higgins, J. B.; Schlenker, J. L., A new family of mesoporus molecular-sieves prepared with liquid-crystal templates. *J. Amer. Chem. Soc.* **1992,** *114*, 10834-10843.

217. Mercier, L.; Pinnavaia, T. J., Access in mesoporous materials: Advantages of a uniform pore structure in the design of a heavy metal ion adsorbent for environmental remediation. *Adv. Mater.* **1997,** *9*, 500-503.

218. Zhao, D. Y.; Feng, J. L.; Huo, Q. S.; Melosh, N.; Fredrickson, G. H.; Chmelka, B. F.; Stucky, G. D., Triblock copolymer syntheses of mesoporous silica with periodic 50 to 300 angstrom pores. *Science* **1998,** *279*, 548-552.

219. Lee, H. I.; Kim, J. H.; Stucky, G. D.; Shi, Y.; Pak, C.; Kim, J. M., Morphology-selective synthesis of mesoporous SBA-15 particles over micrometer, submicrometer and nanometer scales. *J. Mater. Chem* **2010,** *20*, 8483-8487.

220. Pathan, S.; Solanki, P.; Patel, A., Functionalized SBA-15 for controlled release of poorly soluble drug, Erythromycin. *Microporous Mesoporous Mat.* **2018,** *258*, 114-121.

221. Vallet-Regi, M.; Colilla, M.; Izquierdo-Barba, I.; Manzano, M., Mesoporous Silica Nanoparticles for Drug Delivery: Current Insights. *Molecules* **2018,** *23*, 47.

222. Yang, Y.; Chang, J. W.; Rioux, R. M., Structural elucidation of supported Rh complexes derived from RhCl $(PPh_3)_{(3)}$ immobilized on surface-functionalized SBA-15 and their catalytic performance for C-heteroatom (S, O) bond formation. *J. Catal.* **2018,** *365*, 43-54.

223. Mori, K.; Masuda, S.; Tanaka, H.; Yoshizawa, K.; Che, M.; Yamashita, H., Phenylamine-functionalized mesoporous silica supported PdAg nanoparticles: a dual heterogeneous catalyst for formic acid/CO_2-mediated chemical hydrogen delivery/storage. *Chem. Commun.* **2017,** *53*, 4677-4680.

224. Li, R. Y.; Song, H. Y.; Chen, J., Propylsulfonic Acid Functionalized SBA-15 Mesoporous Silica as Efficient Catalysts for the Acetalization of Glycerol. *Catalysts* **2018,** *8*, 297.

225. Zhu, Y.; Cheng, Z. X.; Xiang, Q.; Chen, X. K.; Xu, J. Q., Synthesis of functionalized mesoporous TiO2-SiO2 with organic fluoroalcohol as high performance DMMP gas sensor. *Sens. Actuators, B* **2017,** *248*, 785-792.

226. Lewandowski, D.; Schroeder, G.; Sawczak, M.; Ossowski, T., Fluorescence properties of riboflavin-functionalized mesoporous silica SBA-15 and riboflavin solutions in presence of different metal and organic cations. *J. Phys. Chem. Solids* **2015,** *85*, 56-61.

227. Castillo, R. R.; Baeza, A.; Vallet-Regi, M., Recent applications of the combination of mesoporous silica nanoparticles with nucleic acids: development of bioresponsive devices, carriers and sensors. *Biomater. Sci.* **2017,** *5*, 353-377.

228. Hou, L.; Feng, F.; You, W. B.; Xu, P. C.; Luo, F.; Tian, B. W.; Zhou, H. M.; Li, X. X., Pore size effect of mesoporous silica stationary phase on the separation performance of microfabricated gas chromatography columns. *J. Chromatogr., A* **2018,** *1552*, 73-78.

229. Mafra, L.; Cendak, T.; Schneider, S.; Wiper, P. V.; Pires, J.; Gomes, J. R. B.; Pinto, M. L., Amine functionalized porous silica for CO_2/CH_4 separation by adsorption: Which amine and why. *Chem. Eng. J* **2018,** *336*, 612-621.

230. Yang, Z.; Chen, G.; Weng, H. Q.; Shen, W. L.; Huang, Z. Y.; Lin, M. Z., Efficient and selective separation of U(VI) and Th(IV) from rare earths using functionalized hierarchically mesoporous silica. *J. Mater. Sci.* **2018,** *53*, 3398-3416.

231. Hopkins, P. D.; Mastren, T.; Florek, J.; Copping, R.; Brugh, M.; John, K. D.; Nortier, M. F.; Birnbaum, E. R.; Kleitz, F.; Fassbender, M. E., Synthesis and radiometric evaluation of diglycolamide functionalized mesoporous silica for the chromatographic separation of actinides Th, Pa and U. *Dalton Trans.* **2018,** *47*, 5189-5195.

232. Gok, M.; Sert, S.; Ozevci, G.; Eral, M., Efficient adsorption of Th(IV) from aqueous solution by modified SBA-15 mesoporous silica. *Nucl. Sci. Tech* **2018,** *29,* 94-103.

233. Ye, L.; Wang, Y.; Chen, X. Y.; Yue, B.; Tsang, S. C.; He, H. Y., Three-dimensionally ordered mesoporous Pd networks templated by a silica super crystal and their application in formic acid electrooxidation. *Chem. Commun.* **2011,** *47,* 7389-7391.

234. Liu, J. L.; Li, C. Y.; Li, F. Y., Fluorescence turn-on chemodosimeter-functionalized mesoporous silica nanoparticles and their application in cell imaging. *J. Mater. Chem* **2011,** *21,* 7175-7181.

235. Guo, F.; Zhu, G. R.; Gao, C. J., Organic-Inorganic Hybrid Mesoporous Silicas and Their Applications in Environmental Protection. *Prog. Chem.* **2011,** *23*, 1237-1250.

236. Fu, X. C.; Chen, X.; Wang, J.; Liu, J. H., Fabrication of carboxylic functionalized superparamagnetic mesoporous silica microspheres and their application for removal basic dye pollutants from water. *Microporous Mesoporous Mat.* **2011,** *139,* 8-15.

237. Cho, Y. N.; Ben Borgens, R., The preparation of polypyrrole surfaces in the presence of mesoporous silica nanoparticles and their biomedical applications. *Nanotechnology* **2010,** *21,* 205102.

238. Kim, M. H.; Na, H. K.; Kim, Y. K.; Ryoo, S. R.; Cho, H. S.; Lee, K. E.; Jeon, H.; Ryoo, R.; Min, D. H., Facile Synthesis of Monodispersed Mesoporous Silica Nanoparticles with Ultralarge Pores and Their Application in Gene Delivery. *Acs Nano* **2011,** *5*, 3568-3576.

239. Yang, C. M.; Zibrowius, B.; Schuth, F., A novel synthetic route for negatively charged ordered mesoporous silica SBA-15. *Chem. Commun.* **2003**, 1772-1773.

240. Tsai, H.-H. G.; Jheng, G.-L.; Kao, H.-M., Direct evidence for interactions between acidic functional groups and silanols in cubic mesoporous organosilicas. *J. Amer. Chem. Soc.* **2008,** *130,* 11566-11567.

241. Tsai, C.-T.; Pan, Y.-C.; Ting, C.-C.; Vetrivel, S.; Chiang, A. S. T.; Fey, G. T. K.; Kao, H.-M., A simple one-pot route to mesoporous silicas SBA-15 functionalized with exceptionally high loadings of pendant carboxylic acid groups. *Chem. Commun.* **2009**, 5018-5020.

242. Aliev, A.; Ou, D. L.; Ormsby, B.; Sullivan, A. C., Porous silica and polysilsesquioxane with covalently linked phosphonates and phosphonic acids. *J. Mater. Chem. A* **2000,** *10*, 2758-2764.

243. Corriu, R. J. P.; Datas, L.; Guari, Y.; Mehdi, A.; Reye, C.; Thieuleux, C., Ordered SBA-15 mesoporous silica containing phosphonic acid groups prepared by a direct synthetic approach. *Chem. Commun.* **2001**, 763-764.

244. Yang, Q. H.; Yang, J.; Liu, J.; Li, Y.; Li, C., Synthesis and characterization of phosphonic acid functionalized organosilicas with bimodal nanostructure. *Chem. Mater* **2005,** *17,* 3019-3024.

245. Mauder, D.; Akcakayiran, D.; Lesnichin, S. B.; Findenegg, G. H.; Shenderovich, I. G., Acidity of Sulfonic and Phosphonic Acid-Functionalized SBA-15 under Almost Water-Free Conditions. *J. Phys. Chem. C* **2009,** *113*, 19185-19192.

246. Margolese, D.; Melero, J. A.; Christiansen, S. C.; Chmelka, B. F.; Stucky, G. D., Direct syntheses of ordered SBA-15 mesoporous silica containing sulfonic acid groups. *Chem. Mater* **2000,** *12*, 2448-2459.

247. Kanthasamy, R.; Mbaraka, I. K.; Shanks, B. H.; Larsen, S. C., Solid-state MAS NMR studies of sulfonic acid-functionalized SBA-15. *Appl Magn Reson* **2007,** *32*, 513-526.

248. Jin, Y. G.; Qiao, S. Z.; Xu, Z. P.; Yan, Z.; Huang, Y.; da Costa, J. C. D.; Lu, G. Q., Phosphonic acid functionalized silicas for intermediate temperature proton conduction. *J. Mater. Chem* **2009,** *19*, 2363-2372.

249. McKeen, J. C.; Yan, Y. S.; Davis, M. E., Proton Conductivity of Acid-Functionalized Zeolite Beta, MCM-41, and MCM-48: Effect of Acid Strength. *Chem. Mater* **2008,** *20*, 5122-5124.

250. Marschall, R.; Bannat, I.; Caro, J.; Wark, M., Proton conductivity of sulfonic acid functionalised mesoporous materials. *Microporous Mesoporous Mat.* **2007,** *99*, 190-196.

251. Burkett, S. L.; Sims, S. D.; Mann, S., Synthesis of hybrid inorganic-organic mesoporous silica by co-condensation of siloxane and organosiloxane precursors. *Chem. Commun.* **1996,** *11*, 1367-1368.

252. Walcarius, A.; Delacote, C., Rate of access to the binding sites in organically modified silicates. 3. Effect of structure and density of functional groups in mesoporous solids obtained by the co-condensation route. *Chem. Mater* **2003,** *15*, 4181-4192.

253. Macquarrie, D. J., Direct preparation of organically modified MCM-type materials. Preparation and characterisation of aminopropyl-MCM and 2-cyanoethyl-MCM. *Chem. Commun.* **1996**, 1961-1962.

254. Corriu, R. J. P.; Hoarau, C.; Mehdi, A.; Reye, C., Study of the accessibility of phosphorus centres incorporated within ordered mesoporous organic-inorganic hybrid materials. *Chem. Commun.* **2000,** *1*, 71-72.

255. Bibent, N.; Charpentier, T.; Devautour-Vinot, S.; Mehdi, A.; Gaveau, P.; Henn, F.; Silly, G., Solid-State NMR Spectroscopic Studies of Propylphosphonic Acid Functionalized SBA-15 Mesoporous Silica: Characterization of Hydrogen-Bonding Interactions. *Eur. J. Inorg. Chem.* **2013,** *13*, 2350-2361.

256. Bibent, N.; Mehdi, A.; Silly, G.; Henn, F.; Devautour-Vinot, S., Proton Conductivity versus Acidic Strength of One-Pot Synthesized Acid-Functionalized SBA-15 Mesoporous Silica. *Eur. J. Inorg. Chem.* **2011,** *21*, 3214-3225.

257. Green, C. C.; Lochmann, S. E.; Straus, D. L., Acute toxicity of isopropyl methylphosphonic acid, a breakdown product of sarin, to eggs and fry of golden shiner and channel catfish. *J. Toxicol. Environ. Health* **2005,** *68*, 141-149.

258. Munro, N. B.; Talmage, S. S.; Griffin, G. D.; Waters, L. C.; Watson, A. P.; King, J. F.; Hauschild, V., The sources, fate, and toxicity of chemical warfare agent degradation products. *Environ Health Perspect.* **1999,** *107*, 933-974.

259. Bossle, P. C.; Martin, J. J.; Sarver, E. W.; Sommer, H. Z., High-performance liquid chromatography analysis of alkyl methyl phosphonic acids by derivatization. *J. Chromatogr.* **1983,** *267*, 209-212.

260. Zeidan, R. K.; Hwang, S. J.; Davis, M. E., Multifunctional heterogeneous catalysts: SBA-15-containing primary amines and sulfonic acids. *Angew. Chem. Int. Ed.* **2006,** *45*, 6332-6335.

261. Izquierdo-Barba, I.; Sousa, E.; Doadrio, J. C.; Doadrio, A. L.; Pariente, J. P.; Martinez, A.; Babonneau, F.; Vallet-Regi, M., Influence of mesoporous structure type on the controlled delivery of drugs: release of ibuprofen from MCM-48, SBA-15 and functionalized SBA-15. *J.Sol-Gel Sci. Technol* **2009,** *50*, 421-429.

262. Lyssenko, K. A.; Grintselev-Knyazev, G. V.; Antipin, M. Y., Nature of the P-O bond in diphenylphosphonic acid: experimental charge density and electron localization function analysis. *Mendeleev Commun.* **2002,** *12*, 128-130.

263. Mafra, L.; Cendak, T.; Schneider, S.; Wiper, P. V.; Pires, J.; Gomes, J. R. B.; Pinto, M. L., Structure of Chemisorbed CO_2 Species in Amine-Functionalized Mesoporous Silicas Studied by Solid-State NMR and Computer Modeling. *J. Amer. Chem. Soc.* **2017,** *139*, 389-408.

264. Uribe, E. C.; Mason, H. E.; Shusterman, J. A.; Lukens, W. W., Organic layer formation and sorption of U(VI) on acetamide diethylphosphonate-functionalized mesoporous silica. *Dalton Trans.* **2017,** *46*, 5441-5456.

265. Carbonneau, C.; Frantz, R.; Durand, J. O.; Granier, M.; Lanneau, G. F.; Corriu, R. J. P., New silica-based hybrid organic-inorganic solids containing oligoarylene-vinylene fluorophore-terminated phosphonates. *New J. Chem.* **2001,** *25*, 1398-1402.

266. Dudarko, O. A.; Mel'nyk, I. V.; Zub, Y. L.; Chuiko, A. A.; Dabrowski, A., Template-directed synthesis of mesoporous silicas containing phosphonic acid derivatives in the surface layer. *Inorg. Mater.* **2006,** *42*, 360-367.

267. Wang, P. Y.; Zhao, L.; Wu, R.; Zhong, H.; Zou, H. F.; Yang, J.; Yang, Q. H., Phosphonic Acid Functionalized Periodic Mesoporous Organosilicas and Their Potential Applications in Selective Enrichment of Phosphopeptides. *J. Phys. Chem. C* **2009,** *113*, 1359-1366.

268. Pan, Y. C.; Tsai, H. H. G.; Jiang, J. C.; Kao, C. C.; Sung, T. L.; Chiu, P. J.; Saikia, D.; Chang, J. H.; Kao, H. M., Probing the Nature and Local Structure of Phosphonic Acid Groups Functionalized in Mesoporous Silica SBA-15. *J. Phys. Chem. C* **2012,** *116*, 1658-1669.

269. Aiello, D.; Folliet, N.; Laurent, G.; Testa, F.; Gervais, C.; Babonneau, F.; Azais, T., Solid state NMR characterization of phenylphosphonic acid encapsulated in SBA-15 and aminopropyl-modified SBA-15. *Microporous Mesoporous Mat.* **2013,** *166*, 109-116.

270. Lee, Y. J.; Bingol, B.; Murakhtina, T.; Sebastiani, D.; Meyer, W. H.; Wegner, G.; Spiess, H. W., High-resolution solid-state NMR studies of poly(vinyl phosphonic acid) proton-conducting polymer: Molecular structure and proton dynamics. *J Phys Chem B* **2007,** *111*, 9711-9721.

271. Ren, J.; Eckert, H., DQ-DRENAR: A new NMR technique to measure site-resolved magnetic dipole-dipole interactions in multispin-1/2 systems: Theory and validation on crystalline phosphates. *J. Chem. Phys.* **2013,** *138*, 164201.

272. Uribe, E.; Mason, H.; Shusterman, J.; Bruchet, A.; Nitsche, H., Probing the interaction of U(VI) with phosphonate-functionalized mesoporous silica using solid-state NMR spectroscopy *Dalton Trans.,* **2016,** *45*, 10447-10458.

273. Kim, H. J.; Yang, H. C.; Chung, D. Y.; Yang, I. H.; Choi, Y. J.; Moon, J. K., Functionalized Mesoporous Silica Membranes for CO_2 Separation Applications. *J. Chem.* **2015,** *2015*, 202867.

274. VanRossum, B. J.; Boender, G. J.; deGroot, H. J. M., High magnetic field for enhanced proton resolution in high-speed CP/MAS heteronuclear ^{1}H-^{13}C dipolar-correlation spectroscopy. *J. Magn. Reson., Ser. A* **1996,** *120*, 274-277.

275. Hayashi, S.; Hayamizu, K., Chemical shift standards in high resolution solid-state NMR ^{13}C, ^{29}Si and ^{1}H nuclei. *Bull. Chem. Soc. Jpn.* **1991,** *64*, 685-687.

276. Cattaneo, A. S.; Ferrara, C.; Villa, D. C.; Angioni, S.; Milanese, C.; Capsoni, D.; Grandi, S.; Mustarelli, P.; Allodi, V.; Mariotto, G.; Brutti, S.; Quartarone, E., SBA-15 mesoporous silica highly functionalized with propylsulfonic pendants: A thorough physico-chemical characterization. *Microporous Mesoporous Mat.* **2016,** *219*, 219-229.

277. Protsak, I. S., Morozov, Y.M., Dong, W., Le.Z., Zhang.D., Henderson.I.M.,, A ^{29}Si, ^{1}H, and ^{13}C solid-state NMR study on the surface species of various depolymerized organosiloxanes at silica surface. *Nanoscale. Res. Lett* **2019,** *14*, 160.

278. Trebosc, J.; Wiench, J. W.; Huh, S.; Lin, V. S. Y.; Pruski, M., Solid-state NMR study of MCM-41-type mesoporous silica nanoparticles. *J. Amer. Chem. Soc.* **2005,** *127*, 3057-3068.

279. Grunberg, B.; Emmler, T.; Gedat, E.; Shenderovich, I.; Findenegg, G. H.; Limbach, H. H.; Buntkowsky, G., Hydrogen bonding of water confined in mesoporous silica MCM-41 and SBA-15 studied by ^{1}H solid-state NMR. *Chem. Eur. J.* **2004,** *10*, 5689-5696.

280. Gonzalez, L.; Mo, O.; Yanez, M.; Elguero, J., Very strong hydrogen bonds in neutral molecules: The phosphinic acid dimers. *J. Chem. Phys.* **1998,** *109*, 2685-2693.

281. Mehring, M.; Schurmann, M.; Ludwig, R., tert-butylphosphonic acid: From the bulk to the gas phase. *Chem. Eur. J.* **2003,** *9*, 837-849.

282. Nolde, C.; Schurmann, M.; Mehring, M., A sterically hindered phosphonic acid with a hydrogen-bonded cage structure: 14-tert-Bu-2,6-MeS_2-$C_6H_2P(O)(OH)_2.H_2O_4$. *Z. Anorg. Allg. Chem.* **2007,** *633*, 142-150.

283. Louis D. Quin, A. J. W., *Practical Interpretation of ^{31}P NMR Spectra and Computer-Assisted Structure Verification*. Advanced Chemistry Development: Toronto, **2004**.

284. Pan, Y.-C.; Tsai, H.-H. G.; Jiang, J.-C.; Kao, C.-C.; Sung, T.-L.; Chiu, P.-J.; Saikia, D.; Chang, J.-H.; Kao, H.-M., Probing the Nature and Local Structure of Phosphonic Acid Groups Functionalized in Mesoporous Silica SBA-15. *J. Phys. Chem. C* **2012,** *116*, 1658-1669.

285. McLauchlan, K. A., Nuclear magnetic resonance spectroscopy - A physicochemical view. *Nature* **1983,** *304*, 668-668.

286. Akbey, U.; Graf, R.; Peng, Y. G.; Chu, P. P.; Spiess, H. W., Solid-State NMR Investigations of Anhydrous Proton-Conducting Acid-Base Poly(acrylic acid)-Poly(4-vinyl pyridine) Polymer Blend System: A Study of Hydrogen Bonding and Proton Conduction. *J. Polym. Sci., Part B: Polym. Phys.* **2009,** *47*, 138-155.

287. Brown, S. P.; Schnell, I.; Brand, J. D.; Mullen, K.; Spiess, H. W., The competing effects of pi-pi packing and hydrogen bonding in a hexabenzocoronene carboxylic acid derivative: A ^{1}H solid-state MAS NMR investigation. *Phys. Chem. Chem. Phys* **2000,** *2*, 1735-1745.

288. Spiess, H. W., Deutron NMR- A new tool for studying chain mobility and orientation in polymers. *Adv. Polym. Sci.* **1985,** *66*, 23-58.

289. Wang, L., Menakath, A., Han, F., Wang, Y., Zavalij, P. Y., Brown, S. P., Iuga, D., Wang, C., Xu, K., Eichhorn, B. W., Identifying the components of the solid-electrolyte interphase in Li-ion batterries. *Nat. Chem.* **2019,** *11*, 789-796.

290. Verma, P.; Maire, P.; Novak, P., A review of the features and analyses of the solid electrolyte interphase in Li-ion batteries. *Electrochim. Acta* **2010,** *55*, 6332-6341.

291. Wang, A. P.; Kadam, S.; Li, H.; Shi, S. Q.; Qi, Y., Review on modeling of the anode solid electrolyte interphase (SEI) for lithium-ion batteries. *Npj Comput. Mater.* **2018,** *4*, 15.

292. Endo, M.; Kim, C.; Nishimura, K.; Fujino, T.; Miyashita, K., Recent development of carbon materials for Li ion batteries. *Carbon* **2000,** *38*, 183-197.

293. Wakihara, M., Recent developments in lithium ion batteries. *Mater. Sci. Eng., R* **2001,** *33*, 109-134.

294. Ohzuku, T.; Ueda, A., Why transition metal di oxide are the most attractive materials for batteries. *Solid State Ionics* **1994,** *69*, 201-211.

295. Morgan, D.; Van der Ven, A.; Ceder, G., Li conductivity in Li_xMPO_4 (M = Mn, Fe, Co, Ni) olivine materials. *Electrochem. Solid-State Lett.* **2004,** *7*, A30-A32.

296. Lee, Y. S.; Sun, Y. K.; Adachi, K.; Yoshio, M., Synthesis and electrochemical characterization of orthorhombic $LiMnO_2$ material. *Electrochim. Acta* **2003,** *48*, 1031-1039.

297. Ozawa, K., Lithium-ion rechargeable batterries with $LiCOO_2$ and carbon electrodes-The $LiCOO_2$ C system. *Solid State Ionics* **1994,** *69*, 212-221.

298. Thackeray, M. M.; Dekock, A.; Rossouw, M. H.; Liles, D.; Bittihn, R.; Hoge, D., Spinel electrodes from the Li-Mn-O system for rechargeable lithium battery applications. *J. Electrochem. Soc.* **1992,** *139*, 363-366.

299. Paolo Prosini, P., *Iron Phosphate Materials as Cathodes for Lithium Batteries*. Springer London, **2011**.

300. Guyomard, D.; Tarascon, J. M., Rocking chair or lithium-ion rechargeable lithium batteries. *Adv. Mater.* **1994,** *6*, 408-412.

301. Peled, E., The electrochemical behavior of alkali and alkaline earth metals in non-aqueous battery systems- The solid electrolyte interphase model. *J. Electrochem. Soc.* **1979,** *126*, 2047-2051.

302. Fong, R.; Vonsacken, U.; Dahn, J. R., Studies of lithium intercalation into carbons using nonaqueous electrochemical cells. *J. Electrochem. Soc.* **1990,** *137*, 2009-2013.

303. Andersson, A. M.; Edstrom, K., Chemical composition and morphology of the elevated temperature SEI on graphite. *J. Electrochem. Soc.* **2001,** *148*, A1100-A1109.

304. Peled, E.; Tow, D. B.; Merson, A.; Gladkich, A.; Burstein, L.; Golodnitsky, D., Composition, depth profiles and lateral distribution of materials in the SEI built on HOPG-TOF SIMS and XPS studies. *J. Power Sources* **2001,** *97-8*, 52-57.

305. Aurbach, D.; Markovsky, B.; Shechter, A.; EinEli, Y.; Cohen, H., A comparative study of synthetic graphite and Li electrodes in electrolyte solutions based on ethylene carbonate dimethyl carbonate mixtures. *J. Electrochem. Soc.* **1996,** *143*, 3809-3820.

306. Edstrom, K.; Herstedt, M.; Abraham, D. P., A new look at the solid electrolyte interphase on graphite anodes in Li-ion batteries. *J. Power Sources* **2006,** *153*, 380-384.

307. Aurbach, D.; Eineli, Y.; Chusid, O.; Carmeli, Y.; Babai, M.; Yamin, H., The correlation between the surface chemistry and the performance of Li-carbon intercalation anodes for rechargeable rocking-chair type batteries. *J. Electrochem. Soc.* **1994,** *141*, 603-611.

308. Aurbach, D.; Levi, M. D.; Levi, E.; Schechter, A., Failure and stabilization mechanisms of graphite electrodes. *J. Phys. Chem. B* **1997,** *12*, 2195-2206.

309. Zhuang, G. R. V.; Ross, P. N., Analysis of the chemical composition of the passive film on Li-ion battery anodes using attentuated total reflection infrared Spectroscopy. *Electrochem. Solid-State Lett.* **2003,** *6*, A136-A139.

310. Aurbach, D.; Gofer, Y., The behavior of lithium electrodes in mixture of alkyl carbonates and ethers. *J. Electrochem. Soc.* **1991,** *138*, 3529-3536.

311. Kang, S. H.; Abraham, D. P.; Xiao, A.; Lucht, B. L., Investigating the solid electrolyte interphase using binder-free graphite electrodes. *J. Power Sources* **2008,** *175*, 526-532.

312. Zhuang, G. R. V.; Xu, K.; Yang, H.; Jow, T. R.; Ross, P. N., Lithium ethylene dicarbonate identified as the primary product of chemical and electrochemical reduction of EC in 1.2 m $LiPF_6$/EC : EMC electrolyte. *J. Phys. Chem. B* **2005,** *109*, 17567-17573.

313. Nie, M. Y.; Chalasani, D.; Abraham, D. P.; Chen, Y. J.; Bose, A.; Lucht, B. L., Lithium Ion Battery Graphite Solid Electrolyte Interphase Revealed by Microscopy and Spectroscopy. *J. Phys. Chem. C* **2013,** *117*, 1257-1267.

314. Dedryvere, R.; Gireaud, L.; Grugeon, S.; Laruelle, S.; Tarascon, J. M.; Gonbeau, D., Characterization of lithium alkyl carbonates by X-ray photoelectron spectroscopy: Experimental and theoretical study. *J. Phys. Chem. B* **2005,** *109*, 15868-15875.

315. Shi, F. F.; Ross, P. N.; Zhao, H.; Liu, G.; Somorjai, G. A.; Komvopoulos, K., A Catalytic Path for Electrolyte Reduction in Lithium-Ion Cells Revealed by in Situ Attenuated Total Reflection-Fourier Transform Infrared Spectroscopy. *J. Amer. Chem. Soc.* **2015,** *137*, 3181-3184.

316. Ota, H.; Wang, X. M.; Yasukawa, E., Characterization of lithium electrode in lithium imides/ethylene carbonate, and cyclic ether electrolytes -I. Surface morphology and lithium cycling efficiency. *J. Electrochem. Soc.* **2004,** *151*, A427-A436.

317. Michan, A. L.; Leskes, M.; Grey, C. P., Voltage Dependent Solid Electrolyte lnterphase Formation in Silicon Electrodes: Monitoring the Formation of Organic Decomposition Products. *Chem. Mater* **2016,** *28*, 385-398.

318. Gireaud, L.; Grugeon, S.; Laruelle, S.; Pilard, S.; Tarascon, J. M., Identification of Li battery electrolyte degradation products through direct synthesis and characterization of alkyl carbonate salts. *J. Electrochem. Soc.* **2005,** *152*, A850-A857.

319. Aurbach, D.; Daroux, M. L.; Faguy, P. W.; Yeager, E., Identification of surface-films formed on lithium in propylene carbonate solutions. *J. Electrochem. Soc.* **1987,** *134*, 1611-1620.

320. Xu, K.; Zhuang, G. R. V.; Allen, J. L.; Lee, U.; Zhang, S. S.; Ross, P. N.; Jow, T. R., Syntheses and characterization of lithium alkyl mono- and dicarbonates as components of surface films in Li-lon batteries. *J. Phys. Chem. B* **2006,** *110*, 7708-7719.

321. Seo, D. M.; Chalasani, D.; Parimalam, B. S.; Kadam, R.; Nie, M. Y.; Lucht, B. L., Reduction Reactions of Carbonate Solvents for Lithium Ion Batteries. *ECS Electrochem. Lett.* **2014,** *3*, A91-A93.

322. Blanc, F.; Leskes, M.; Grey, C. P., In Situ Solid-State NMR Spectroscopy of Electrochemical Cells: Batteries, Supercapacitors, and Fuel Cells. *Acc. Chem. Res.* **2013,** *46*, 1952-1963.

323. Pecher, O.; Carretero-Gonzalez, J.; Griffith, K. J.; Grey, C. P., Materials' Methods: NMR in Battery Research. *Chem. Mater* **2017,** *29*, 213-242.

324. Haber, S.; Leskes, M., What Can We Learn from Solid State NMR on the Electrode-Electrolyte Interface? *Adv. Mater.* **2018,** *30*, 1706496.

325. Leskes, M.; Moore, A. J.; Goward, G. R.; Grey, C. P., Monitoring the Electrochemical Processes in the Lithium-Air Battery by Solid State NMR Spectroscopy. *J. Phys. Chem. C* **2013,** *117*, 26929-26939.

326. Meyer, B. M.; Leifer, N.; Sakamoto, S.; Greenbaum, S. G.; Grey, C. P., High field multinuclear NMR investigation of the SEI layer in lithium rechargeable batteries. *Electrochem. Solid-State Lett.* **2005,** *8*, A145-A148.

327. Hu, Y. Y.; Liu, Z. G.; Nam, K. W.; Borkiewicz, O. J.; Cheng, J.; Hua, X.; Dunstan, M. T.; Yu, X. Q.; Wiaderek, K. M.; Du, L. S.; Chapman, K. W.; Chupas, P. J.; Yang, X. Q.; Grey, C. P., Origin of additional capacities in metal oxide lithium-ion battery electrodes. *Nat. Mater.* **2013,** *12*, 1130-1136.

328. Fulmer, G. R.; Miller, A. J. M.; Sherden, N. H.; Gottlieb, H. E.; Nudelman, A.; Stoltz, B. M.; Bercaw, J. E.; Goldberg, K. I., NMR Chemical Shifts of Trace Impurities: Common Laboratory Solvents, Organics, and Gases in Deuterated Solvents Relevant to the Organometallic Chemist. *Organometallics* **2010,** *29*, 2176-2179.

329. Jin, Y. T.; Kneusels, N. J. H.; Marbella, L. E.; Castillo-Martinez, E.; Magusin, P.; Weatherup, R. S.; Jonsson, E.; Liu, T.; Paul, S.; Grey, C. P., Understanding Fluoroethylene Carbonate and Vinylene Carbonate Based Electrolytes for Si Anodes in Lithium Ion Batteries with NMR Spectroscopy. *J. Amer. Chem. Soc.* **2018,** *140*, 9854-9867.

330. Leskes, M.; Kim, G.; Liu, T.; Michan, A. L.; Aussenac, F.; Dorffer, P.; Paul, S.; Grey, C. P., Surface-Sensitive NMR Detection of the Solid Electrolyte Interphase Layer on Reduced Graphene Oxide. *J. Phys. Chem. Lett.* **2017,** *8*, 1078-1085.

331. https://researchbriefings.parliament.uk/ResearchBriefing/Summary/POST-PN-0596, . **2019**.

332. Paruzzo, M. F., Walder, J. B., Emsley, L., Line narrowing in ^{1}H NMR of powdered organic solids with TOP-CT-MAS experiments at ultra-fast MAS. *J. Magn. Reson., Ser. A* **2019,** *305*, 131-137.